The role of microstructure on strain localization in the near-alpha titanium alloy TIMETAL®834

A thesis submitted to
The University of Manchester
for the degree of
Doctor of Philosophy in Faculty of Science and Engineering

2020

Claudius Dichtl

Faculty of Science and Engineering
School of Natural Sciences
Department of Materials

Blank page.

List of contents

Word count: 45'031

List of tables

List of figures[1]

[1] Please note that the figures for each manuscript are self-contained and so are not listed here.

Abbreviations

APT	Atom Probe Tomography
at.%	Atomic Percentages
BCC	Body Centred Cubic
BSE	Back Scattered Electron
CASINO	monte CArlo SImulation of electroN trajectory in sOlids
CDF	Cold Dwell Fatigue
CFRP	Carbon Fibre Reinforced Polymers
CP modelling	Crystal Plasticity modelling
CP titanium	Commercially Pure titanium
CRSS	Critically Resolved Shear Stress
DaVis	La Vision Digital Image Correlation Software
DIC	Digital Image Correlation
EBSD	Electron Backscatter Diffraction
EPMA	Electron Probe Micro Analysis
FEM	Finite Element Modelling
FFT	Fast Fourier Transform
FIB	Focused Ion Beam
HCP	Hexagonal Close Packed
HR-DIC	High Resolution Digital Image Correlation
LCF	Low Cycle Fatigue
RDR	Relative Displacement Ratio
RSS	Resolved Shear Stress
RT	Room Temperature
SAED	Selective Area Electron Diffraction
SDD	Silicon Drift Detector
SE	Secondary Electron
SEM	Scanning Electron Microscopy
SPP	Second Phase Particle
SRO	Short Range Ordering
STA	Slip Trace Analysis
TEM	Transmission Electron Microscopy
Tm	Melting Temperature/Melting Point
UTS	Ultimate Tensile Stress
WDS	Wavelength-Dispersive X-Ray Spectroscopy
wt.%	Weight Percentages
γ_{eff}	Effective Shear Strain
ε_{eff}	Effective Strain
$\sigma_{0.2\%}$	0.2% proof stress

Abstract

Near-α titanium alloys for applications at elevated temperatures like TIMETAL®834 can exhibit susceptibility to cold dwell fatigue (CDF), a type of failure due to cyclic loading with superimposed dwell or load-hold periods. The reduction in the number of cycles to failure observed is associated with room temperature creep, or cold creep, during the dwell cycles. In this study, the effect of the microstructure on the deformation mechanisms during initial loading to stresses below macroscopic yield and holds of up to 10 minutes were investigated. The selected loading conditions are similar to the dwell cycle of CDF tests and therefore results of these experiments are relevant to the mechanisms of cold-creep and CDF deformation. The material studied was TIMETAL®834 with a bi-modal microstructure, and the microstructures investigated enabled comparisons between materials with large and small prior β grain sizes, and with coarse and fine transformation products.

The first part of the study was an in-depth microstructural characterisation of the material. Correlative microscopy, using Electron Probe Micro-Analysis (EPMA), Atom Probe Tomography (APT) and Transmission Electron Microscopy (TEM) characterisation, revealed that primary α-grains grew during cooling after the solution heat treatment, with element partitioning leading to the formation of a core-shell structure. Microchemical analysis has shown that the shell is depleted in α stabilising and enriched in β stabilising elements compared to the core and, as a result of this partitioning effect, α_2 precipitates are absent in the shell region.

In the second part of the study, local slip mechanisms were investigated at the sub-grain length scale after loading to three different stress levels below the macroscopic proof stress. In-situ High-Resolution Digital Image Correlation (HRDIC), based on SEM imaging and coupled with Electron Back Scatter Diffraction data, was used to determine the strain distributions and local, quantifiable strain values. Slip Trace Analysis (STA) was used to determine the activated slip systems at each load step. To help explain the experimental observations and improve the mechanistic understanding for slip activation under the applied loading conditions, crystal plasticity modelling was used to determine the local stresses in the microstructures.

The analysis of these experiments showed that, for all material conditions, slip is observed at stress levels as low as 70% of the 0.2% yield stress., Material with larger prior β-grains exhibited higher strain values and higher deformation heterogeneity than material with finer prior β-grains at stresses close to the 0.2% proof stress, but no difference could be measured at lower stress levels. Regarding the secondary alpha phase, produced by transformation on cooling, it was found that a coarser grain structure leads to higher strain values and local strain concentrations at all loading steps, which suggests that a coarser grain structure leads to a stronger susceptibility to cold creep deformation. Initial plastic deformation was localised in the primary α grains, suggesting that they have lower yield strength than the secondary alpha colonies. Activation of slip in secondary α colonies was more difficult for a finer transformation product, which explains its superior resistance against plastic deformation during initial loading, and during the 10-minute load hold periods. At the onset of plastic deformation, basal slip was the dominant slip mode for all microstructures. While the elastic anisotropy of titanium increases the RSS values for basal slip compared to prismatic slip, based on this observation the difference in elastic properties could not explain the early activation of basal slip, leading to the conclusion that CRSS values must be lower for basal slip.

The findings are discussed in view of the proposed mechanisms for CDF, the correlation of microstructural features and CDF behaviour, and the implications for modelling techniques used to predict CDF performance.

Declaration

No portion of the work referred to in the thesis has been submitted in support of an application for another degree or qualification of this or any other university or other institute of learning.

Copyright Statement

Acknowledgements

I would like to thank my academic supervisors Prof. Michael Preuss and Prof. João Quinta da Fonseca for all their advice, continuous support, and patience during my PhD. My industrial supervisors Rebecca Sandala, Matthew Thomas and Iain Berment-Parr for supporting me during my PhD studies and helping me understand the industrial relevance of our academic research. Rebecca Sandala, Kate Fox and David Rugg for the great experience during my internship at Rolls Royce. Special thanks to Prof. Dave Rugg for being a great mentor and taking the time to introduce me to the current challenges in the aero-engine industry.

Special thanks to David Lunt for the help with the experimental work, as well as data analysis and especially for the support during the write-up period. Rhys Thomas, Michael Atkinson, Bartosz Barzdajn and Adam Plowman for their help with the data analysis, crystal plasticity simulations and your support during the challenging moments of coding and debugging. I would also like to thank Ken Gyves, Dave Strong and Michael Faulkner who provided me with training and technical support throughout my PhD.

Many thanks to my friends in the CDT and the office. Special thanks to Zaheen Shah, Ben Jones, Emmanouil Stavroulakis and Yudong Peng for all the nice moments we shared in and out of the office.

Maria, thank you for supporting me and being there for me, especially during the difficult stretches of my PhD. Your support helped my to get through these stressful times.

Last but not least, my most heartfelt thanks to my parents, Emmeran and Gudrun, for supporting me not only during my PhD program but throughout my complete education.

1 Introduction

1.1 Application of titanium alloys

Titanium is a metallic element with a density of 4.5 g/cm³, which lies in between the densities of aluminium (2.7 g/cm³) and steel (~8.0 g/cm³). Several parameters make titanium and titanium alloys the material of choice for a wide range of structural applications, namely its superb corrosion resistance, the high specific strength (ratio of strength to density) and the high strength, which is maintained even at elevated temperatures of up to 600°C [1]–[4]. Due to the good corrosion resistance in various kinds of aggressive environments, e.g. sea-water and aqueous acid environments, commercially pure (CP) titanium is widely used in the chemical, food, and oil and gas industry [5]. Based on its superior properties the possible applications of titanium alloys as a structural material appear unlimited, but due to its high cost, industrial applications are narrowed down to high price applications, including high-performance sports equipment, racing sports, and mainly medical and aerospace applications. High cost for Ti-alloys arises from the costly pyrometallurgical process to extract metallic Ti (Kroll process), the complex melting and thermo-mechanical processing routes, the high waste rate, and the costs for expensive alloying elements (e.g. Nb, Mo, V). Therefore, there is a strong research interest in developing new processing routes to lower the cost of titanium and enabling a wider range of applications for titanium alloys [6]–[14].

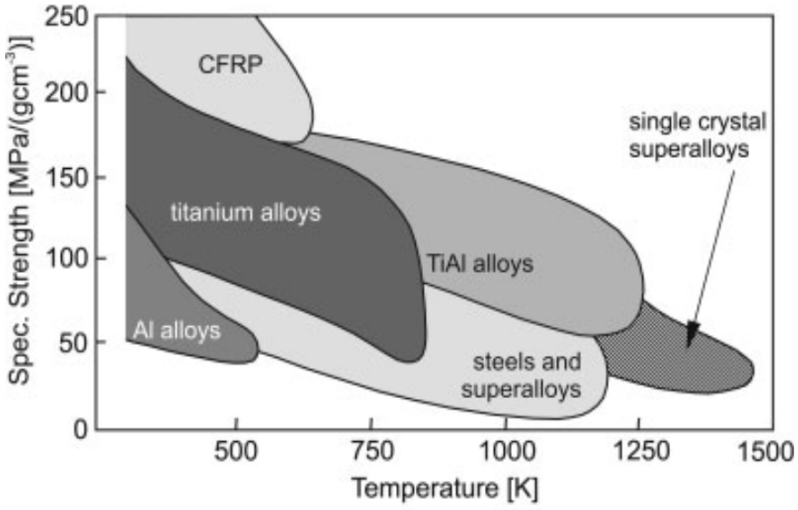

Fig. 1-1: Plot of the specific strength as a function of the applicable service temperature for structural materials used in aero engines. Image: [15]

Initially, titanium alloys were developed for military-aerospace applications, but soon after titanium alloys started being used in the civil aerospace industry. One of the main applications for titanium alloys is in aero engines, due to the superior mechanical properties at elevated temperatures in combination with lightweight [16], [17]. In recent years the fraction of titanium alloys in air-frames of civil aircraft has also increased (e.g. 14% in Airbus A350) [18]. This is due to large amounts of carbon fibre reinforced polymers (CFRP) being used in new generations of long-haul aeroplanes. While aluminium, historically the main material for civil airframes, forms a high electrochemical potential with carbon material leading to enhance corrosion rates [19], titanium alloys exhibit electrochemical compatibility to carbon material [20].

Within aero-engines titanium alloys are competing with a series of other structural materials (see **Fig. 1-1**), namely CPRP, aluminium and nickel-based superalloys. CFRPs have a higher specific

strength than titanium alloys, but only for operating temperatures of up to 300°C and therefore are only used in cold parts of the engines, e.g. for replacing titanium as the material of choice for fan-blades [15], [21]. Aluminium alloys have lower specific strength than titanium alloys and CFRP, and have limited maximum operating temperature compared to titanium. Therefore aluminium is not used for engine cores and its main application is for engines casings, e.g. the fan casing [22]. Nickel-based superalloys can be used at higher temperatures than titanium alloys, but have a lower specific strength, making parts heavier than if they were made from titanium alloys [1], [15]. One of the main applications of titanium and nickel alloys is for rotative parts (in this case discs and blades) in aero-engine compressors and nickel also in turbine stages. In the compressor, temperature and pressure increase constantly in the direction of the airflow, up to the inlet to the combustion chamber. Titanium alloys are used on the colder side of the compressor, up to the point where its temperature limit is reached (up to approximately 600°C), from which point onwards nickel-based-super-alloys are used [23]. To reduce the overall weight of engines, one aim is to develop titanium alloys suitable for operation at even higher temperatures, to be able to replace nickel alloys in the compressor. Better high-temperature capacities are also required, as improvements in fuel efficiency in jet engines in the last years have been achieved by increasing the temperature and pressure ratios in the engine core [24].

These requirements led to the development of the near-α titanium alloy TIMETAL®834, with the nominal composition Ti-5.8Al-4Sn-3.5Zr-0.7Nb-0.5Mo-0.35Si-0.06C (wt.%), providing a good compromise between high specific strength, good fatigue properties and superior creep resistance at elevated temperatures. This alloy has been designed for operating temperatures of up to 600°C and therefore is a potential substitute for nickel-base superalloys used for compressor discs and blades in advanced gas turbine jet engines [1]–[4], [25]–[27]. TIMETAL®834 used for disc applications has a low volume fraction of primary α grains of approximately 14 % [28] to 15 % [29], [30], as this results in the ideal combination of high strength, and fatigue and high temperature creep properties. The β-transus temperature of Ti-834 is 1045°C [25], [31], [32] and a volume fraction of 15% primary α-phase can be achieved by heat-treating the alloy at 1015°C [29]. The alloy addition of small amounts of carbon leads to a shallow β-approach curve compared to other α+β titanium-alloys, reducing the sensitivity to temperature variations during heat treatments [25], [26], [33]. The beta-approach curve describes the change of beta-phase volume fraction as a function of the temperature [34]. For a shallow beta-approach curve a given change in temperature results in a smaller change in the beta-phase volume fraction compared to a steeper beta-approach curve. Alloys having a shallow beta-approach curve are advantageous, especially for industrial processes, as it is easier to control the primary α-volume fraction and makes the processing more reliable.

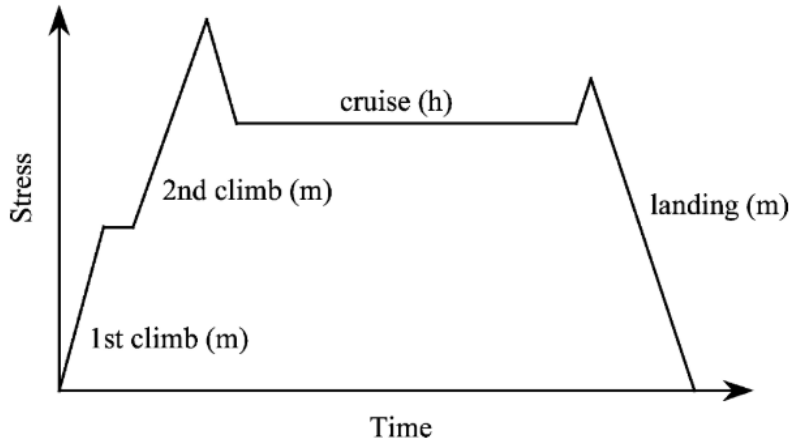

Fig. 1-2: Schematic load curve for rotating parts, e.g. discs and blades, during a single flight cycle for a civil gas turbine engine. Timescales in minutes (m) and hours (h). Image: [35]

It has been demonstrated that TIMETAL®834 can maintain its superior mechanical properties even in access of 600°C and up to 650°C [4]. However, at these temperatures, TIMETAL®834, and in general, all other titanium alloys, display fast oxidation rates and also an increased risk of titanium fires in aero engines. These seem to be the main reason why no titanium alloys with temperature capabilities beyond 600°C have been developed since the introduction of TIMETAL®834. A subject of current research is the development of intermetallic Ti-Al compounds, which stand out for their high specific strength and high operating temperature limits. Current limitations are difficult manufacturing routes, and low ductility and fracture toughness [36], [37].

Similar to most other near-α titanium alloys, it has been observed that TIMETAL®834 is susceptible to cold-dwell-fatigue (CDF) loading conditions. CDF fatigue was observed first for the near-α titanium alloy IMI685, where a superimposed load hold, or dwell period during low cycle fatigue loading conditions, resulted in a significant reduction in cycles to failure (dwell debit) and eventually to failure of a compressor disc during operation [38]. On 30. September 2017, it came to an uncontained disk failure caused by CDF during the cruise phase of an Airbus A380. According to the Bureau of Enquiry and Analysis for Civil Aviation Safety (BEA), one factor contributing to the incident was a lack of understanding for CDF in the titanium alloy Ti-64 [39], showing the necessity for further research in this field to improve understanding for underlaying mechanisms of this failure mechanism. Understanding this specific failure mechanism is of importance for titanium alloys used for rotating parts in jet engines, due to the in-service loading conditions, where one flight cycle represents on CDF load cycle (see **Fig. 1-2**). During take-off, peak stresses are reached for several minutes, after which lower stresses are held for several hours during cruise [35]. During service, parts are exposed to varying loading cycles and temperature profiles, which are different for every aircraft operator; hence covering all different loading conditions by mechanical testing is not possible. Also, results from lab-scale samples cannot be directly transferred to full-scale components. The larger scale and differences in the geometry of real components can result in stress states that are different from uniaxial loading. Furthermore, there are varying stress states and temperatures throughout the parts. This can result in different types of deformation and failure mechanisms. For example, the bore of a disc is typically limited by strength and fatigue, while for the rim of the disc creep is the limiting factor [40].

The mechanical performance of Ti-alloys, especially sensitivity to dwell fatigue, is strongly influenced by microstructure and therefore is strongly related to the thermomechanical processing route. Compressor discs are safety-critical parts of jet engines and failure can result in a risk to airframe integrity [41], [42]; therefore predicting accurately the lifetime of components is crucial. Reducing the uncertainty in lifetime predictions requires a good understanding of all deformation and failure mechanisms. Neither microstructural features nor deformation mechanisms can be considered separately. It is important to understand the correlation between microstructures and failure mechanisms, as this allows the optimisation of alloys, processing routes and lifetime predictions for these applications [43], [44].

1.2 Aims and Objectives

1.2.1 Aims

The aim was to investigate and understand the macroscopic and local plastic deformation behaviour of the near-α titanium alloy TIMETAL®834 with a bimodal microstructure when subjected to load-hold at different stress levels below the macroscopic proof stress at room temperature. The specific load regime was selected due to the similarity to the dwell-cycle/load-hold during cold dwell fatigue (CDF) loading, which is known to significantly influence the life expectance of aero-engine components. Therefore, improving mechanistic understanding for cold creep deformation can give valuable insights to also better understand CDF. Better mechanistic understanding will also potentially improve computational models and enable better lifetime predictions.

In the present work, different microstructures, focussing on the prior-β grain morphology and the transformed β-phase were investigated in respect of their susceptibility to plastic deformation during load-hold experiments at stresses below the macroscopic yield point and the associated deformation mechanisms. As changes to the thermomechanical processing route do not only affect a single but all microstructural features, a full multiscale characterisation of the microstructures was necessary, ranging from the nm-scale (short-range ordering (SRO) and precipitation) up to the mm and cm-scale (prior-β grain size and texture/microtexture). Special focus was placed on element partitioning in primary α grains, which has been observed and reported in the literature before but hasn't been characterised and investigated in depth [2].

1.2.2 Objectives

In this chapter the objectives of this study are highlighted, explaining the details of how the research questions are going to be approached. **Chapter 2** (literature **review)** provides a comprehensive literature review, including an introduction to the microstructure, processing routes, mechanical properties of titanium alloys and the current advance of research regarding initial plastic deformation and cold creep and cold dwell fatigue are also discussed. **Chapter 3** (experimental methods) introduces the initial material received from the manufacturer and the heat treatments applied to it to achieve the desired microstructures, and all experimental techniques used in this study.

Objective 1: The first objective was to create samples with well-defined differences in microstructure, to enable a comparison to be made between different material conditions and to allow investigation of the effect of specific microstructural features on the plastic response of the

[2] A study investigating element partitioning in primary α grains was published by Gao et al. in 2017 [218], which has been overlooked when 'Manuscript 1' was published.

material. In this study samples of TIMETAL®834 with two different prior-β phase morphologies and two different transformation products were analysed. Having samples differing only in one microstructural aspect enabled a pairwise comparison of samples to evaluate the effect of only the specific feature.

Objective 2: The second objective was to fully characterise the microstructure of all four material conditions. The initial baseline characterisation of grain size (primary α grains and colonies) and the room-temperature α/β morphology (lamellae spacing) was based on optical and scanning electron microscopy techniques. The determination of the prior-β grain structure, or high-temperature β-phase, was achieved using a reconstruction algorithm based on the crystallographic orientation maps of the α-phase. Crystallographic orientation maps, which were recorded by EBSD mapping, were also used to analyse texture, micro-texture, local misorientations and Schmid-factor distributions. In each publication (1-3) the baseline characterisation of the analysed areas and samples was included at the beginning of the manuscript. Additional crystallographic orientation maps, which covered larger areas or were recorded in respect to a different sample orientation, are included in the appendix. Low voltage SEM-EDS/EDX was used for an initial analysis of silicides at α/β interfaces (appendix). The first publication contains an in-depth analysis of element segregation in primary α grains and the local effect on precipitation of the α_2-phase. EPMA-WDS was used to characterise and quantify the element segregation and a correlative approach, combining APT and TEM analysis enabled characterisation of α_2-precipitates.

Objective 3: The third objective was to determine the macroscopic mechanical properties of all material conditions. For the mechanical baseline characterisation, stress-strain curves were recorded by tensile testing at a constant strain rate to then determine the 0.2% proof stress of each material condition. The 0.2% proof stress was used as a reference value for defining load steps as relative values of the proof stress for all further mechanical tests that were carried out at stress-levels below the macroscopic yield point.

Objective 4: The fourth objective was to analyse local plastic deformation for applied stresses below the macroscopic yield point. For applying the stresses, an in-situ setup was used, that allowed imaging the sample during the mechanical test. Two different experimental techniques were used for analysing local slip events: firstly a slip trace observation technique based on optical microscopy was used, which enables the resolution of single slip bands, while imaging large areas, but which doesn't provide any quantification of strain. Secondly, High-Resolution Digital Image Correlation (HRDIC) was used for strain mapping with a sub-micron spatial resolution, while also providing quantifiable strain values. The samples of all material conditions were subjected to a 10-minute load hold at 3 stress levels below macroscopic yield and analysed by HRDIC. Results of these experiments are presented and discussed in paper 2 & 3. In Paper 2 a pairwise comparison, coarse/fine transformation product and the two different β-grain morphologies, was carried out using three samples, focussing on the differences in strain histograms between the material conditions and the localisation of slip bands in the constituents. A more detailed analysis of the local plasticity in the two constituents was done in Paper 3, analysing only two samples and focussing on the differences between a coarse and fine transformation product.

Objective 5: The fifth objective was to identify the active slip systems operating during initial plastic deformation and investigate the change of active slip systems with increasing stress levels. Slip

systems were identified using Slip Trace Analysis (STA) technique in combination with relative displacement (RDR) analysis, which was both based on the HRDIC data and the correlated crystallographic orientation maps. The results of the slip system analysis are presented in Paper 3, comparing differences in slip activity for material conditions with coarse and fine transformation product.

Objective 6: The sixth objective was to improve the mechanistic understanding of the deformation mechanisms, which have been observed experimentally, by correlating experimental and modelling results. The crystal plasticity framework DAMASK was used to determine the local elastic stress states for the microstructures and loading conditions of the HRDIC experiments. The main focus was on how elastic anisotropy of the α-phase (HCP) in titanium affects local stress states just before the onset of local plasticity. Additionally, residual stresses, caused during cooling due to the anisotropy of the thermal expansion coefficient, were simulated. The effect of the thermal residual stresses on the early local plasticity was investigated by combining the simulation of thermal residual stresses with the applied stresses.

2 Literature Review

2.1 Titanium and titanium alloys

2.1.1 Crystallography of Titanium

Titanium is an allotropic material, which means that it can exist in two different crystal structures, namely the hexagonal-closed-packed **HCP** α-phase and the body-centred cubic **BCC** β-phase. For pure titanium, the α-phase is stable for temperatures below 882°C and the β-phase is stable above this temperature [5], [45], [46].

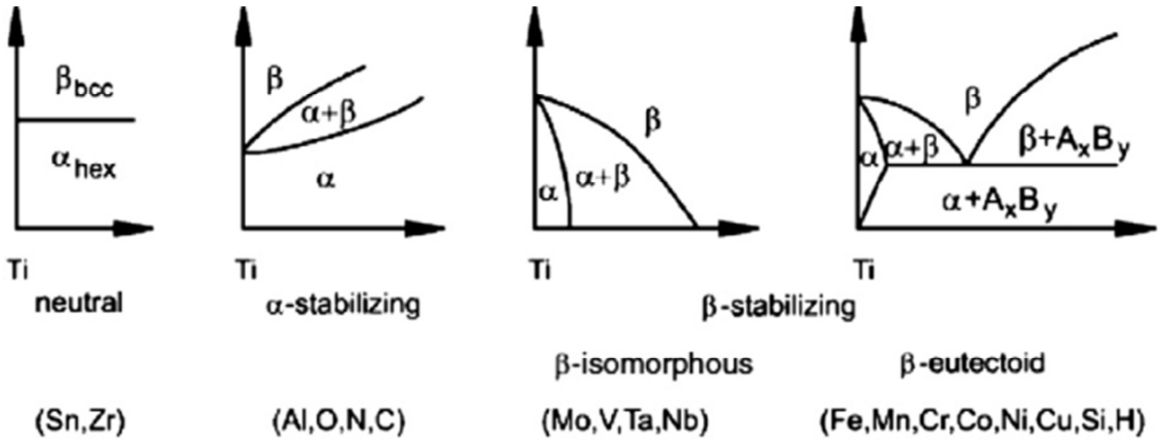

Fig. 2-1: Phase diagrams showing the effect of different groups of alloying elements. The alloying elements are divided into 'neutral', 'α-stabilizing' and 'β-stabilizing' elements [47].

The addition of alloying elements leads to the formation of two-phase regions in the phase diagram (**Fig. 2-1**) for all but the neutral alloying elements. Consequently, for titanium alloys the α- and β-phase can be stable at the same time. Therefore, two transition temperatures can be defined, namely the α-transus (α↔α+β) and the β-transus (α+β↔β) temperature [46]. For Ti-alloys that contain α- and β-phase at room temperature (RT), only the β-transus temperature is important for determining processing routes, as the α-transus would only be reached for temperatures below RT, where diffusion rates and transformations are slow. In two-phase regions, the equilibrium fraction of each phase can be calculated based on the phase diagram using the lever rule.

The phase fractions and transitions temperatures are strongly influenced by the addition of alloying elements. Elements that increase the β-transus temperature, and therefore increase the stability of the α-phase at elevated temperatures, are called 'α-stabilising' elements; on the other side, elements that reduce the β-transus temperature are called 'β-stabilising' elements. The 'neutral' alloying elements do not affect the transition temperatures. Titanium alloys that are highly β-stabilized can consist completely of β-phase at room temperature [5], [47].

The effects of alloy additions have often been investigated for binary systems consisting of Ti and one further alloying element. However, it has been observed that alloying elements may be interacting with each other in more complex Ti alloys. For example, in binary alloys, Sn is considered to be a neutral alloying element, as it does not affect the transus temperatures, while on the other hand, in Ti-Al-Sn alloys, Sn acts as an α-stabiliser, as it can replace Al in the ordered Ti_3Al phase [5]. Therefore it is important to keep in mind that the interactions between all elements need to be considered to understand more complex, industrial, alloys [5].

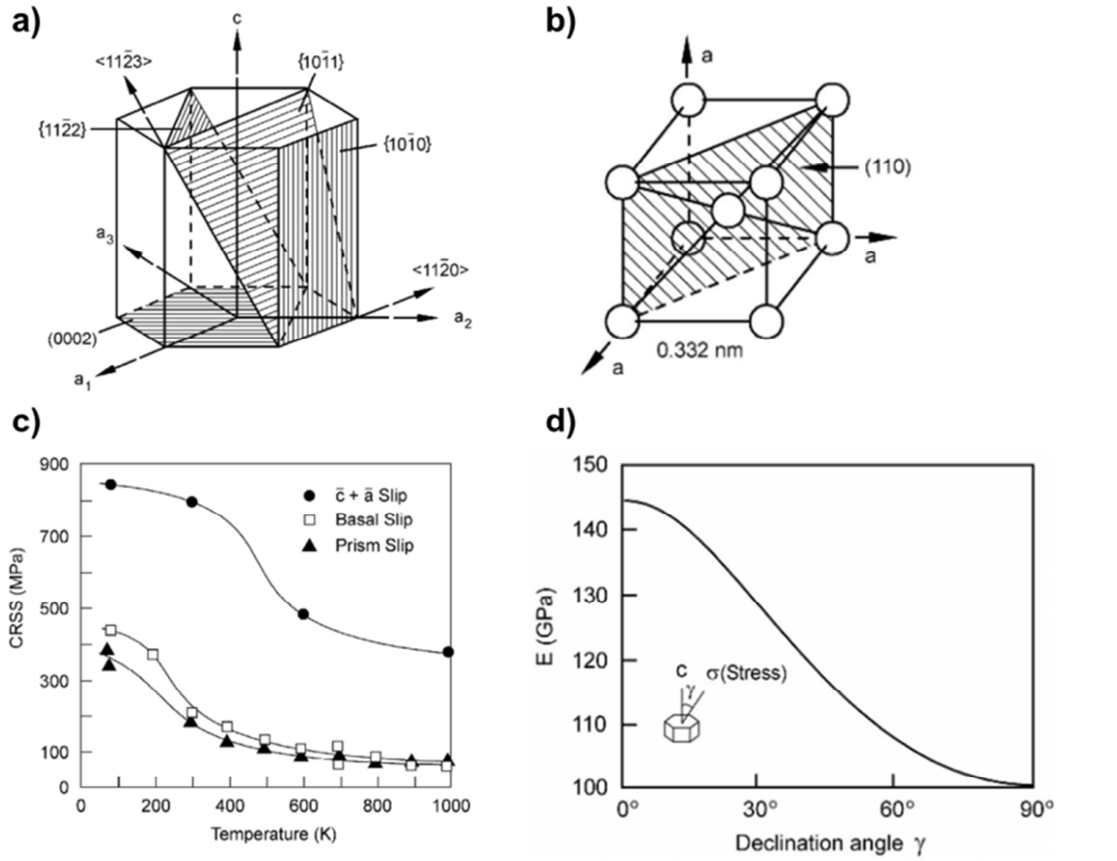

Fig. 2-2: Crystal structure and slip systems of a) HCP structures and b) BCC structures. c) The critical-resolved-shear-stress CRSS of 3 different slip systems as a function of temperature in single crystals of Ti-6.6Al. d) The elastic modulus of α-phase changes as a function of the declination angle from the c-axis in CP-titanium [5].

The α-phase has anisotropic elastic and plastic properties (see paragraph 2.3.2). The elastic modulus is the lowest (~100 GPa) for loading perpendicular and highest (~145 GPa) parallel to the c-axis [5], [48]. This means that the modulus is about 45 % higher for the stiff orientation, but these commonly stated values for the modulus only apply for commercially-pure (CP) titanium. The additions of Al and in particular the formation of ordered Ti_3Al (α_2) precipitates lead to an increase in stiffness [49]. The directional stiffness values reported for Ti-6Al-4Al by Kasemer et al. range from 110 GPa (perpendicular) to approximately 168 GPa (perpendicular to the c-axis) and therefore are over 20 GPa higher for loading along the c-axis, but only 10 GPa perpendicular to it [50]. So it appears that the ratio of stiffness values for loading parallel to perpendicular to the c-axis increases for Ti-6Al-4Al compared to CP-titanium.

2.1.2 Different types of microstructures

Industrial titanium alloys often contain both α- and β-stabilizing alloying elements (paragraph 2.1.1), which allows adjusting the volume fraction of α- and β-phase. Alloys containing only one phase are designated as α- or β-alloys, while α+β alloys can have a wide range of different α/β-volume fractions. TIMETAL®834 is a near-α Ti-ally, which is a sub-category of α+β alloys, which means that it only contains a small fraction of β-phase (in the order of a few %). The expression ‘near-α Ti alloys’ is commonly used, but it is difficult to find a clear definition that allows distinguishing these alloys from other α+β alloys. In some cases, the definition is used that near-α titanium alloys contain less than 2wt.% β-stabilising elements [25], [51].

In contrast to the BCC-phase, the HCP-phase has a closest packed crystal structure. Therefore diffusion processes are slower in the α-phase, resulting in better high-temperature creep properties compared to the β-phase [40]. For this reason, for applications at elevated temperatures that require good creep resistance, alloys with a high volume fraction of α-phase are used [3], [25].

α+β-alloys can exhibit different types of microstructures. These are fully lamellar, fully equiaxed and bimodal microstructures (see **Fig. 2-8**). Equiaxed microstructures consist of larger α-grains, with the β-phase being located at their boundaries, especially at the triple-points between α-grains. Fully lamellar microstructures consist completely of lamellar α+β-phase, or 'transformed β-phase'. By contrast, bimodal microstructures exhibit two different features: these are equiaxed primary α grains and the 'transformed β-phase'. The α-phase in the transformed β-phase is referred to as secondary-α.

For both, fully lamellar and bimodal microstructures, variations in the microstructure of the transformed β-phase can be observed. The microstructure can be divided into three different groups: Widmannstätten (colony type), basketweave or martensitic microstructures. In Widmannstätten microstructures, small sub-regions (colonies) are formed. The colonies consist of parallel α+β-lamellae. Within one colony all the α-phase has the same crystallographic orientation. In the basketweave microstructure, different crystallographic orientations of the α-phase can be observed within one region. Also, single α-laths or plates that are not parallel to any other laths can be formed [52]. Examples for these types of microstructures are shown in **Fig. 2-3**. Changes in the thermomechanical processing route can result in variations of the colony size and lamella-width (see paragraph **2.2**).

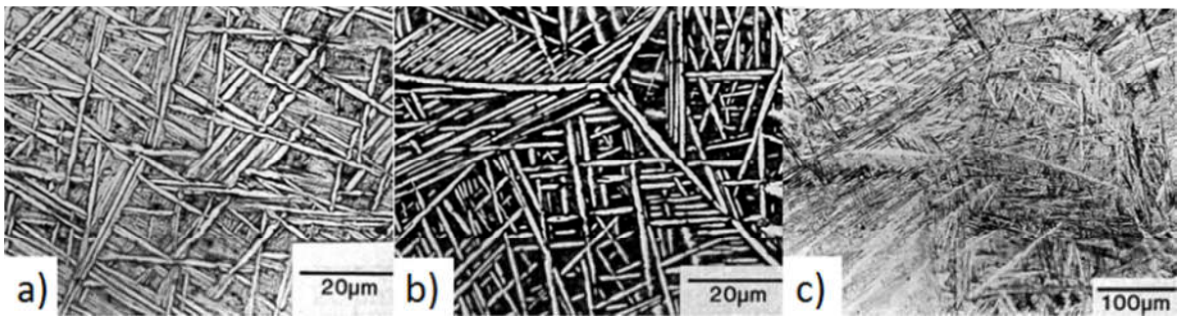

Fig. 2-3: Examples for a) basketweave, b) Widmannstätten and c) martensitic microstructures [40].

For fully lamellar microstructures, parameters for describing the microstructure are the size of the colonies and the width of the lamellae. Parameters for describing a bimodal microstructure are the same as for the fully lamellar microstructure and additionally the volume fraction, average size and size distribution of primary α grains. The crystallographic orientation of the α-phase, with respect to the orientation of the β-phase, is described by the Burgers-relationship (see paragraph 2.1.4).

2.1.3 Texture and micro texture

As described in paragraph **2.1.1**, α-phase has strongly anisotropic elastic and plastic properties. The mechanical properties mainly depend on the orientation of the c-axis of the hexagonal crystals to the loading direction. For a titanium alloy with fine, randomly orientated grains, it can be assumed that the macroscopic properties are isotropic. However, forged and rolled titanium products often exhibit a texture of both the HCP and BCC phase. Texture, often presented using pole figures, statistically describes the crystallographic orientations in respect to the orientation of

the macroscopic sample. The bulk texture in pole figures only takes the frequencies of orientations into account but does not consider the spatial distribution of grains with specific crystallographic orientation. So an alloy possibly does not exhibit an overall preferred texture, but locally, clusters of grains may have the same or similar crystallographic orientations. This means that the pole figure of these sub-regions would indicate a textured microstructure. These local features can be designated as ‘micro-texture’ or ‘local-texture’ [53], [54]. In common speech, the term ‘macro-zone’ is often used [44], [55]–[57]. This term, which is not clearly defined, normally refers to clusters of grains with similar orientations [44]. Depending on the processing route, the size of these micro-textured regions can range from centimetres down to multiples of the grain size.

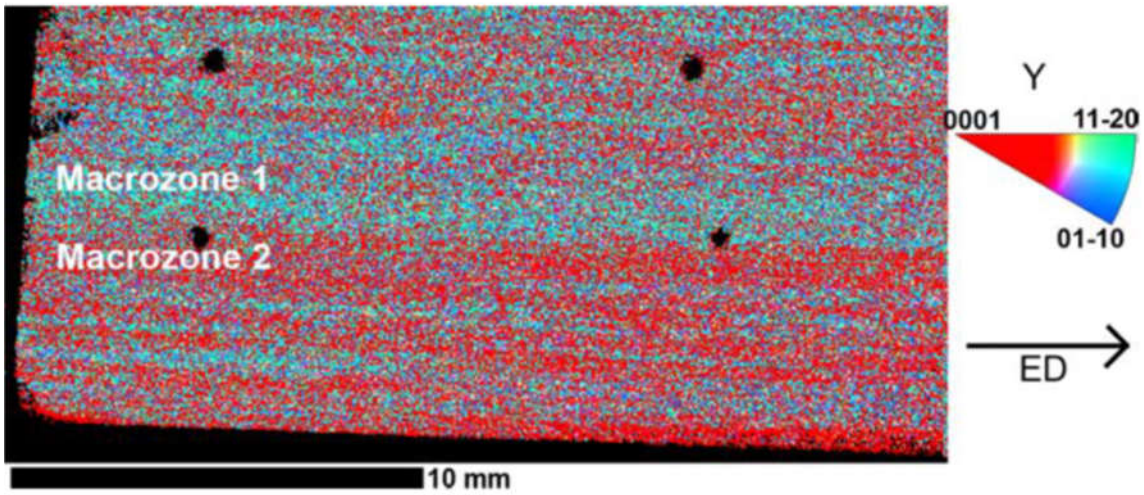

Fig. 2-4: EBSD-map of a forged Ti-834 billet, showing local zones with strong texture, elongated in elongation direction ED. Y is the radial direction of the billet and is perpendicular to the sample surface [54].

The main application of TIMETAL®-834 is for compressor discs and blades in jet engines. The microstructure of TIMETAL®-834 in billet form and how it is affected by different forging parameters has been analysed extensively [31], [54], [55], [57]–[60]. It has been observed that often sharp, band-like, textured regions can be formed during the forging process. These band-shaped regions are orientated in the elongation direction of the billet. The most common orientation in these macrozones is the c-axis of the α-phase being close to parallel to the radial direction of the billet. While this is the most common orientation, the orientations can vary significantly between the macrozones. An orientation map (based on EBSD scan), showing an example of this kind of macrozones, is displayed in **Fig. 2-4** [54].

In a final forging step, the billet is deformed into a shape, close to the shape of the final compressor disk. This final forging step is done at a lower temperature, compared to the forging of the billet. In this step, the strain is highly inhomogeneous. In areas close to the centre, deformation is low, but the strain increases significantly in the outer areas of the disc. In areas, with lower strain levels the macrozones are not broken up successfully. In areas with higher strain, the macrozones inherited from the billet are still present, but there are more orientation-variations and the shape of the textured regions is no longer as sharp as in the billet and less pronounced. In the areas with the highest strain, even a complete breakup of the macrozones can be observed [53].

2.1.4 Burgers relationship

At elevated temperatures, above the β-transus temperature, titanium exhibits a microstructure which consists of β-phase only. α-phase is formed when the alloy is cooled below the β-transus temperature. The α-phase nucleates in the β-phase and there is a relationship between the crystallographic orientations of these two phases, which is called the 'Burgers relationship'. Two correlations link the crystallographic orientations of α and β-phase. Firstly the basal plane of the α-phase is parallel to the {110} plane of the β-phase. Secondly, one <100> direction of the β-phase is parallel to a <2-1-10> direction of the α-phase within this plane (**Fig. 2-5**). This results in 12 possible orientations for the α-phase that nucleated within one β-grain, which are called variants [47], [58], [61], [62].

$$<100>_{\beta} \parallel <2\text{-}1\text{-}10>_{\alpha} \quad (2\text{-}1)$$

$$\{110\}_{\beta} \parallel \{0002\}_{\alpha} \quad (2\text{-}2)$$

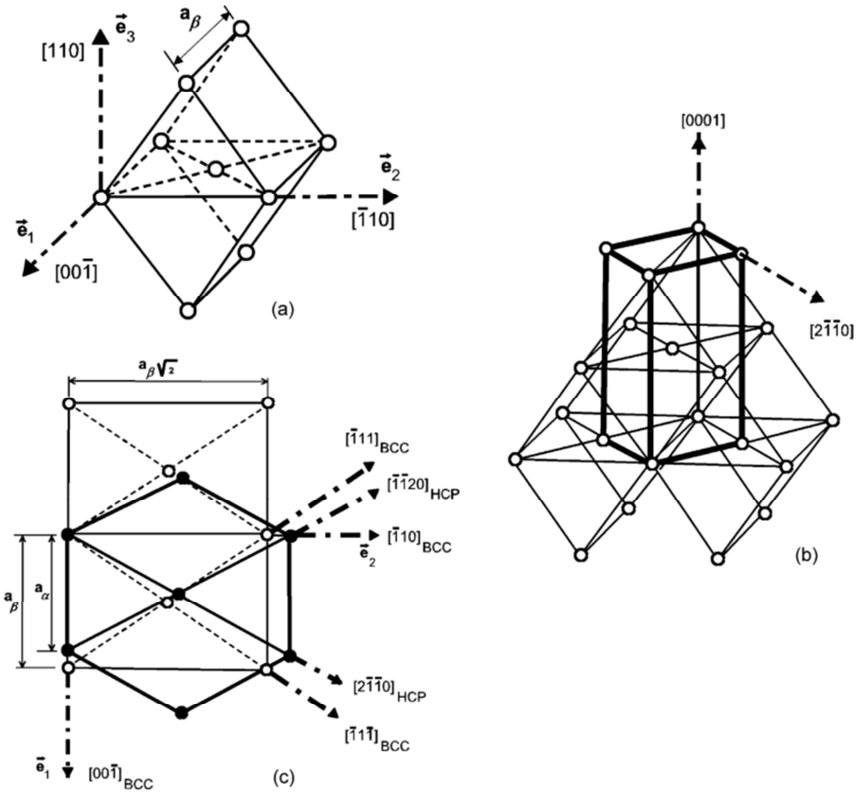

Fig. 2-5: Crystallographic orientation relation between the BCC and HCP phase according to the Burger's relation [58].

As near-α titanium alloys have a high volume fraction of α-phase and vice versa a low fraction of β-phase, determining the orientation and microstructure of the β-phase experimentally can be difficult. Therefore, a method was developed to determine the orientation and grain structure of the high-temperature β-phase, based on the crystallographic orientation of the α-phase in secondary-α colonies [63]. It is assumed that the Burgers relationship is valid within colonies. Considering only the orientation of the α-phase in a single colony, several crystallographic orientations are possible for the β-phase. When the orientation of several adjacent α-colonies is known, a common, unambiguous orientation of the β-phase in this region can be determined. An algorithm that

enables the reconstruction of the microstructure of the β-phase, based on crystallographic orientation maps of the α-phase, was developed by Davies et al. [31].

2.1.5 Second Phase Particles (SPPs) in Titanium 834

The near-α titanium alloy Ti-834 was developed for applications in jet engine compressors, especially disks and blades, operating at a temperature of up to 600°C [1], [2], [27], [58], [59], [64]–[66]. Ti-834 has superior high-temperature creep properties and oxidation behaviour in combination with high strength and fracture toughness. The improved creep resistance is achieved by adding small amounts of silicon as an alloying element. The improved creep strength is related to the solid solution strengthening of silicon and the formation of fine, silicon-rich second phase particles **SPP** on α/β boundaries [4], [30], [31], [67]. The chemical composition and crystal structure of the silicon-rich particles, and the crystallographic orientation relation between the SPPs and the secondary α has been analysed in detail by Singh et al. [67]. The chemical composition of these particles is $(Ti, Zr)_6Si_3$; but variations in stoichiometry are possible, depending on the exact alloy composition, distribution of alloying elements and applied heat treatments. The precipitation of silicide particles increases the strength, but increasing the size and volume fraction of them only enhances these effects to a certain extend. When the silicide particles are growing too large, it comes to a depletion of Si in the Ti-matrix and as Si contributes to solid solution strengthening, the overall strength is reduced [27].

The second type of precipitates, α_2-precipitates, can be found in Ti-834. These are coherent precipitates with a chemical composition of Ti_3(Al, Sn, Si). The stoichiometric composition of aluminium, tin and silicon in the particles is variable. The morphology of the α_2-precipitates depends on the temperature at which they are formed and the local Al-concentration [30]. The solvus temperature of these particles in Ti-834 is at about 750°C, which is significantly higher than for Ti-6Al-4Al (550°C) [5]. The precipitation process can already be observed at temperatures of 500°C to 550°C, therefore α_2 precipitation may continue during service of a component in a jet engine. Depending on the temperature, the time until precipitates can be observed varies between 2 hours and several weeks [30].

Precipitation of α_2 can be observed when the solubility limit of Al in the α-phase has been exceeded. Generally, an Al concentration of at least 5 wt.% is required for the precipitation of α_2 [68], [69], but local Al concentration may be varying depending on the microstructure. For example in alloys with bimodal microstructure, partitioning effects during heat treatments in the α+β temperature range lead to a higher concentration of Al in primary α grains [23], [70], [71]. Generally, precipitation is possible both in the primary and secondary α phase, but due to the higher Al concentration, it is expected to be more pronounced in primary α grains than in colonies.

The precipitation of α_2 increases the elastic and plastic anisotropy and increases the modulus due to the higher stiffness of α_2/Ti_3Al [72]–[74]. It also strengthens the material, but this comes at the cost of reduced ductility [27], [69], [75], [76]. The initial shearing of the coherent α_2-precipitates is difficult, but as soon as the first dislocations have passed through them, further shear events are getting easier, which leads to localised and planar slip behaviour. As sharp slip bands are possible sites for crack initiation, this leads to earlier failure and lower ductility [2], [27], [28], [30], [68], [69], [76], [77]. Lunt et al. have reported that the presence of α_2 leads to more heterogeneous strain distributions and higher strain values within slip bands [78]. The more localised strain after initial

shearing also leads to reduced life under low-cycle-fatigue loading conditions [2], [76]. Similar to the silicide precipitates, strengthening effect is limited, as when the particles are growing larger, the titanium matrix is depleted of Al and Zr, which have a solid-solution-strengthening effect. The effect of α_2-precipitation on cold creep behaviour is discussed in paragraph 2.3.8.

2.2 Material processing

2.2.1 Thermomechanical processing route

Titanium alloys undergo a complex thermo-mechanical processing route to achieve ideal material properties. The steps of a possible thermomechanical processing route for titanium with a bimodal microstructure are displayed in **Fig. 2-6**. Depending on the manufacturer and the alloy, there may be a variation in the steps that are carried out. For example, sometimes a forging step above the β-transus temperature is conducted [79]. In other cases, this forging step is skipped because it is assumed that forging in the two-phase α+β-region provides a more effective way of breaking up the β-grain structure [80].

After the casting of an initial ingot, the microstructure is coarse with a grain size of up to several centimetres and also segregation effects occur [79]. For Ti-alloys used in safety-critical components in the aero-engine industry, triple vacuum arc melting is applied to remove impurities and macro segregations [81]. Heating above the β-transus temperature (see **Fig. 2-6**) leads to a homogeneous distribution of the alloying elements. In a first forging step above the beta-transus temperature, the coarse beta-grain structure is broken up and recrystallization leads to a finer grain structure [79]. Subsequent cooling under β-transus temperature leads to the formation of coarse α-lamellae. The crystallographic orientations of the α- and β-phase are linked by the Burger's relationship, limiting the number of possible crystallographic orientations of α-phase within one β-grain to 12 variants. Also, the dimensions of the α-lamellae are limited by the size of the β-grains. Therefore a fine β-grain structure with a randomised texture also results in a more homogeneous structure of the α-phase and the formation of more different crystallographic orientations [56], [61]. The α-phase formed in this step will later become the primary α-phase in a bimodal microstructure. A higher cooling rate after the homogenisation treatment results in the formation of thinner lamellae and therefore smaller primary-α grains during TMP.

As only a limited number of α-variants can be formed in a single β-grain, it could be assumed that size and morphology of macrozones are directly correlated to the grain structure of the high-temperature β-phase. However, Bocher et al. demonstrated that macrozones can be larger than the grains in the high-temperature β-phase [60]. According to the Burgers-relationship, the $\{110\}_{bcc}$ and the $\{0001\}_{hcp}$ planes are parallel. Even when two β-grains are significantly misaligned to each other, as long as they have a pair of parallel {110}-planes, α-phase nucleated within these grains will have a common (0001)-orientation. This has been observed for hot-rolled Ti-6Al-4Al by Obasi et al. [82]. In-situ neutron diffraction experiments confirmed that β-grains with parallel {110}-planes can promote the selection of specific α-variants [83].

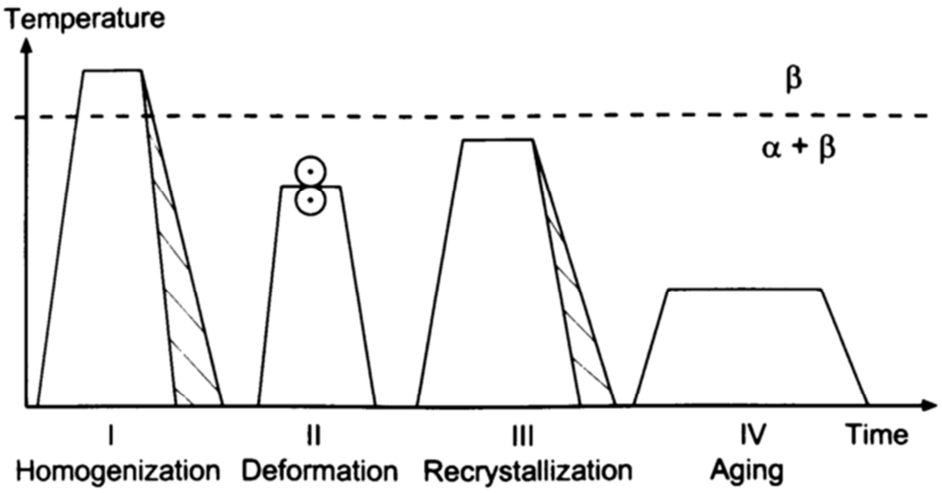

Fig. 2-6: Stages of thermomechanical processing for titanium alloys with bimodal microstructure [80].

The aim of forging steps and heat treatments in the α+β-temperature range (**Fig.** 2-6, step II and III) is to create small, evenly distributed α-grains with independent crystallographic orientations. Forging in the α+β region breaks up the lamellar structure and leads to a rotation of the α-phase, which is referred to as globularization. These forging steps lead either to dynamic recrystallization during deformation or recrystallization during the subsequent heat treatment [25], [57], [80], [84], [85]. The fraction of recrystallized grains depends on temperature during deformation, strain rate and the total amount of plastic strain [84]. Generally, higher plastic strains in this step result in finer α-grains and a higher fraction of recrystallized grains [85]. According to Muszka et al., a strain of 30% to 60% is required (for Ti-6Al-4V) to start the recrystallization of the α-phase [86]. As a higher degree deformation results in stronger rotation of the α-grains, it could be expected that a high enough deformation would result in a fine microstructure with a randomized texture. If sufficient independent rotation of the primary α-grains was achieved, the Burger's relation between the primary α and β-phase would not be valid anymore, yet it has been observed, that the α-grains often rotate around a common axis and that even for strains of about 80% macro- and micro-texture can still be observed [85]. Germain et al. observed that globularization leads to the formation of finer primary α-grains, but it only leads to the formation of a few new orientations because of the rotation being mainly around the c-axis. This process can even lead to an alignment of c-axis in a common direction, resulting in the formation of sharp, textured regions. It was observed, that the orientation relations ship between primary α- and β-phase is not broken up [61]. Prakash et al. observed that for Ti-6Al-4Al, which was rolled at different temperatures, the Burgers relation was still valid [56].

Subsequent heat treatment in two-phases α+β region serves two purposes: Firstly it leads to the recrystallization of both the α- and β-phase. Secondly, the temperature of the heat treatment step defines the volume fraction of primary α.

2.2.2 Solution heat treatment and subsequent cooling

Commonly two heat-treatment steps are applied to Ti-alloys with a bimodal microstructure after the final forging step, influencing the final microstructure. These are a solution-heat-treatment followed by cooling to RT at a controlled rate, which determines the final α-β morphology and ageing treatment, which for alloys with high enough Al concentration leads to the precipitation of α_2 [79],

[87]. Firstly, in the solution heat treatment, the material is heated to a temperature below the β-transus temperature. In this step, according to the phase diagram, the temperature determines the volume fraction of the primary α phase. For TIMETAL®834 a solution heat treatment temperature of 1015°C is commonly used, which is 30°C below the β-transus temperature, resulting in a volume fraction of primary α phase of 15%. Depending on the cooling rate different types of microstructures can be formed. For slow cooling rates, approximately 1 K/min [78], the primary-α phase can grow and an 'equiaxed' microstructure is formed. This microstructure consists of equiaxed α-grains with retained β-phase at its boundaries (e.g. **Fig. 2-8**, (b)). For faster cooling rates, there is less time for diffusional processes to take place and the β-phase is transformed into a Widmänstetten or basket-weave type microstructure (e.g. see **Fig. 2-3,** (c)). For high enough cooling rates, e.g. above 410K/min for Ti-6Al-4V, martensitic phase transformation is also possible [87]. In case that a lamellar microstructure is formed, the spacing between the lamellae, respectively the width of the lamellae, and the size of the colonies are directly related to the cooling rate. Faster cooling-rates result in a finer spacing of the lamellae, while a slower cooling results in a wider spacing (**Fig. 2-7**, (a)) [87].

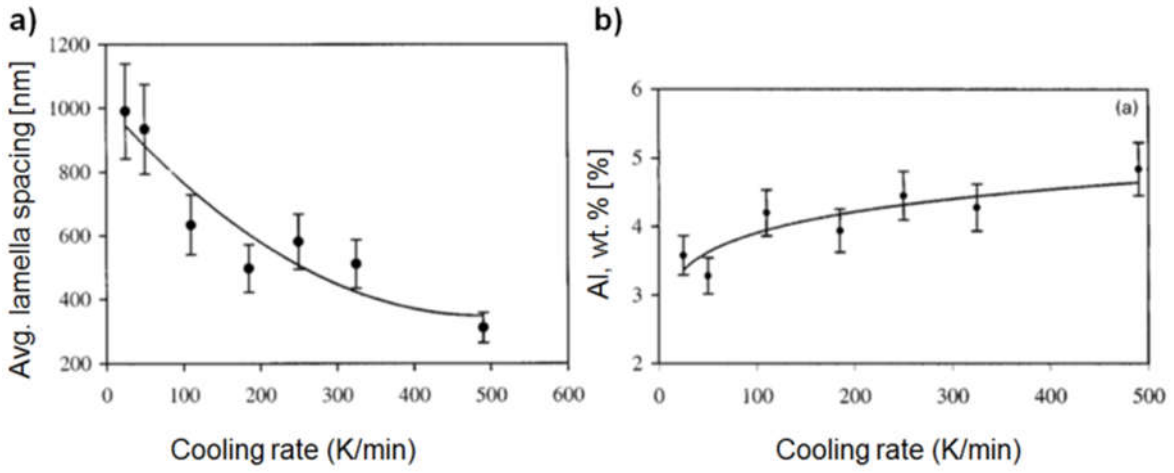

Fig. 2-7: a) Average lamella spacing and b) weight percentages of aluminium in lamellae as a function of cooling rate for Ti-6Al-4V [87].

For high enough cooling rates it can be assumed that primary-α grain growth is inhibited, while intermediate cooling rates result in both a slight growth of the primary-α phase and the formation of a Widmanstätten-type microstructure.

When equilibrium conditions are reached during the solution heat-treatment, concentrations of α-stabilising elements are higher in the α-phase than in the β-phase and vice versa. As secondary α lamellae are nucleated in the β-phase, they always have a lower concentration of α-stabilising elements than primary α grains. A higher volume fraction of α-phase during the solution treatment reduces the concentration of α stabilisers in the β-phase and therefore also in the secondary α lamellae [87]. Slow cooling rates after the solution treatment lead to an increase in the volume fraction of the primary α grains, and therefore to a lower concentration of α stabilising elements in the β-phase and finally in the secondary α lamellae (see **Fig.** 2-7, b)) [87].

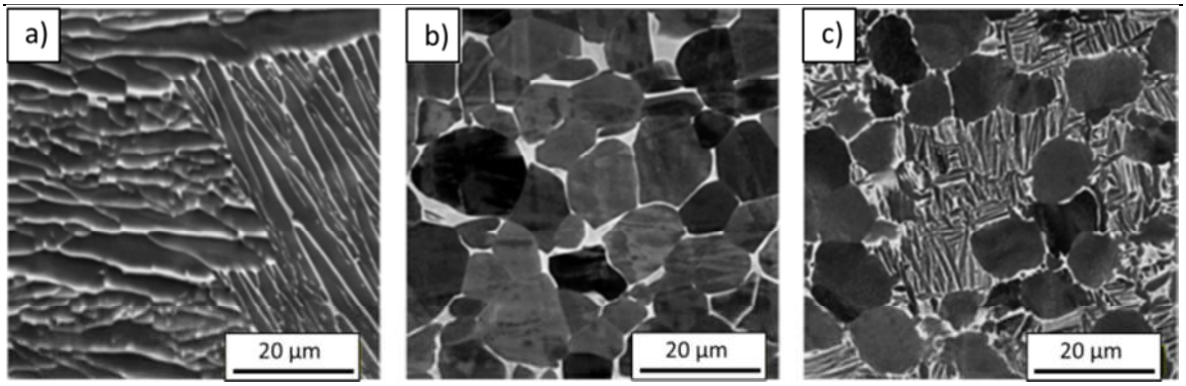

Fig. 2-8: BSE-SEM images of Ti-6Al-4V, exemplary with (a) fully lamellar, (b) fully equiaxed and (c) bimodal microstructure [88].

Ideally, the orientations of secondary α colonies in one prior β grain would exhibit all 12 variants with a random distribution. During β→α+β transformation, the secondary α-phase nucleates on β-grain boundaries or at primary α-grains (epitaxial growth), which can lead to a strong variant selection. When secondary α colonies are formed by epitaxial growth nucleated at a primary α grain, both the primary α grain as well as the colony have the same crystallographic orientation, therefore effectively forming a large grain. It has been observed experimentally that the favourable orientation of the α phase in colonies is the c-axis being parallel to the one of a primary α grain [56], [58]. Also, the orientation of neighbouring β-grains, lattice strain caused by the transformation and cooling rates influence the variant selection [62], [83], [89]. Variant selection is generally less distinctive for higher cooling rates and higher undercooling [62].

2.2.3 Comparison of fully lamellar and bimodal microstructure

For both fully lamellar and bimodal microstructures, a smaller colony size and lamella spacing result in higher yield and tensile strength [90], [91]. As described before, the colony size and lamella spacing are strongly influenced by the thermomechanical processing route, especially the cooling rate after the solution heat treatment. Another factor influencing the colony size, are nucleation sites for the secondary-α phase. These can either be β-grain boundaries or primary-α grains. The maximum size of colonies is restricted by the spacing between primary-α grains or the size of β-grains. The smallest colony size is received when the primary α-volume fraction is high and when the primary α-grains are small and evenly distributed, resulting in a smaller mean distance between the grains. As only bimodal microstructures contain primary α grains, the same cooling rate results in smaller colony size in alloys with a bimodal microstructure, compared to alloys with a fully lamellar microstructure [79], [80]. However, the primary α volume fraction can only be increased to a certain extent, as an increase in primary α volume fraction reduces the concentration of α-stabilising elements in the transformed β-phase and therefore reduces the strength of secondary α colonies.

Fully lamellar microstructures can have a higher resistance against crack propagation and therefore exhibit a better high cycle fatigue performance. Also, fully lamellar microstructures exhibit slower creep rates than bimodal microstructures. On the other hand, bimodal microstructures have higher ductility, higher strength for the same applied cooling rate and better low cycle fatigue properties, due to the higher resistance against crack initiation. For bimodal microstructures the creep rate increases for higher primary α-volume fractions [5], [80].

2.3 Mechanical properties of titanium alloys

2.3.1 Resolved shear stress (RSS)

The resolved shear stress (RSS) is the stress acting on dislocations in slip direction. It depends on the local magnitude of the applied stress, the slip direction and the plane normal of the slip plane. The calculation of RSS values when the full stress tensor is known is described in paragraph 3.10.3, equation (3-9). Schmid's law can be used to calculate RSS values when the stress in loading direction is known. This could either be that the local stress is known, e.g. from simulations, or that the assumption is made, that the stress is homogeneous throughout the sample and therefore the stress at each point and in each grain is equal to the stress applied to the complete sample. The RSS is calculated by multiplying the stress in loading direction with the Schmid Factor (eq. (2-3)).

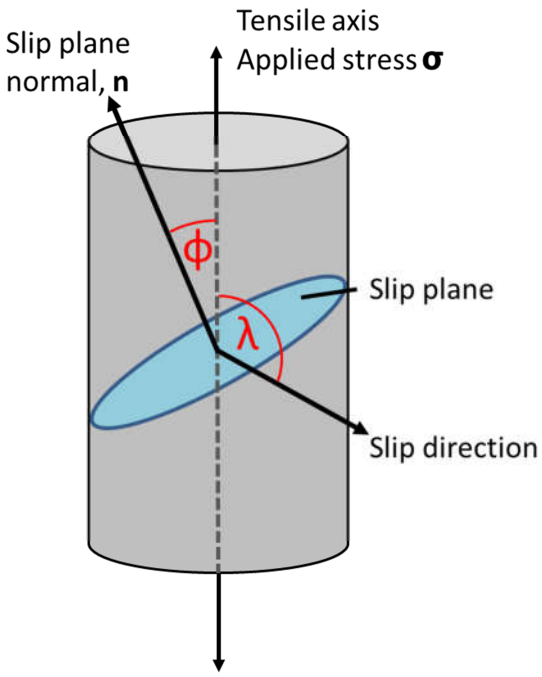

Fig. 2-9: Schematic showing the angles between the slip plane normal, the slip direction and the load axis.

$$\tau_{rss} = \sigma_{applied} \cos(\phi) \cos(\lambda) = \sigma_{applied} SF \quad (2\text{-}3)$$

$\cos(\phi) \cos(\lambda)$: Schmid factor (SF)

ϕ: Angle between slip plane normal and load axis

λ: Angle between slip direction and load axis

The Schmid factor is defined as the product of the cosines of the angle between the slip plane and the stress axis and the angle between the slip direction and the stress axis. Each of the cosines-terms would be highest when the angles are equal to 0°. However, as the slip plane normal and the slip direction are perpendicular to each other, if one of the angles is 0°, the other one has to be 90° and therefore one of the cosines terms and consequently the Schmid factor are equal to zero. The maximum value of the Schmid factor is 0.5, which is reached when both angles are 45°. Consequently, the maximum RSS value is half of the applied axial stress. According to Schmid's

law, for slip systems requiring the same stress for slip activation, the slip system with highest Schmid factor will be activated first during plastic deformation [92].

Based on the Schmid factor, the crystallographic orientation at which the RSS on a slip system is highest, and therefore the activation of the slip system is most likely, can be determined. In HCP crystals, the RSS on the basal slip system is highest when the angle between the loading direction and the c-axis of the crystal (declination angle) is 45°. RSS on prismatic slip systems is highest for declination angles of 90°.

2.3.2 Slip systems in Titanium alloys

For plastic deformation of α+β-alloys, slip needs to take place in both phases. Due to its high volume fraction, slip behaviour in the α-phase dominates the mechanical properties of near-α Ti-alloys, e.g. of TIMETAL® 834 [93]. Nevertheless, the β-phase can strongly influence the mechanical properties of these titanium alloys. The β-phase, which is present in the form of ligaments in colonies or is retained at grain boundaries of α-grains, can restrict the deformation of the α-phase and also affects the slip-transfer between grains [94], [95].

Slip systems are defined by a slip plane and a Burgers vector **b**, which lies within the slip-plane. The required stress to activate dislocation movement in a specific slip system is called the critical-resolved-shear-stress **CRSS**. The CRSS is proportional to the length of the Burgers vector and therefore is lower for shorter **b**-vectors. For HCP crystals, the shortest Burger's vectors are <a>-type-vectors (1/3<11-20>), which lie within the close-packed basal-plane (0002). There are three Burgers vectors of this type, but as they are co-planar only two of them are independent. <11-20>-type Burgers vectors lie within three crystallographic planes, namely the basal-plane (0002), the prismatic-planes {10-10} and the first-order pyramidal-planes {10-11} (see **Fig. 2-2**, 2a)). The Burgers vectors in the second-order pyramidal-planes {11-22} are the <c+a>-type-vectors, which are orientated in <11-23 > direction. Based on the Burgers vector, slip can be classified as <a>-type or <c+a> slip. As the <c+a>-Burgers vectors are about 60% longer than the <a>-type Burgers vectors, the required CRSS at room temperature for <c+a>-slip is more than two times higher than the CRSS for <a>-slip on the basal or prismatic plane (see **Fig. 2-2**, c)). For elevated temperatures CRSS values decrease for all systems, but increasing the ratio of CRSS-values of <c+a>-type to <a>-type slip even further [96].

According to the von Mises criterion, 5 independent slip systems are required to accommodate arbitrary shape changes in a crystal [97]. There are a total of 10 physically different slip systems with <a>-type Burger's vector: basal {0002}<11-20>, two slip systems; pyramidal {10-10}<11-20>, two slip systems; first-order pyramidal {10-11}<11-20> six slip systems. The number of slip systems, based on the <11-20>-Burgers vector would be sufficient to fulfil the von Mises criterion, but these systems are not independent of each other. Also, as all Burgers vector have only an <a>-type component, only plastic deformation parallel to the basal plane is possible. To accommodate homogeneous deformation, also in direction of the **c**-axis, further deformation mechanisms are required. Therefore slip with a <c+a>-Burgers vector needs to be activated, despite the significantly higher CRSS-values [93], [98], [99].

Transmission electron microscopy (TEM) analysis can be used to identify burgers vectors, by imaging samples along specific zone axes to fulfil the invisibility criteria [100]–[103]. For details

regarding the experimental procedure, we refer the reader to [104]. As <a>-type basal, prismatic and pyramidal slip has the same type of Burgers vector, it can be assumed that the CRSS values for the three slip systems are of the similar magnitude and that all three slip systems can be observed when plastically deforming a Titanium alloy. While the activation of <a> type basal and prismatic, as well as <c+a>-type pyramidal slip, has been observed experimentally [100], [105]–[108], there is only little evidence for the activation of <a>-pyramidal slip [109]. Cross-slipping, which is the process of a screw-dislocation changing from it's initial to an intersecting slip plane, can frequently be observed in titanium. While there is a lack of experimental confirmation for <a>-type pyramidal slip, cross slipping of screw-dislocations from the prismatic onto the first-order pyramidal ({1011}) plane has been confirmed experimentally [100], [105], [110], [111].

Another possible mechanism that could enable deformation in the direction of the c-axis is twinning. Twinning can be observed readily in commercially pure titanium, but normally not in near-α Ti-alloys, e.g. TIMETAL® 834, because of the small phase dimensions, second phase particles in the matrix and high content of alloying elements in solution [5], [112].

Deformation of the β-phase is mainly accommodated by slip on the {110}-planes with <111>-type Burgers-vectors. The combination of these slip planes and Burgers vector provides enough independent slip systems to enable homogeneous deformation in the β-phase. This especially influences the mechanical properties with alloys with a high β-volume fraction or pure β-alloys.

2.3.3 CRSS values for basal and prismatic slip

In previous work on industrial α+β titanium alloys (Ti-6Al-4V, Ti-6242, Ti-6246), slip activation at stress levels below the macroscopic yield point has been observed, with basal slip being the dominant slip mode during the initial slip activation [93], [113]–[117]. The early activation of basal slip has been explained by microtextured regions forming stress hotspots [114], stress heterogeneity due to elastic anisotropy and grain interactions [118] and by a lower critical resolved shear stress (CRSS) values for basal than for prismatic slip [116]–[118]. The CRSS value is a threshold that needs to be exceeded to enable the activation of slip, but a wide range of CRSS values for basal and prismatic slip have been reported, wherein some studies suggest CRSS(Ba)>CRSS(Pr) [93], [100], [119]–[124] and others CRSS(Ba)<CRSS(Pr) [50], [73], [116]–[118], [125], [126]. These discrepancies in CRSS are attributed to many factors including variations in chemical composition, in particular Al-concentration (see **Fig. 2-10**) [100], [120], [127], α_2-precipitates [73], lamellae spacing and orientation [102], [119], [121] and grain size [127], [128]. Therefore, CRSS values can only be directly compared for alloys with similar compositions and microstructures, in our case α+β or near-α Ti alloys with an Al-concentration of close to 6 wt.%. Reported CRSS values also depend on the method used for determining them. Micro-pillar or microcantilever testing can be used to determine CRSS values in titanium alloys [94], [122], [123], but these values are typically lower than in bulk material, as hardening mechanisms and constraints by neighbouring grains are not considered [129]. In-situ slip trace observation can be used to determine the macroscopic stress at which the first local slip activity is observed and a correlation to crystallographic orientation data enables the identification of the activated slip system [73], [93], [120], [126], [127]. This could be considered to be the most appropriate method, as local slip activation is considered instead of the 0.2% proof stress [100], [119] for identifying the required stress for activating slip, which is important as a changeover in the dominant slip system can be

observed before macroscopic yield, as it has been shown in the current and previous studies [93], [113]–[117]. A study combining this approach with crystal plasticity (CP)-modelling to determine local RSS values reported that CRSS values are lower for basal (338 MPa) than for prismatic (352 MPa) slip in Ti-6Al-4V [117], which is in contradiction with other values published litareature (e.g. in **Fig. 2-10**, [100]).

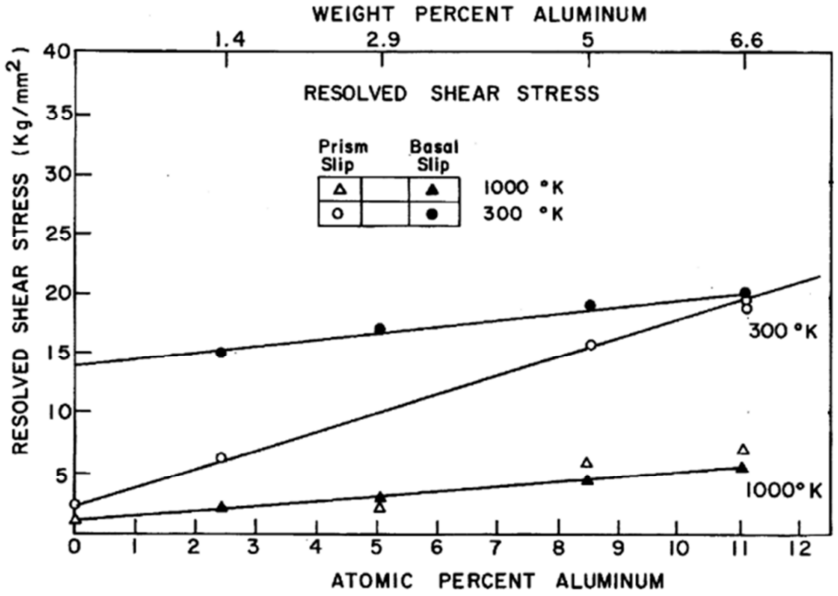

Fig. 2-10: CRSS values for basal (solid symbols) and prismatic symbols (open symbols) as a function of the Al-concentration in the range of 0 to 6.6 wt.% [100].

2.3.4 Local plastic deformation below the macroscopic yield point

Even before the onset of plastic deformation on the macroscopic scale, local slip activation has been observed for several industrial near-α and α+β titanium alloys, including Ti-6Al-4V, Ti6242 and Ti-6246 at stress levels as low as 80% of the 0.2% proof stress [73], [93], [114]–[118], [130]. The 0.2% proof stress is commonly used as a criterion for the onset of macroscopic yield, which is defined by the stress at which 0.2% of plastic deformation is reached in a stress-strain curve. This approach considerers the average behaviour of polycrystalline specimen and therefore can not describe the onset of local plasticity [127]. The onset of local plastic deformation is difficult to determine based on macroscopic stress-strain curves for uniaxial tensile loading, as the first local slip events may only result in little plastic deformation on the macroscopic level, which may not be possible to be detected when measuring macroscopic strain. Therefore slip trace observation techniques are required to determine the stresses at which the first slip bands are formed. In these tests, the applied stress on a sample is increased incrementally, while the adequately prepared sample surface is imaged using a technique that can detect slip bands at the sample surface, e.g. optical or electron microscopy. The first load step, respectively the lowest applied stress, at which slip bands have been overserved, can be used to define the onset of local plasticity. However, this technique does not guarantee that no slip bands have been formed at even lower stresses, as slip bands may have been missed due to their location, low displacement or if they didn’t cause any observable change in the sample for the used microscopy technique, e.g. optical microscopy is sensitive to out-of-plane, but not in-plane displacements. Also, the applied stress needs to be increased in small increments, until first slip bands are observed. For optical microscopy the

acquisition of an image only takes less than 1 second, therefore making it possible to cover many load-steps and determining the on-set of the local plasticity accurately.

When analysing the activated slip systems, it needs to be distinguished between the onset and the later stages of plastic deformation. For initial plastic deformation in several α+β alloys (e.g. Ti-6Al-4V, Ti6242 and Ti-6246), it has been consistently reported that basal slip has been identified as the dominant slip system [93], [113]–[118], [130]. This observation has been made for alloys with different microstructures and seems to be valid independently of whether the sample exhibits microtextured regions or not [118]. A possible explanation for the early activation of basal slip is based on stress heterogeneities due to elastic anisotropy and grain interactions [118] and lower critical resolved shear stress (CRSS) values for basal than for prismatic slip [116]–[118]. The effect of elastic anisotropy on slip activation will be investigated in this study, using experimental and modelling techniques (see **chapter 3**). CRSS values for basal and prismatic slip are discussed in **chapter 2.3.3**. Another possible explanation is that basal slip is activated due to stress hot spots caused by microtextured regions [114], [130]. However, basal slip has also been identified to be the dominant slip system at low stress levels in samples without macrozones. Therefore it may be possible that macrozones further increase the activation of basal slip, but it cannot be used as a general explanation for the early activation of basal slip.

For increasing stress levels, the fraction of activated slip systems changes. When the applied stress is close to the macroscopic yield point, a change-over from basal to prismatic slip as the dominant slip system can be observed [93], [118]. At this stage, the fraction of activated basal to prismatic slip systems, as well as strain distributions, are strongly influenced by microstructure and microtextured regions [114], [118], [130]. Macrozones generally contribute to the formation of long-range slip bands and increased strain heterogeneity [131]. The change-over from basal slip during initial deformation to prismatic slip at higher macroscopic strain values might be explained by higher strain hardening and strain rate sensitivity of basal slip [94], [132], [133]. The changeover in the dominant slip system may also be due to stress redistributions after the initial deformation by basal slip. Also, a difference between the primary α and secondary α constituent can be observed. It has been reported, that primary α grains deforming by basal slip exhibit higher average strain values than the ones deforming by prismatic slip, but this effect cannot be observed for secondary α colonies [134].

2.3.5 Cold dwell fatigue

It has been observed that TIMETAL®834 is susceptible to cold dwell fatigue (CDF) [135]. This failure mechanism is observed for homologous temperatures of less than 0.3 (~230 °C, [136], [137]) and is therefore designated as '**cold**' dwell fatigue. Dwell fatigue is when a load hold, at or near the maximum stress, is superimposed on low cycle fatigue (LCF) loading conditions. Adding a dwell time can decrease the fatigue life of a component significantly compared to LCF loading at the same maximum stress. The reduction of the cycles to failure is called dwell debit. Work by Evans et al. showed that the cycles to failure decreased by a factor of up to 100 when a dwell time of 5 minutes was applied (IMI685) [138]. The dwell-debit increases with the dwell time, but saturated after a certain time. The dwell-debit is higher for stress holds, compared to load holds during the dwell period [139].

Fracture surfaces of dwell fatigue samples always exhibit quasi-cleavage like facets, which is not observed for LCF loading conditions. Faceting has been observed both for laboratory-based tests, as well as for real engineering components during service. Earlier studies have shown that the facets are perpendicular to the loading direction and have the size of single grains. Texture analysis showed that the faceting grains have their c-axis orientated parallel to the loading direction [33], [38], [143], [66], [85], [89], [135], [138], [140]–[142]. For these orientations, the stiffness in loading direction is highest (see paragraph 2.1.1) and the grains are unfavourably orientated for basal and prismatic slip. Therefore it can be stated that facets are formed in hard (elastically and plastically) grains. Though in contrast to these observations, a recent study has shown that facts are inclined to the loading direction by approximately 30° [144].

Bache et al. compared the fatigue life of TIMETAL®834 alloys with different bimodal microstructures for cycling loading with and without a superimposed load hold. For applied peak stresses above a certain value, a significant dwell debit could be observed [138], while for stresses below this value, the fatigue life was independent of the dwell time. Therefore it seems like there is a threshold value for applied stresses, below which, applying load hold does not have any effect on the fatigue life. This threshold value is dependant of the microstructure. The susceptibility to CDF generally decreases with smaller grain size, both for the α-phase and the high-temperature β-phase [136], [138], [145]. For alloys with bimodal microstructure, basketweave compared to colony type microstructure reduces the dwell debit. For colony type transformation product, smaller colony size is favourable. Therefore a higher cooling rate after the solution heat treatment reduces the susceptibility to CDF [145]. Bache et al. investigated the effect of primary-α morphology, showing that larger and elongated primary α have a detrimental effect on CDF properties [135].

The susceptibility of titanium alloys to CDF is temperature dependant. The susceptibility of titanium alloys to CDF fatigue increases with temperature, but at a certain temperature (approximately 120°C [32], [137]) a maximum is reached and a further increase in temperature decreases the susceptibility [137], [146]. Ready et al. reported that for Ti-6242 the susceptibility to CDF is almost eliminated for temperatures above 200 to 230 °C [136], [137].

2.3.6 Proposed models for dwell fatigue

A widely acknowledged theory describing the mechanisms of dwell fatigue, which is based on the Stroh model, has been proposed by Evans and Bache [35], [138], [147]. This model is based on a specific, local arrangement of grains: a ‘soft grain’, which is well-aligned for easy slip, is located next to a ‘hard grain’, in which slip cannot be activated easily. In the first step slip only occurs in the soft grain. The dislocations in the soft grain will start piling up when they reach the boundary to the hard grain, which acts as a strong obstacle to further dislocation movement. The pile-up will impose stresses in the hard orientated grain. Two different stress states are present at this point in the hard grain: firstly the externally applied tensile stress and secondly the shear stress induced by the dislocation pile-up in the adjacent grain. As the activation of slip is difficult in the hard grain, the combination of these two stresses may lead to decohesion of atomic planes and finally to the formation of facets and eventually initiation of cracks. As the hard grains have a high stiffness in the loading directions, stresses within them are higher, which supports the decohesion process [141]. The cracks would have the same size as the hard orientated grain and appear as a facet on the fracture surface. Facets may act as nucleation sites for cracks or may accelerate the

propagation of cracks under cyclic loading conditions [35], [56], [66]. The local arrangement of grains used to explain CDF mechanisms is called ‘rogue grain combination’ [41], [139]. For HCP materials the hard grain is orientated with the c-axis parallel to the applied load, as therefore slip on the basal and prismatic plane is difficult. The soft grain has a crystallographic orientation that enables easy activation of <a>-type slip (basal or prismatic) [41], [44], [141], [148].

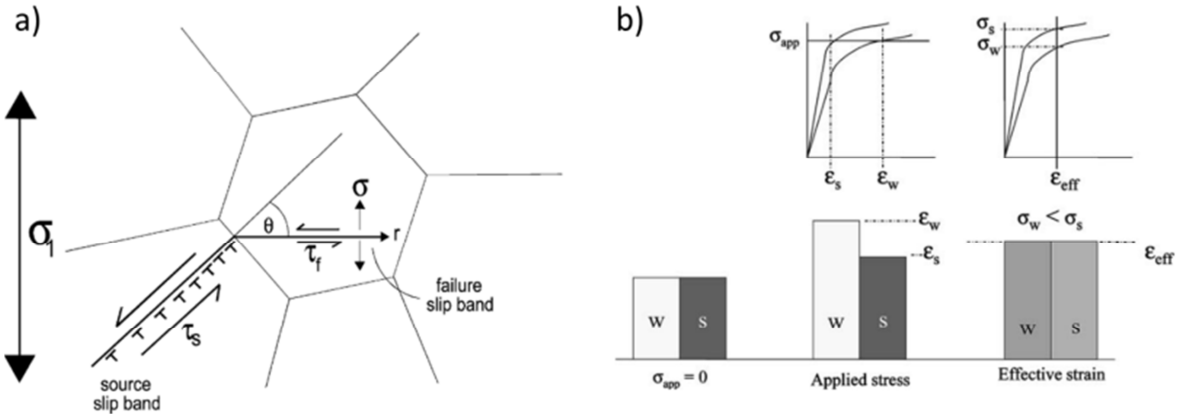

Fig. 2-11: a) Pile-up of dislocation at a grain boundary in grain with weak orientation and induced stress in adjacent strong grain according to the Stroh model [147]. b) Schematic of stress redistribution based on the two-element model [35].

A further possible explanation, namely the two-element model, has been proposed by Bache [35], which is based on the elastic anisotropy of α-phase titanium. It also assumes a hard-soft grain combination, but in this case, only regarding the elastic properties. For the hard grain, the c-axis is parallel to the loading direction, resulting in a high stiffness in loading direction (see paragraph 2.1.1), while the soft grain ideally has a declination angle of close to 90°, resulting in a low stiffness. Based on the differences in stiffness, applying the same stress to both grains would result in a higher strain in the soft grain. However, for polycrystalline material, it is assumed that the deformation is constrained by the neighbouring grains and therefore the effective strain (ε_{eff}) is the same in all grains (**Fig. 2-11**). Therefore, due to the higher stiffness, stresses are higher in the hard grain, which has been described as a redistribution of stress from the soft to the hard grain. Due to the higher stresses initiation sites for the formation of facets and cracks would be in hard grains. This implication is identical to the slip-band model proposed by Evans and Bache.

Based on the models proposed by Evans and Bache, it would be expected that the plane normal of facets on the fracture surface of samples failed under CDF loading conditions are parallel to the loading directions [35], [138], [147], [149]. This fits with earlier observations but contradicts with the more recent study that has shown that facets are tilted approximately 30° from the loading directions [144] (see paragraph 2.3.5). As facets are normally close to parallel to the (0002)-plane [135], [149], [150], this leads to the conclusion that grains in which facets are formed have a declination angle of approximately 30° between the loading direction and c-axis. In the latter case, for these crystallographic orientations, the activation of basal slip would be possible, therefore no hard-soft grain combination would be given. However, the following should be kept in mind: for cyclic (non-dwell) loading conditions, it has been observed that the plane normal of facets have higher misorientation from the loading direction than for CDF loading conditions, e.g. Jha et al. reported that most facets have angles in the range of 30° to 60° for cycling loading [151]. CDF and cyclic loading conditions are similar and cannot always be distinguished easily, e.g. for short dwell

times or samples being tested under CDF conditions, but at stress levels that are too low to lead to a dwell debit. Therefore it seems difficult to exclude the possibility that some facets formed under CDF loading conditions may be having higher misorientations from the expected orientation. In combination with challenging experimental procedures for determining the orientation of the facets, as well as the crystallographic orientations of the grains, this makes this analysis a non-trivial task. Also, a large enough number of faces needs to be analysed to enables a statistical analysis of the distribution of orientations. Moreover, as laboratory tests are not always a perfect representation of in-service loading conditions, the analysis of large scale components using spin tests would be favourable, but which is difficult to realise due to high costs (>£150'000) and long testing times [41]. Analysis of facets formed in an aero-engine-disc during a spin test has shown that plane normal facets were misaligned no further than 15° from the principal stress direction [141].

As stated in chapter 2.3.5, susceptibility to CDF diminishes above a certain temperature. This is explained by the activation of <c+a>-type pyramidal slip becoming possible in the hard grain. As slip can be activated in the hard grain, there is no-longer a hard-soft grain combination given that could lead to the pile-up of dislocations and the formation of local stresses [136]. However, this explanation stands in contradiction with the general observations of the temperature dependant slip behaviour of titanium alloys (Chapter 2.1.1, **Fig. 2-2** (c)); for increasing temperature the CRSS values drop for <a>-type, as well as for <c+a>-type slip, but the ratio of CRSS values of <c+a>-type to <a>-type slip actually increases with temperature. Therefore, at higher temperatures, the activation of pyramidal slip in the hard grain would be even more difficult compared to basal and prismatic slip than at room temperature.

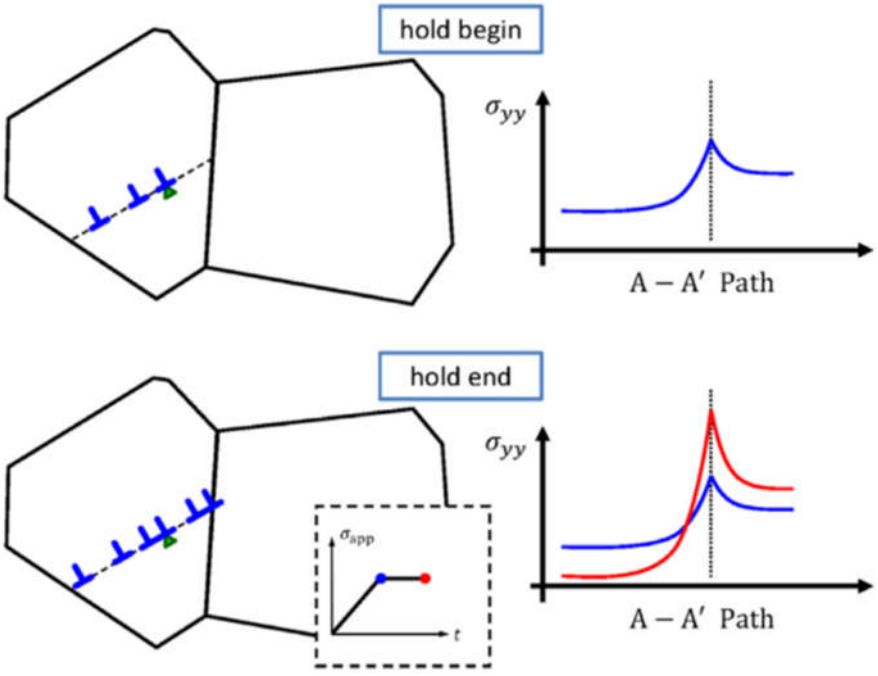

Fig. 2-12: Schematic of how the piled-up dislocations at the boundary between a hard and a soft grain during the dwell-period lead to the formation of localised stresses at the interface between the two grains [146].

A further model used for describing the mechanisms of CDF is termed 'load-shedding' [94], [137], [139], [146], [148], [152]. Similar to the aforementioned models, a 'rogue grain' combination is required and initial plastic deformation is localised in the soft grain, which results in a redistribution

of stress from the soft to the hard grain and final the formation of facets in the hard grains. A pile-up of dislocations in the soft grain at the boundary leads to stress concentrations at the interface between the two grains. The plastic deformation in the soft grain is assumed to be accommodated by time dependant local creep deformation. Initial loading leads to a certain pile-up of dislocations and therefore stress concentration at the grain interface. The creep process leads to further pile-up of dislocations and accumulation of strain, and therefore increases the local stresses with dwell time. The schematic in **Fig. 2-12** displays the differences in dislocation pile-up and local stress localisation between the beginning and end of the dwell period for constant applied stress. This model explains the correlation between the holding/dwell time and the dwell debit, which hasn't been provided by the model initially proposed by Evans and Bache. The initial increase in CDF susceptibility for temperatures of up to approximately 120° [137] is explained by the enhanced slip activity in the soft grain, accelerating the build-up of stresses at the interface to the hard grain. The reduced susceptibility at even higher temperatures is assumed to be due to thermally activated creep leading to a redistribution of stresses at the interface.

2.3.7 Correlation between CDF to microstructure

As it has been mentioned in chapter 2.3.5, susceptibility to cold creep is related to the underlying microstructure. Firstly, the susceptibility to CDF fatigue increases with increasing structural unit sizes, namely primary α grains, as well as secondary α colonies [136], [138], [145]. Larger grains have a detrimental effect, both regarding soft and hard grains. Larger soft grains lead to a longer free slip path and therefore lead to the pile-up of more dislocations at the boundary between hard and soft grains, leading to higher stress concentrations [153]. Larger hard grains result in larger facets, which can promote crack initiation and propagation, and therefore an early failure.

Texture analysis of fracture surfaces has shown that the facets do not only form in single grains but that they can grow in areas with a similar texture [89], [154]. For grains with the same or similar orientations, grain boundaries may not be an effective obstacle to dislocation movement [155]. The slip length is getting longer and more dislocations will pile up at the next effective boundary, which results in higher induced stress in the adjacent grain. Therefore macrozones can have a detrimental effect on the dwell fatigue life. Also, limited variant selection contributes to the size of these structural units. As macrozones are significantly bigger than grains, they lead to an increased size of the facets and therefore the length of initiated cracks. Also, macrozones might lead to longer slip bands and more dislocations that then pile-up at a grain boundary, resulting in higher induced stresses in the adjacent grain. This both leads to a reduction in fatigue life [41], [89], [142], [156].

Based on the models discussed in chapter 2.3.6, it can be assumed that microstructural features inhibiting slip in the soft grains would improve the overall creep performance, as pile-up of dislocations at grain boundaries is reduced. Based on this assumption it may be expected that precipitates reduce the dwell sensitivity, as they provide strong obstacles to dislocation movement. Contradictory to this assumption, it has been reported unanimously, that precipitates have a detrimental effect on dwell fatigue properties and significantly reduce the cycles to failure. This has been observed, both for LCF as well as for CDF. It has been explained by the instability of Ti_3Al particles. Once these precipitates undergo shearing, they do not provide an effective obstacle to

further slip, leading to higher slip planarity and higher strain localisation [2], [27], [142], [157]. Therefore, the pile-up of dislocations at grain boundaries and local stresses may be increased.

2.3.8 Cold-creep

As the deformation in the soft grain during CDF is accommodated by a creep-process, it is important to understand creep mechanisms in titanium alloys at room temperature (cold creep) [139]. Normally creep occurs at elevated temperature (> 0.3 T_M), but in near-α and α+β titanium alloys creep deformation has been observed at lower temperatures, with a focus on room temperature, at stress levels as low as 60-65% of $\sigma_{0.2\%}$ [64], [158]–[161].

Harrison et al recorded a creep curve for Ti-6Al-4V, with a primary α-volume fraction of 60%, at 20°C (**Fig. 2-12**). For applied stress of 892MPa, the sample fractured after one week at a strain of about 16% [162]. Similarly to high-temperature creep, the curve exhibits three different stages: primary, secondary and tertiary creep. It needs to be kept in mind that this curve was recorded for stress close to the 0.2% proof stress, which is higher than the stresses applied in industrial applications or CDF tests. At lower stress levels, after the primary creep stage [159], [163], [164] it comes to saturation of creep strain and no steady-state creep stage has been observed afterwards [158], [164]. Which stages can be observed is strongly dependant on the applied stress and testing temperature.

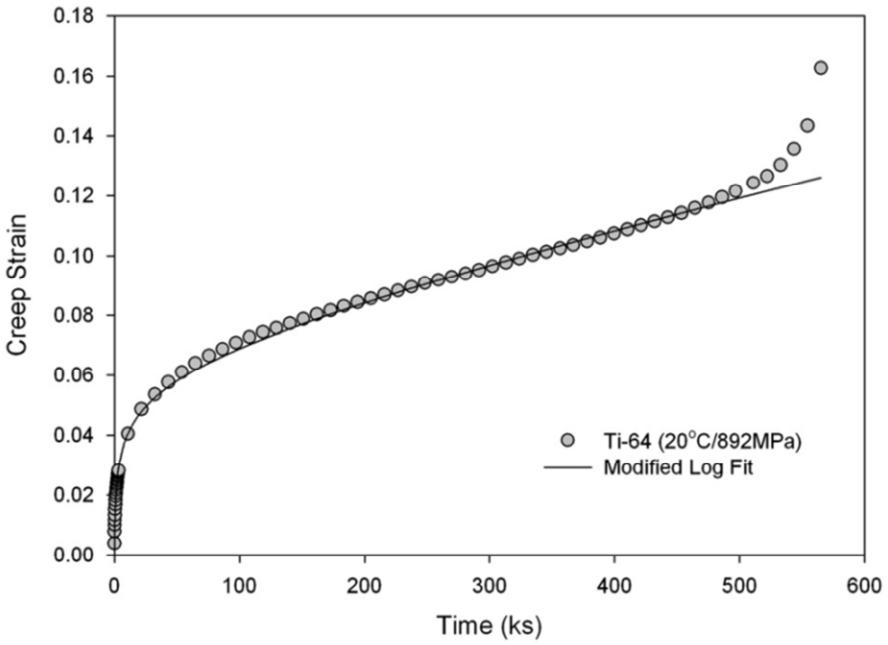

Fig. 2-13: Creep curve for Ti-6Al-4V for applied stress of 892MPa at 20°C [162].

In several studies that observed room temperature creep, explanations for the underlying deformation mechanisms have been proposed, but until today there is no coherent mechanistic understanding for cold creep deformation in Ti alloys. Proposed mechanisms are sliding at colony boundaries [164], self-diffusion controlled mechanisms [163] and dislocation creep, where pinned dislocation can overcome obstacles by thermal activation [159], [161]. Two factors that seem to enhance the susceptibility to cold creep are the low work hardening rates [158] and the lack of recovery [164] in titanium alloys. Statements that the creep sensitivity arises from the high strain rate sensitivity [137], [159] do not provide a mechanistic explanation. Rather the other way around, cold creep deformation could be the reason for the high strain rate sensitivity of titanium alloys.

The majority of studies on cold creep behaviour have shown that the creep rate at room temperature is strongly related to the microstructure. According to Miller et al. [164], Widmannstätten (colony) type microstructures result in the fastest creep rates. This is supposed to be due to the long slip length within the colonies [90], [91], and sliding at boundaries of colonies and α/β phase boundaries. This fits other observations that smaller grain sizes improve cold creep behaviour and that a basket weave-type microstructure is better than a colony type microstructure [158], [160], [164]. It can be stated that microstructures that reduce susceptibility to cold creep also appear to reduce susceptibility to CDF.

The effect of SRO and α_2-precipitates can have opposing effects on cold creep behaviour. On one hand, SRO and α_2 -precipitates lead to planar deformation and therefore reduce work hardening, which leads to a higher susceptibility to cold-creep [158]. On the other hand, they have a strengthening effect and inhibit initial dislocation movement. Therefore creep strength might be enhanced in early stages of deformation [165]. Also, the initial positive effect of SRO and α_2-precipitates may be diminishing under cyclic load, as second phase particles become sheared [4].

Studies by Odegard and Thompson [159], [161] have shown that applying a prestrain can reduce cold creep rates. This is not explained by an increase in dislocation density, but it is assumed that slip systems that can be activated at low stress levels are getting ‘exhausted’ and therefore no longer can contribute to plastic deformation during the creep test.

3 Experimental methods

3.1 Initial material

In this study, the near-α titanium alloy TIMETAL®834, nominally Ti-5.8Al-4Sn-3.5Zr-0.7Nb-0.5Mo-0.35Si-0.06C (wt.%), was analysed. Two slices (thickness 5 cm) taken from forged ingots of this material, with a radius of 20 to 25 were supplied by TIMET, UK.

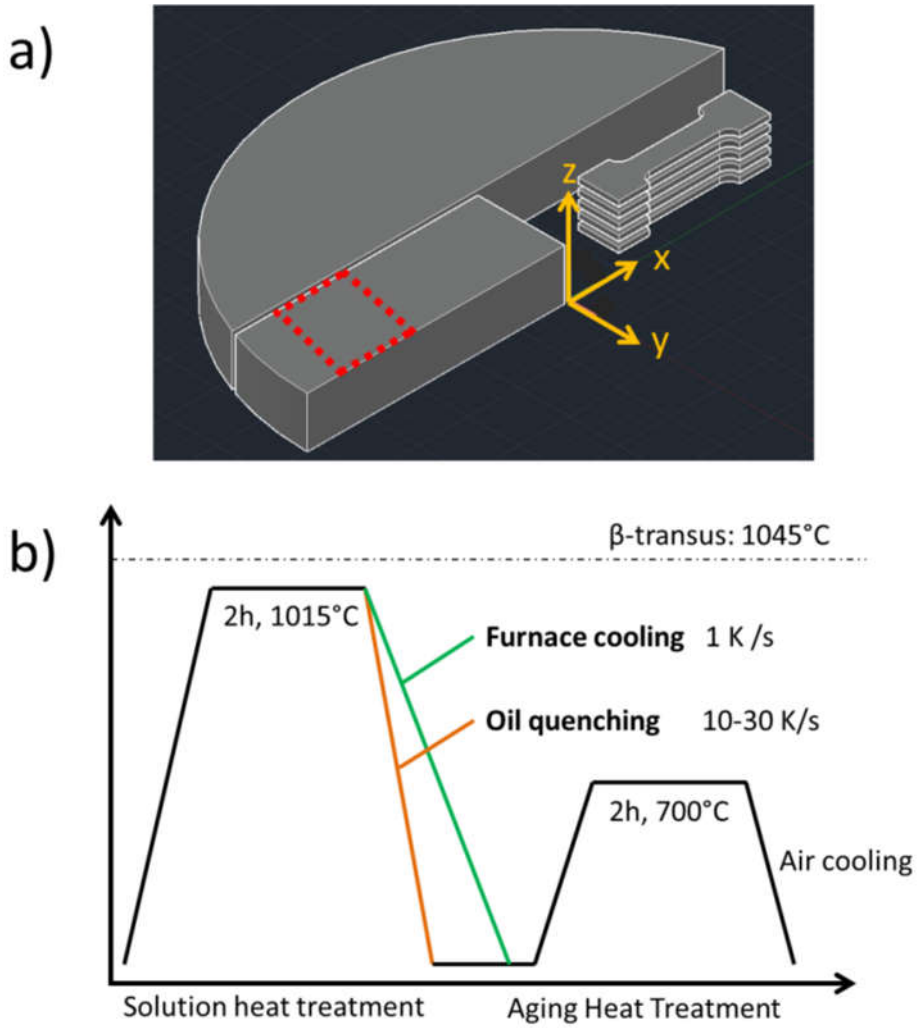

Fig. 3-1: a) Schematic CAD-drawing showing the geometry of the received billet material and the position and orientation of the heat-treated blocks. The red box indicates the area for baseline characterisation. b) The sequence of heat treatments applied to the received material

Orientations relative to the samples are described by the directions **x**,**y** and **z** (see **Fig. 3-1, a**), with the **z**-direction being the elongation direction **ED** of the forgings. Blocks with a size of 2x2x8 cm³ were cut for applying heat treatments. As the blocks were not cut directly from the centre of the forgings, **x** is the radial and **y** the circumferential direction.

The thermomechanical processing history of the received material was not given for any of the two material conditions. Optical micrographs (Fig. 3-2) of both materials in the as-received condition reveal bimodal microstructures, indicating that both materials may have been forged below the β-transus temperature. ‘Material B’ (Fig. 3-2, b) exhibited a homogeneous distribution of primary α-grains, with most grains having roughly the same size and most of the grains being spherical. Some grains are slightly elongated in the y-direction, with local clustering of primary α grains. The volume fraction of primary α is slightly above 40%.

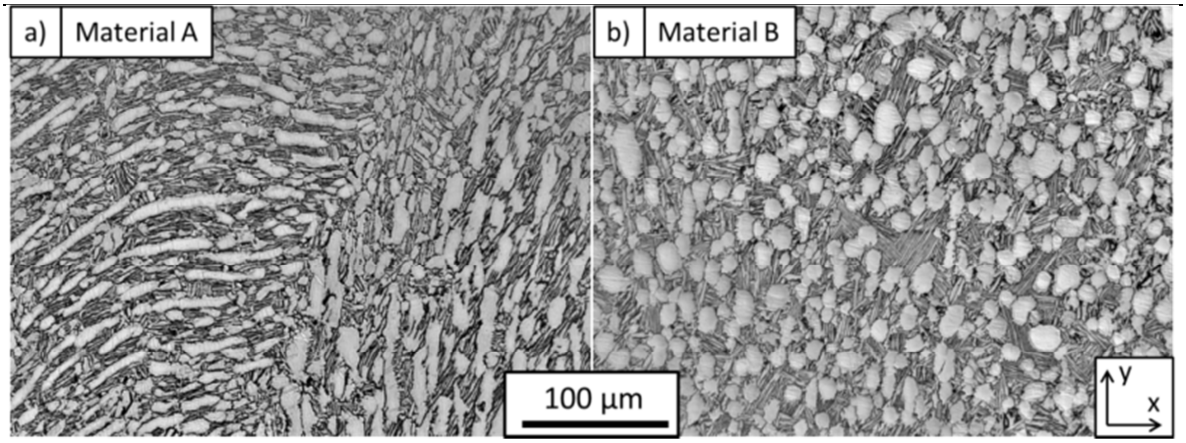

Fig. 3-2: Optical micrographs of a) Material A and b) Material B in the as-received condition.

The micrograph of 'Material A' reveals a wider range of primary α-grain sizes. There are large grains that are strongly elongated and smaller, spherical grains in-between. The larger grains were about 5 to 10 times larger in area than the smaller ones and had an aspect ratio of up to 10 to 1. Two different areas could be identified, which differed from each other by the orientation of the elongated primary α-grains. On the left side of the image, the elongated grains are orientated in the x-direction, while they are orientated in the y-direction on the right side. These two areas may be correlated to two different β-grains. The volume fraction of primary α-phase was about 36 percentage in Material A. The number of detected primary α-grains was significantly higher for 'Material A' compared to 'Material B', which is mainly due to the fine grains between the larger and elongated ones. As described in **chapter 2.2.1,** primary α is initially formed by the beak up of α-lamellae during thermomechanical processing (TMP). It appears that the microstructure of 'Material A' stills reveals the morphology of these coarse, initial α-lamellae that have only been broken up partially during the forging process.

3.2 Material preparation

3.2.1 Heat treatments

A bimodal microstructure with a primary α volume fraction of around 15% was produced by solution heat treating two blocks of material for two hours at 1015 °C, 30 °C below the β transus temperature [166]. Subsequently, one of the blocks was cooled rapidly by oil quenching (10 – 30 K/s), leading to the formation of a fine transformation product. The other block was furnace cooled to room temperature at a rate of 1 K/s, resulting in a coarser transformation product. To achieve this cooling rate after the solution heat treatment, the sample was placed in an area of the tube furnace, where the temperature was approximately 400 °C, resulting in a cooling rate slower than air-cooling, but faster than conventional furnace cooling. After reaching a temperature of 700 °C, the sample was taken out of the furnace and air-cooled to room temperature. The cooling rates were determined by fixing a thermocouple in the centre of a block of titanium, which had the same size as the heat-treated samples, and recording the temperature-time curves while applying the heat treatments. Cooling rates were determined for the temperature range of 1015 °C to 700 °C, as it was assumed that the β→α+β phase transformation was completed when a temperature of 700 °C was reached. Subsequently, both blocks were annealed for two hours at 700 °C, which is known to lead to the precipitation of Ti_3Al (α_2) predominantly in the primary α phase [167].

3.2.2 Metallographic Preparation

Flat dog-bone specimens, with a gauge volume of 1 mm x 3 mm X 26 mm were electrical discharge machined for uniaxial tensile testing. The loading direction was parallel to the x-direction (**Fig. 3-1, a**). Subsequently, both sides of all samples were ground with #800 grit paper to remove deep scratches and oxides formed during machining. The samples were further ground to #4000 grit paper, followed by hand polishing in water-based colloidal silica solution (4:1) for 10 mins for further characterisation and HRDIC. To reveal the microstructure by optical microscopy, the polished samples were etched with Kroll's reagent (2 ml HF, 4 ml HNO_3, 94 ml H_2O).

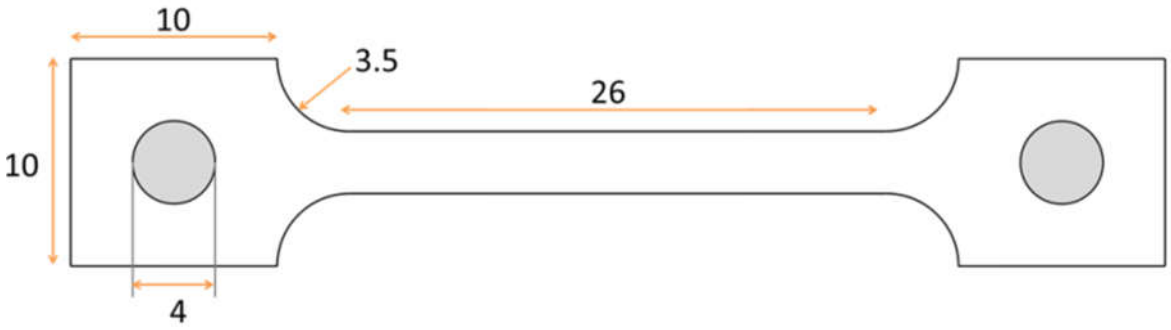

Fig. 3-3: Geometry of the dog-bone specimens used for all mechanical tests. Units are in mm.

3.3 Optical microscopy

Optical microscopy was used for the metallographic characterisation of all material conditions, analysing grain size, volume fraction of each constituent and spacing of a/β lamellae. Optical bright-field microscopy uses a light source with a spectrum in the visible range (wavelengths of 0.4 µm to 0.7 µm [168]) illuminating the sample close to perpendicular to the sample surface and parallel to the lenses. On flat specimen with a mirror-like surface finish, most of the light is reflected directly towards the lenses, making the sample appear bright. For revealing the microstructure of a material, samples are etched after polishing (see paragraph 3.2.2). Firstly, material is removed faster at grain- and phase-boundaries, creating pits at the sample surface. At these pits, light is scattered and therefore less light is collected by the lens, making the boundaries appear dark in the bright-field micrographs (Fig. 3-4). Depending on the crystallographic orientation, etching can remove material at different rates, leading to the formation of facets for different orientations. As this affects the reflection of light, areas with different crystallographic orientations can be distinguished by their grey-scale values in optical micrographs [168], [169].

Spatial resolution in microscopy is defined by the size and distance between features that can be observed and distinguished. The highest spatial resolution in optical microscopy is given by the diffraction limit, according to which the resolution cannot be better than half the wavelength of the light used for imaging.

For recording images covering larger areas (~2 mm²), which were used to analyse volume fractions and the morphology of the primary α grains, a ZEISS Axioscope optical microscope was used. When a higher spatial resolution is required, e.g. for determining α/β lamellae spacing, Keyence X200K 3D Laser Microscope was used. In this case, 2D images were recorded, not utilising the 3D imaging capacity of the microscope. As the microscope is equipped with a 408 nm (violet) laser as

a light source, which is at the low end of the visible spectrum, the highest possible spatial resolution for optical microscopy can be achieved.

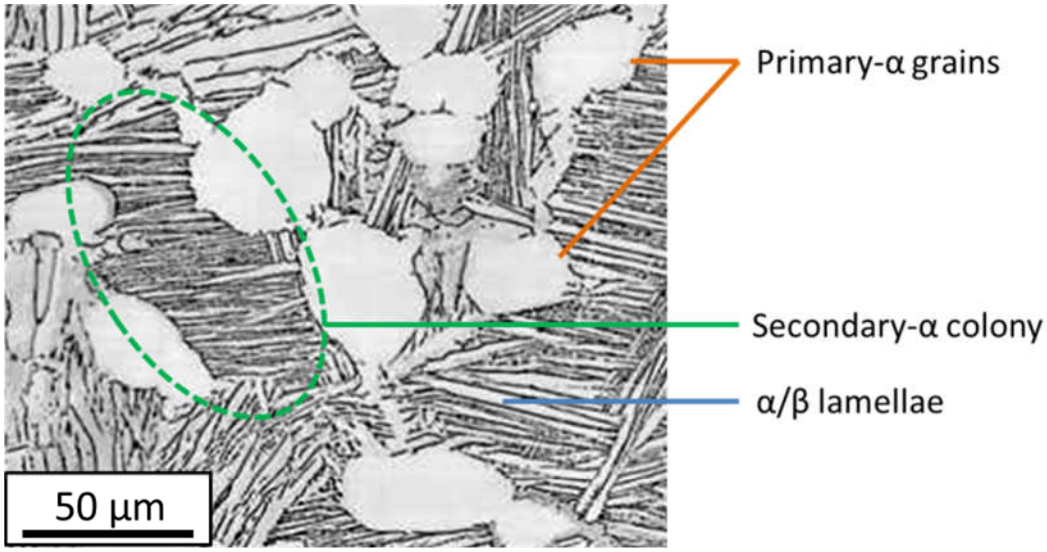

Fig. 3-4: Example for material with bimodal microstructure (Material B, coarse microstructure), indicating primary-α grains, secondary-α colonies and α/β lamellae.

For each material condition, an area of 2 mm² was characterised using optical bright-field microscopy to determine the average grain size and volume fractions of the individual constituents. Segmentation of the primary α constituent was performed, using the image analysis software 'Fiji' [170], based on the differences in grey-scale values between the two constituents. The 'characterise particles' function was used to determine the average size and volume fraction of primary α grains. The spacing of secondary α lamellae was calculated using the line intercept method for 30 secondary α colonies.

3.4 Scanning Electron Microscopy (SEM)

3.4.1 Principals of SEM imaging

Scanning Electron microscopy (SEM) is a versatile imaging technique. A range of different detectors allows analysing microstructure, crystallographic orientations and local chemical composition, to name but a few. Images are created by scanning a focused electron beam over a region of interest (ROI) and collecting signal at each scanning point. In comparison to optical microscopy, where the complete ROI is imaged at the same time, SEM images are recorded by subsequently imaging one point after the other. This needs to be kept in mind when imaging a sample that changes with time during image acquisition, e.g. a sample that is plastically deforming in an in-situ experiment. Just like optical microscopy (see paragraph 3.3), the spatial resolution of electron microscopy techniques is theoretically limited by the diffraction limit. The wavelength of electrons is determined by calculating the 'de Broglie wavelength', which is indirectly proportional to the momentum of the electron, in this case, the acceleration voltage. Even for an acceleration voltage of 1 kV, which is on the low end of acceleration voltages commonly used for SEM imaging, the wavelength is less than 0.04 nm. Therefore the spatial resolution for SEM imaging techniques is practically not limited by the diffraction limit, as other parameters, e.g. lens aberrations, electron spot size and electron-specimen interaction volume (see paragraph 3.4.7), influence the achievable resolution more. This shows that higher spatial resolutions than in optical microscopy can be achieved [171], [172].

3.4.2 Electron sources

SEMs can be equipped with different types of electron sources, two of them being tungsten filament and field emission guns (FEG). Tungsten filaments are using thermionic emission for creating an electron beam. In FEGs, a fine tungsten needle is charged with several kV, enabling electrons to tunnel out of the tip. In both cases, two voltages are applied: one for extracting the electrons from the source and a second one for applying the acceleration voltage. While being more expensive than tungsten filament sources, FEGs have several advantages providing better imaging conditions: Firstly the energy spread of the emitted electrons is lower, approximately by factor 10. Secondly, smaller electron probe size can be achieved, while at the same time providing higher beam currents. This enables imaging at higher spatial resolutions and gives a better signal to noise ratio. On the other hand, for large probe radii (> 1µm), tungsten filaments can provide higher beam currents, giving an advantage for imaging at lower spatial resolutions. All electron microscopes used in this project are equipped with FEG electron sources [171], [173].

3.4.3 Back Scatter Electron (BSE) – imaging

There are different ways the incident electron beam can interact with the matter in the specimen. One possibility is that the electrons interact with the core of the atoms, resulting in inelastic scattering. Electrons can be scattered back from the sample by one or a series of elastic scattering events.

If electrons are scattered purely elastic, the energy of the BSEs will be close to the energy of the incident electrons. A combination of elastic and plastic scattering is also possible, leading to lower remaining energy of the BSE. A higher density of the material and higher atomic numbers increase the probability of the electrons being scattered back. As the brightness of the recorded BSE-SEM image is correlated to the number of detected electrons, higher brightness indicates higher density or atoms with a higher atomic number [172], [174], [175].

The Crystallographic orientation of grains influences how electrons are scattered, resulting in orientation contrast in BSE-micrographs. It enables distinguishing between areas with different orientations, but Electron Back Scatter Diffraction (EBSD) mapping is required to determine the crystallographic orientations [15].

3.4.4 Electron Back Scatter Diffraction (EBSD)

3.4.4.1 Principals of EBSD mapping

When electrons are scattered at crystalline material, it comes to positive and negative interference, according to Bragg's law. If electrons are scattered more than once, positive interference, or maxima, are not observed only along one specific orientation for the diffracted electrons, but there are multiple directions, forming a diffraction cone in 3-dimensions. When the diffracted electrons are recorded on a 2-dimensional detector, each cone, which correlates to a specific crystallographic plane, appears as a line. The lines from all crystallographic planes create a pattern (Kikuchi pattern) that is distinctive for each crystallographic phase and orientation. An algorithm in the imaging software (Oxford Instruments AZtec) can determine the crystallographic orientation at each scanning point, based on the Kikuchi patterns and the geometry and set up of the sample, microscope and EBSD-detector. For EBSD-mapping the sample is tilted by 70° and the detector is close to perpendicular to the incident electron beam, positioned so that Kikuchi pattern is centred on the detector [176].

3.4.4.2 Imaging conditions

Depending on the imaging conditions, two different SEMs were used for EBSD mapping. FEI Quanta 650 FEG-SEM equipped with Oxford Instruments HKLNordlys EBSD detector was used for recording the crystallographic orientation maps smaller than 0.5 mm² with a step size of 0.2 µm (acceleration voltage 15 kV, Manuscript 1) and 0.75 µm (acceleration voltage 20 kV, Manuscript 2&3). In the latter case, the same microscope was used both for EBSD mapping as well as for the HRDIC experiment. For recording crystallographic orientation maps larger than 10 mm² with a step size of 7.5 µm at an acceleration voltage of 20 kV, TESCAN Mira3 FEG-SEM with Oxford Instruments Symmetry EBSD detector was used. For the used conditions, this set-up allows recording up to 2000 data points per second, compared to approximately 50 data points per second on the HKL Nordlys EBSD detector. This makes the recording of crystallographic orientation maps up to 40 times faster, enabling to cover larger areas.

3.4.4.3 Reconstruction of the high temperature β-phase

As the β-phase volume fraction was low and the β-phase is distributed evenly throughout the sample, orientation maps of the β-phase cannot be recorded directly using EBSD mapping. Therefore, crystallographic orientation maps of the high-temperature β-phase were reconstructed from the orientation map of the α-phase (see chapter 2.1.4) [31], [63]. The indexing rate of the orientation maps of the α-phase (Fig 3-5, **a)** and **b)**) was high (98.2% and 99.2%) both for material with coarse and fine microstructure. The orientation maps of the β-phase (Fig. 3-5 **c)** and **d)**) reveal that the reconstruction worked better (higher reconstruction rate) with the material with fine (77%) than with coarse (54%) microstructure. This is expected to be due to more crystallographic variants being formed in the transformed β-phase of the material with fine microstructure. Furthermore, the material with coarse microstructure had a higher volume fraction of primary α grains, respectively a lower volume fraction of transformed β-phase, which results in a lower reconstruction rate.

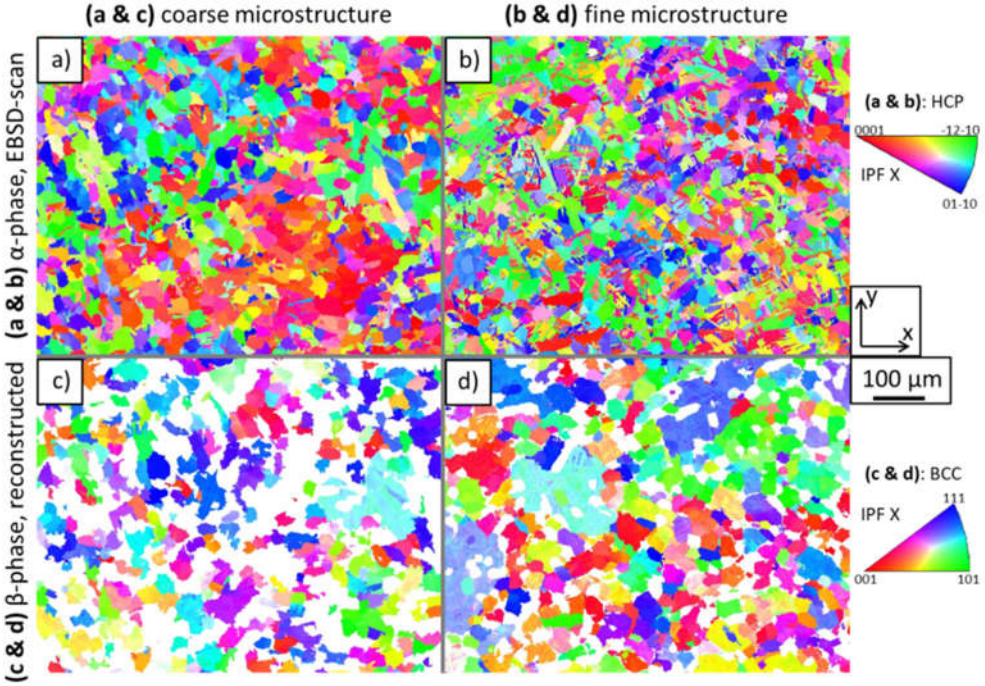

Fig. 3-5: Crystallographic orientation maps of Material B in the material condition with a) coarse microstructure and b) fine microstructure. For both maps, the indexing rate is at least 98%. The maps of the high-temperature β-phase (c & d) have been generated using β-reconstruction algorithm.

3.4.5 Energy-dispersive X-ray spectroscopy (EDS)

The interaction of the SEM electron beam with the specimen leads to the emission of a spectrum of X-rays, which consists of a continuous background and characteristic peaks. The background is caused by the Bremsstrahlung (breaking radiation), which are X-rays that are emitted when the incident electrons are scattered inelastically. The characteristic radiation is emitted when an electron from one of the inner shells of the atoms in the specimen is ejected after inelastic interaction with the incident electron beam and electrons from the outer shell migrating to the created vacancy. As the energy of these X-rays is characteristic for each element, they can be used for determining the local chemical composition of the specimen. Silicon drift detectors (SDD) are used to detect the intensity of the emitted X-rays as a function of their energy. In SDD-EDS detectors the energy of the X-rays is determined by the amount of ionisation caused in the detector. A possible problem occurs when two X-rays are detected simultaneously, as this may be registered as one X-ray with the accumulated energy of both. [177]

SEM-EDS analysis was used to analyse silicide precipitates with a size of approximately 100 nm (See Fig. 7-10), using Zeiss Merlin FEG-SEM equipped with Oxford Instruments X-Max Extreme detector. An acceleration voltage of 4 kV was used, which is low for SEM-EDS imaging, as this reduces the electron-specimen interaction volume, enabling higher special resolution (see paragraph 3.4.7). Compared to conventional equipment, the used detector doesn't have a protective polymer window in front of the detector, which allows detecting X-rays with energy as low as 1 kV. [178], [179]

3.4.6 Electron Probe Microanalysis - Wavelength-Dispersive X-Ray Spectroscopy (EPMA - WDS)

Depending on the elements in the analysed material, energies of characteristic peaks of different elements may be similar and difficult to differentiate using EDS-detectors. WDS allows recording the X-ray spectrum with higher spectral-resolution, which allows discriminating characteristic peaks that may be overlapping in EDS analysis. The principal of WDS is that the X-rays are diffracted at an analytical crystal with specific lattice spacing. The specimen, the crystal and the detector or positioned on a Rowland circle, so that only X-rays with a wavelength that satisfy the Bragg conditions are diffracted onto the detector. Therefore only X-rays with a specific wavelength, respectively energy, are detected. Which X-ray energies are getting detected can be defined by adjusting the position of the analytical crystal and the detector. For each element that is supposed to be analysed in a scan, a separate WDS detector is required, limiting the number of analysed elements in each scan. An EPMA is an instrument similar to an SEM, in which a sample is analysed by scanning a focused electron beam over it. EPMA is specialised for micro-chemical analysis, with the requirement for high beam stability over time. High stability is also achieved by using specific sample stages and holders [177], [180], [181].

The microchemical analysis was carried out using a Jeol JXA-8230 EPMA equipped with WDS detectors, operating at an acceleration voltage of 7 kV. Before analysing the specimen, the EPMA was calibrated using standards for each element.[3]

[3] Acknowledgment: Jonathan Fellowes carried out the EPMA-WDS analysis at University of Manchester, Department of Earth and Environmental Sciences

3.4.7 Electron matter interaction

To determine the best spatial resolution for imaging using SEM techniques, it is necessary to analyse the interaction between electrons and the sample. If the interaction volume is larger than the selected scanning step size, the signal emitted from material outside the analysed area will be collected and the effective spatial resolution would be lower than the step size. Therefore the scanning step-size and electron acceleration voltage need to be selected according to each other. The electron-sample interaction is simulated using 'monte CArlo SImulation of electroN trajectory in sOlids' (CASINO) software [182], [183]. Simulations for electron acceleration voltages in a range of 4 – 20 kV are run (Fig. 3-6), assuming a beam radius of 10 nm. Electron trajectories have been plotted for 200 electrons, separating between electrons that are absorbed within the material (Fig. 3-6, blue) and electrons leaving the sample surface (red). For imaging techniques that are based on the detection of the back-scattered electrons (BSE, EBSD) the relevant interaction volume is described by the red trajectories, as only these electrons can be detected. For micro-chemical analysis, which is based on detecting characteristic X-rays emitted from atoms in the sample, the blue trajectories need to be considered. This is because for X-rays the probability of being reabsorbed by the material is lower than for electrons; therefore even X-rays emitted deeper within the sample may leave the sample and be detected by the EDS or WDS sensor.

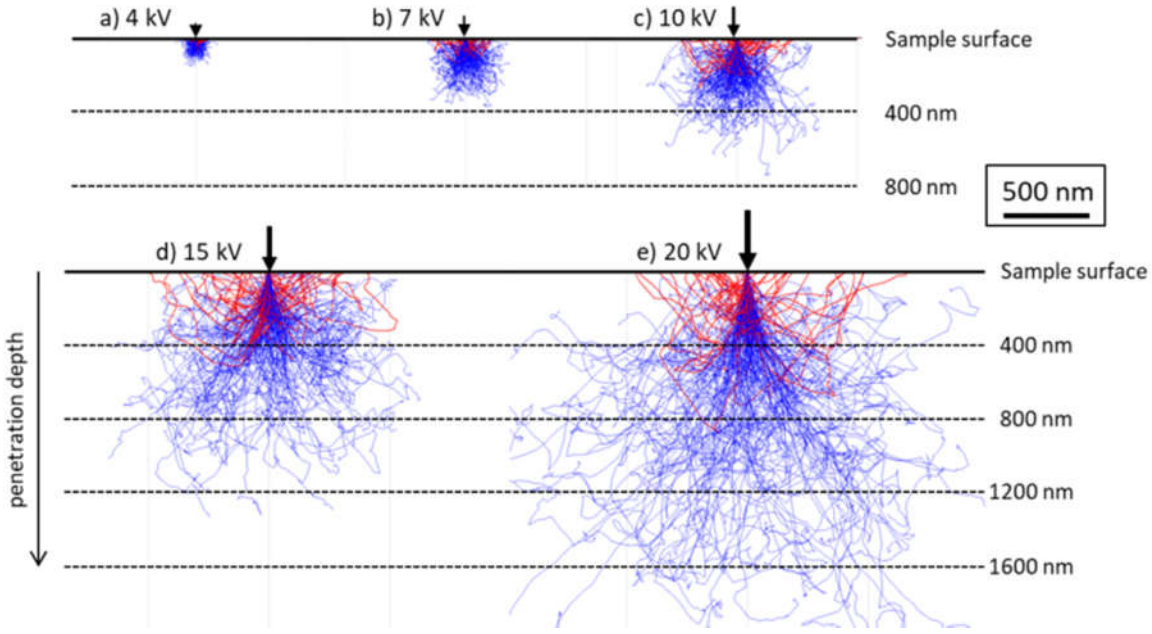

Fig. 3-6: Electron-sample interactions for different acceleration volumes: a) 5kV, b) 7 kV, c) 10 kV, d) 15 kV and 20 kV. The trajectories are for 200 electrons that either are absorbed by the sample (blue) or leaving through the sample surface.

For SEM-EDS analysis at 4 kV, the interaction volume is up to 100 nm, which is approximately three times lower than for EPMA-WDS analysis at 7 kV (~300 nm). An acceleration voltage of 10 kV was used for HRDIC analysis (see chapter 3.9), resulting in a penetration depth of up to 175 nm (Fig. 3-6, c). Due to its higher density, the penetration depth is lower for gold (approximately 50 nm). Assuming that the thickness of the gold-speckles is higher than the thickness of the initially deposited gold layer (50 – 80 nm [184]), the BSE signal will come predominantly from the gold particles and not the underlying titanium, when imaging the speckles, resulting in strong contrast to the areas not covered by gold.

For EBSD mapping with a step size of 0.2 µm, an acceleration voltage of 15 kV has been selected (see manuscript 1). The interaction volume has a depth of 300 nm and a width of up to 700 nm. Therefore the interaction volumes of adjacent points in the map are overlapping and it can be concluded that a lower acceleration voltage would have been required for achieving a true spatial resolution of 0.2 µm. For EBSD mapping with step sizes of 0.75 µm and higher the acceleration voltage was set to 20 kV, resulting in an interaction volume of 600 nm (depth) by 1 µm (width). However, reducing the acceleration voltage is not always feasible, as it leads to a reduction in signal and therefore deterioration of the signal to noise ratio.

3.5 Transmission Electron Microscopy (TEM)

3.5.1 Sample preparation

TEM-samples are prepared from the material condition with coarse microstructure, using twin-jet electropolishing. At first abrasive cutting is used to prepare a slice of material with a thickness of 1 mm. The thickness of the slice is reduced to approximately 80 µm by evenly removing material on both sides of the sample using 800-grid abrasive paper. Several specimens with a radius of 3 mm are punched out of the thin slice. The samples are electropolished in a TENUPOL 5 (Struers) twin jet polisher, using 10% perchloric acid and 90% methanol as etchant at a temperature of -32 °C. One specimen that has only one small hole in the centre of the disc is selected for the TEM analysis.

3.5.2 Selective Area Electron Diffraction Analysis (SAED)

TEM-diffraction analysis was used to analyse how variations in Al-concentration within primary-α grains affect the formation of α_2-precipitates. When recording diffraction-patterns along the [11-20]-zone axis in hcp-titanium, α_2-precipitates cause additional super-lattice diffraction spots. Therefore TEM-diffraction analysis can be used to determine if α_2-precipitates have been formed and the intensity of the super-lattice diffraction spots can be used to give a relative indication about their volume fraction.

The TEM-analysis was carried out using FEI Tecnai 20 operating at 200 kV. At first, a suitable primary-α grain is selected. The grain needs to be close to the hole in the sample so that the material is thin enough to be electron-transparent. The thickness should not vary throughout the grain, providing consistent imaging condition for the diffraction analysis. It is necessary to analyse a complete grain so that it is possible to determine the distance to the nearest grain boundary at each point and to be able to analyse a cross-section through the grain. Selective Area Electron Diffraction (SAED) is used to record diffraction patterns along a cross-section of a primary-α grain. The images were recorded using DATABIS imaging plates, which have a higher dynamic range than a CCD camera. This is necessary to be able to image both types of diffraction spots at the same time, as super-lattice diffraction spots have a lower intensity than principal diffraction spots. After recording the images, the imaging plates need to be removed from the microscope and scanned in the image-plate scanner (DITABIS Micron) to receive digital images. The output images have a depth of 16-bit. [185]

3.5.3 Data analysis

Analysing super-lattice reflection spots does not provide a quantitative analysis of the volume fraction of α_2-precipitates, but it enables to see if α_2-precipitates are present in a region and it allows comparing their volume fractions for different areas. The intensity of the super-lattice

diffraction spots from different areas cannot be compared directly to each other, as the intensities are affected by several parameters, e.g. the thickness of the sample. Instead, the intensities along a line through the lattice and super-lattice diffraction spots are plotted. The intensity of both peaks is determined by fitting a Voigt-function to them [186]. Then the ratio of the intensities of lattice to super-lattice diffraction spots is calculated, which can be used to compare different areas, as both the lattice and super-lattice diffraction spots should be equally affected by variations in sample thickness.

3.6 Atom Probe Tomography (APT)

3.6.1 APT – principle

Atom Probe Tomography (ATP) is a destructive characterisation technique that enables a 3D-analysis of chemical distributions with close to atomic resolution. This can, for example, be used to analyse the morphology, size and chemical composition of nano-scale precipitates. The functional principle of APT is that an electrical pulse is applied to a needle-shaped specimen with a radius of less than 100 nm, while the specimen is simultaneously struck by a laser pulse [187]. This leads to the extraction and ionisation of ideally one atom at a time. The charge to mass ratio of the ion is determined in a time of flight spectrometer that also detects in which direction the ion was extracted from the specimen. This information is used to reconstruct a 3D-dataset that contains the location and atom species of all detected ions [188].

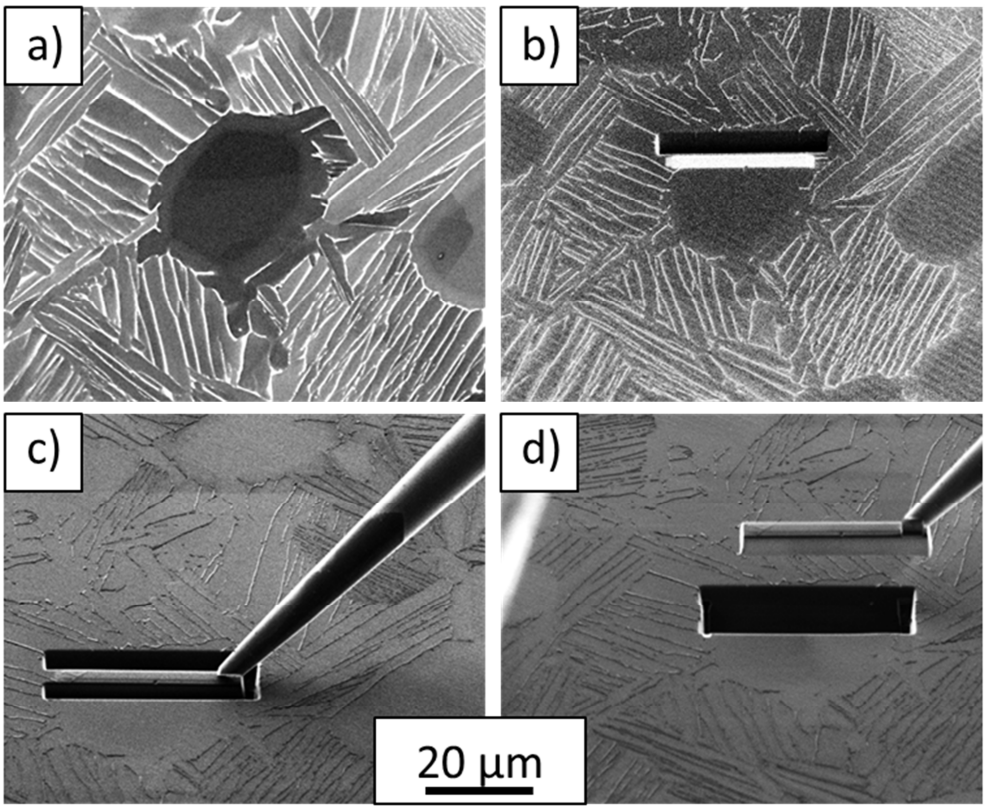

Fig. 3-7: Steps of the FIB lift-out: (a) The ROI selected for analysis. (b) Shows the trench machined next to the ROI (c) Shows the tip of the manipulator getting attached to the lift out before (d) being lifted from the bulk material.[4]

[4] Acknowledgment: Anna Radecka carried out the APT sample preparation and recorded the images displayed in Fig. 3-4 and 3-5.

3.6.2 Sample preparation

APT requires needle-shaped specimen with a radius less than 100 nm [187] that are prepared using Focused Ion Beam (FIB) machining. During the APT analysis, the radius at the tip of the specimen is increasing, which eventually leads to failure of the sample. The longer the time is before the sample fails, the larger the analysed sample volume can be. A circular cross/section increases the lifetime of the specimen [189], while lifetime is decreased by cracks, protrusions and a rough surface [190]. Features that are located less than 100 nm from the specimen tip have the highest probability of being within the analysed volume [191], [192].

A ROI was identified on the surface of a sample which had been polished and then etched (Fig. 3-4, a) to reveal the microstructure when imaging in secondary electron mode before FIB-machining. As shown in Fig. 3-4 b, the ROI was covered with two Pt layers using electron beam deposition (5 kV, 10 nA). The purpose of the first, thin layer (thickness ~20 nm) is to prevent sample modifications during further steps, while the second, thicker layer (thickness ~1000 nm) protects the atom probe specimen from getting damaged during ion-milling. In this work, a Helios NanoLab 600 equipped with an Omniprobe^{TM} and platinum GIS deposition system, was used to prepare needle-shaped specimens. Three trenches were milled around the ROI using a Ga beam with an acceleration voltage of 30 kV and a beam current of 700 pA. Beam damage was prevented by cutting a cleaning cross-section at a reduced current close to the ROI. In this way, a triangle-shaped lift-out was created, which was then attached to the silicon tip of a micromanipulator using Pt weld (Fig. 3-7, c&d).

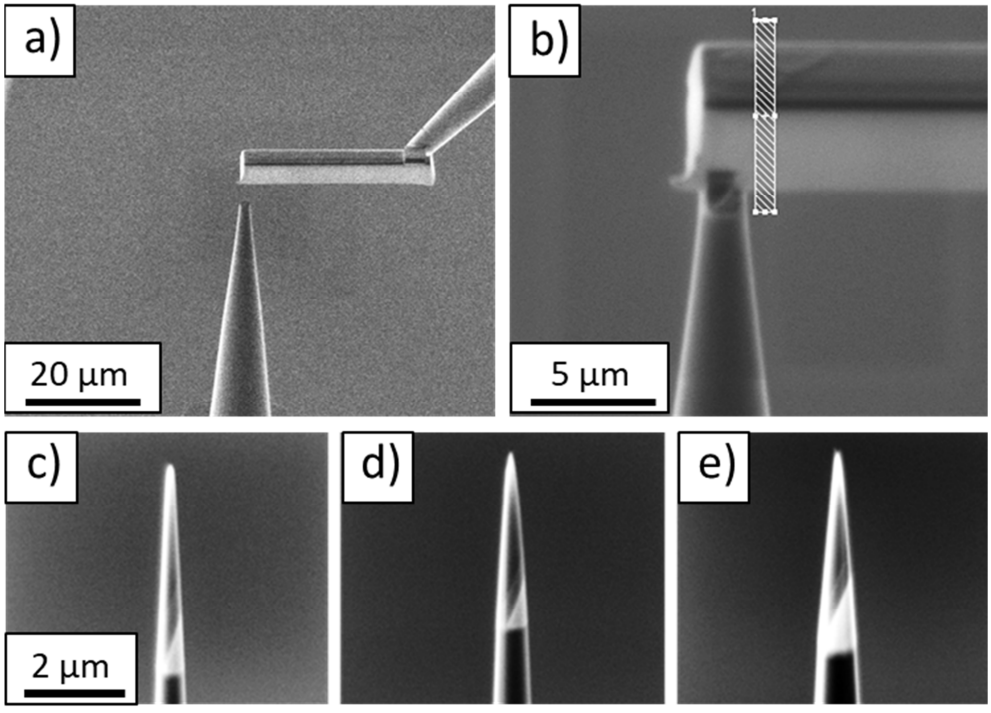

Fig. 3-8: Figures illustrating the second stage of specimen preparation using focused ion beam machining. a) The lift-out being attached to a post. b) Cutting off 3 µm wide cuboidal samples. c-e) finished APT samples.[1]

One side of the lift-out was attached to a post, before cutting off a region of approximately 3 µm. This step is repeated, creating a total of 8 specimens with a triangular-prism shape (Fig. 3-8, a&b). To create a needle-shaped geometry with a radius of 50 to 100 nm (Fig. 3-8, c-e), a sequence of

annular milling patterns was used. In the first milling step, the bulk material was removed, while subsequent milling steps create the final tip shape and radius. Until the last step of the sample preparation, an acceleration voltage of 30 kV is used for ion-milling. As Ga penetration is a function of the acceleration voltage [190], a final clean-up step was carried out at a lower acceleration voltage, removing material from the tip, which has been subject to Ga damage.

3.6.3 Experimental conditions

The prepared APT-samples were analysed using CAMECA Local Electron Atom Probe (LEAP) 5000XR. The scans were run at a stage temperature of 50 K with a laser pulse energy of 50 pJ.[5]

3.6.4 Data analysis

Data analysis of the APT-datasets is carried out using CAMECA IVAS software. At first, the average chemical composition of each of the 3 specimens was calculated. The data-sets have the same shape as the needles that were analysed, giving the position and atomic species of each atom/ion that has been detected. Near the surface of the sample, contaminations can be detected, which may be caused by oxidation or deposition of Gallium during the sample preparation in the FIB. If included, these contaminations would affect the calculated average chemical compositions of the specimens. Therefore the data-sets are cropped to a cylindrical shape, removing all areas that are close to the sample surface. The size of the cylinder was 50 nm (diameter) x 100 nm (height) for all specimens so that the same number of atoms is considered for each specimen. The size was selected so it fits for the smallest dataset. The atomic concentration can be determined directly by calculating the average frequency for each element. This was done by dividing the counts for each element by the counts for all elements. The concentration can then be transformed from atomic percentages **at.%** to weight-percentage **wt.%**.

The size and morphology of segregations can be analysed using iso-surface thresholding. A threshold value is set for the concentration of a selected element or group of elements. An algorithm finds areas in which the average concentration of the selected elements is higher, or respectively lower, than the set threshold. Then a surface element is created, that defines the interface between the areas of higher and lower concentrations. Along the created surface the concentration is constant and equal to the predefined threshold value. The iso-surfaces can be used for visualising segregations and analyse their shape and morphology.

As α_2-precipitates are enriched in Al, Al is used determining the iso-surfaces of the precipitates. The threshold value needs to be set between the average concentration of the sample (~10 at.%) and the theoretical concentration of the precipitates (25 at.%). The threshold value was determined following an approach carried out previously by Homma et al. [193]. The iso-concentration value was varied and the value which produces the narrowest interface width in the proximity histogram was selected.

[5] Acknowledgment: Paul Bagot carried out the APT analysis at Oxford University, Department of Materials

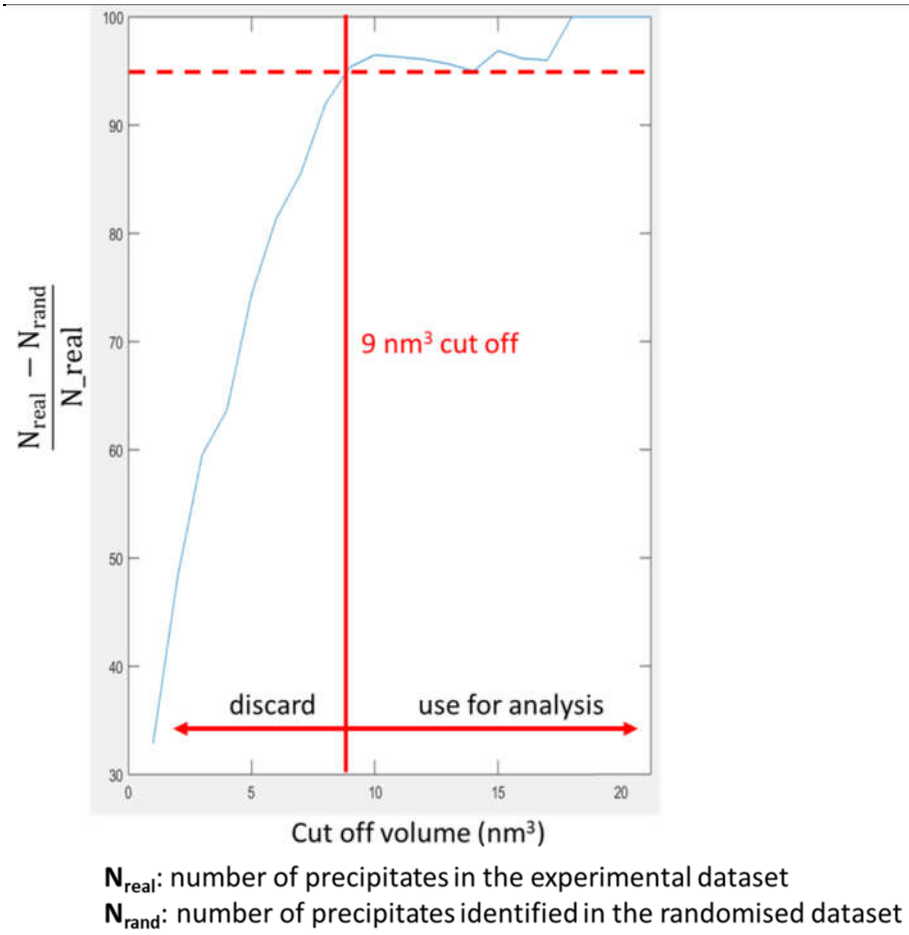

Fig. 3-9: Plot used to determine the cut off volume in the precipitate analysis of the APT datasets.

When small volumes (in the nm³ range) of the experimental datasets are analysed, there are high variations in the determined chemical composition, as only a small number of atoms is considered. Therefore the iso-surface analysis will show a large number of small precipitates, which most likely are artefacts. To discard those artefacts, a precipitate-volume-cut-off value needs to be defined. At first, a randomised dataset is created. This is done by keeping all the sites at which atoms have been determined in the as-measured data set, but randomly changing the atomic species at each site, while keeping the overall composition of the whole sample volume constant. Then the iso-surface analysis, using the same isoconcentration value, is applied to both the as-received as well as the randomised dataset. For each cut-off-volume, the number of remaining precipitates is determined. N_{real} is defined as the number of precipitates identified in the as-measured, experimental dataset, while N_{rand} is the number of precipitates identified in the randomised dataset. A value of cut off volume was chosen such that the percentage of clusters identified in the randomised dataset was less than 5% of those observed in the as-measured, experimental dataset. i.e. $(N_{real}-N_{rand})/ N_{real} \geq 95\%$ (**Fig. 3-9**) [194]. The determined cut off value is different for each data set and is in the range of 9-12 nm³.

3.7 Mechanical testing

3.7.1 Tensile testing to failure

Stress-strain curves were recorded to determine Young's modulus, yield stress, ultimate tensile stress (UTS) and strain to failure for all material conditions. The samples were loaded under uniaxial-stress at a constant strain rate of 0.005 mm/mm/s, according to ASTM standard [195],

[196]. Flat dog-bone specimens, as described in paragraph 3.2.2 were used. The tests were carried out using an Instron 5669 electromechanical tester, with a 50 kN load-cell. According to the specifications of the manufacturer, the accuracy of the recorded stress is +/- 0.4%, respectively +/- 3-4 MPa for the stress-values at the yield point, considering the sample geometry. The strain was measured using an extensometer, which is clipped onto the specimen. The extensometer was calibrated before the experiment, using a micrometre. Based on the reading of the extensometer, the strain-rate was calculated at any time of the experiment. A feedback loop was used to control and adjusts the speed of the cross-head of the mechanical tester so that the resulting strain rate in the sample was close to the pre-set value. The specimens were tested until failure, but the extensometer (10 mm) did not cover the whole length of the sample gauge (26 mm); therefore the specimens may fail outside the area which is covered by the extensometer. Before necking starts, this doesn't affect the determined strain values, as the deformation is assumed to be uniform throughout the sample gauge. If the specimen starts necking outside the area covered by the extensometer, the calculated values would be an underestimation of the real strain values. This doesn't affect Young's modulus, yield point and ultimate tensile stress and UTS, but it would affect the strain to failure. For all stress-strain curves, the engineering stress and strain were plotted (Fig. 7-11).

The Young's modulus was determined by fitting a linear regression line to the data points in the elastic regime and determining its slop, with the slope of the line being the Young's modulus. The upper end of the data range that is used for calculating Young's modulus is defined by the onset of plastic deformation or yield point, at which the stress-strain curve starts deviating from the linear behaviour in the elastic regime.

In this work, the 0.2%-proof stress ($\sigma_{0.2\%}$) was used for characterising all material conditions. The yield point describes the stress at which the first plastic deformation can be observed on a macroscopic level, while at the 0.2% proof stress already 0.2% plastic strain has been accumulated. It is determined by plotting a straight line, parallel to the elastic regime, which was shifted towards higher strain-values by 0.2%. The intersection of this line with the stress-strain curve defined the 0.2% proof stress. UTS was determined by finding the maximum stress-value in the engineering stress-strain curve.

3.7.2 Room temperature creep testing

To analyse the cold-creep properties of the different material conditions, creep curves were recorded at room temperature (26.0 ± 0.5 °C) in a temperature-controlled room. A constant load was applied, while strain was measured as a function of time. Creep rigs were used for this experiment, in which calibrated weights were placed at the end of a lever, applying a constant uniaxial load to the sample. The stress in the sample was constant, assuming that the cross-section of the sample did not change (equation 3-1). Increasing plastic strain leads to a reduction in the cross-section and therefore an increase in stress, as the load stays constant throughout the creep experiment. The maximum plastic deformation was <0.15% at 80% of $\sigma_{0.2\%}$ and <0.9% at 90% $\sigma_{0.2\%}$. For these strain values, the resulting true stresses (equation 3-3) are 80% of $\sigma_{0.2\%}$ 91% of $\sigma_{0.2\%.}$

Engineering stress: $\sigma_E = \frac{F_A}{A_0}$ (3-1)

Engineering strain: $\varepsilon_E = \frac{\Delta L}{L_0}$ (3-2)

Trues Stress: $\sigma_T = \sigma_E \ (1 + \varepsilon_E)$ (3-3)

True strain: $\varepsilon_T = \ln(1 + \varepsilon_E)$ (3-4)

In equation (3-1) and (3-2), L_0 is the initial sample length, ΔL is the change in sample length, F_A is the applied load and A_0 is the Initial cross-section of the sample.

The creep rigs used were designed for cylindrical samples, which are threaded at both ends. The threads are used for holding the samples and applying the mechanical load. For the creep experiment, flat dog-bone specimen were used (Fig. 3-3), which had flat tabs with a pinhole at both ends; therefore it was necessary to design an adapter which allowed for the testing of flat dog bone-specimen in the creep rigs. The adaptor (Fig. 3-10) had a 12mm thread on one side, which was screwed into the load bars of the creep rig. On the other side, they had a slot which was slightly wider than the thickness of the used specimens. A hole with a diameter of 4mm, which was perpendicular to the slot, allowed securing the specimen with a pin. Therefore, the complete load application into the sample was through the pins. Before the sample holders where machined, finite element analysis (FEA) using ABAQUS was carried out, simulating the loads and local stresses in the sample holder and the specimen. For simplification, a purely elastic simulation was run. To achieve this, the yield-stress is set to be infinitely high, which doesn't allow for any plastic deformation. Therefore the resulting stresses may be higher locally than the yield stress of the material. In this case, it can be assumed that these areas deform plastically. For the elastic properties, average values of the uniaxial tensile tests were used. For the steel pin, material properties of plain carbon steel have been used. Results of this simulation are shown in Fig. 3-10 (b). The results of the simulation and later on the experiment show that the pin and sample holder were strong enough to withstand the load. In the tab of the dog-bone specimen, local stress concentrations can be observed, but in the gauge of the sample, the stress appears to be homogeneous and without any local concentrations. Based on these observations, it was decided that the geometry of the samples in combination with these sample holders were suitable for running creep experiments.

For strain measurements, linear strain-gauges (Omega) with a size of 3x1 mm² and a resistance of 350 Ω are attached to the tensile specimen using hot curing epoxy-resin adhesive (HBM-EP150). The sample surface was prepared by grinding off any oxide layers formed during EDM-machining, using 400-grid abrasive paper. Afterwards, the sample was cleaned with acetone, ethanol and a mild acid (Omega-acid primer). After the sample surface was cleaned with the light acid, Omega-neutraliser was applied.

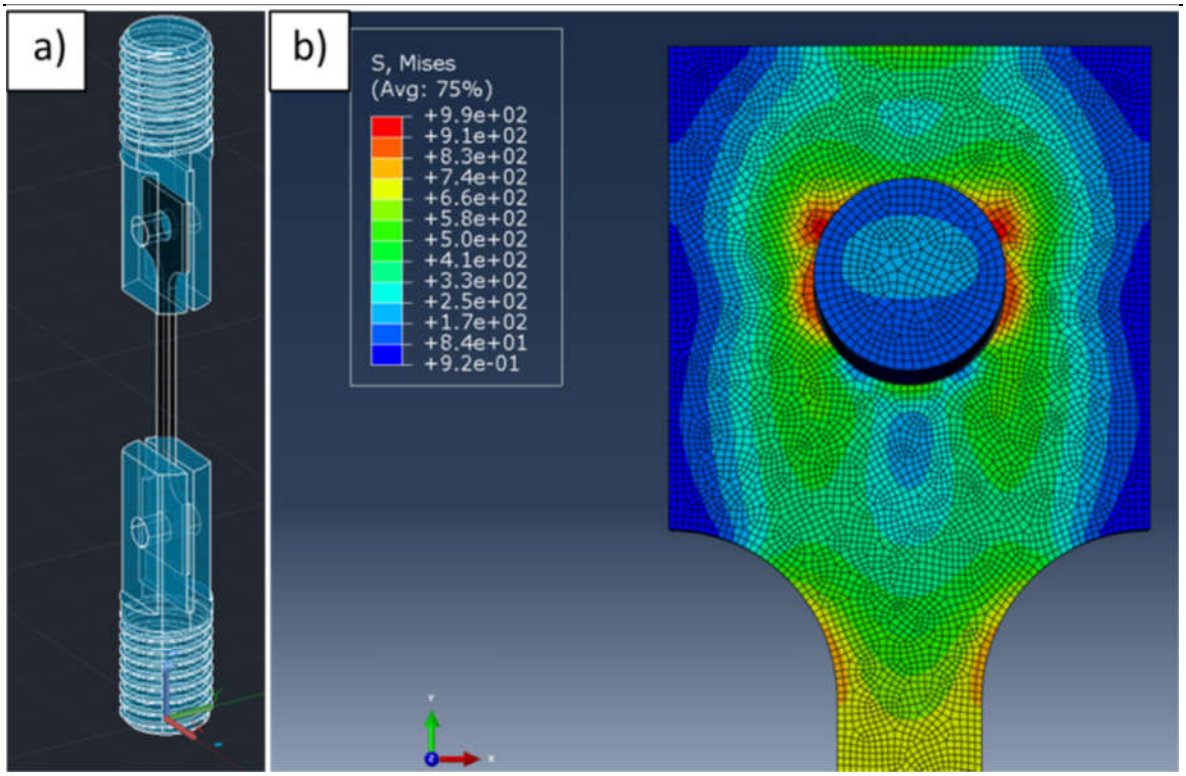

Fig. 3-1: a) Setup of the sample holder and dog-bone specimen used for creep testing. b) Results of FEA-simulations showing stress distribution in the tab of the dog-bone specimen during creep loading.

At first, the strain gauge was fixated at the intended position on the sample surface, using heat resistant poly-amid tape. The tape with the strain-gauge on it was then peeled back and the adhesive was applied both to the strain-gauge as well as the sample surface. The adhesive was dried in a furnace at 100 °C for 30 minutes. Then the strain-gauge was placed again on the intended position and a pressure of approximately 50 N/cm² was applied with a clamp. The adhesive was cured at 180°C for 3 hours before it was slowly cooled to room temperature. The tape was removed carefully, avoiding damaging the strain gauge.

MicroMeasurement P3 strain-recorder was used for recording strain values. Accurate measurements are achieved with the internal Wheatstone bridge of the strain recorder using 350 Ω resistors for balancing the strain gauge which, in the undeformed state, has the same resistance.

The mechanical load for the creep experiment was specific for each sample and was given as a percentage of the 0.2% proof stress. All samples were tested at 80% and 90% of $\sigma_{0.2\%}$. At these stress levels, macroscopic creep deformation was observed, while at 70% of $\sigma_{0.2\%}$ the macroscopic plastic strains were too low to be measured reliably. The deformation rate was fastest at the beginning of the experiment and then reduced quickly. All samples were tested for at least 20 days. After this time the creep rates had dropped by around 3-5 orders of magnitude, depending on the material condition, and further deformation took place only relatively slowly.

As the deformation rate was faster at the beginning, the time step for recording data was set to a shorter value (5 s) at the beginning. After around 3 days, when the strain rate had reduced by at least 3 orders of magnitude, the sampling rate was reduced to one data point every 2 minutes. For post-processing, a Python script was used to reduce the number of data points and to calculate

strain rates. The difference in strain was calculated for two time-steps *n* and *(n + 1)*; if the difference is larger than the threshold value of $5x10^{-6}$ mm/mm, the average of both points is calculated, both for the time and strain values, and saved to a file. If the difference is less than the threshold value, the second point is discarded and the difference between the points *n* and *(n + 2)* is calculated. This step was repeated until the difference is above the threshold and the average value was calculated and saved.

3.7.3 Error analysis for mechanical testing

The samples used for all tests had a cross-section of 3x1 mm². To calculate the required load to reach a defined stress level, the exact cross-section was needed. Therefore, before each test, the width and thickness of the samples were determined using callipers. We assumed an accuracy of ±0.02 mm. During in-situ testing, the load was measured by the load cell of the microtester, which has an accuracy of ±0.4% of the total load. For our tests, this relates to approximately ±10 N in load. For the tests in the creep-rigs, we assume the same accuracy. Based on these assumptions, the applied stresses were 70 ± 2.2%, 80 ± 2.5% and 90 ± 2.8% of $\sigma_{0.2\%}$.

3.8 Slip trace observations using optical microscopy

3.8.1 Experimental setup

Optical microscopy with dark-field contrast can be used to visualise slip bands with an out-of-plane component. This technique was used to analyse the formation and evolution of slip-patterns during cold-creep, during constant load-holds at 80% and 90% of $\sigma_{0.2\%}$ during periods of 24 hours.

For dark field contrast in optical microscopy, the lens of the microscope was perpendicular to the sample surface, while the light source is at a flat angle to the sample surface. For areas on the sample surface that are flat and well-polished, light is reflected at the incident angle and is not collected by the lens; therefore these areas appear dark.

When the sample is plastically deformed, dislocations start cutting through the surface, creating sharp steps. These steps are scattering light, which can be collected by the lens. As the rest of the sample is still flat, there is a strong contrast between slip bands and the surrounding area. To achieve good contrast it is essential that the sample is well polished and cleaned thoroughly before the experiment. This technique allows observing how slip-bands emerge, get longer and to a certain extend increase in intensity, but it doesn't allow quantifying the strain in the slip bands.

A Keyence VHX-5000 optical confocal microscope was used for the slip trace observations. The microscope was used as a conventional optical microscope, still, its set up provides advantages over other optical microscopes. Firstly, the distance between the lenses and the sample is several centimetres, which is larger than for other optical microscopes. This gives enough space to fit a mechanical microtester for in-situ experiments. Also, the larger working distance results in a higher depth of field, which makes it easier to keep the sample in focus during testing. Secondly, the microscope can be focused by adjusting the height of the lenses instead of the stage. This is necessary as the weight of the microtester (>2 kg) may damage the fine mechanics of the stage or the weight may push the stage down during the experiment and the sample out of focus. For our experiment, the stage was unlocked and brought to the lowest position. Spacers were placed under the microtester to roughly adjust the height before focussing with the lens-system. For dark-field imaging, an annular light source was used. The magnification is set to 500 times, which results in a

field of view of 680 x 510 µm², at a resolution of 4800 x 3600 pixels. The exposure time is 2 seconds at the highest setting of the light source.

The optical dark-field technique was used for two experiments: Firstly for observing at which stress level the first slip bands are formed and secondly for observing the evolution of the slip pattern during room temperature creep. The creep experiments were carried out at 80% and 90% of $\sigma_{0.2\%}$ as these are the stress levels at which creep deformation can be observed on a macroscopic level.

The sample was loaded into the micro-tester and both were placed under the microscope. Micro-indents on the sample surface were used to identify and analyse specific areas. In the first step, the specimen was loaded to 50% of $\sigma_{0.2\%}$; at this level, in none of the experiments, slip bands were observed. Then the load was increased by 1% of $\sigma_{0.2\%}$ increments until the first slip bands could be observed. Starting at this point, images were recorded at every step, which allows observing emerging slip bands and changes in the slip-pattern with increasing stress levels. When 70% of $\sigma_{0.2\%}$ was reached, a further image was recorded, and then the load was increased directly to 80% $\sigma_{0.2\%}$. No intermediate steps were recorded in the range of 70% to 80% of $\sigma_{0.2\%}$, as during this time it may already come to an accumulation of creep strain during the image acquisition.

When the stress of 80% of $\sigma_{0.2\%}$ was reached, the stress was kept constant and images were taken every minute, which was the fastest imaging rate that can be achieved with the specified imaging conditions. This limitation was not given by the exposure time, but by the time it takes for the internal computer of the microscope to process and save an image. After the first hour, the deformation rate decreased significantly (by approximately 2 orders of magnitude) and the imaging rate was reduced to one per 15 minutes.

3.8.2 Data processing

During the test, the sample deforms and therefore the area of interest may change position. In a post-processing step, all images are aligned to the first image. This is done automatically using ImageJ and the ‘StackReg’-plugin, which aligns the images using rigid body transformation [197].

3.9 High-Resolution Digital image correlation (HRDIC)

3.9.1 Principals of HRDIC analysis

Digital Image Correlation (DIC) is an analysis technique that enables to spatially resolve and quantify elastic and plastic deformation at the surface of specimens. Therefore an ROI was imaged before and after the specimen was deformed. A DIC algorithm tracks how local features on the sample surface get displaced relative to each other. From the displacement values strain components, e.g. strain parallel or perpendicular to the loading direction, are calculated. DIC analysis can be based on different imaging techniques, and can, therefore, be used on different length scales. In this project, BSE-SEM imaging was used, which enables to determine displacements with a spatial resolution on the sub-µm scale and therefore the technique is designated as **high-resolution** DIC, for example in contrast to DIC based on optical microscopy. A characteristic pattern of features at the sample surface is required, which ideally is closely spaced, but still, the features need to be distinguishable from each other. For the HRDIC experiment, a gold speckle pattern is applied to the polished surface using the gold remodelling technique [78], [157], [184], [198].

3.9.2 HRDIC - experimental

3.9.2.1 Speckle pattern

Firstly, a thin film of gold was deposited onto the sample surface, at a current of 40 mA and pressure of 0.5 mbar for 5 minutes, using an Edwards S150B sputter coater. The film was then remodelled in a water-vapour environment at 275 °C for four hours [157], [184], producing isolated individual speckles of which 99% have a diameter in the range of 28 to 150 nm. The size distribution was not completely homogeneous, with the pattern showing local variations in particle size and spacing (see Fig. 3-12, e & f). While in one area the particles are densely and evenly spaced, in other areas the particles and the spacing in-between them was larger.

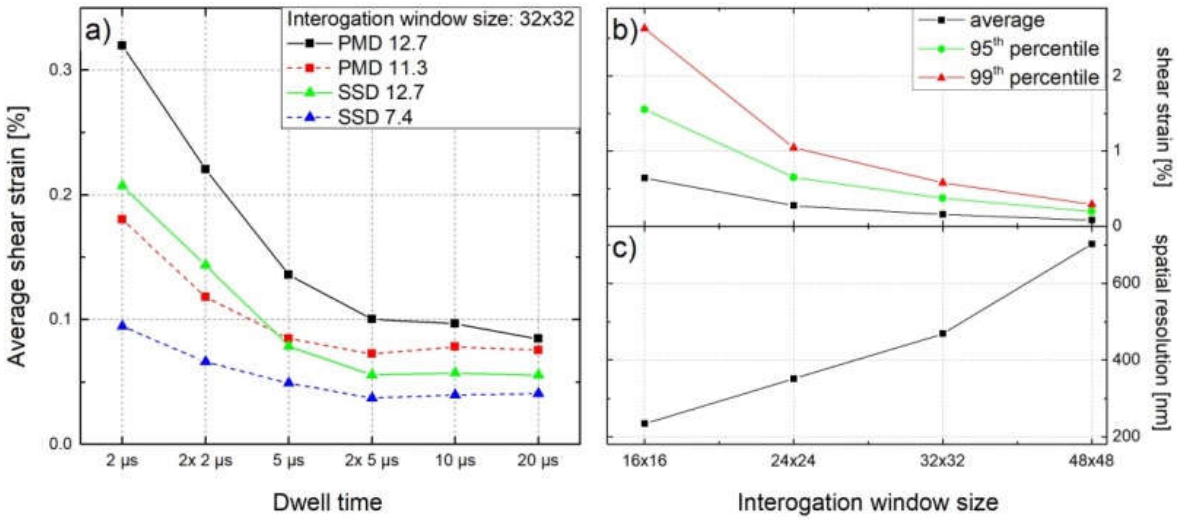

Fig. 3-10: a) Average shear strain from HRDIC analysis in an undeformed sample using two different BSE-SEM detectors and dwell times in the range of 2 µs to 20 µs for SEM imaging. b) Shear strain (average and 95^{th}/99^{th} percentiles) in the undeformed sample depending on the correlation window size. c) Spatial resolution for the used imaging parameters as a function of correlation window size.

3.9.2.2 Imaging conditions

As imaging conditions need to be optimised specifically for the used equipment and analysed samples, a systemic study was carried out to evaluate the effect of dwell-time, detector and working distance on the results. To quantify the error, an undeformed sample was imaged twice under the same imaging conditions and deformation maps were computed. As the sample was not deformed, all strain values were considered to be noise. An acceleration voltage of 10 kV was used to match the size of the electron-specimen interaction volume with the spatial resolution of the experiment (see paragraph 3.4.7).

Firstly, when the dwell time was increased from 2 µs to 10 µs the error reduced approximately by factor 3, but a further increase to 20 µs led to no more improvements. For the DIC error, there was no difference between recording the image in a single scan (10 µs) and using frame averaging (2x 5 µs). However, a longer beam dwell can lead to image distortion due to drift and charging issues [199]. Therefore, frame averaging (2x 5 µs) was used, as for the same accumulated dwell time of 10 µs the beam stays at the same spot for a shorter time compared to recording the image in a single frame [200]. Also, the imaged area of 250 x 250 µm² for HRDIC analysis was covered by recording an image matrix of 12 x 12 images (area of each frame was 30 x 27 µm², respectively

2048 x 1832 pixels) with an overlap of 20%, which were then stitched together before DIC-processing using the 'Grid/Collection stitching' plug-in in 'Fiji' [170], [201]. Stitching of single images eliminates image distortions on the length scale of the whole analysed area.

For the working distance, there was a clear trend that a shorter working distance results in a lower DIC error. Though there is a limit of how close the specimen can be brought to the pole piece due to constraints of the experimental setup. A comparison of two BSE-detectors shows that for the same working distance and dwell time, the error is lower for the solid-state detector SSD compared to the photomultiplier detector PMD (Deben Centaurus). For this reason, the SSD detector was used in a previous study by Lunt et al., in which the same microscope and remodelling technique was used for HRDIC analysis of a titanium alloy. However, as this was an ex-situ experiment, the working distance could be set as low as 6 mm [78], [157]. In the current study we were using the PMD detector despite the slightly higher DIC-error at the same working distance, as this detector, due to its geometry, can be positioned right in between the grips of the microtester, enabling smaller working distances than for the SSD detector. In this case, the limiting factor for reducing the working distance is that the detector, which has a thickness of 10 mm, is positioned in-between the pole piece and the specimen. The working distance for the HRDIC experiments is 11.7 mm.

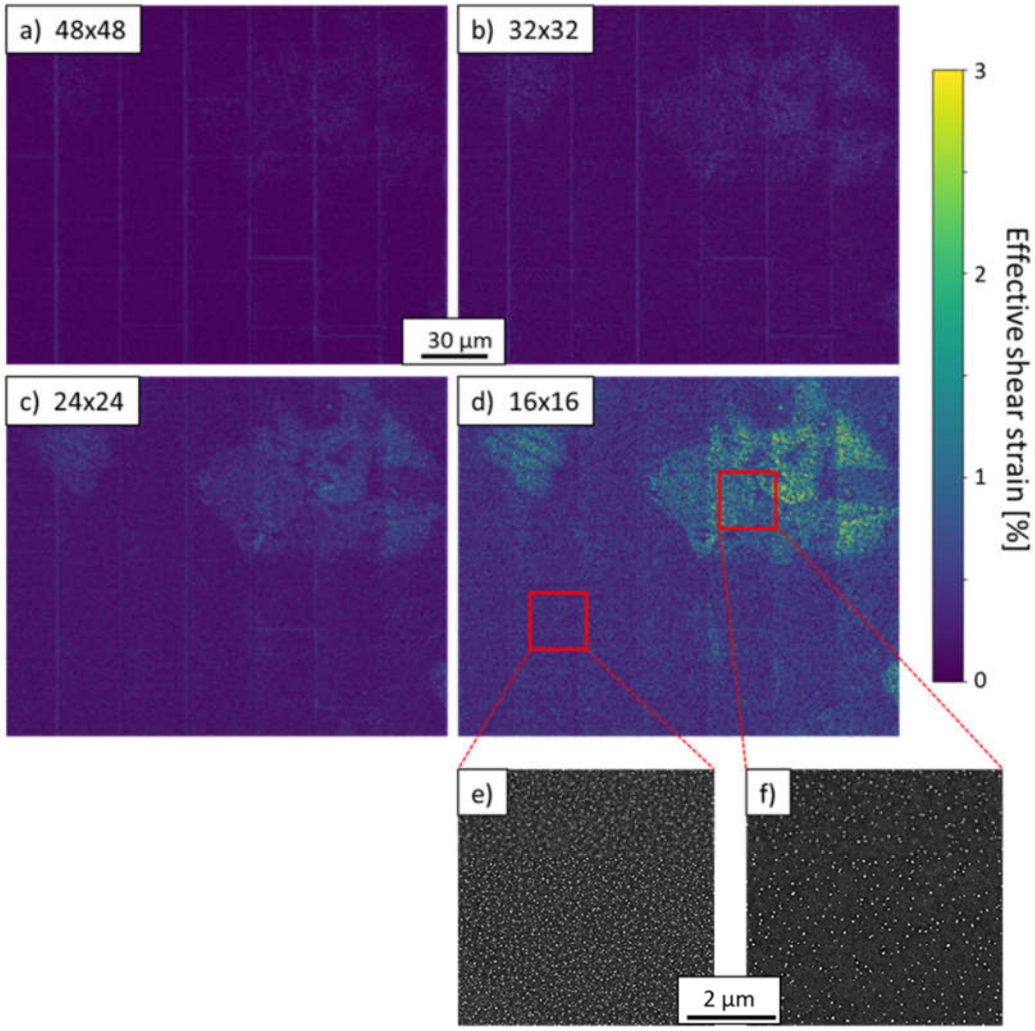

Fig. 3-11: Effective shear strain maps of an undeformed sample using a correlation window size of a) 48x48, b) 32x32, c) 24x24 and d) 16x16. e) & f) BSE-SEM images showing the local differences of the gold speckle pattern.

3.9.2.3 Loading and imaging steps

For the HRDIC analysis, in-situ loading experiments were performed using a 5 kN tensile stage (Deben) placed inside an 'FEI Quanta 650' FEG-SEM. This setup enables imaging specimens while the stress is applied. As imaging is carried out at load, possible reverse strain during unloading can be avoided. This procedure avoids any possible issues with repeated loading and unloading, affecting strain distributions and leading to enhanced accumulation of plastic deformation. Hence, the set-up enables the recording of a series of subsequent deformation steps to monitor the strain evolution during a single loading process.

As material conditions with different yield strengths are compared, the load steps were defined as the relative values of 70, 80 and 90% of the 0.2% proof stress (Table 7-1). For each load step, a stress hold of 10 minutes was applied. Afterwards, the stress was reduced by 5%, e.g. from 70 to 65% of the 0.2% proof stress to avoid further plastic deformation during the imaging step, which took around 1.5 hours (Fig. 7-12).

3.9.2.4 Differences between in-situ and ex-situ HRDIC experiment

Firstly, as the samples are not unloaded during an in-situ experiment, all steps need to be conducted right after each other, as during interruptions the sample is still under mechanical load. This would effectively result in a longer stress hold, which could lead to uncontrolled deformation of the sample. The total duration of the experiment is limited by the available uninterrupted time on the SEM equipment. This influences the selection of experimental parameters like imaging conditions and the number of load steps. In comparison, ex-situ experiments allow for higher flexibility, as they can be interrupted and SEM equipment is only required for the imaging steps. Therefore slower imaging conditions can be used, improving the imaging quality and/or allowing for the acquisition of larger areas under the same imaging conditions or more deformation steps. Secondly, the weight of the micro-tester on the SEM stage causes increased vibrations during stage movement. Vibrations take longer to decay, eventually affecting the first part of the acquisition of each image. Therefore a larger overlap between images is set, which allows cropping of the affected part of the image. For ex-situ experiments, only the sample needs to be placed in the microscope, therefore there is no problem with mechanical vibrations and no geometrical constraints caused by a micro-tester, e.g. regarding the choice of BSE-detectors and working distance (see paragraph 3.9.2.2).

3.9.2.5 Experimental problems

Serval problems have been encountered during the in-situ HRDIC experiment. Firstly, the first set of specimens was machined without pin-holes in the tabs (see Fig. 3-3). This made it difficult to align the gauge parallel to the loading direction, which could lead to a deviation from a uniaxial stress state in the gauge. Also, the sample was only held by the tabs being clamped in the grips. Without the additional support of the pins, the sample was able to start slipping when the mechanical load is applied. Therefore it was difficult to keep the stress constant during the experiment and sometimes it is not possible to reach the required stress levels and the experiment needs to be aborted. Secondly, the microtester must be mounted completely level within the microscope, as no further adjustments are possible afterwards and as the used microscope doesn't have any function to compensate for it, e.g. focus interpolation. As large areas are imaged at high spatial resolution, some parts of the imaged area will be out of focus, if the sample itself isn't level.

If this happens, only parts of the recorded maps can be used for HRDIC analysis. Thirdly, there can be electrical interferences between the microscope and the microtester, which leads to a uniform pattern of artefacts in the maps. Therefore, during the imaging step, the control unit of the microtester is turned off and the connection between it and the microtester is unplugged. Finally, the cable from the control unit to the microtester might not be connected properly, but in some cases, there is still a reading from the load cell, but the values may be incorrect. Therefore it is possible that the sample is loaded to the incorrect stress levels. The damage of loading to a stress level that is too high is not reversible and leads to failure of the experiment.

3.9.3 HRDIC – data analysis

3.9.3.1 Interrogation window size

The displacement maps for each deformation step were computed using LaVision's digital image correlation software package DaVis version 8.4.0 [202]. For 'Material B – coarse microstructure', the undeformed sample was recorded twice and deformation maps were computed. As the sample was not deformed, all strain values were artefacts/noise and the average values of the effective shear strain of the complete maps are used to evaluate the error in the HRDIC analysis for given experimental parameters. After recording the first map of the undeformed sample, the sample stage was lowered and the electron beam was turned off. Then the sample is brought back to the right position and the imaging conditions were restored. By repeating these steps, it is ensured that variations in the set-up process, e.g. adjusting focus and astigmatism of the SEM, are included in the error calculation. As the sample stays within the microscope throughout the whole in-situ experiment, it is not necessary to vent the chamber and take the sample out of the microscope for the error analysis.

To determine the appropriate interrogation window size, the strain maps of the undeformed sample were computed for different interrogation window sizes in the range from 16x16 to 48x48 (Fig. 3-11 (b & c), Fig. 3-12). The effective shear strain maps (Fig. 3-12), especially for smaller interrogation window sizes, exhibited local variations in the quality of the correlation, which was due to variations of the gold speckle pattern. In areas with fine and evenly distribution gold particles, the correlation already works well for smaller interrogation window sizes, while in the areas with larger particles and wider spacing in-between the particles, a larger interrogation window size is required to reduce the noise. Due to this heterogeneity in the speckle pattern, the difference between the average value and the 95^{th}/99^{th} percentiles of the complete maps was high for small interrogation window sizes and did get smaller for an interrogation window size of 32x32 and 48x48. While larger interrogation sizes reduce the error and noise, it leads to a lower spatial resolution. Therefore, an interrogation window size of 32 x 32 pixels was selected as it represents a good trade-off between spatial resolution (468 nm) and error (0.15% effective shear strain).

In comparison, in a previous ex-situ HRDIC study using the same equipment an interrogation window size of 8 x 8 pixels² was used, resulting in a spatial resolution of 147 nm [78]. There are two reasons why it was possible to achieve a higher spatial resolution at similar data reliability: Firstly, it was an ex-situ experiment which allowed for more favourable imaging conditions (see chapter 3.9.2.4). Secondly, the slightly higher error due to the higher spatial resolution was acceptable, as the analysed strains were significantly higher, giving an increased signal to noise

ratio. As plastic strains are lower in our experiment, a lower error is more important than higher spatial resolution.

3.9.3.2 Calculation of effective shear strain

The in-plane displacements calculated by the DIC software can be differentiated to determine the desired strain tensors and subsequent data analysis was performed using in-house Python routines [203] and the NumPy numerical library [204]. The deformation maps contain three vectorial components, which are the shear strain (ε_{xy}), and the strain parallel (ε_{xx}) and perpendicular (ε_{yy}) to the loading direction. For the data analysis, we used the effective shear strain (γ_{eff}) defined by equation (3-5), as it takes all in-plane shear components into account [142], [184].

$$\gamma_{eff} = \sqrt{\left(\frac{\varepsilon_{xx}-\varepsilon_{yy}}{2}\right)^2 \quad \varepsilon_{xy}^2} \tag{3-5}$$

3.9.3.3 Separation of primary α and secondary α constituents

Strain distributions and average strain values have been determined separately for primary and secondary α constituents. The separation is based on the BSE-SEM image of the undeformed sample of the DIC analysis. Therefore, the SEM image and the deformation maps are inherently perfectly aligned. A binary image of the constituent was created by selecting all primary α grains in the BSE-SEM image with the 'Freehand selection'-tool in 'Fiji' [170]. This image was then used to mask out either the primary or secondary α constituent in the deformation maps (Paper3, Fig. 6, (e-h)) and to calculate the average values, as well as the 99.5th percentiles of the effective shear strain maps (Paper 3, Fig. 6, (a-d)).

Crystallographic orientation maps were used to detect all grains within the HRDIC area using the 10° misorientation criterion. By correlating the crystallographic orientation map with the mask that was used for segmenting the constituents, it was possible to determine for each grain whether it is a primary-α grain or a secondary-α colony. In some cases, a primary α grain and an adjacent secondary α colony had the same crystallographic orientation and therefore appeared as one grain in the orientation map. Therefore, the number of primary α grains and secondary α colonies is lower than the total number of grains.

3.9.3.4 Determination of slip systems

The active slip systems in deformed grains can be determined by using Slip Trace Analysis (STA) technique [108], [205], [206]. Initially, the direction of a slip trace at the sample surface in the deformation maps was determined by fitting a line to it. The projection of the observed slip line was cross-correlated to the theoretical directions of all possible slip systems based on the crystallographic orientation of a grain (Fig. 3-13). For accepting a slip system as a solution, the maximum angle criterion between the experimental and theoretical value was 5°. If a slip line does not match with any of the possible slip systems, it was labelled as 'no match'. Slip lines of different slip systems may have the same direction at the sample surface [207]. In this case, the solutions were categorised as 'ambiguous' and all possible solutions were reported. In the case of ambiguous solutions, relative displacement ratio (RDR) analysis can be used to determine the Burger's vector direction associated with the slip line [108], [208]. If the Burger's vector matches with only one of the slip systems, it is possible to unambiguously determine the activated slip system. By determining the type of Burger's vector, RDR analysis allows distinguishing between <a> and <c+a> type pyramidal slip.

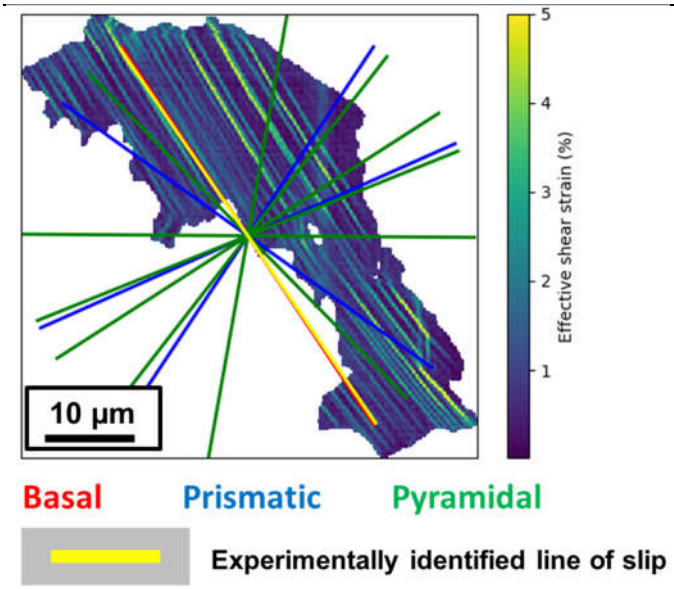

Fig. 3-12: Example of slip trace analysis applied on one grain in Material A – coarse microstructure. The red (basal), blue (prismatic) and green (pyramidal) lines on top of the effective shear strain map indicate the traces at which all possible slip systems are intersecting the sample surface. The yellow line indicates the slip trace identified from the slip pattern in the deformation map. In this example, the activated slip system is identified to be basal.

3.10 Crystal Plasticity Modelling

3.10.1 Description of DAMASK

Crystal Plasticity (CP) modelling is used to determine local stress states in the microstructures analysed by HRDIC, focusing on the elastic regime. The information of where first localised plastic deformation occurs and what are the active slip systems was determined from the combined EBSD and HRDIC data. The aim was to use simulation in the elastic regime to evaluate the effects of elastic anisotropy and microstructure on local stress states to explain experimental observations.

It was assumed that in the elastic regime all local stresses scale linearly with the macroscopic stress. In the simulations, plastic deformations were allowed, but as the focus was only on the elastic regime, simulations were run for lower stresses (1% of $\sigma_{0.2\%}$) at which even local plastic deformation is insignificant. The stresses were then linearly scaled to the stress level of the HRDIC experiment to facilitate direct comparison. With this approach, one could avoid any effects of local plastic deformation and stress redistribution.

For CP-simulations the Düsseldorf Advanced Material Simulation Kit (DAMASK) version 2.0.2 is used [209]. The used CP-frame work is capable of simulating elastic, as well as plastic deformation. However, in this study simulations were run at such low stress levels, so that the material response was purely elastic. Despite not being used for the simulations of elastic strains/stresses, the constitutive law used in DAMASK is shown for the sake of completeness in equation (3-6) [210], [211].

$$\gamma^{\alpha} = \gamma_0 sgn\left(\frac{\tau^{\alpha}}{g^{\alpha}}\right)\left|\frac{\tau^{\alpha}}{g^{\alpha}}\right|^{\frac{1}{m}} \tag{3-6}$$

In equation (3-6), τ^{α} is the resolved shear stress, γ_0 the reference shear rate, g^{α} the slip resistance/CRSS and m the strain rate sensitivity.

Fast Fourier Transform (FFT) based modelling was used, as the FFT approach, in contrast to finite element modelling (FEM), doesn't require meshing. Therefore it was possible to directly use experimental data, in the present case crystallographic orientation maps, as input files for simulations. As the FFT approach requires periodic boundary conditions, buffer zones were added on each side of the geometry (Fig. 3-14) [212], [213].

As TIMETAL®834 is a near-α titanium alloy with a low volume fraction of β-phase, which is finely dispersed throughout the microstructure, we assumed that the β-phase has no considerable effect on the elastic properties of the material. Therefore only α-phase was included in the simulation and secondary α colonies were treated as single α grains [214].

3.10.2 Geometry and input files

A 2.5D or quasi 3D microstructure was used for CP-modelling [215], which was created by extruding crystallographic orientation maps parallel to the plane normal (Fig. 3-14). Hence, there was no variation of microstructure in the extrusion direction. The crystallographic orientation maps were taken from the HRDIC areas, but the number of pixels was reduced from 520x520 to 260x260 pixels. This was done to reduce the total number of voxels in the geometry, accelerating simulations and post-processing, and reducing the data size of the output files. As both the HRDIC experiment and the CP simulations were linked to the same crystallographic orientation maps, both datasets were inherently perfectly aligned with each other, making it trivial to link the datasets from experiments and simulations for post-processing and data analysis.

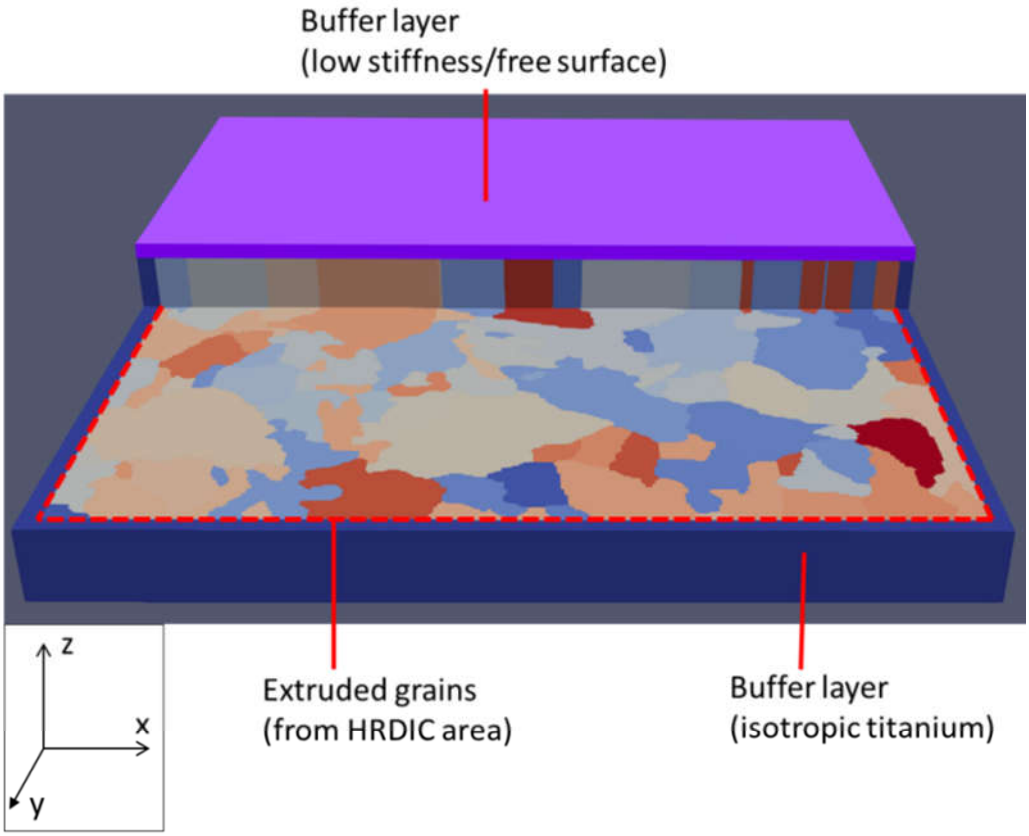

Fig. 3-13: Visualisation of a geometry file used for simulations in DAMASK, showing the extruded grains and the buffer layers.

The thickness of the extruded layer was 38 pixels, which was similar to the average grain diameter [215]. On top of the surface, a buffer layer with a thickness of 5 pixels was added, which had a

stiffness value that was around 3 orders of magnitude lower than the stiffness of titanium (Table 1), representing the free sample surface in the DIC experiment [216]. On the other 5 sides, a buffer layer of 5 pixels was added with isotropic properties and the same average stiffness as α-titanium. The sample thickness in pixels needs to be a multiple of the number of processors/cores used for running the simulations. Together with the buffer layers, the overall thickness of the samples was 48 pixels and 16 processors/cores were used.

Except for the buffer layers, the properties of commercially pure CP-titanium were assigned to all grains (Table 1) as their elastic properties and anisotropy are expected to be similar to TIMETAL®834. Note that the plastic properties of CP-titanium are known to be significantly different from TIMETAL®834. However, as the focus of these simulations was on the effect of elastic anisotropy, this difference was of no importance.

Table 3-1: Summary of elastic, plastic and thermal properties used for crystal plasticity simulation.

Material	Application	Elastic properties [Gpa]					Plastic properties [Mpa]									Thermal properties [10-6 m/(mK)]	
							Basal <a>			Prismatic <a>			Pyramidal <c + a>			Expansion coefficient	
		c11	c12	c13	c33	c44	n_{slip}	τ_0	τ_S	n_{slip}	τ_0	τ_S	n_{slip}	τ_0	τ_S	α - <a>	α - <c>
Anisotropic Ti	Bulk	160	90	66	182	47	3	349	568	3	150	1502	6	1107	3420	9.5	5.6
Isotropic Ti	Buffer	176	91	-	-	-	-	-	-	-	-	-	-	-	-	8.4	8.4
Free surface	Buffer	0.1	0.0	-	-	-	-	-	-	-	-	-	-	-	-	8.4	8.4

n_{slip} Number of slip systems
τ_0 initial slip resistances
τ_S saturation slip resistances
α Coefficient of thermal expansion

3.10.3 Calculation of RSS values

The output of the CP-simulation gives the full stress tensor at each point in the analysed area. In combination with the crystallographic orientations, resolved shear stress values can be calculated for different slip systems. Three different calculation methods (3-7, 3-8 and 3-9) were used to determine RSS values and the differences between them are evaluated. For the first method, the local stresses are assumed to be homogeneous throughout the sample, equal to the macroscopic stress. RSS values were calculated by multiplying the applied stress with the Schmid factor values of each grain.

RSS from SF, Homogeneous stress

$$RSS = SF \times \sigma_{xx}(applied) \quad (3\text{-}7)$$

SF: Schmid Factor

σ_{xx}(applied): macroscopically applied stress

The second method is also based on Schmid factors but takes into account the elastic anisotropy and its effect on local stresses. For calculating RSS values, the local stress in loading direction was multiplied with the Schmid Factor of the grain.

RSS from SF, Local axial stress

$$RSS = SF \times \sigma_{xx}(local) \quad (3\text{-}8)$$

SF: Schmid_Factor

σ_{xx}(local): stress in loading direction

The third method uses the full stress tensor for the calculation of RSS values. In this case, also stress components perpendicular to the loading directions and shear stresses were taken into account.

RSS calculation with full stress tensor

$$RSS = \bar{b} \cdot \bar{\bar{\sigma}} \cdot \bar{n} \tag{3-9}$$

$$\bar{b} = \begin{pmatrix} b_1 \\ b_2 \\ b_2 \end{pmatrix} \qquad \bar{n} = \begin{pmatrix} n_1 \\ n_2 \\ n_3 \end{pmatrix}$$

$\bar{b}$: slip direction $\bar{n}$: slip plane normal

$$RSS = b_1 n_1 \sigma_{11} + b_1 n_2 \sigma_{12} + \ \ldots + b_3 n_3 \sigma_{33}$$

3.10.4 Load cases

Crystal plasticity simulations were run for three different scenarios. For the first scenario, uniaxial stress was applied to initially stress-free material. The applied stress was equivalent to 70% of the proof stress of each of the two samples, equal to the stress applied during the first deformation step in the HRDIC experiment. Also, the loading direction was the same as in the HRDIC experiment. The purpose of this experiment was to analyse the effect of the elastic anisotropy on local stresses and ultimately RSS values.

In the second scenario, thermal residual stresses were calculated, which evolve during cooling from a heat treatment due to the thermal anisotropy of α-titanium. The material was set to be stress-free at a temperature of 500 K above room temperature. It was then instantly cooled to room temperature, where the stress state in the material was solved so that the average macroscopic stresses were equal to zero. According to Pawar et al., values for the coefficient of thermal expansion are set to be $\alpha_c = 5.6 \cdot 10^{-6} \cdot °C^{-1}$ parallel to the c-axis and $\alpha_a = 9.5 \cdot 10^{-6} \cdot °C^{-1}$ along a-direction [217].

The third scenario was a combination of scenario 1 and 2. The microstructure initially had thermal residual stresses caused by cooling, and then the same uniaxial stress was applied as in the first simulation.

4 Papers and manuscripts

4.1 Paper 1 - Element segregation and α_2 formation in primary α of a near-α Ti-alloy

Claudius Dichtl[1], Zhenbo Zhang[1], Hazel Gardner[2], Paul Bagot[2], Anna Radecka[5], David Dye[3], Matthew Thomas [4,6], Rebecca Sandala[5], João Quinta da Fonseca[1], Michael Preuss[1]

[1] University of Manchester, Manchester, M13 9PL

[2] University of Oxford, Oxford, OX1 3PH

[3] Imperial College London, London SW7 2AZ

[4] TIMET UK, PO Box 704, Witton, B6 7UR

[5] Rolls-Royce plc, Derby, DE24 8BJ

[6] The Manufacturing Technology Centre, Ansty Park, Coventry, CV7 9JU

The manuscript was published in Materials Characterization, Volume 164, June 2020, 110327.

https://doi.org/10.1016/j.matchar.2020.110327

Highlights of this paper

Observation of chemical gradient in primary α grains as a result of controlled cooling through detailed EPMA analysis

Differences in α_2 precipitation within primary α observed by TEM and APT, which can be correlated to the chemical gradient.

Contributions

For **Paper 1** titled '**Element segregation and α_2 formation in primary α of a near-α Ti-alloy**', Claudius Dichtl, Michael Preuss and João Quinta da Fonseca designed the study. Claudius Dichtl applied the heat treatments to the sample, carried out the initial metallographic preparation of the specimen and performed the crystallographic orientation mapping using EBSD-SEM technique and prepared the manuscript. Jonathan Fellowes performed the EPMA-WDS experiment and supported the data analysis. Zhenbo Zhang performed the analysis of precipitates using TEM. Anna Radecka prepared the samples for APT analysis using FIB-SEM technique. Paul Bagot performed the APT experiment and together with Hazel Gardener supported the analysis of the APT data. Input regarding the interpretation of the APT data was provided by Michael Moody. Hazel Gardner wrote the paragraph regarding the methodology used for quantifying precipitates in the APT datasets. All authors contributed to writing and editing the final version of the paper.

Abstract

Alloy TIMETAL®834 is a near-α Ti-alloy typically processed to have a complex bimodal microstructure that provides a good combination of mechanical properties at temperatures in excess of 450°C. Due to the high Al content, typical ageing procedures result in the formation of intragranular and coherent nano-scale Ti_3Al precipitation (α_2), which increase strength but also promotes slip planarity. The present study focuses on chemical partitioning as a result of sub-β-transus heat treatment and the consequences for the two different constituents in the bimodal microstructure. The detailed chemical and structural analysis were carried out by combining Electron **P**robe **M**icro-**A**nalysis (**EPMA)**, **W**avelength **D**ispersive **Sp**ectroscopy (**WDS**), **T**ransmission **E**lectron **M**icroscopy (**TEM**) and **A**tom **P**robe **T**omography (**APT**) for investigating local compositional variations and their effect on the formation of α_2-precipitates. The detailed microchemical analysis shows a core-shell composition arrangement of α-stabilisers with the shell composition similar to the one of secondary α. Selected area electron diffraction in the TEM and APT analysis demonstrates that those local variations in α stabilisers affect the level of α_2 precipitation. In addition, EPMA maps show that while Zr and Sn are often considered to be neutral alloying elements in Ti-alloys, they do segregate to the β-phase during sub-β-transus heat treatment.

1 Introduction

In typical two-phase Ti-alloys, the α phase is strengthened by solution-strengthening and in some cases also precipitation strengthening. Solution strengthening is achieved by the addition of α-stabilising and neutral elements such as Al, O, Sn and Zr. These elements display fairly large differences in atomic radii compared to Ti, but at the same time show sufficiently high solid solubility limits in the α-titanium matrix [1]. The difference in size results in lattice strain, which affects the mobility of dislocations and therefore causes a strengthening effect [2,3]. According to Collings et. al, the strengthening effect of alloying elements is based on the electron states of the alloying elements, i.e. the formation of tight and directional bonds between the alloying and titanium atoms [4]. In the range of 0-15 at.%, the strengthening effect of aluminium in solid solution is linearly proportional to the concentration of aluminium [3]. However, it is well established that commercial two-phase titanium alloys that contain at least 5 wt.% aluminium can form Ti3Al (α_2) precipitates when aged below the α_2 solvus [5]. According to Namboodhiri et al, an aluminium concentration of over 13 at.% is required for obtaining α_2 precipitation when the material is aged at 700°C [6]. However, this value applies for the overall composition of the alloy and doesn't consider local variations in the aluminium concentration. In addition, some work has demonstrated that short-range ordering might take place before α_2 precipitation is observed [6]. A detailed analysis by Atom Probe Tomography (APT) on the evolution of α_2-precipitates with ageing time and temperature has been carried out by Radecka et al. [7,8]. This work has shown that zirconium, silicon, molybdenum and vanadium accelerate the formation of α_2-precipitates, compared to pure Ti-Al systems. It was also found that tin and silicon are stronger α_2 formers than aluminium and therefore can replace aluminium atoms in α_2.

The situation regarding α_2 formation is further complicated in titanium alloys with bimodal microstructures since during solution treatment below the β-solvus, aluminium partitions to the primary α phase. Upon cooling, sufficiently fast to trigger the formation of secondary α rather than exclusive growth of primary α, the concentration of α-stabilising elements is lower in the secondary α than in the primary α constituent. Since aluminium is the main α-stabilising element and also has the most significant effect on solid-solution strengthening, primary α might be the stronger of the two α constituents. However, secondary α tends to have a very fine lath structure providing Hall-Petch strengthening. An interesting aspect of the bimodal microstructure evolution is that unless the material is quenched at fast rates, primary α grains can also grow by up to a few microns [9].

TIMETAL®834 (Ti-5.8Al-4Sn-3.5Zr-0.7Nb-0.5Mo-0.35Si-0.06C) is a near-α titanium alloy, which is typically processed to display a bimodal microstructure and a primary α volume fraction of approximately 10 to 15 % [10]. This alloy has been developed for applications in jet-engines with temperature capabilities well in excess of 450 °C through the minimisation of β phase, utilisation of molybdenum and niobium instead of vanadium as a β-stabiliser, addition of 4 wt.% Sn and about 0.3 wt.% Si to enhance creep performance. The relatively high levels of aluminium and tin TIMETAL®834 are known to lead to a significant level of α_2 precipitation in the α phase [11–13].

In the present work, detailed microstructural and chemical analyses have been carried out to shed new light on the segregation of alloying elements in a bimodal microstructure of TIMETAL®834 caused by α + β solution treatment, and on the consequences, these have on α_2 formation using a variety of electron microscopy techniques and APT analysis.

2 Experimental

2.1 Sample preparation

Forged TIMETAL®834 ingot material was supplied by TIMET, UK. The as-received material was solution heat-treated below the β-solvus at 1015°C for 2 hours followed by cooling the material to ambient temperature at a cooling rate of 1K/s resulting in a bimodal microstructure, with the transformed β-phase consisting of single-variant colonies with a lamella-spacing of around 2.5 µm. Thin layers of β-phase are retained between the lamellae of the α-phase. The material was subsequently aged for 2 hours at 700°C which is known to promote α_2 precipitation [7].

For imaging of the microstructure in the SEM and microchemical analysis, samples were prepared using standard metallographic procedures: grinding with abrasive SiC-paper of 4000 grit and polishing in colloidal-silica suspension. Foils for transmission electron microscopy were prepared by grinding (800 grit SiC-paper) material to a thickness of around 100µm before punching out 3 mm diameter discs and electropolish those in a TENUPOL5 (Struers) twin-jet polisher using 10 % perchloric acid, 90 % methanol solution at a temperature of -32 °C to achieve a region that is electron-transparent.

Samples for APT were prepared using focused-ion-beam (FIB) milling. Etched samples were used to enhance the contrast in secondary electron (SE) imaging. First, a cantilever-beam was machined from a single grain, along the same cross-section for which the concentration profile had been measured by EPMA (see Fig. 4). APT-needles with a tip radius of less than 100 nm [14,15] were prepared from this beam at equal distances, giving samples at different distances from the grain/interface boundary.

2.2 Scanning electron microscopy and electron backscatter diffraction (EBSD)

Back-Scattered-Electron (BSE)-SEM imaging at 15 keV was used for the morphological analysis of the microstructure. BSE contrast can be sensitive to crystallographic orientation and chemical variations. If the contrast in an image arises from the chemical composition, higher brightness correlates to areas with higher densities and higher atomic numbers than in the darker regions [16]. To distinguish between chemical and orientation contrast, grain orientation mapping was carried out in addition to BSE-SEM imaging using Electron-Back-Scattered-Diffraction (EBSD) in an SEM at an acceleration voltage of 15 keV and a step size of 0.2 µm. For both imaging modes, an FEI Quanta 650 Field Emission Gun Scanning Electron Microscope (FEG-SEM) was utilised equipped with an Oxford Instruments HKLNordlys EBSD detector.

2.3 Electron-probe microanalysis EPMA-WDS

The microchemical analysis was carried out using a Jeol JXA-8230 electron-probe-microanalysis (EPMA) with Wavelength-Dispersive-Spectroscopy (WDS). In this method, an electron beam is scanned over the sample and the intensities of the emitted X-rays are measured as a function of the wavelength of the photons. The chemical composition is determined based on the characteristic X-rays emitted by the analysed material [17].

The microchemical analysis was carried out at an acceleration voltage of 7 keV, as a Monte-Carlo-simulation using Casino v2.48' [18] showed that at this voltage the interaction volume is less than

300 nm in width and depth for TIMETAL®834. Therefore, the interaction volumes of two adjacent scanning points are not overlapping for mapping or line-scans at a step size of 1µm. Two types of datasets were recorded for the microchemical analysis: qualitative maps to assess spatial distribution for each analysed element and quantitative line-scans. For the latter, the EPMA was calibrated using standards for each element before the line-scan. Line-scans were taken along the cross-sections of primary α grains to quantify the difference in chemical composition caused by element partitioning. The average relative error of the chemical composition for Al was 1.1 %, correlating to an absolute error of 0.06 wt.%. As error bars would be of a similar size as the symbols used, they are not included in the figures. For all other elements, the absolute error was smaller than the one for Al.

In areas of higher density or where the concentration of elements with larger atomic number is higher, more X-ray Bremsstrahlung is generated, resulting in higher continuous background. When background signal is not compensated in the data processing, higher continuous background could result in an overestimation of the concentration of other elements. Background signal was compensated for in the quantitative line-scans, but not for the qualitative maps.

2.4 Transmission electron microscopy (TEM)

TEM characterisation was performed on an FEI Tecnai TF20 microscope operating at 200 kV. Selected Area Electron Diffraction (SAED) was used to quantify the intensity of the superlattice reflections from the ordered α_2-precipitates to obtain qualitative information about α_2 volume fraction changes [19]. In order to achieve this, primary α grains were investigated along the [11-20] zone axis. Diffraction patterns were recorded for several positions along the cross-section of a primary α grain, similar to the line scan taken in the EPMA-WDS analysis. As the intensity of the superlattice reflection spots tends to be weak compared to the fundamental reflections, DITABIS imaging plates were used for recording the diffraction patterns, providing an exceptional high dynamic range. After recording the diffraction patterns, the plates were removed from the TEM and scanned in an image-plate-scanner (DITABIS Micron) to retrieve the digital images [20].

The intensity of the α_2 superlattice reflections is affected by the accurate alignment of the grain along the given zone-axis and the thickness of the foil. For this reason, the integrated intensities of the superlattice reflections were normalised by the integrated intensities of the corresponding fundamental reflections sitting between the superlattice reflections. The diffraction spots were fitted utilising a Voigt-function [21]. Effects of the background were compensated by subtracting a line from the intensity profile that goes through the minima on both sides of the peak.

2.5 Atom Probe Tomography (APT)

The experiment was carried out using a CAMECA Local Electrode Atom Probe (LEAP) 5000XR (at a stage temperature of 50 K and with a 50 pJ laser pulse energy) and post-processing and data analysis utilised the CAMECA IVAS software. [22]

Pearson coefficient (μ) values [23] were calculated for each of the three atom probe samples. The two atom probe samples nearest the centre of the alpha grain had a higher μ value (0.09 and 0.08) than the sample nearest the grain boundary (0.04), indicating a higher degree of non-randomness in the centre-grain samples. All three μ values were much greater than the μ value measured for a random solid solution, demonstrating statistical significance.

Aluminium isoconcentration surfaces were used to identify the precipitates in the atom probe datasets. Proximity histograms (proxigrams) were generated for a range of isoconcentration values. Proxigram interface width, calculated using the method described by Homma et al [24], was plotted as a function of isoconcentration value. An isoconcentration value of 12 at.% Al was selected, as this corresponded to a narrow interface thickness for both the centre-grain samples. Ions contained within this isoconcentration surface were identified as belonging to the α_2-precipitates and were extracted. Only isoconcentration surfaces that did not intersect the edge of the atom probe dataset were considered.

During an atom probe experiment, evaporation artefacts can cause density fluctuations. To distinguish between these artefacts and chemical clustering, the mass-to-charge values of the data points in each of the atom probe datasets were randomly exchanged. 12 at. % Al isoconcentration values were created on these 'randomised' datasets, and any precipitates extracted were considered to be 'random' precipitates resulting from the evaporation artefacts. To control the number of 'random' precipitates included in the analysis, a precipitate cut off volume was chosen such that the percentage of clusters identified in the randomised dataset is less than 5% of those observed in the as-measured, experimental dataset. i.e. $(N_{real}-N_{rand})/ Nreal \geq 95\%$, where N_{real} is defined as the number of precipitates identified in the as-measured, experimental dataset and Nrand is defined as the number of precipitates identified in the randomised dataset. The procedure is similar to that outlined in the paper by Williams et al. [25].

Once extracted, the composition of the precipitates was measured, taking into account mass spectrum peak overlaps as described by London [26]. Precipitate volume fraction was calculated by taking the number of ions within the precipitates and dividing by the number of ions within the whole dataset.

The small size of the precipitates in the present case (~2nm radius) means that the spatial resolution of atom probe is being pushed to the detectable limit. In a study on the effective spatial resolution limits of APT, De Geuser et al. reported that it is possible to detect particles with a radius of approximately 1 nm, but that in this case, the accuracy of the determined particle size and composition is limited [27]. This means that qualitative comparisons between datasets are appropriate, but quantitative conclusions from absolute numbers of cluster sizes and volume fractions should be treated with some caution.

3 Results

3.1 Observation of a core and shell structure in primary α grains

Water quenching thinner sections of TIMETAL®834 has shown that α+β solution heat treatment at 1015°C results in a primary α volume fraction of 15 to 16 %. However, due to primary α grain growth, the primary α volume fraction, when cooled at 1 K/s, was determined to be 25 %. The average grain size of primary α grains is 21 ± 9 µm, with some of the grains exhibiting an elongated shape. A core-shell structure was observed in primary α grains, both in optical (not shown here) and BSE-SEM images. Fig. 1a and Fig. 2a and c are examples of such core-shell structures with darker inner areas and brighter areas close to the grain boundaries. The shell width is 2-6 µm and the volume fraction of the inner darker area was determined to be close to the expected value of 15 %. Fig. 2 also shows an example of primary α grains being clustered together. Here, three grains

are connected to each other, with each of them exhibiting core-shell structures apart from the region where they contact each other.

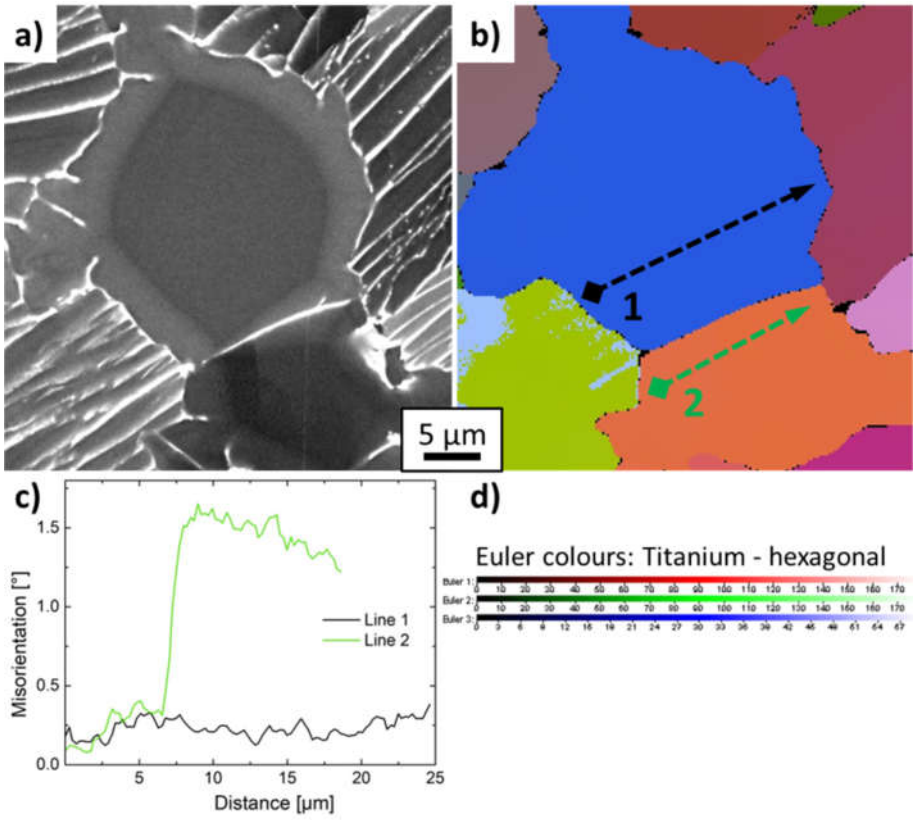

Fig. 1: **a)** BSE-SEM image of two primary α grains, **b)** crystallographic orientation map (α phase) of the same area, using Euler-colours **d)**. The misorientation along the black (1) and green (2) lines, in reference to the starting point (square), are displayed in figure **c).**

3.2 Analysis of crystallographic orientation and crystal structure

In order to explore the possibility of a crystallographic orientation effect causing the core-shell appearance, primary α grains were further analysed by EBSD-based orientation mapping. However, as can be seen in Fig. 1b, the Euler map clearly shows misorientation-free primary α grains with no indication of any substructure within the grains. Further, Fig. 1c also confirms only small misorientations within 0.3° along trace 1 indicated in Fig. 1b. In the case of the primary α grain below (orange grain in Fig. 1b), an additional distinct contrast can be observed next to the core-shell structure in Fig. 1a. The line scan along trace 2 confirms a misorientation step at around 6-8 µm, at which the crystallographic orientation changes by over 1°, corresponding well with the dark appearance in that particular grain. On both sides of the step, the misorientation variation again stays below 0.3°. Hence, the observed shell structure in the BSE-SEM images is not related to any orientation changes within the primary α grains.

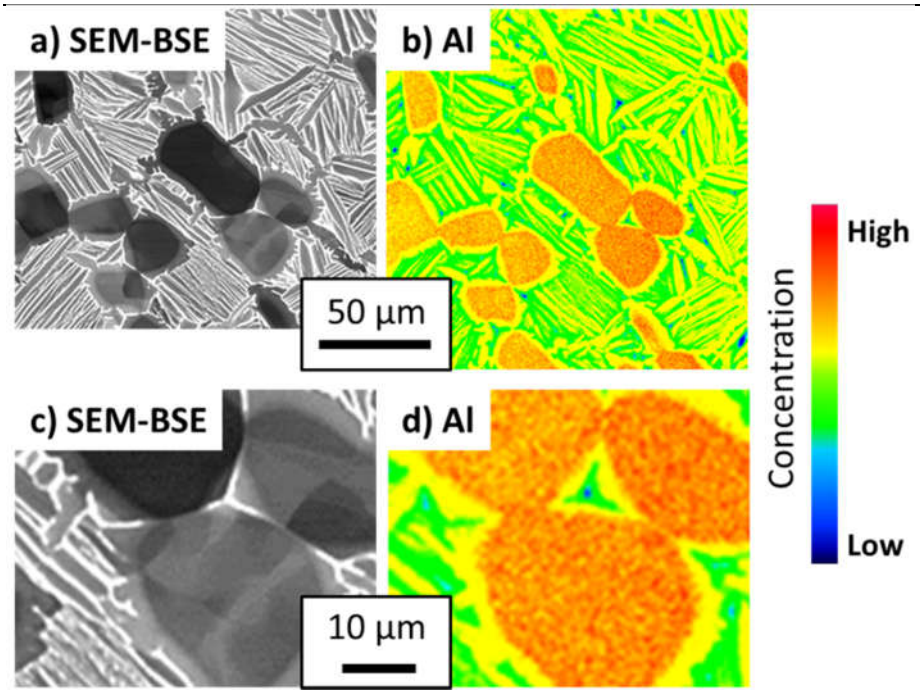

Fig. 2: Electron-Probe-Micro-Analysis (EPMA) of several primary α grains, showing the SEM-BSE-image (**a** & **d**) and qualitative chemical map recorded using wavelength-dispersive-spectroscopy (WDS) of aluminium (**b** & **d**). In the images (**c** & **d**) a region of the maps (**a** & **b**) is displayed at a higher magnification.

3.3 Analysis of the chemical gradient using EPMA-WDS

In order to relate the core-shell appearance to possible chemical variations within the primary α grains, qualitative chemical maps were recorded in the same regions by EPMA-WDS. Fig. 2b and d show detailed aluminium maps, highlighting that aluminium concentration is generally higher in primary α grains compared to the transformed β-phase region, including secondary α. As expected, the aluminium content is lowest within the β phase. The aluminium map reveals a core-shell structure within primary α that aligns well with the one observed in BSE-SEM images. The centre of the primary α grains is enriched in aluminium, while the outer area is depleted. The chemical distribution is homogeneous within these areas on this length-scale. It is also noticeable that the concentration of aluminium in the outer areas of the primary α grains is similar to the concentration in the secondary α phase, presumably because they are both formed at similar temperatures, during cooling at the end of the solution heat treatment. In the centre of the map, three grains are clustered together. These grains are shown at higher magnification in Fig. 2c & d. At the points where the grains are in contact with each other, the shell is interrupted, and the cores are in direct contact. Therefore, there is a line between two adjacent grains, where no chemical gradient can be observed. Towards the triple point in the centre of these three grains, the depleted shell is narrower with a thickness of 1 to 2 µm. In the BSE-SEM images, additional areas of varying contrast can be observed within primary α grains. This structure does not show up in the chemical distribution map of aluminium and is most likely related to slight orientation variations as already highlighted for the orange grain in Fig. 1.

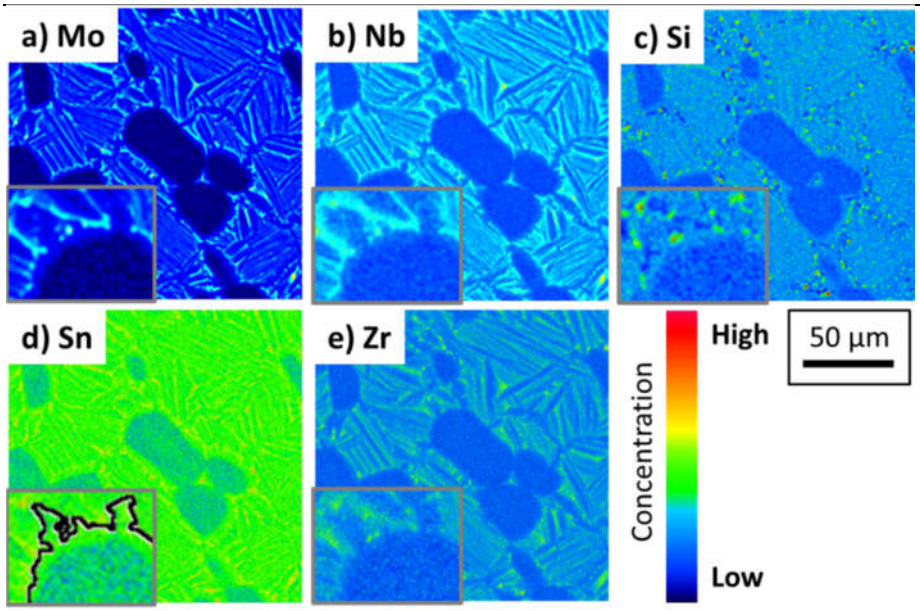

Fig. 3: Qualitative chemical maps recorded using EPMA-WDS for the same area shown in Fig 2. for the β-stabilizing elements molybdenum, niobium and silicon (**a-c**) and the neutral alloying elements tin and zirconium (**d** & **e**). Insets (width 30 µm) display the boundary between primary α grains and transformed β at a higher magnification. Grains boundaries are highlighted by a black line for the map of tin (**d**).

In Fig. 3 qualitative chemical distribution maps are shown for the β-stabilizing elements molybdenum, niobium and silicon (a-c) and the neutral alloying elements tin and zirconium (d & e). The chemical distribution of Mo and Nb is exactly opposite to the one of Al; the concentrations are high in the β-phase, lower in the secondary α phase and lowest in primary α phase. The chemical map of Mo (Fig. 3a) also shows a core-shell structure within primary α grains, with the concentration being lower in the core and higher in the shell. Hardly any Mo signal was recorded from the centre of the primary α grains. The niobium, silicon and zirconium maps also indicate a core-shell structure, with slightly increased concentrations in the shell, but in this case, the contrast is significantly weaker than for Al and Mo. Considering that Zr is usually seen as a neutral element, this observation seems surprising. Sn, also usually considered a neutral alloying element, clearly shows higher concentrations in the transformed β phase region compared to primary α. In addition, there are indications that Sn reaches higher levels at β triple points.

Table 1: Summary of concentrations in wt.% for different location determined by EPMA-WDS (see Fig. 4) and APT. Needle-1 and needle-2 are from the centre of the grain, while needle-3 is from close to the grain boundary.

	Concentration wt.%					
	EPMA-WDS			APT		
Elements	Centre	Near - GB	transformed-β	Needle-1	Needle-2	Neddle-3
AL	6.00	5.10	5.30	5.88	6.10	5.42
Sn	3.99	4.41	4.36	3.61	3.69	3.84
Zr	3.01	3.51	3.54	2.94	3.00	3.27
Si	0.38	0.49	0.47	0.37	0.34	0.42
Nb	0.45	0.67	0.72	0.34	0.36	0.46
Mo	0.08	0.34	0.48	0.15	0.12	0.19

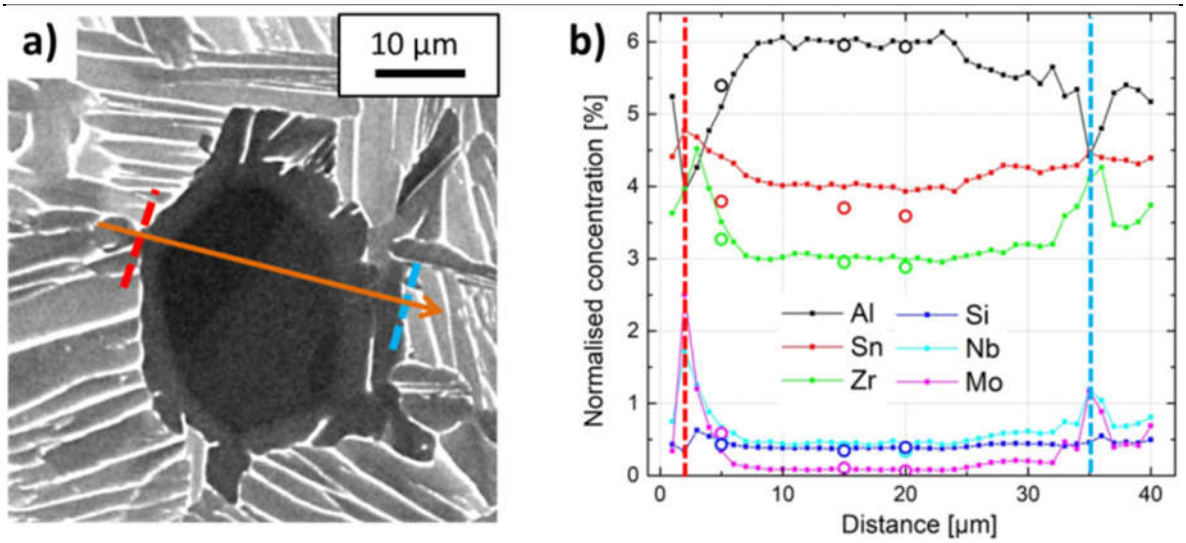

Fig. 4: **a**) BSE-SEM image of a primary α grain analysed by EPMA, the orange line shows the location of the line scan for the quantitative WDS-analysis. The crystallographic orientation map of the grain is attached in the appendix. It shows that the grain has only one crystallographic orientation. **b**) The normalised concentration along the black line is displayed for Al, Sn, Zr, Si, Nb and Mo. The grain boundaries of the primary α grain are marked with a red and a blue dashed line. Open circles show the average concentrations that have been calculated for the three APT-data sets.

Fig. 4 shows a BSE-SEM image of a primary α grain together with quantitative concentrations of 6 elements (Al, Sn, Zr, Si, Nb and Mo) taken from an EPMA-WDS line scan recorded across that particular primary α grain. The concentration was measured at equidistant points with a spacing of 1 µm. The locations of the primary α grain boundaries related to the EPMA-WDS line scan are indicated by two dashed lines in Fig. 4a and b. The concentration profile confirms the observations from the qualitative chemical maps: the core of the primary α grains is enriched in Al and depleted in all other alloying elements. Towards the grain boundary, the concentrations of Mo, Nb, Sn and Zr increase significantly. For these elements, this effect is pronounced, e.g. for Mo, the concentration is up to approximately 30 times higher than in the centre of the grain. For Si, this effect is less pronounced and the EPMA analysis indicates a concentration in the β-phase, which is only 50 % higher, compared to the primary α phase. It is also noticeable that the element concentrations change several microns before the primary α grain boundaries showing significant chemical variations within the shell structure of the primary α grain. For example, the concentration of aluminium drops from 6 mass.% to 4.5 mass.% about 1 µm before the grain boundary. The same effect applies for all other elements, but instead of decreasing, the concentrations increase when getting closer towards to grain/interface boundary.

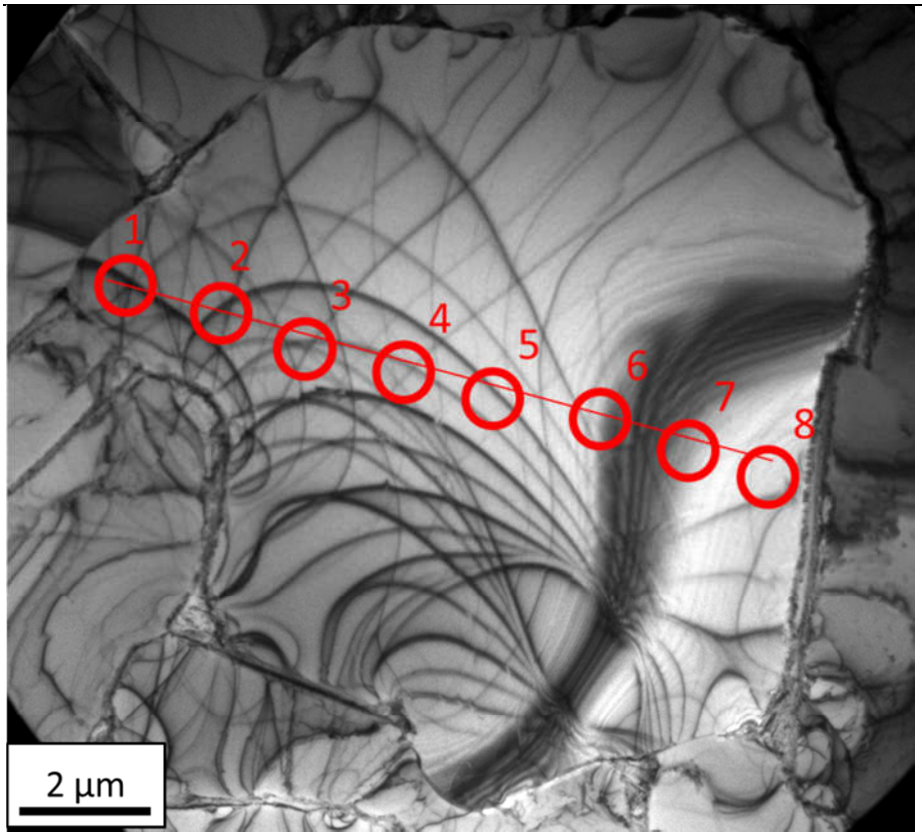

Fig. 5: TEM images of primary α: the red circles (1 - 8) indicated position within grains where diffraction patterns have been recorded using selective area aperture.

3.4 TEM and SAED analysis

Fig. 5 shows a primary α grain highlighting the selected areas where diffraction patterns were recorded. Accordingly, Fig. 6 shows selected area diffraction patterns taken along the [11-20] zone axis from near the grain boundary (a) and the centre of the grain (b). For the diffraction patterns recorded near the grain boundaries, only diffraction spots of the matrix can be observed, while further inside the grain the typical α_2 superlattice reflections are observed. These differences were further confirmed by plotting the line intensity profile through the (0000) diffraction spot, Fig. 6c and d. Hence, the initial observation implies that α_2-precipitates are present in the centre of the grain and that there is less or no α_2-precipitation closer to the grain boundaries.

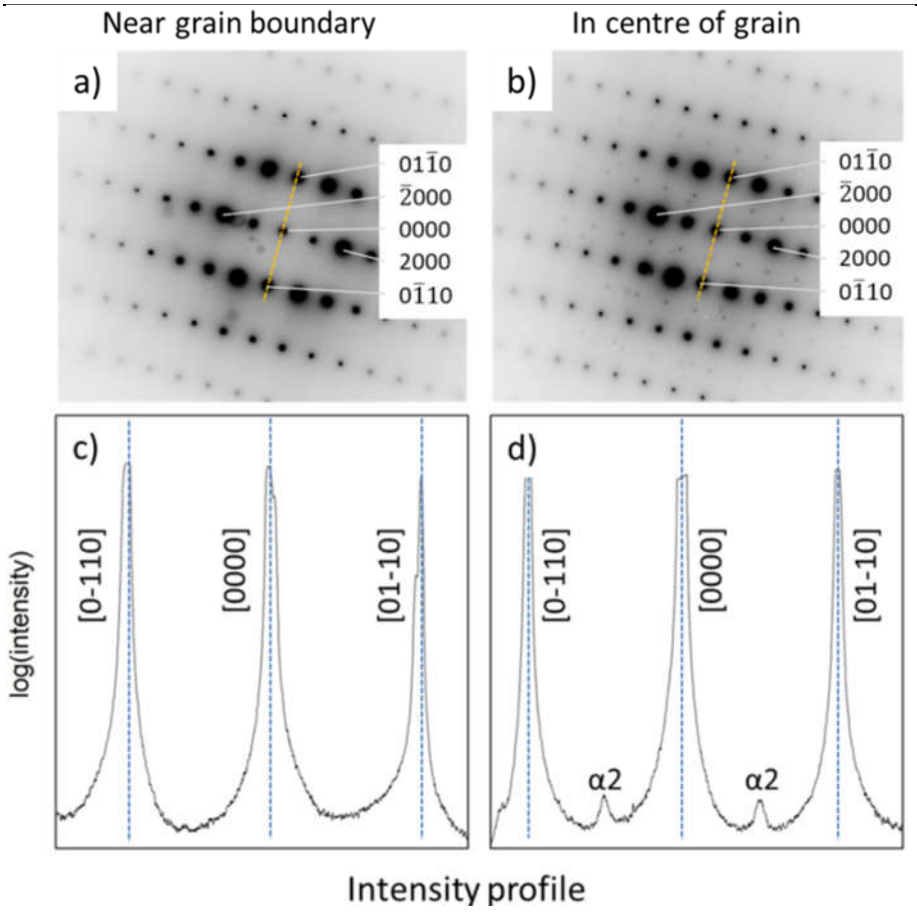

Fig. 6: a), b) Diffraction pattern along [11-20]-zone axis using selective area aperture. c), d) Intensity profile for orange lines. Diffraction patterns have been recorded a), c) near the grain boundary and b), d) the centre of the grain.

To analyse the variations in α_2 precipitation as a function of distance from the grain boundary, the ratio of integrated intensities of the superlattice to matrix diffraction spots is plotted in Fig. 7. It can be seen that four points in the centre of the grain (Fig. 5) have similar values, forming a plateau region, indicating the strong presence of α_2 in this region at least 5 µm away from the grain boundary. For both of the areas that are closest to the grain boundary (less than 2 µm away from the grain-boundary), no superlattice diffraction spots are observed and consequently the intensity ratio is zero. In the transition regions from the grain boundaries towards the centre of the grain (points 2 and 7), superlattice diffraction spots can be observed, but their intensity is lower than in the centre of the grain. This applies for both sides of the grain, but on the right side of the grain, the change in intensity appears steeper than on the left side. It can be seen in Fig. 5 that on the right, the line on which the analysed areas are aligned is perpendicular to the grain boundary, while there is a bulge on the left side of the grain. Therefore point 2 might be closer to grain boundaries than point 7 (see Fig. 4). It needs to be kept in mind that a 2D-cross section has been analysed, not considering the 3D-shape of the grain. 3D-geometry effects could lead to variations of the chemical gradient near the grain boundary, e.g. as it has been observed in Fig.4 and influence α_2 precipitation.

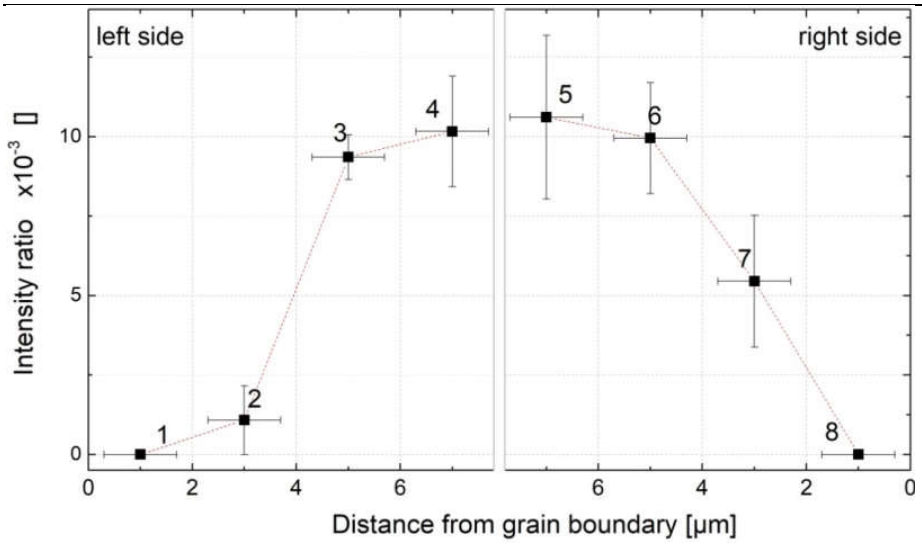

Fig. 7: Ratio of the integrated intensity of superlattice diffraction spot to [0000]-diffraction spot. The number next to the data points identify the areas defined in Fig.5. The bars in the x-direction indicate the width of areas analysed by selective-area diffraction.

3.5 APT analysis

Average concentrations have been calculated for three APT-specimens and these are summarised in Table 1. The results have been plotted together with the concentration profile of the EPMA-WDS analysis in Fig. 4. For the two samples in the centre of the grain, the results of both techniques align well. Only for the Sn concentration, the values determined by APT are significantly lower than the ones from EPMA-WDS. One possible explanation is that Sn has a lower evaporation field than Ti and the other alloying elements [28], which means all Sn ions may not be evaporating on the laser pulses as intended. When moving closer to the grain boundaries, both techniques are showing the same trend: the concentration of Al decreases, while the concentration increases for all other elements.

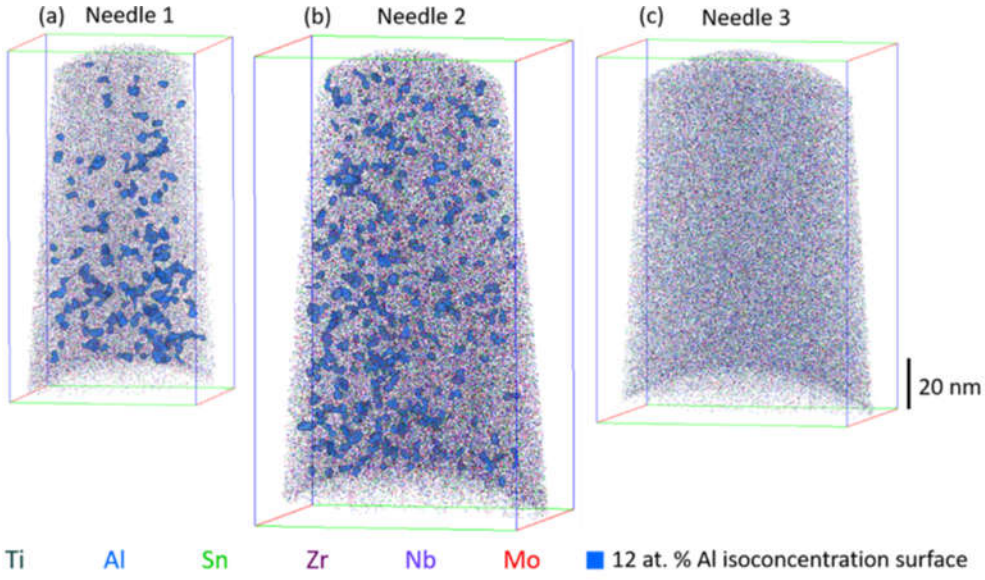

Fig. 8: Atom maps for the needle taken from the centre of the primary-α grain (a), (b) and the needle taken nearest to the grain boundary (c). 12 at.% Al isosurfaces have been used to highlight the precipitates in (a) and (b).

The atom maps for the three needles, seen in figure 8, show precipitates in the two needles nearest the centre of the grain (needle 1&2), but not in the needle near the grain boundary (needle 3). When a 12 at. % Al isoconcentration surface was applied to needle three, in line with the standardised analysis method described in section 2.5, no precipitates were seen; it was not possible to identify any precipitates lower than 12 at.% Al using this analysis method. Thus, whilst it cannot be said that there is no precipitation in needle 3, there is a greater degree of precipitation in needles 1 and 2 than in needle 3.

The compositions of the precipitates in needles 1 and 2 are reported in table 2 as 15.7-16.1 at. % Al and 79.1-79.5 at. % Ti. The precipitates are rich in aluminium and the concentration is close to that reported for the α_2 phase; 75 at. % Ti and 22.5-39 at. % Al [29]. α_2-precipitates also contain Sn and Si with an expected Ti:(Al,Sn,Si) ratio of 3:1 [7]. For the analysed particles the concentration of α_2 stabilising elements is lower than expected, with a Ti:(Al,Sn,Si) ratio of 4.4:1 (needle-1) and 4.3:1 (needle-2).

Table 2: Chemical composition of α_2-precipitates in needle-1 and needle-2

	Concentration (at. %) Precipitates in	
Element	Needle-1	Needle-2
Ti	79.47	79.07
Al	15.68	16.05
Sn	1.68	1.80
Zr	1.56	1.62
Si	0.64	0.59
Nb	0.17	0.19
Mo	0.07	0.03

Based on the measured precipitate composition and the ageing conditions experienced by the sample, the precipitates are identified as α_2 phase. The precipitate volume fractions in needle 1 and 2 were 0.10 % and 0.08 %, respectively. Equivalent precipitate radius was calculated by approximating the precipitates as spheres. This returns representative precipitate diameters of 1.9 nm for needle 1 and 1.8 nm for needle 2.

4 Discussion

The motivation for this work originated from the initial observation of the core-shell structure observed in primary α grains of a near-α Ti-alloy with bimodal microstructure when using BSE-SEM imaging. It is worth pointing out that such a core-shell structure is also observed by optical microscopy when analysing a sample etched with Kroll's reagent. However, in the latter case, one might assume the darker shell is a result of over-etching.

To exclude the possibility of variations in crystallographic orientation being the root cause for the brighter shell structure in the BSE-SEM images, crystallographic orientation mapping was used to demonstrate that the shell region has the same crystallographic orientation as the core region within a range of approximately 0.3°. In some cases, slightly higher misorientations can be found within primary α grains, which then also results in a change of contrast, but they are not associated with the core-shell structure.

Detailed quantitative chemical mapping using EPMA-WDS, Fig. 4, also revealed a decrease of aluminium (α-stabiliser) and an increase of Mo, Nb, Si, Sn and Zr within the shell area towards the grain/interface boundary. It should be pointed out that this analysis was carried out at relatively low accelerating voltage (7 keV) and therefore the spatial resolution in width and depth was 300 nm, which means that only the data point closest to the α/ β phase boundary might be affected by the electron-interaction volume cutting across two phases. Atom probe analysis confirmed both the absolute numbers and relative trends recorded by EPMA-WDS. Considering the variation of the alloying elements within the shell area, i.e. loss of elements lighter than Ti (except Si) and gain of elements heavier than Ti, it becomes clear why the shell appears brighter in BSE-SEM imaging than the core area. It also demonstrates that the shell structure must form during cooling from the sub-β-transus solution temperature, as the β phase at that stage will be depleted in α-stabilisers and enriched in β-stabilisers. It is however interesting to see that Sn and Zr segregate to the β phase, which is apparent from the line scan in Fig. 4, but also from the qualitative chemical maps presented in Fig. 3. The binary phase diagrams of Ti-Sn [30] and Ti-Zr [31] show that for the concentrations of each of the elements in TIMETAL®834, both Zr and Sn are reducing the β-transus temperature. Therefore, Sn and Zr are β-stabilising elements within the given range, which explains the higher concentrations in the transformed β-phase.

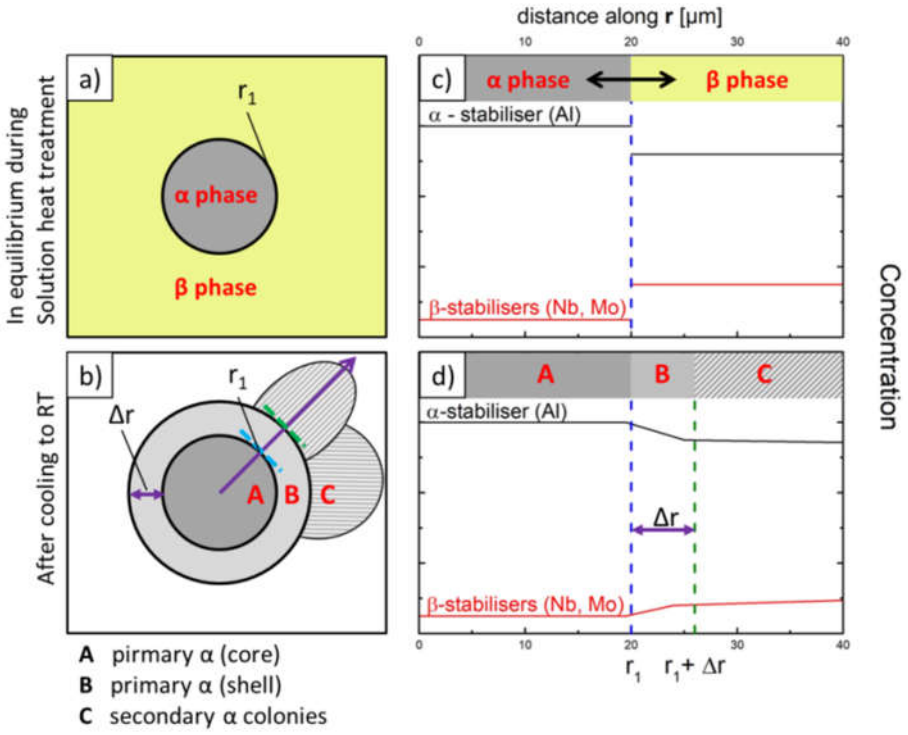

Figure 9: Schematic drawing of (a & b) and schematic concentration profile across (c & d) a primary α grain during solution heat treatment (a & c) and after cooling to room temperature (b & d). In (c), the concentration profile is plotted for the α grain, as well as the surrounding β phase; in (d) the profile is plotted for the α phase only and the retained β phase in area C is disregarded.

The schematic in Fig. 9 is used for explaining the mechanism that leads to the formation of the observed core-shell structure. It is assumed that at the end of the solution heat treatment equilibrium is reached and therefore the chemical composition is constant throughout each of the two phases (Fig. 9, a & c). During cooling from the solution temperature, primary α grains grow into the β-phase, which contains relatively low concentrations of α-stabilising elements and high

concentrations of β-stabilising elements. Therefore, a shell is formed around primary-α grains, which is depleted in α-stabilising elements, respectively Al, and slightly enriched in β-stabilising elements. Eventually, the β to α phase transformation switches over from growth of primary α to epitaxial growth of secondary α. Throughout the transformation, the β stabilising elements try to try to diffuse away from the approaching β/α interface resulting in the retention of some β-phase at room temperature with increased levels of β stabilisers. However, some of the β- stabilising elements will be trapped in the α-phase as they cannot diffuse away quickly enough. This applies particularly for Mo, due to its low diffusion rate in Titanium [32,33]. One might expect that the trapping of β stabilisers in the α-phase might increase as cooling proceeds, due to lower diffusion rates at a lower temperature. At the same time, it needs to be kept in mind that the equilibrium chemical composition also changes as a function of temperature, which potentially influences local compositions. The growth of secondary α-phase is often initiating at the grain boundaries of primary α grains (Fig. 9, a & b (r1 and blue line)) and direction of growth is in radial direction away from the primary α grains (Fig. 9, b: purple arrow). Therefore, secondary α phase further away from primary α grains has formed at lower temperatures and therefore can be expected to have slightly higher concentrations of β-stabilising elements.

Regarding the low concentrations of Al, Sn and Si in what is suggested to be α_2, characterised by APT, there are two possible explanations for low concentrations. Firstly, the ageing time experienced by the sample was short, meaning the precipitates are in the early stages of α_2 formation and have not had sufficient time to become fully enriched in Al, Sn and Si. Secondly, there is an interface region between matrix and precipitates, as has been shown by Radecka et al [7]. As the isoconcentration surface of 12 at.% is lower than the Al concentration expected in the α_2-precipitates, it can be assumed that the interface region has been included in our analysis, resulting in a lower average concentration of Al, Sn and Si than expected for Ti3(Al, Sn, Si). Another possible explanation is that in the centres of the primary α grains contain ordered domains of α_2 as a consequence of spinodal decomposition, instead of of the ideal α_2 precipitation.

It is not clear at this stage to what extent the solid solution strengthening effect changes from the core to the shell structure. While less aluminium would reduce solid solution strengthening, the increase of the other elements would increase it again. An important question that arises from the change of aluminium content is if α_2 formation is suppressed in the shell area. As pointed out more recently by Radecka et al. [7,8], it is not only aluminium that promotes α_2 formation but also zirconium, silicon, molybdenum and vanadium. Indeed, their work highlighted that tin and silicon are stronger α_2 formers than aluminium. Hence, the observed absence of α_2-precipitates in the shell area studied by SAED in a TEM, as well as in APT, was not a foregone conclusion. The formation of α_2-precipitates is important for several reasons. It provides precipitation strengthening, but it also enhances strain-localisation [34,35] resulting in greater stress concentrations near grain boundaries and potentially earlier failure. To what extent the absence of α_2 in the shell structure of primary α grains might mitigate against such stress concentration by localised shear is not clear at this stage, but it highlights the potential importance of the present finding.

5 Conclusions

Primary α grain growth during cooling after sub-β-solvus solution heat treatment of a near-α Ti alloy results in chemical segregation, which can be seen in BSE-SEM images in form of a core-shell structure in primary α. Microchemical analysis has shown that the shell has a similar chemical composition as secondary α; depleted in Al and enriched in β-stabilising alloying elements. Despite being described as neutral alloying elements in literature, it has been shown that Sn and Zr act as β-stabilising elements. The reduced concentration of Al near the grain/interface boundary results in the absence of α_2 despite the high level of Sn and Si that also promote α_2 formation, while α_2 has been found in the centre of primary α grains.

Acknowledgement

The authors would like to thank the EPSRC funding the project through the CDT in Advanced Metallic Systems. The authors would also like to thank Rolls-Royce plc and TIMET for providing additional funding and the provision of material.

This work was supported by the Henry Royce Institute for Advanced Materials, funded through EPSRC grants EP/R00661X/1, EP/S019367/1, EP/P025021/1 and EP/P025498/1.

We are grateful for the use of the JEOL JXA-8530F FEG-EPMA, EPSRC award EP/M028097/1. We would like to thank Jonathan Fellowes for his support with EPMA-WDS experiment and data analysis.

We would like to acknowledge Matthew Topping and Xu Xu for their help with TEM experiment and sample preparation.

Data Availability Statement

The datasets generated during and/or analysed during the current study are available from the corresponding author on reasonable request

References

[1] G. Lütjering, J.C. Williams, Titanium : Engineering Materials and Processes, Ed. Springer. second edi (2007) 1–442. doi:10.1007/978-3-540-73036-1.

[2] H. Conrad, Effect of interstitial solutes on the strength and ductility of titanium, Prog. Mater. Sci. 26 (1981) 123–403. doi:10.1016/0079-6425(81)90001-3.

[3] H.W. Rosenberg, W.D. Nix, Solid solution strengthening in Ti-Al alloys, Metall. Trans. 4 (1973) 1333–1338.

[4] E.W. Collings, H.L. Gegel, A physical basis for solid-solution strengthening and phase stability in alloys of titanium, Scr. Metall. 7 (1973) 437–443. doi:10.1016/0036-9748(73)90092-6.

[5] G. Lütjering, S. Weissmann, Mechanical properties of age-hardened titanium-aluminum alloys, Acta Metall. 18 (1970) 785–795. doi:10.1016/0001-6160(70)90043-X.

[6] T.K.G. Namboodhiri, C.J. McMahon, H. Herman, Decomposition of the α-phase in titanium-rich Ti-Al alloys, Metall. Trans. 4 (1973) 1323–1331.

[7] A. Radecka, J. Coakley, V.A. Vorontsov, T.L. Martin, P.A.J. Bagot, M.P. Moody, D. Rugg, D. Dye, Precipitation of the ordered α2 phase in a near-α titanium alloy, Scr. Mater. 117 (2016) 81–85. doi:10.1016/j.scriptamat.2016.02.015.

[8] A. Radecka, P.A.J. Bagot, T.L. Martin, J. Coakley, V.A. Vorontsov, M.P. Moody, H. Ishii, D. Rugg, D. Dye, The formation of ordered clusters in Ti-7Al and Ti-6Al-4V, Acta Mater. 112 (2016) 141–149. doi:10.1016/j.actamat.2016.03.080.

[9] O.N. Senkov, J.J. Valencia, S. V Senkova, M. Cavusoglu, F.H. Froes, Effect of cooling rate on microstructure of Ti-6Al-4V forging, Mater. Sci. Technol. 18 (2002) 1471–1478. doi:10.1179/026708302225007808.

[10] B.S.S.C. Rao, M. Srinivas, S.V. Kamat, The effect of volume fraction of primary α phase on fracture toughness behaviour of Timetal 834 titanium alloy under mode I and mixed mode I/III loading, Mater. Sci. Eng. A. 520 (2009) 29–35. doi:10.1016/j.msea.2009.05.007.

[11] K.V.S. a I. Srinadh, N. Singh, V. Singh, Role of Ti3Al / silicides on tensile properties of Timetal 834 at various temperatures, Bull. Mater. Sci. 30 (2007) 595–600.

[12] A. Kumar, N. Singh, V. Singh, Influence of stabilization treatment on low cycle fatigue behavior of Ti alloy IMI 834, Mater. Charact. 51 (2003) 225–233. doi:10.1016/j.matchar.2003.11.004.

[13] A.K. Singh, C. Ramachandra, Characterization of silicides in high-temperature titanium alloys, J. Mater. Sci. 32 (1997) 229–234. doi:10.1023/A:1018516324856.

[14] G.B. Thompson, M.K. Miller, H.L. Fraser, Some aspects of atom probe specimen preparation and analysis of thin film materials, Ultramicroscopy. 100 (2004) 25–34. doi:10.1016/j.ultramic.2004.01.010.

[15] K. Thompson, D. Lawrence, D.J. Larson, J.D. Olson, T.F. Kelly, B. Gorman, In situ site-specific specimen preparation for atom probe tomography, Ultramicroscopy. 107 (2007) 131–139. doi:10.1016/j.ultramic.2006.06.008.

[16] G.E. Lloyd, Atomic Number and Crystallographic Contrast Images with the SEM: A Review of Backscattered Electron Techniques, Mineral. Mag. 51 (1987) 3–19. doi:10.1180/minmag.1987.051.359.02.

[17] W. Reuter, Electron probe microanalysis, 25 (1971) 80–119.

[18] D. Drouin, A.R. Couture, R. Gauvin, monte CArlo Simulation of electroN trajectory in sOlids Casino, (2011).

[19] A.P. Woodfield, P.J. Postans, M.H. Loretto, R.E. Smallman, The effect of long-term high temperature exposure on the structure and properties of the titanium alloy Ti 5331S, Acta Metall. 36 (1988) 507–515. doi:10.1016/0001-6160(88)90082-X.

[20] N. Mori, T. Oikawa, T. Katoh, J. Miyahara, Y. Harada, Application of the “imaging plate” to TEM image recording, Ultramicroscopy. 25 (1988) 195–201. doi:10.1016/0304-3991(88)90014-9.

[21] B.H. Armstrong, Spectrum line profiles: The Voigt function, J. Quant. Spectrosc. Radiat. Transf. 7 (1967) 61–88. doi:10.1016/0022-4073(67)90057-X.

[22] D.J. Larson, T. Prosa, R.M. Ulfig, B.P. Geiser, T.F. Kelly, Local electrode atom probe tomography, New York, US Springer Sci. (2013).

[23] M.P. Moody, L.T. Stephenson, A. V Ceguerra, S.P. Ringer, Quantitative binomial distribution analyses of nanoscale like-solute atom clustering and segregation in atom probe tomography data, Microsc. Res. Tech. 71 (2008) 542–550. doi:10.1002/jemt.20582.

[24] T. Homma, A. Arafah, D. Haley, M. Nakai, M. Niinomi, M.P. Moody, Effect of alloying elements on microstructural evolution in oxygen content controlled Ti-29Nb-13Ta-4.6Zr (wt%) alloys for biomedical applications during aging, Mater. Sci. Eng. A. 709 (2018) 312–321. doi:10.1016/J.MSEA.2017.10.018.

[25] C.A. Williams, D. Haley, E.A. Marquis, G.D.W. Smith, M.P. Moody, Defining clusters in APT reconstructions of ODS steels, Ultramicroscopy. 132 (2013) 271–278. doi:10.1016/j.ultramic.2012.12.011.

[26] A.J. London, Quantifying Uncertainty from Mass-Peak Overlaps in Atom Probe Microscopy, Microsc. Microanal. 25 (2019) 378–388. doi:10.1017/S1431927618016276.

[27] F. De Geuser, B. Gault, Metrology of small particles and solute clusters by atom probe tomography, (2019). http://arxiv.org/abs/1910.10532.

[28] B. Gault, M.P. Moody, J.M. Cairney, S.P. Ringer, Atom probe microscopy, Springer Science & Business Media, 2012.

[29] C.Y. Jones, W.E. Luecke, E. Copland, Neutron diffraction study of oxygen dissolution in α2-Ti3Al, Intermetallics. 14 (2006) 54–60. doi:10.1016/j.intermet.2005.04.011.

[30] F. Yin, J.-C. Tedenac, F. Gascoin, Thermodynamic modelling of the Ti–Sn system and calculation of the Co–Ti–Sn system, Calphad. 31 (2007) 370–379. doi:10.1016/J.CALPHAD.2007.01.003.

[31] K.C. Hari Kumar, P. Wollants, L. Delacy, Thermodynamic assessment of the Ti-Zr system and calculation of the Nb-Ti-Zr phase diagram, J. Alloys Compd. 206 (1994) 121–127. doi:10.1016/0925-8388(94)90019-1.

[32] R.P. Elliott, Diffusion in titanium and titanium alloys, Armour Research Foundation Chicago IL, 1962. https://apps.dtic.mil/dtic/tr/fulltext/u2/290336.pdf.

[33] G.B. Gibbs, D. Graham, D.H. Tomlin, Diffusion in titanium and titanium—niobium alloys, Philos. Mag. 8 (1963) 1269–1282.

[34] D. Lunt, X. Xu, T. Busolo, J. Quinta da Fonseca, M. Preuss, Quantification of strain localisation in a bimodal two-phase titanium alloy, Scr. Mater. 145 (2018) 45–49. doi:10.1016/j.scriptamat.2017.10.012.

[35] D. Lunt, T. Busolo, X. Xu, J. Quinta da Fonseca, M. Preuss, Effect of nanoscale α2 precipitation on strain localisation in a two-phase Ti-alloy, Acta Mater. 129 (2017) 72–82. doi:10.1016/J.ACTAMAT.2017.02.068.

Appendix

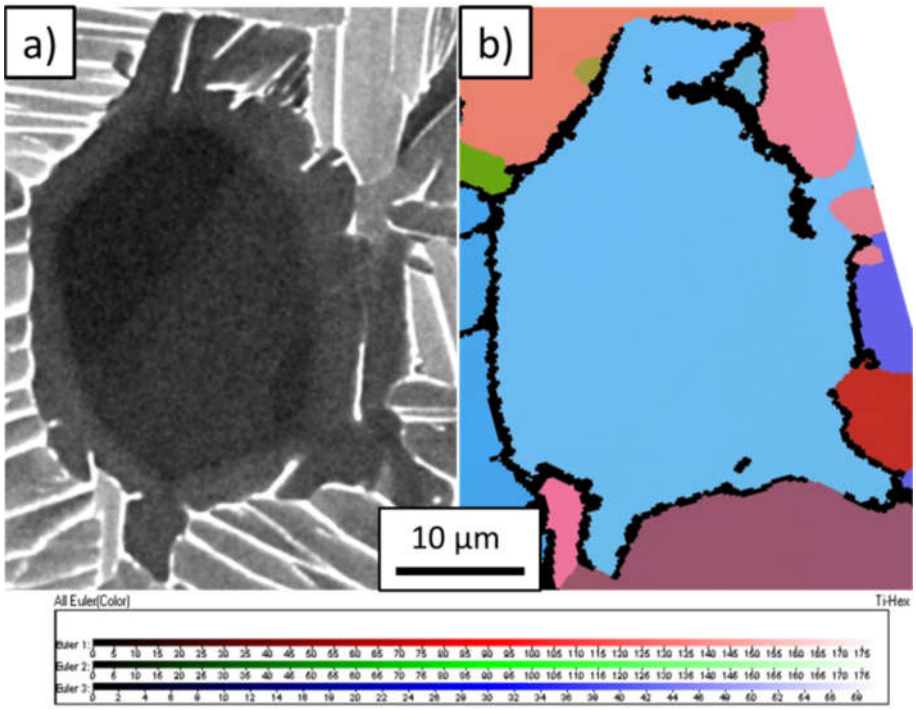

Appendix 1: BSE-SEM image and crystallographic orientation map, using Euler colours, of the primary α grain analysed in **Fig. 4** (**a**).

4.2 Paper 2 - Understanding strain localisation behaviour in a near-α Ti-alloy during initial loading below the yield stress

Claudius Dichtl[1*], David Lunt[1], Rhys Thomas[1], Michael Atkinson[1],Matthew Thomas[2], Dave Rugg[3], Rebecca Sandala[3], Joao Quinta da Fonseca[1], Michael Preuss[1]

[1] University of Manchester, Manchester, M13 9PL

[2] TIMET UK, PO Box 704, Witton, B6 7UR

[3] Rolls-Royce plc, Derby, DE24 8BJ

The manuscript was published in MATEC Web Conf.

Volume 321, October 2020, Article Number 11039.

https://doi.org/10.1051/matecconf/202032111039

Highlights of this paper

Observation of shear-bands at macroscopic loads as low as 70% of yield-stress

Material with coarse transformation product accumulate more plastic strain at the same relative stress level than material with fine transformation product

At low stress levels, average strains were identical for materials with different prior β-grain morphology, but differences can be observed for the maximum strain values and strain distribution

Even at low stress levels, slip can be observed in primary α, as well as in transformed-β grains

Contributions

For **Paper 2** titled '**Understanding strain localisation behaviour in a near-α Ti-alloy during initial loading below the yield stress**', Claudius Dichtl, Michael Preuss and João Quinta da Fonseca designed the study. Claudius Dichtl performed the experiments and prepared the manuscript. David Lunt supported sample preparation and data processing. Michael Atkinson supported the in-situ HRDIC experiment and together with Rhys Thomas contributed to the data analysis. All authors contributed to writing and editing the final version of the paper.

Abstract

Near-α Ti-alloys such as TIMETAL® 834 are known for their superior mechanical properties at high temperature, and as such are found in applications where high strength and improved fatigue performance at elevated temperatures (>450°C) are required. However, these alloys can be susceptible to cold-dwell fatigue; a failure mechanism that is not well understood. The present work investigates the strain localisation behaviour during cold creep and the implications it has in terms of dwell susceptibility for two different bi-modal microstructures. Slip traces and strain distributions have been analysed for different material conditions by employing High-Resolution Digital Image Correlation (HRDIC) in combination with orientation mapping. Using this approach, it was possible to distinguish deformation patterns in primary α grains and transformed-β colonies, loaded incrementally to stress levels of 70%, 80% and 90% of the yield stress. Different prior β-grain morphologies didn't affect the average strains when stresses are low, but strain distributions have been affected by the β-grain morphology. Material with coarse transformation product accumulated larger amounts of plastic strain compared to the material with fine transformation product, at the same relative stress levels. At low stress levels, slip bands have been detected both in primary α, as well in the transformed-β phase, cutting through the lamellae, for the material condition with a coarse transformation product; on the other hand, for the material conditions with a fine transformation product, slip bands are localised only in primary α grains at low stress levels. It was also found for both conditions that at low stress levels slip bands are found in grains that are well oriented for basal slip. Based on these observations it is discussed if β-ligaments are significant obstacles to dislocation movement. Finally, we will discuss the requirement of crystal-elasticity modelling to take into account differences in crystallographic orientations and the elastic and plastic anisotropy of HCP-titanium.

1 Introduction

Titanium alloys are often used in high-performance applications, such as aerospace applications, due to their high specific strength, fracture toughness and corrosion resistance. However, it has frequently been reported that titanium alloys exhibit cold creep at low temperature ($T/T_m<0.2$ [1]) and stresses well below the yield strength [2], [3]. Cold creep in titanium is commonly explained by either a high strain rate sensitivity [4] or interface sliding [5], [6].

In titanium alloys solution treated in the high α+β phase regime the lamellar spacing of secondary α, i.e. the transformation product, depends on the cooling rates. This means that high cooling rates result in high tensile strength, which is explained by reduced slip lengths in secondary α [7]. It has been found that when the Burgers Orientation relationship between the secondary α and the retained-β is valid, dislocations might easily cut through the colony at least for one of the three possible <a> Burgers directions in the α-phase. However, with further misorientation from it, α/β boundaries become a strong obstacle for dislocation movement [1], [8], [9].

Plastic deformation in titanium alloys is accommodated by dislocation movement in five distinct groups of slip systems: basal slip, prismatic slip and first-order pyramidal slip with <a>-type Burger's vector, and additionally first and second-order pyramidal slip with <c+a>-type Burger's vector [10]. The critically resolved shear stress at room temperature for <c+a>-type slip is more than two times higher than for basal and prismatic slip with <a>-type Burger's vector [7]. Bridier et al. showed that the active slip systems during tensile testing of Ti-6Al-4V are basal, prismatic and first-order pyramidal slip [10]. For stress levels below the yield-stress, basal and prismatic slip are the dominant slip systems [11], with basal slip being activated at the lowest stress levels [11], [12]. While this applies for lower stresses, at higher stresses pyramidal and prismatic slip are dominantly contributing to strain localisation [13].

In a previous study, High-Resolution Digital Image Correlation (HRDIC) was used to show and analyse the formation of slip-bands in the α+β titanium alloy Ti-6Al-4V for stresses below the yield point. McLean et al. focused on the effect of micro-textured regions in equiaxed microstructures on strain localisation behaviour [13]. It was found that pyramidal <c+a> slip can be activated at low stress in micro-textured regions with basal normal preferentially orientated in the loading direction, but that the formation of long bands of localised strain was formed by prismatic slip. In the present study, we carry out a similar study on the titanium alloy TIMETAL®834 with a bi-modal microstructure. We use two ingots with different thermo-mechanical processing history (Material A & B) and two different transformation products to study the effect of microstructure on the strain localisation. At first Materials A & B, both with fine transformation product were analysed to study the effect of prior β-grain morphology. Then two conditions of Material B with different transformation products were tested to study the effect of cooling rate and lamella width. HRDIC analysis of images obtained in-situ during mechanical testing was used to probe the differences in mechanical response between primary α grains and secondary α colonies.

2 Experimental

2.1 Material

Two ingots of TIMETAL-834, with different forging histories, were supplied by TIMET, UK. The two ingots have differences in the morphology of prior β-grains and are referred to as 'Material A'

(smaller prior β-grains) and 'Material B' (larger prior β-grains). After forging, two different heat-treatments were applied to each material condition. The heat-treatments consisted of a 2 h solution-heat treatment at 1015 °C followed by cooling to room temperature with either slow cooling (1 K/s) or fast cooling (10-30 K/s). The heat-treatment produces a bi-modal microstructure with either coarse (slow cooling) or fine (fast cooling) transformation product. Both conditions were subsequently annealed for 2 hours at 700 °C leading to the formation of α_2-precipitates predominantly in the primary α grains [14], [15].

2.2 Microstructure

The morphologies of the β-grains in near-α titanium alloys cannot be easily obtained by EBSD-based orientation mapping of the β-phase, as the volume fraction is low and the width of the β-lamellae is only around 0.1µm. Instead, crystallographic orientation maps of α-phase were recorded using EBSD from which the β-phase was reconstructed using an algorithm, based on the Burgers orientation relationship [16]. The material conditions with the fine transformation product were used for the comparison, as the secondary α colonies are smaller, which has proven to result in a higher fraction of data points with successful β-reconstruction. Only one material condition for each Material A & B was analysed, as it is assumed that the β-morphology is not changed by the cooling rate or annealing heat treatment. For EBSD-mapping a TESCAN Mira3 field emission gun scanning electron microscope equipped with the Oxford Instrument-Symmetry detector was utilised. The beam settings were 20 kV, 96 nA and a step size of 7.5 µm was used.

Optical bright field microscopy was used to determine the volume fraction and size distribution of primary α grains and the lamella spacing of the transformation product for all material conditions. Specimens were ground with abrasive paper (to 4000 grid), polished in a colloidal silica solution and then etched with Kroll's reagent (2 ml HF, 4 ml HNO3, 94 ml H_2O) to reveal the underlying microstructure. The difference in brightness of primary α phase compared to transformed-β phase was used to separate the two phases and create a binary image. The 'Detect particle' function in 'Fiji' was then utilised to determine the volume fraction of primary α. The lamella spacing of secondary α was determined by applying the line intersection method on 30 colonies.

2.3 Mechanical testing

For the mechanical baseline characterisation and HRDIC experiments, flat dog-bone specimens with a cross-section of 3x1 mm² were used. Uniaxial tensile testing was carried out on an Instron 5569 electromechanical tester at a constant strain-rate of 0.005 1/s to record stress-strain curves and to determine the 0.2%-proof stress of each material condition [17]. The results are shown in Table 2.

HRDIC analysis requires a pattern of distinct features on the sample surface. Therefore the samples were ground and polished with colloidal silica. A thin layer of gold was deposited on the surface using a sputter-coater. The gold-layer was broken up and transformed to distinct nano-sized particles using water-vapour remodelling process at a temperature of 275°C for 2 hours [18].

The HRDIC experiments were carried out in-situ, using a 'Deben' 5kN tensile stage inside an 'FEI-Quanta 650' FEG-SEM. This allows the sample to be mechanically loaded during imaging. All mechanical loading is at stress levels relative to the 0.2 proof stress of each specimen. Three load steps were used: 70, 80 and 90 % of the 0.2% proof stress, referred to here as the yield stress

($\sigma_{0.2\%}$). After being loaded to the first load step, the stress was held constant for 10 minutes to accommodate the plastic deformation. Then the load was reduced by 5 %, e.g. from 70 % of $\sigma_{0.2\%}$ to 65 % of $\sigma_{0.2\%}$, to stop any further deformation process. At this stress level, the samples were imaged, before the next load steps were applied in the same way. The images were recorded at 10 kV and a working distance of 11.7 mm with 2048 pixels wide at a field width of 30 µm. A mosaic of 8x8 images was recorded, which were then stitched into a large image, using 'Grid/Collection stitching' plug-in for 'Fiji' [19], [20], resulting in a stitched image of 180 x 180 µm².

2.4 Processing of DIC data

Digital image correlation (DIC) was performed using LaVision DaVis 8.4.0 software. In DIC, the local displacements are determined by comparing the undeformed image to the deformed image at each load step. For the correlation process, a sub-window size of 24 x 24 pixels was used, resulting in a spatial resolution of 350 nm. As there is a variation in the morphology of the gold pattern between grains, some areas exhibit higher noise levels than others. To reduce noise, a Gaussian filter is applied to the strain data. The deformation maps consist of strain components parallel (ε_{xx}) and perpendicular (ε_{yy}) to the loading direction x, and a shear component (ε_{xy}). From these three vectorial components, the scalar γ_{eff} is calculated, which is referred to as the effective shear strain (1) [18], [21]. Effective shear strain is used as it takes all in-plane shear components into account.

$$\gamma_{eff} = \sqrt{\left(\frac{\varepsilon_{xx}-\varepsilon_{yy}}{2}\right)^2 \quad \varepsilon_{xy}^2} \tag{1}$$

To display slip-bands and overlay them on top of microstructural maps, areas of high strain are segmented in the strain maps. Due to low levels of strain and higher than usual experimental noise due to the in-situ setup, the noise level can be close to the strain values. Segmenting the strain data helps in displaying deformation patterns without random noise. All data points in a strain map with strain values higher than a threshold value are accepted, while all other points are discarded. The threshold value is set to be the 99th percentile of the strain distribution, as noise and artefacts might also be segmented for lower threshold values. This segmentation results in a binary image of slip-bands were the exact values within the slip-bands are lost.

To calculate the expected elastic strain, equation (1) is used and Poisson-ratio is assumed to be 0.3 and the shear component ε_{xy} needs to be set to zero. Tensile testing determined Young's modulus to be 117 GPa.

3 Results

In Fig.1 the β-phase morphology of Material A and Material B is displayed. Material A exhibits what seem to be small β grains, but in some cases, there are areas with common crystallographic orientation that are several millimetres in size. While there appears to be a preferential orientation within each area, there are also other orientations present. These areas of preferential crystallographic orientations have no clear boundaries, making it difficult to define a clear prior β-grain size. In Material B, grains with a size of up to 500 µm are present. These grains only have one crystallographic orientation and a clear boundary. These clearly defined grains are separated from each other by regions with randomised texture. Overall, Material A exhibits smaller β grains, but there are long chains of similarly orientated β-grains. The β-grains in Material B are larger than

individual β-grains in Material A but smaller and with sharper outlines compared to the areas of similarly orientated β-grains in Material A.

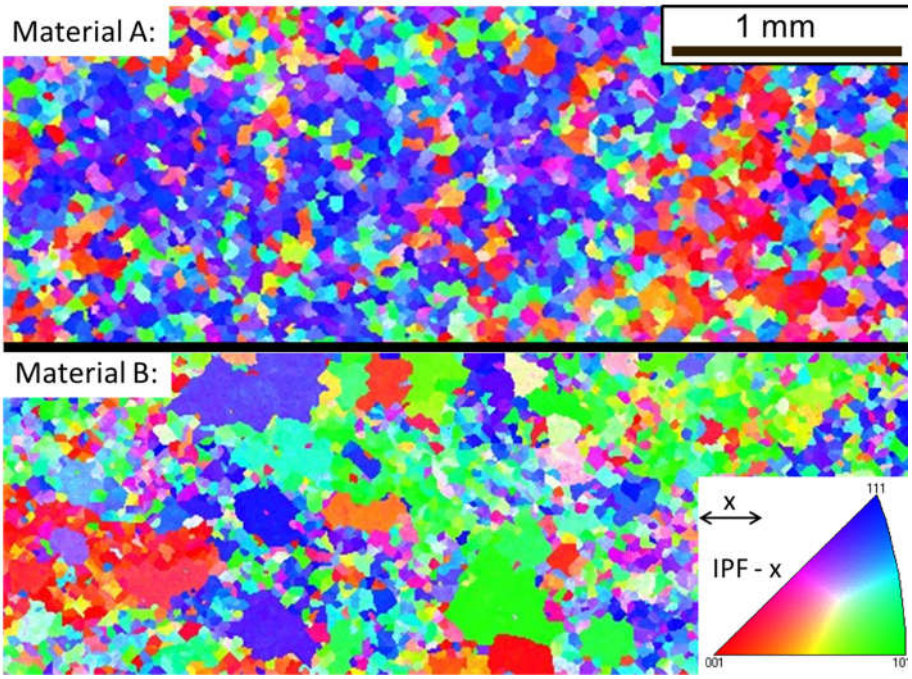

Fig. 1: Crystallographic orientation maps of β-phase for two material conditions A & B. The IPF-colouring is displayed for the reference direction 'X', which is in parallel to the loading direction. The maps have been created from EBSD-data of α-phase using a reconstruction algorithm.

The grain size and volume fractions of the different phases for the microstructures displayed in Fig.2 are summarised in Table 1. For material A & B, the fast cooling rate results in similar lamella spacing of just over 1 µm. While the primary α volume fraction is similar for both materials, material B exhibits a smaller average primary α grain size; a difference which originates from differences in the initial thermomechanical processing route. Comparing different cooling rates for material B reveals that slower cooling results in the lamella spacing being approximately 60 % wider than for the faster cooling rate. The material condition with coarse transformation product (slower cooling) has a higher primary α volume fraction (23 %) than the condition with a fine transformation product (18 %). This is due to the slower cooling rate giving more time for primary α grain growth [22].

Table 1: Summary of microstructure analysis based on micrographs displayed in Fig. 2

	Material A	**Material B**	
	Fine lamellae	Fine lamellae	Coarse lamellae
Lamella spacing	1.2 ± 0.1 µm	1.1 ± 0.3 µm	1.8 ± 0.4 µm
Primary α Volume fraction	19.7 ± 0.7 %	18.2 ± 1.0 %	23.1 ± 0.3 %
Average α(P) grain size (area)	506 ± 9 µm²	379 ± 18 µm²	469 ± 11 µm²

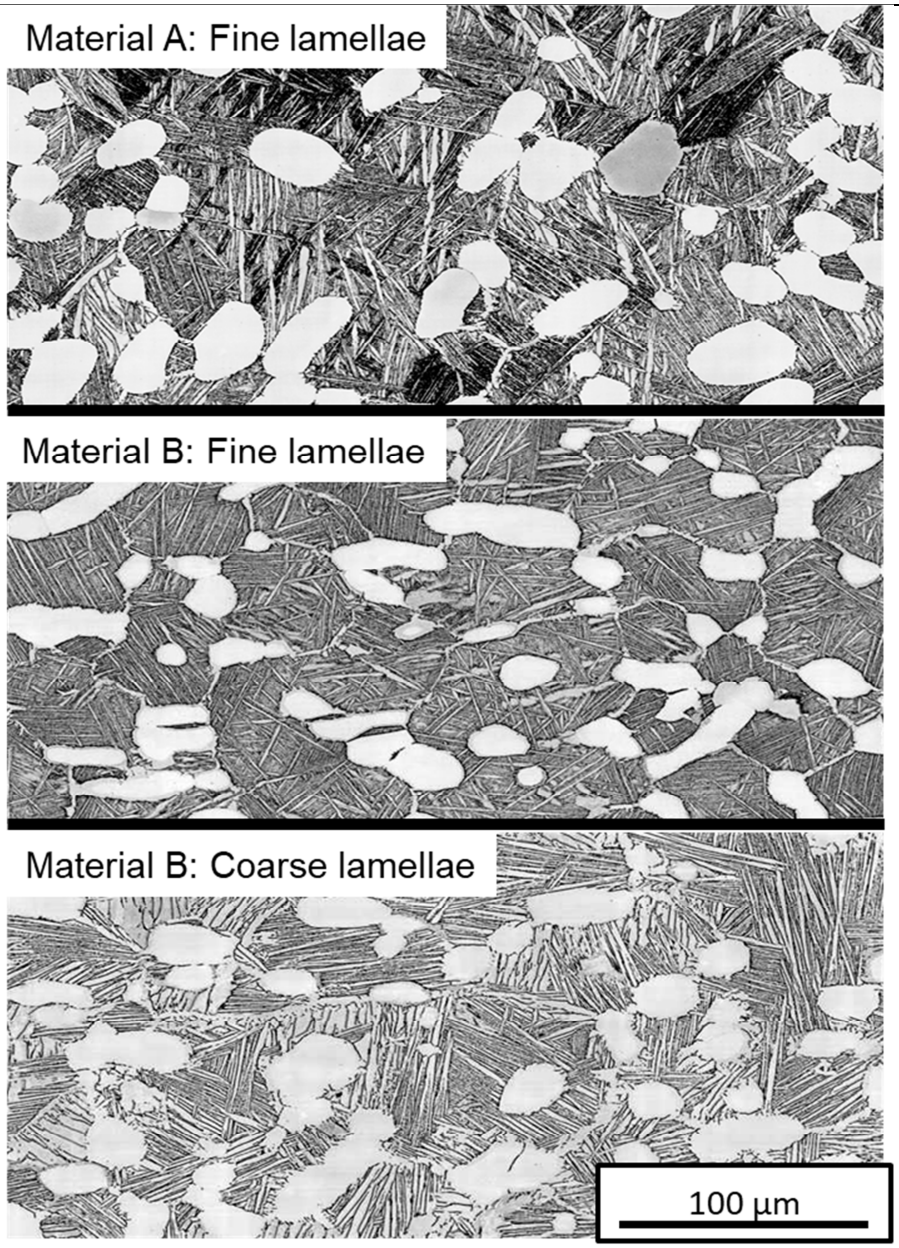

Fig. 2: Optical micrographs of etched specimens for three material conditions, showing the morphology of primary α grains and secondary α/β lamellae.

The average strain values are summarised in Table 1 and plotted in Fig.3. First, a comparison is made between material A & B with fine lamella spacing. As both materials have similar yield strength (see Table 1), the applied stresses are almost identical. At 70 and 80 % of $\sigma_{0.2\%}$ both materials are performing identically. At the first two load steps, the effective shear strain is approximately 0.2 % higher than the expected elastic strain. From the 70 to 80 % of $\sigma_{0.2\%}$ load step the strain develops parallel to the expected elastic response (Fig. 3, b). In conclusion, the increase of strain from the first to the second load step is mainly elastic and little additional plastic strain is accumulated in the samples. Going from the 80 to 90 % of $\sigma_{0.2\%}$ load step, the strain increases two times more for material A – fine lamella (increase of ~0.8 %) than for material B – fine lamella (increase of ~0.3 %). Additional analysis of the microstructure, e.g. EBSD maps of larger areas and BSE-SEM at higher spatial resolutions, are attached in the appendix of the thesis (see chapter 7.1).

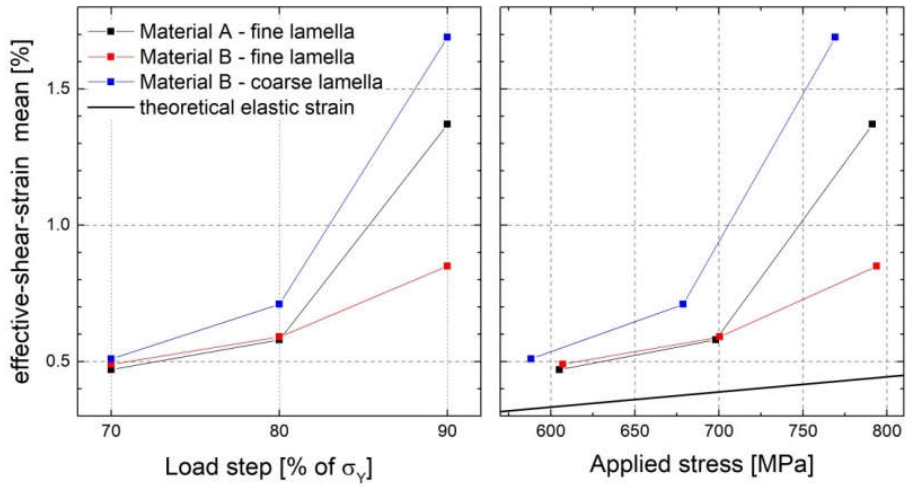

Fig. 3: The mean effective shear strain for each load step and material condition is plotted as a function of a) load step and b) applied stress. The stresses in b) refer to 65, 75 and 85 % of $\sigma_{0.2\%}$, which are the stress levels at which the strain maps have been recorded. The black line in plot b) shows the theoretical elastic response of the material.

Next samples with coarse and fine transformation product (both Material B) are compared. For the load step at 70% of $\sigma_{0.2\%}$ load step, both material conditions exhibit similar average effective shear strain. As the material with coarse secondary α lamella has a lower strength, it was tested at lower applied stresses. This can be seen by the curve of material B – coarse lamella being shifted to lower stress values when plotted as a function of stress (Fig. 3 b)). For the 80 % and 90 % of $\sigma_{0.2\%}$ load step strain increases more for the material with coarse lamella, particularly for the 90 % of $\sigma_{0.2\%}$ load step, where the strain is almost twice as high.

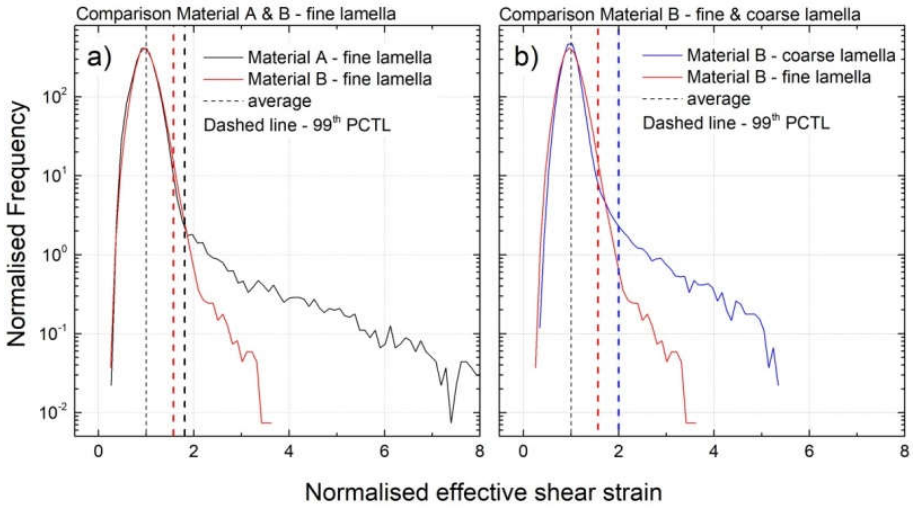

Fig. 4: Normalised frequency distribution of the effective shear strain at 70% of $\sigma_{0.2\%}$, comparing a) Material A & B with fine lamella and comparing b) coarse and fine lamella for Material A. The dashed lines show the normalised 99th PCTL for each material condition.

In Fig. 4 frequency distributions of the effective shear strain at 70% of $\sigma_{0.2\%}$ is plotted for a) material A & B fine lamella and b) fine and coarse lamella in material B. Figure 4 a) shows that for normalised shear strain values lower than 2, both curves are almost completely identical. Also, while the values of the 99th percentile of the strain distribution are close together for both materials, for values higher than 2, significant differences between both samples are revealed. For material B the highest effective shear strain values are approximately 3.5 times higher than the average value.

For material A this value is more than twice as high, with values of up to 8 times the average strain. This indicates that in material A – fine lamella the strain distribution is more heterogeneous and that slip bands with higher strain values are formed. The frequency of the strain values higher than two times the average is low; therefore these high strain values only have a small impact on the average strain.

The comparison of material B between coarse and fine lamella shows similar behaviour. However, the value below which the strain distribution looks similar is lower, at 1.5 times the average value. In this range, the distribution around the average value looks narrower for the material with coarse lamella, which indicates a more homogeneous strain distribution. However, for values above this range, the frequency is up to one order of magnitude higher for the material with coarse lamella. Also, the maximum effective shear strain values of material B – coarse lamella is around 65 % higher than for material B – fine lamella. As higher frequencies of high strain values have been observed at the same average strain, the strain distribution of the material with coarse lamella is more heterogeneous.

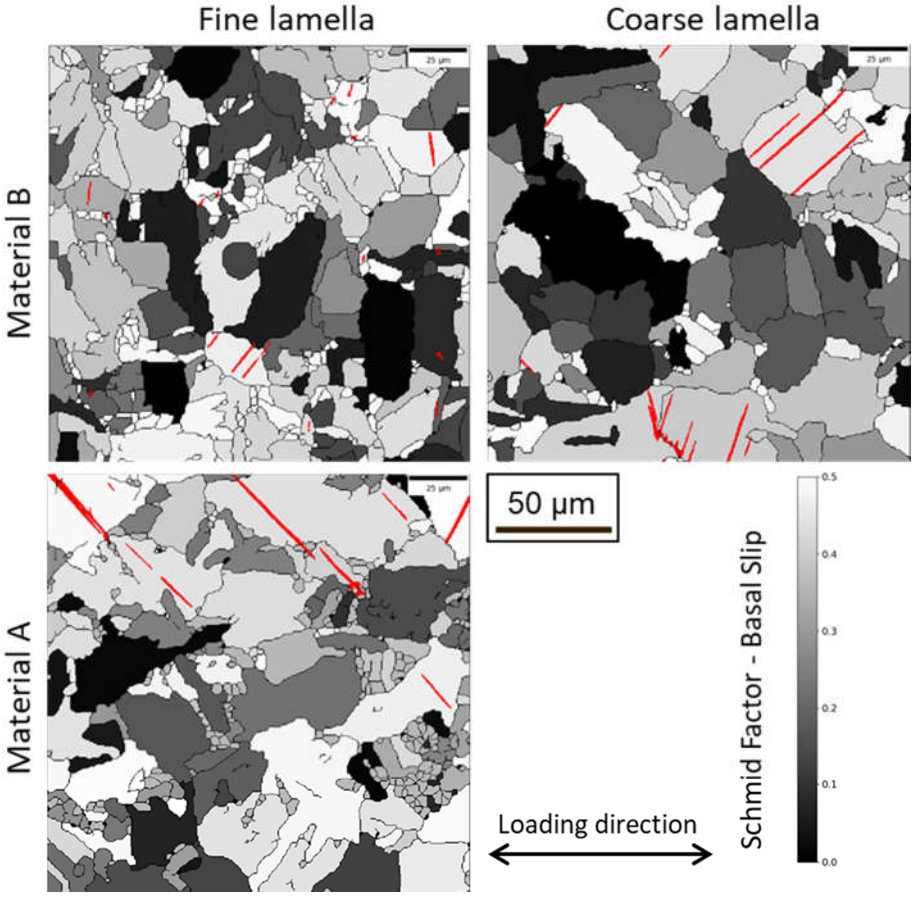

Fig. 5: The 99th PCTL of the effective shear strain is used for segmenting the strain maps of the 70% load step. The values for each material for the 99th PCTL are given in Table 2. Areas with strain values above this threshold are displayed in red. The strain data is displayed on top of Schmid-factor maps for basal slip.

Fig. 5 shows a skeleton map of average Schmid factor for basal slip overlaid with the 99th percentile of effective shear strain at 70% of $\sigma_{0.2\%}$ for all conditions. Basal slip is chosen, as it is assumed to be the slip system that is activated at the lowest stress levels [10]. For all conditions, the high strain slip bands are all in grains with a Schmid factor >0.3. This indicates the dominant active slip system is likely to be basal slip. It should be noted that without more detailed Burgers

vector analysis this is only a qualitative assessment of slip activity. The frequency distributions of the Schmid factors for basal and prismatic slip (Fig. 6) show similar distributions for both slip systems. Hence, based on the crystallographic orientations and the Schmid factors, the activation of both slip systems is equally likely. For material A – fine lamella and material B – coarse lamella, well-defined slip bands, 25 to 50 µm long can be observed. These are the two material conditions that exhibit higher strain values than material B – fine lamella; relative to their average strain values (see Fig. 5). In contrast, for material B – fine lamella the slip bands are shorter.

Table 2: Loading conditions and results of mechanical testing and HR-DIC testing. Mean value and 99th percentile (PCTL) of effective shear strain are determined for complete deformation maps.

	Transformation product	Yield stress σ_Y [%]	Load step [% of σ_Y]	Load step [MPa]	Effective shear strain [%] Mean	99th PCTL
Material A	Fine	931	70	652	0.47	0.85
			80	745	0.58	2.07
			90	838	1.37	6.33
Material B	Fine	934	70	654	0.49	0.77
			80	747	0.59	1.06
			90	841	0.85	2.89
	Coarse	905	70	634	0.51	1.02
			80	724	0.71	2.51
			90	815	1.69	7.06

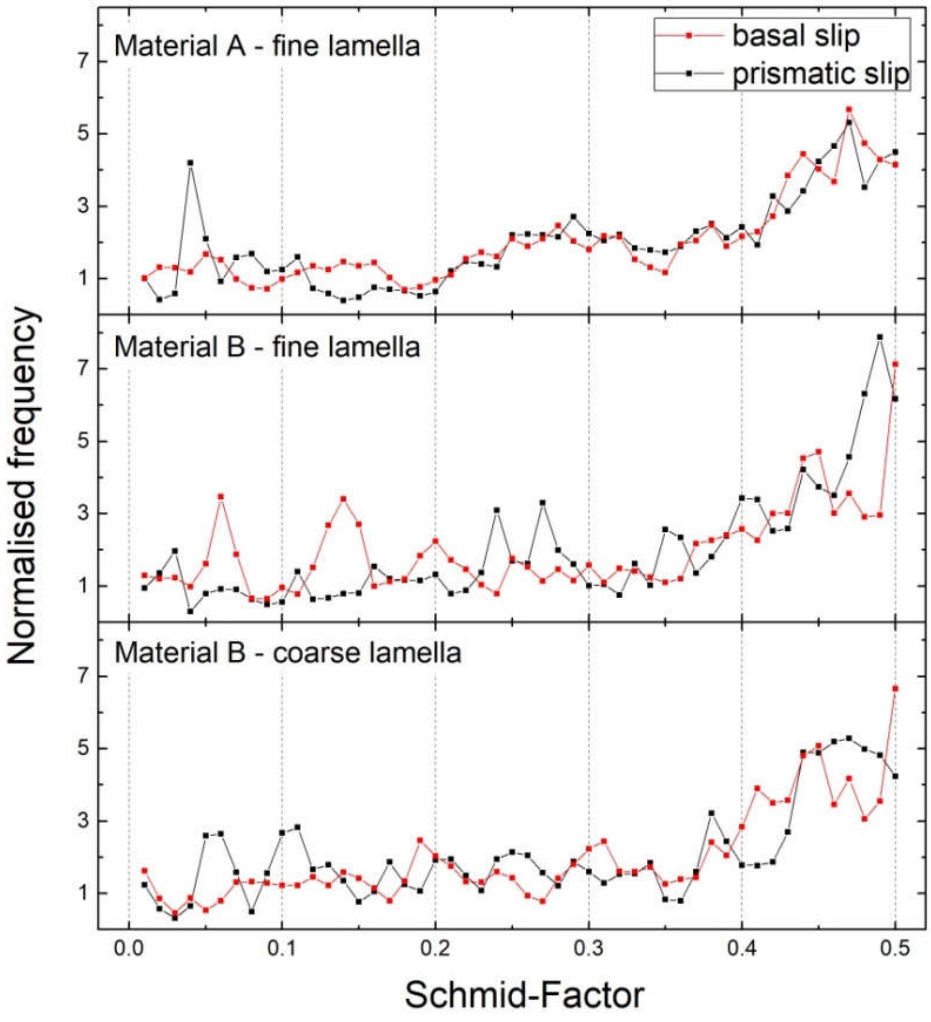

Fig. 6: Frequency distributions of Schmid factors of basal and prismatic slip.

Fig. 7 shows the effective shear strain values higher than the 99th percentile (for 70% of $\sigma_{0.2\%}$ load step) overlaid in red on top of backscattered electron images of the microstructures for both conditions for 'Material B'. The sample with the coarser transformation product exhibits high strain slip-bands in both primary α and secondary α colonies, where the slip bands in the secondary α colonies are cutting across the lamellae. Conversely, slip-bands are only observed in the primary α grains for the material with the finer transformation product.

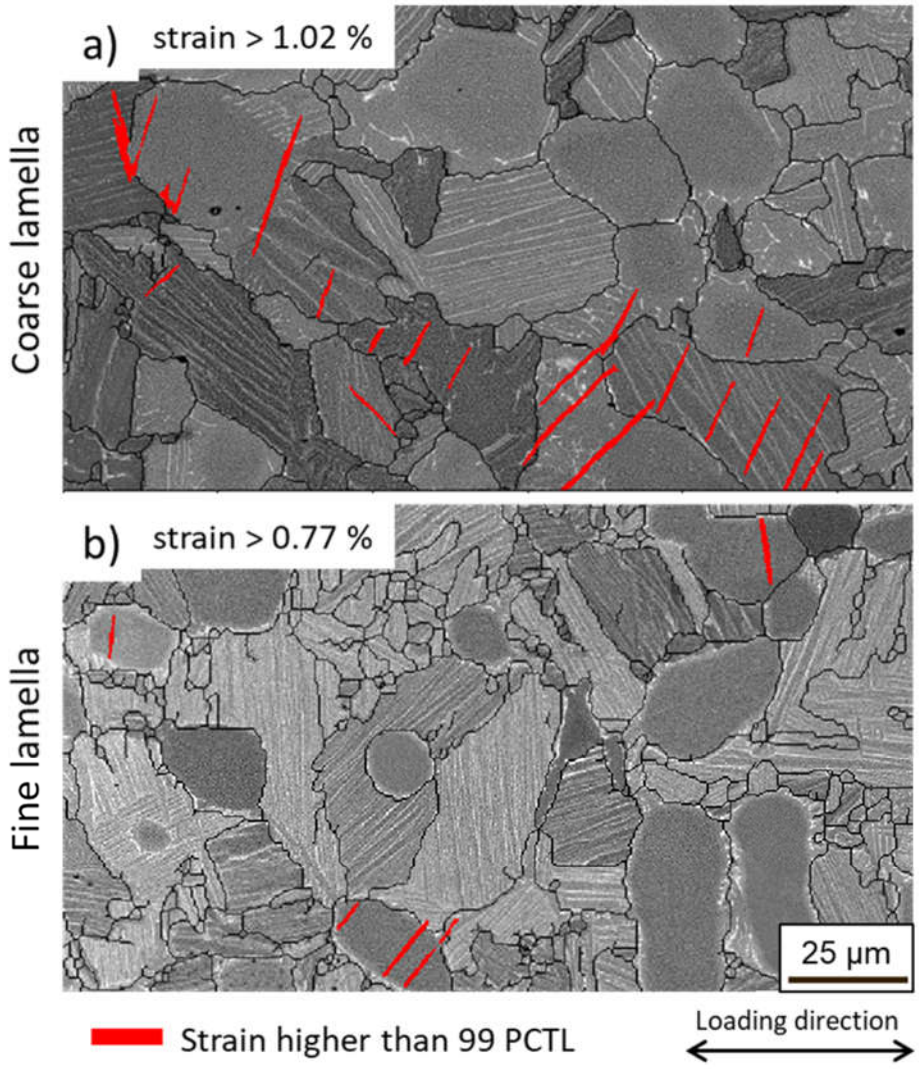

Figure 7: Areas with strain values above the 99 PCTL are displayed in red. The strain data is displayed on top of BSE-image showing the microstructure of the material condition with a) coarse and b) fine transformation product for Material B. Black lines are showing grain boundaries which were identified in the correlated crystallographic orientation maps using the 10° misorientation criterion.

4 Discussion

The morphology of the prior β-grain structure has been analysed for two materials. Material A exhibits large areas of similarly orientated β grains reaching several mm in size. In Material B the β-grains are better defined and sharper, but smaller (less than 1 mm) than the similar orientated β grain regions for material A. At low stress levels (70 and 80 % of $\sigma_{0.2\%}$) the average strain values did not reveal any difference between materials A & B. Only at a stress level of 90% of $\sigma_{0.2\%}$ Material A exhibits higher strain values than Material B. On the other hand, in material A, even at

low applied stress (70% of $\sigma_{0.2\%}$) a few events of much higher shear strain values can be found, leading to a more heterogeneous strain distribution.

When comparing material with fine and coarse transformation product, it was shown that material with coarse lamella was accumulating more plastic deformation at the same relative stress levels than material with fine lamella. Also, the strain distribution is more heterogeneous for material with coarse lamella. As the yield stress is lower for material with coarse lamella, the same relative stress levels correlate to lower applied stress.

Slip-bands can be seen in all material conditions even at 70% of $\sigma_{0.2\%}$, but the small number of slip-bands only has a small effect on the average strain. At lower strain levels, noise and measuring artefacts can influence the results, making it harder to interpret differences between samples. Therefore segmented strain maps have been displayed, which show the high strain regions and allow removing noise.

The correlation of HRDIC results with crystallographic orientation data showed that at 70 % of $\sigma_{0.2\%}$, all observed strain higher than the 99th PCTL were located in grains well aligned for basal slip. Despite this not being a confirmation of the activated slip system, the observation aligns with results in the literature that basal slip is activated at the lowest stresses. In future work, the 'relative displacement ratio' (RDR) technique will be used to unambiguously determine the activated slip system.

The difference in strength between fine and coarse β-transformation product correlates with the strain localization behaviour. For the material with coarse transformation product slip bands can be found in both phases, suggesting there is no difference in strength between primary α and transformed β. In the secondary α colonies, slip bands cut through the lamellae in the transformed β-phase. In the material with the finer transformation product, no strain above the 99th percentile has been observed in secondary α colonies. This is in agreement with the assumption that finer transformation product has a more significant strengthening effect [7]. However, these observations cannot prove that there are no slip-bands in the transformed-β phase, as the observed areas are not large enough and as strains below the 99th percentile were not considered.

The analysed samples are similar in texture on a macroscopic scale, but there are variations in local texture which, in combination with the elastic anisotropy of titanium, might have effects on local average strains and strain distributions. Therefore crystal-elasticity modelling is required to take the effects of local texture and elastic and plastic anisotropy into account.

5 Conclusions

- For all material conditions, slip bands have been observed at 70% of yield stress
- Regarding average strain values materials with different prior β-grain structure performed identically at low stress levels
- Material with small prior β-grains but large areas of preferential crystallographic orientations accumulates more plastic strain than the material with larger prior-β grains for stresses close to the yield point
- Material with large prior β-grains exhibits higher strain values and more heterogeneous strain distribution for low stresses

- At low stress level slip can be observed in primary α, as well as in transformed β-phase for material with coarse transformation product
- For material with fine transformation product, slip bands are only observed in primary α grains

Acknowledgement

The authors would like to thank the EPSRC funding the project through the CDT in Advanced Metallic Systems. The authors would also like to thank Rolls-Royce plc and TIMET for providing additional funding and the provision of material.

References

[1] S. Suri, G. B. Viswanathan, T. Neeraj, D.-H. Hou, and M. J. Mills, Acta Mater., vol. 47, no. 3, pp. 1019–1034, 1999.

[2] S. Suri, T. Neeraj, G. S. Daehn, D.-H. Hou, J. M. Scott, R. W. Hayes, and M. J. Mills, Mater. Sci. Eng. A, vol. 234–236, pp. 996–999, Aug. 1997.

[3] M. A. Imam and C. M. Gilmore, Metall. Trans. A, vol. 10, no. 4, pp. 419–425, 1979.

[4] B. C. Odegard and A. W. Thompson, Metall. Trans., vol. 5, no. 5, pp. 1207–1213, 1974.

[5] W. H. Miller, R. T. Chen, and E. A. Starke, Metall. Trans. A, vol. 18, no. 8, pp. 1451–1468, 1987.

[6] S. Ankem and H. Margolin, Metall. Trans. A, vol. 17, no. 12, pp. 2209–2226, 1986.

[7] G. Lütjering and J. C. Williams, Ed. Springer, vol. second edi, pp. 1–442, 2007.

[8] D. Qiu, R. Shi, D. Zhang, W. Lu, and Y. Wang, Acta Mater., vol. 88, pp. 218–231, 2015.

[9] D. He, J. Zhu, S. Zaefferer, and D. Raabe, Mater. Des., vol. 56, pp. 937–942, Apr. 2014.

[10] F. Bridier, P. Villechaise, and J. Mendez, Acta Mater., vol. 53, no. 3, pp. 555–567, 2005.

[11] S. Hémery and P. Villechaise, Mater. Sci. Eng. A, vol. 697, pp. 177–183, Jun. 2017.

[12] S. Hémery, V. T. Dang, L. Signor, and P. Villechaise, Metall. Mater. Trans. A, vol. 49, no. 6, pp. 2048–2056, Jun. 2018.

[13] M. P. Echlin, J. C. Stinville, V. M. Miller, W. C. Lenthe, and T. M. Pollock, Acta Mater., vol. 114, pp. 164–175, Aug. 2016.

[14] K. V. S. a I. Srinadh, N. Singh, and V. Singh, Bull. Mater. Sci., vol. 30, no. 6, pp. 595–600, 2007.

[15] A. Radecka, J. Coakley, V. A. Vorontsov, T. L. Martin, P. A. J. Bagot, M. P. Moody, D. Rugg, and D. Dye, Scr. Mater., vol. 117, pp. 81–85, 2016.

[16] P. S. Davies, The University of Sheffield, 2009.

[17] ASTM Int., Astm, no. C, pp. 1–27, 2009.

[18] F. Di Gioacchino and J. Quinta da Fonseca, Exp. Mech., vol. 53, no. 5, pp. 743–754, 2013.

[19] P. Tomancak, S. Preibisch, and S. Saalfeld, Bioinformatics, vol. 25, no. 11, pp. 1463–1465, 2009.

[20] J. Schindelin, I. Arganda-Carreras, E. Frise, V. Kaynig, M. Longair, T. Pietzsch, S. Preibisch, C. Rueden, S. Saalfeld, B. Schmid, J.-Y. Tinevez, D. J. White, V. Hartenstein, K. Eliceiri, P. Tomancak, and A. Cardona, Nat. Methods, vol. 9, p. 676, Jun. 2012.

[21] T. Goswami, Int. J. Fatigue, vol. 21, no. 1, pp. 55–76, 1999.

[22] O. N. Senkov, J. J. Valencia, S. V Senkova, M. Cavusoglu, and F. H. Froes, Mater. Sci. Technol., vol. 18, no. 12, pp. 1471–1478, 2002.

4.3 Paper 3 - Investigation of slip activity during initial cold creep deformation in a near-α titanium alloy

Claudius Dichtl[1*], David Lunt[1], Michael Atkinson[1], Rhys Thomas[1], Adam Plowman[1], Bartosz Barzdajn[1], Rebecca Sandala[2], João Quinta da Fonseca[1], Michael Preuss[1,3]

[1] University of Manchester, Department of Materials, Manchester, M13 9PL, UK

[2] Rolls-Royce plc, Derby, DE24 8BJ, UK

[3] Monash University, Department of Materials Science and Engineering, Clayton, Vic-3800, Australia

* Corresponding author:

E-mail address: c.dichtl@outlook.com

The manuscript is being prepared for submission to the journal 'Acta Materialia'.

Keywords: High Resolution Digital Image Correlation (HRDIC), Plasticity, Slip, Slip Systems, HCP, Titanium alloys, Room Temperature Creep, Crystal Plasticity Modelling

Highlights of this paper:

For alloys with bimodal microstructure, susceptibility to cold creep increases with a coarser transformation product. This is accompanied by increased slip localisation.

HRDIC analysis shows that the dominant slip mode is basal during cold creep deformation at 70% of the 0.2% proof stress in the near-α titanium alloys TIMETAL®834.

Correlation of HRDIC/EBSD analysis and CP-modelling provides new insight in the role of elastic anisotropy on of possible basal slip activation during initial loading.

Contributions

For **Manuscript 3** titled '**Investigation of slip activity during initial cold creep deformation in a near-α titanium alloy**', Claudius Dichtl, Michael Preuss and João Quinta da Fonseca designed the study. Claudius Dichtl performed the experiments and prepared the manuscript. David Lunt supported sample preparation and data processing. Michael Atkinson supported the in-situ HRDIC experiment and together with Rhys Thomas and David Lunt contributed to the data analysis. Michael Atkinson, Bartosz Barzdajn and Adam Plowman contributed to running the crystal plasticity models. All authors contributed to writing and editing the manuscript.

Abstract

Near-α titanium alloys are known to be susceptible to cold dwell fatigue (CDF), a failure mechanism that has been linked to cold creep during high-load dwell times superimposed onto low cycle fatigue loading. To shed new light on the mechanisms and to understand better the role of the microstructure, two different bimodal microstructures (fine and coarse transformation product) of TIMETAL®834 were investigated at stress levels below the 0.2% proof stress using a combination of grain orientation mapping and in-situ electron microscopy imaging. This enabled in-depth analysis of 2D slip patterns and slip system activity using High-Resolution Digital Image Correlation (HRDIC), showing that in both microstructures basal slip is initially the dominant slip mode before prismatic slip activity increases approaching the 0.2% proof stress. Comparing the two constituents in the bimodal microstructure, first slip bands are localised predominantly in primary α grains, indicating higher strength of colonies, particularly for finer transformation products. During 10-minute load holds at stresses below 0.2% proof stress, more plastic strain and longer connected slip traces across several grains were observed in the sample with coarse transformation product, indicating higher susceptibility to cold creep deformation.

Crystal plasticity modelling was utilised to determine local stresses in individual grains at the onset of plasticity and test the hypothesis that the dominance of basal slip at low stress levels is caused by the elastic anisotropy in Ti alloys. However, while consideration of elastic anisotropy increased resolved shear stress (RSS) values for basal slip relative to prismatic slip, it did not unambiguously explain the early activation of basal slip. Furthermore, thermal residual stresses at the crystal level due to the anisotropy of coefficients of thermal expansion (CTE) were included in the simulation, which created a wider spread of the RSS data but did not preferentially promote high RSS values for grains well aligned for basal slip. In the absence of an unambiguous conclusion, it is hypothesised that basal slip might display lower critical resolved shear stress values than typically reported but high work hardening rates compared to prismatic slip.

1 Introduction

TIMETAL®834 (Ti-5.8Al-4Sn-3.5Zr-0.7Nb-0.5Mo-0.35Si-0.06C) is a near-α titanium-alloy developed for applications at elevated temperatures of up to 600°C, particularly for rotative-parts in aero-engine compressors [1]–[3]. Superior high temperature creep properties are achieved by using Nb and Mo as β-stabilisers instead of V, as e.g. in Ti-6Al-4V, as well as the addition of 0.35wt.% Si and 4wt.% Sn, while strength is increased by the formation of T3Al (α_2) and silicide precipitates [3]–[9]. Typically, the best combination of high strength, creep and fatigue properties are achieved for bimodal microstructures with primary α volume fractions of ~ 15-20% [7], [10], [11].

In near-α and α+β titanium alloys, including TIMETAL®834, creep deformation occurs readily at room temperature and stresses below the macroscopic yield point, often referred to as cold creep [12]–[18]. It is of interest to understand the mechanisms of cold creep deformation and the correlation to the underlying microstructure, as cold creep deformation can contribute to a reduction in cycles to failure (dwell-debit) for cold dwell fatigue (CDF) loading conditions [19]. CDF is cyclic loading with an additional load-hold applied at or close to the maximum applied stress [20], [21], where a load-hold of 120 s is sufficient to lead to dwell-debits of up to a factor 18 [22]. It has been demonstrated that the susceptibility of cold creep [13], [15], [18] and CDF [23], [24] does rise with increasing primary α grain or colony size, respectively coarser microstructures. To improve the mechanistic understanding of these loading conditions, it is important to investigate the activation of slip during the first load cycle and deformation during the load-hold, which has a detrimental effect on material performance.

In previous work on α+β titanium alloys (Ti-6Al-4V, Ti-6242, Ti-6246), slip activation at stress levels below the macroscopic yield point has been observed, with basal slip being the dominant slip mode during the initial slip activation [25]–[30]. The reason for the early activation of basal slip, despite prismatic slip being typically considered as at least as easy to activate as basal slip, has been much debated. Possible explanations put forward include the idea of microtextured regions forming stress hotspots [26], stress heterogeneity due to elastic anisotropy and grain interactions [31] and some authors have also suggested that basal slip does exhibit lower critical resolved shear stress (CRSS) values than prismatic slip [28], [29], [31]. It is interesting to note that the reported CRSS values for basal and prismatic slip in Ti-alloys do indeed cover a wide range and that in some studies basal slip is said to be harder, i.e. CRSS(Ba)>CRSS(Pr) [30], [32]–[38] and in others easier i.e. CRSS(Ba)<CRSS(Pr) [28], [29], [31], [39]–[42]. These discrepancies in CRSS are attributed to many factors including variations in chemical composition, in particular Al-concentration [33], [34], [43], α_2-precipitates [41], lamellae spacing and orientation [32], [35], [44] and grain size [43], [45]. Therefore, CRSS values can only be directly compared for alloys with similar compositions and microstructures. Reported CRSS values also depend on the method used for determining them. Micro-pillar or micro-cantilever testing has been increasingly utilised to determine CRSS values [36], [37], [46], but these values are typically lower than when determining such values in bulk material, as hardening mechanisms and constraints by neighbouring grains are not considered [47]. In-situ slip trace observation can be used to determine the macroscopic stress at which the first local slip activity is observed and a correlation to crystallographic orientation data enables the identification of the activated slip system [30], [34], [41]–[43]. A study combining this approach with

crystal plasticity (CP)-modelling to determine local RSS values reported that CRSS values are lower for basal (338 MPa) than for prismatic (352 MPa) slip in Ti-6Al-4V [29].

As mentioned earlier, the elastic anisotropy of the α phase in titanium alloys is also likely to influence the activation of slip systems due to a 50% stiffer elastic response along the c-axis compared to loading perpendicular to it [31], [48]. Therefore, at the same applied strain, the axial stresses will be highest in grains with their c-axis parallel or showing only a small declination angle from the loading direction. Since a slight increase of the angle between the c-axis and the loading direction still results in high stiffness and hence stresses [40] but also a rapid increase in Schmid factor for basal slip, the elastic anisotropy is a plausible explanation for the dominance of basal slip during the onset of plasticity. Thermal residual stresses, which develop during cooling from heat treatments as a result of anisotropic thermal expansion, may be a further factor influencing early plastic deformation and activation of specific slip systems [49], [50].

In the present study, we investigate slip activation during 10-minute load-hold experiments at three stress levels below the 0.2% proof stress, evaluating the cold creep behaviour of two bimodal microstructures: one with coarse and one with fine transformation product. Whilst previous work has shown that basal slip is the dominant slip system during initial plastic deformation, it is not clear if the same behaviour can be expected for cold creep deformation. In addition, there is no current understanding of the strain distribution in the microstructure under such conditions and its evolution with increasing stress level. The different microstructures and constituents are also evaluated in respect of their susceptibility to cold creep deformation.

To address these questions SEM-based high-resolution digital image correlation (HRDIC) in combination with crystallographic orientation mapping is used to accurately determine slip activity during creep deformation across many grains, whilst also allowing the slip mode to be quantified for both the primary α and secondary α constituents [51]. CP-modelling is used to quantify the impact of elastic anisotropy and thermal residual stresses on the resolved shear stresses of individual grains during elastic loading, to accept or reject proposed mechanisms for early basal slip.

2 Experimental

2.1 Sample preparation

The near-α titanium alloy TIMETAL®834, used in the present work, was supplied by TIMET, UK. A bimodal microstructure with a primary α volume fraction of around 15% was produced by solution heat treating two blocks of material for two hours at 1015 °C, i.e. about 30 °C below the β transus temperature [52]. Subsequently, one of the blocks was cooled rapidly by oil quenching (10 – 30 K/s), leading to a fine transformation product. The other block was furnace cooled to room temperature at a rate of 1 K/s, resulting in a coarser transformation product. Subsequently, both blocks were annealed for two hours at 700 °C, which is known to lead to the precipitation of Ti3Al (α_2), predominantly in the primary α grains [7], [8].

Flat dog-bone specimens, with a gauge volume of 1 x 3 x 26 mm3 (t x w x l) were electrical discharge machined for uniaxial tensile testing. Subsequently, both sides of all samples were ground to #800 grit paper to remove deep scratches and oxides formed during machining. The samples were further ground followed by hand polishing in water-based colloidal silica solution (4:1) for 10 mins to mirror finish. To reveal the microstructure by optical microscopy, polished

samples were etched with Kroll's reagent (2 ml HF, 4 ml HNO3, 94 ml H2O). For mapping strain patterns by high-resolution digital image correlation (HRDIC), a gold speckle pattern was applied to the polished surface using the gold remodelling technique [9], [53]–[55]. To produce the speckle pattern, a thin film of gold was deposited onto the sample surface, at a current of 40 mA and pressure of 0.5 mbar for 5 minutes, using an Edwards S150B sputter coater. The film was then remodelled in a water-vapour environment at 275 °C for four hours [53], [55], producing isolated speckles, of which 99% have a diameter in the range of 28 to 150 nm.

2.2 Baseline characterisation

For each material condition, an area of 2 mm² was characterised by means of optical bright-field microscopy. Segmentation of the primary α constituent was performed, using the image analysis software 'Fiji' [56], based on the differences in grey-scale values between the two constituents. The 'characterise particles' function was chosen to determine the average size and volume fraction of primary α grains. The spacing of secondary α lamellae was calculated utilising the line intercept method for 30 secondary α colonies.

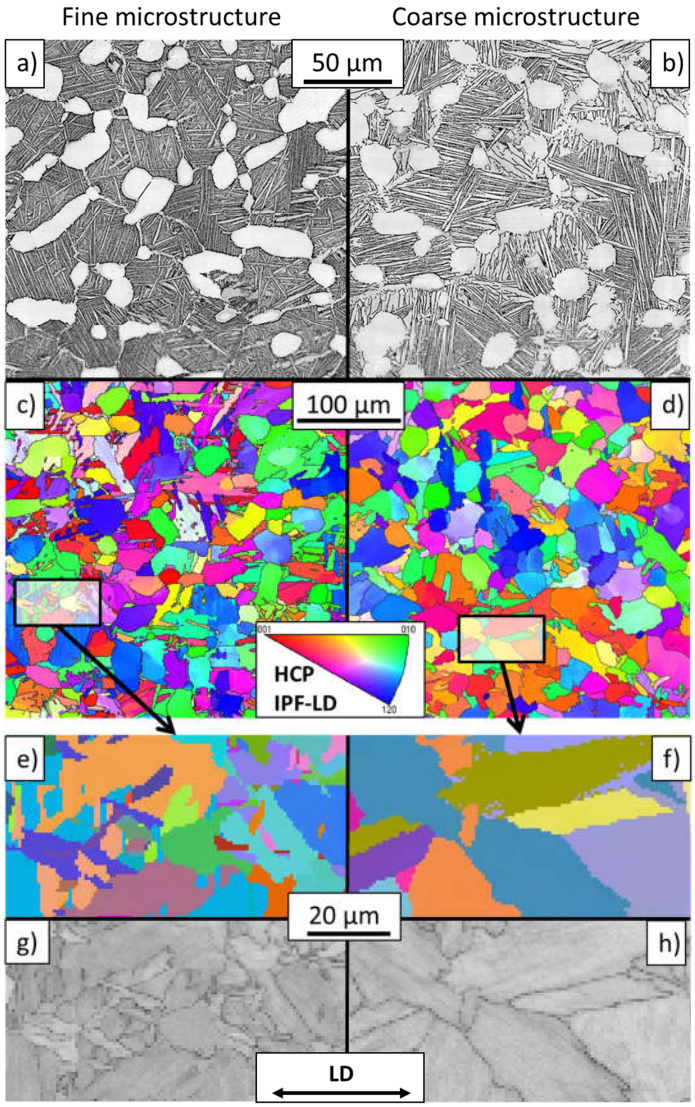

Fig. 1: (**a** & **b**) Optical micrographs of the microstructure and (**c** & **d**) crystallographic orientation maps for material with (**a** & **c**) fine and (**b** & **d**) coarse microstructure. (**e - f**) Area containing transformed β phase at higher magnification, displayed with (**e** & **f**) Euler colours and (**g** & **h**) band contrast.

Crystallographic orientation mapping was performed by means of Electron Back Scattered Diffraction (EBSD) in an 'FEI Quanta 650' field emission gun scanning electron microscope (FEG-SEM) equipped with Oxford Instruments HKLNordlys EBSD detector at an acceleration voltage of 20 kV. An area of 250 x 250 µm2 was analysed with a step size of 1 µm, which coincided with the area analysed later by HRDIC but at approximately twice the interrogation window size. A misorientation of 10° was chosen for grain boundary definition. Grains smaller than 10 µm² were not considered in any subsequent analysis.

Table 1: Lamella spacing, primary α volume fraction and the average size of primary α grains of the complete sample determined by optical microscopy. The number and size of primary α grains and secondary α colonies in the DIC area is based on crystallographic orientation mapping

		Fine microstructure	Coarse microstructure
Grain size analysis using optical microscopy			
Lamella spacing		1.1 ± 0.3 µm	1.8 ± 0.4 µm
Volume fraction of α(P)		18.2 ± 0.7 %	23.1 ± 0.3 %
Average grain size of α(P)	area	379 ± 18 µm²	469 ± 11 µm²
	diameter *	22 ± 1 µm	25 ± 1 µm
Summary of grain statistics in DIC area			
total number of grains		298	175
average grain size		199 µm²	309 µm²
number of α(P) grains		25	21
number of α(S) colonies		235	128

α(P) → primary α
α(s) → secondary α
* assuming spherical grains

Stress-strain curves were recorded for uniaxial tensile tests to determine the 0.2% proof stress ($\sigma_{0.2\%}$) for both material conditions employing an 'Instron 5569' electromechanical tester with a 25 kN load cell at a constant strain rate of 0.005 1/s [57]. Strain was recorded using an axial extensometer with a gauge length of 10 mm.

Table 2: Summary of results of the mechanical baseline characterisation, the applied load steps in the HRDIC experiment, as well as the mean values and 99th percentiles of the effective shear strain determined by HRDIC. The elastic strain response has been calculated based on the applied stress in each load step and Young's modulus of the bulk material.

Microstructure	Yield stress σ_Y [MPa]	Young's modulus [GPa]	Load step [% of σ_Y]	Load [MPa]	Elastic strain [%]	Effective shear strain Mean [%]	Effective shear strain 99th PCTL [%]
Fine	934	117.2 ± 2.3	70	654	0.5	0.4	0.9
			80	747	0.6	0.5	1.2
			90	841	0.7	0.8	3.1
Coarse	905	117.2 ± 2.3	70	634	0.5	0.5	1.0
			80	724	0.6	0.7	2.6
			90	815	0.7	1.6	8.3

2.3 HRDIC – experimental

In-situ loading experiments were performed using a ‘Deben’ 5 kN tensile stage placed inside an ‘FEI Quanta 650’ FEG-SEM. This setup enables imaging specimens at load, avoiding possible strain reversal during unloading and any possible issues with enhanced accumulation of plastic deformation due to repeated loading and unloading [58]. Hence, this procedure was used to record images of the gold patterned sample surface during a series of deformation steps to monitor the strain evolution during a single loading process. As two material conditions with different yield strengths were compared, the load steps were defined as the relative values of 70, 80 and 90% of $\sigma_{0.2\%}$ (Table 2). For each load step, a stress hold of 10 minutes was applied. Afterwards, the stress was reduced by 5%, e.g. from 70 to 65% of $\sigma_{0.2\%}$ to avoid further plastic deformation during the imaging step, which took around 1.5 hours (Fig. 1).

Images for the HRDIC analysis were recorded at an acceleration voltage of 10 kV with a scan speed of 5 µs/pixel and 2 times frame averaging to reduce drift compared to a scan speed of 10 µs/pixel and charging issues [59], [60]. A ‘Deben Centaurus’ photomultiplier detector PMD was utilised as it can be manoeuvred in-between the grips of the micro-tester, allowing for a relatively low working distance of 11.7 mm. The imaged area of 250 x 250 µm² for HRDIC analysis was covered by recording 12 x 12 images (each frame being ~ 30 x 27 µm², 2048 x 1832 pixels) with an overlap of 20%, which were then stitched together before processing using the ‘Grid/Collection stitching’ plug-in in ‘Fiji’ [56], [61].

2.4 HRDIC – data analysis

The displacement maps for each deformation step are computed by using LaVision’s DIC software package DaVis version 8.4.0 [62]. The image of each load step is correlated directly to the undeformed sample, using an interrogation window size of 32 x 32 pixels. This window size represents a good trade-off between high spatial resolution (468 nm) and low noise [63] but provides a lower spatial resolution than typically achieved during ex-situ experiments (147 nm [9]) while the error and noise are comparable.

Calculation of strain tensors by differentiation of the in-plane displacements determined by the DIC software and subsequent data analysis was performed using in-house Python routines [64] and the NumPy numerical library [65]. The deformation maps contain three components, which are the in-plane shear strain (εxy), and the strain parallel (εxx) and perpendicular (εyy) to the loading direction. For the data analysis, we used the effective shear strain (γeff) defined by equation (1), as it takes all in-plane shear components into account [53], [66].

$$\gamma_{eff} = \sqrt{\left(\frac{\varepsilon_{xx}-\varepsilon_{yy}}{2}\right)^2 \quad \varepsilon_{xy}^2} \tag{1}$$

Image correlation of two images of the undeformed sample was used to determine the systematic error of the HRDIC analysis. Between the two image acquisitions, the set-up process of the SEM was repeated without removing the sample from the microscope, as this is also not necessary during the in-situ experiment. The strain uncertainty was calculated to be approximately 0.15% for each measurement point of effective shear strain.

BSE-SEM images of the undeformed samples of the HRDIC analysis, which are inherently perfectly aligned with the deformation maps, were used to generate separate strain maps for primary and secondary α constituents. A binary image of the constituents was created by selecting all primary α grains in the BSE-SEM images, using the 'Freehand selection'-tool in 'Fiji' [56], which was then used to mask out either of the two constituents in the effective shear strain maps (Fig. 6, (e-h)) and to calculate the average values, as well as the 99.5th percentiles (Fig. 6, (a-d)).

This approach was also used to determine the constituent of each grain identified in the crystallographic orientation maps. In some cases, a primary α grain and an adjacent secondary α colony were found to have the same crystallographic orientation and therefore appeared as one grain in the orientation map. These grains were disregarded in further analysis (e.g. Fig. 5, (c & d)). Therefore, the sum of primary α grains and secondary α colonies is lower than the total number of grains in Table. 1.

Active slip systems were determined using Slip Trace Analysis (STA) technique [63], [67], [68]. Initially, the orientation of a slip trace in the deformation maps is determined by fitting a line to it, which is then correlated to the directions of all possible slip systems based on the crystallographic orientation of the grain. The acceptance criterion for a possible slip system was <5° for the angle between the experimental and theoretical slip trace. Slip lines that did not match with any of the possible solutions were labelled as 'no match' (Fig. 5, (a & b)). Different slip systems may exhibit the same slip lines at the sample surface, resulting in 'ambiguous' solutions' [51], in which case all possible solutions were reported. In these cases, relative displacement ratio (RDR) analysis can be used to determine the Burger's vector direction associated with the slip line [68], [69]. If the Burger's vector matches with only one of the possible slip systems, an unambiguous solution can be reported. In Fig. 5 the fractions of grains, weighted by grain size, in which a certain slip system was identified were calculated. First and second order pyramidal slip, both <a> and <c+a> type slip, were summarised as 'pyramidal slip'.

2.5 Crystal plasticity modelling

Crystal plasticity (CP) modelling was used to determine local stresses in the microstructures analysed by HRDIC. As the focus of this work was on the elastic regime leading to the onset of plasticity, simulations were run for low stress levels (1% of $\sigma_{0.2\%}$) avoiding any plastic deformation and stress redistributions. Assuming that in the elastic regime all local stresses scale linearly with the macroscopic stress, the out-puts were then scaled to the stress applied at the first load step in the HRDIC experiment to enable direct comparison between experimental and modelling results. It should be kept in mind that the determined stress values can only be used for the discussion of initial slip activation, as further plastic deformation would lead to stress redistributions, which haven't been considered in our simulations. The CP-simulations were carried out on the Düsseldorf Advanced Material Simulation Kit (DAMASK) version 2.0.2 [70], which is based on the rate-dependent constitutive law in equation (2) [71], [72]. The used CP-frame work is capable of simulating elastic, as well as plastic deformation. However, in this study simulations were run at such low stress levels, so that the material response was purely elastic. Despite not being used for the simulations of elastic strains/stresses, the constitutive law used in DAMASK is shown for the sake of completeness in equation (2).

$$\dot{\gamma}^{\alpha} = \dot{\gamma}_0 sgn\left(\frac{\tau^{\alpha}}{g^{\alpha}}\right)\left|\frac{\tau^{\alpha}}{g^{\alpha}}\right|^{\frac{1}{m}} \quad (2)$$

The resolved shear rate $\dot{\gamma}^{\alpha}$ is defined as a function of the ratio of the resolved shear stress τ^{α} and the slip resistance g^{α} (CRSS), where $\dot{\gamma}_0$ is a reference shear rate and m is the strain rate sensitivity.

DAMASK utilises a Fast Fourier Transform (FFT) based approach to solving for mechanical equilibrium, which enables the direct input of the crystallographic orientation maps to define the simulation microstructure. As TIMETAL®834 has a low β volume fraction, only α phase was included in the simulation and secondary α colonies were treated as single α grains [73].

A 2.5D or quasi 3D microstructure [29], [74] was created by extruding crystallographic orientation maps parallel to the plane normal. The crystallographic orientation maps were taken from the HRDIC areas, but the number of pixels was reduced by a factor of 2 from 520x520 to 260x260 pixels, to accelerate simulations and post-processing. As both the HRDIC experiment and the CP-simulations are linked to the same crystallographic orientation maps, it is trivial to link the datasets for post-processing and data analysis. The thickness of the extruded layer was 38 voxels (~36 µm), which is similar to the average grain diameter [74]. On top of the surface, a 'buffer' layer with a thickness of 5 voxels was added, which has a stiffness value that is around 3 orders of magnitude lower than the stiffness of titanium (Table A 1), representing the free sample surface in the HRDIC experiment [75]. On the other 5 sides, a 'buffer' layer of 5 voxels was added with isotropic properties and the same average stiffness as CP-titanium to produce the conditions of non-periodic material regions [76], [77]. Except for the buffer layers, the properties of commercially pure CP-titanium were assigned to all grains (Table A 1). The elastic properties and anisotropy are assumed to be similar for CP-titanium and TIMETAL®834.

The CP-simulation determined the full stress tensor at each point in the analysed area. In combination with the crystallographic orientations, resolved shear stress (RSS) values can be calculated for each slip system. Three calculation methods (equation (3)-(5)) were used to determine RSS values and the differences between them were evaluated. For the first method, the local stresses were assumed to be homogeneous throughout the sample and equal to the macroscopic stress. RSS values were calculated by multiplying the applied stress (σ_{xx}(applied)) with the Schmid factor (SF) values of each grain (equation (1)).

$$RSS = SF \times \sigma_{xx}(applied) \quad (3)$$

For the second method, local stresses in the loading direction (σ_{xx}(local)) were multiplied with the Schmid factor (SF) of the grain, accounting for the effect of elastic anisotropy on local stresses.

$$RSS = SF \times \sigma_{xx}(local) \quad (4)$$

The third method used the full stress tensor for the calculation of RSS values, also taking into account stress components perpendicular to the loading directions and shear stresses. RSS values were determined by calculating the dot product of the slip direction ($\bar{b}$), the full stress tensor ($\bar{\bar{\sigma}}$) and the slip plane normal ($\bar{n}$) (equation 5).

$$RSS = \overline{b} \cdot \bar{\bar{\sigma}} \cdot \overline{n} = b_1 n_1 \sigma_{11} + b_1 n_2 \sigma_{12} + \quad + b_3 n_3 \sigma_{33} \tag{5}$$

$$\overline{b} = \begin{pmatrix} b_1 \\ b_2 \\ b_2 \end{pmatrix} \quad \overline{n} = \begin{pmatrix} n_1 \\ n_2 \\ n_3 \end{pmatrix} \quad \bar{\bar{\sigma}} = \begin{pmatrix} \sigma_{11} & \sigma_{12} & \sigma_{13} \\ \sigma_{21} & \sigma_{22} & \sigma_{23} \\ \sigma_{31} & \sigma_{32} & \sigma_{33} \end{pmatrix}$$

Some initial work also explored the consideration of thermal residual stresses present in the material at room temperature by setting the material to be stress-free at a temperature of 800 K, instantly cool to room temperature (300 K, ΔT = 500 K) and solve the stress state in the material so that the average macroscopic stresses were equal to zero. While we used thermal expansion coefficients published by Pawar et al. [50] it should be pointed out that there is no consensus on its magnitude or direction [49], [50], [78]–[80].

3 Results

3.1 Baseline characterisation

For the material condition with a ‘coarse microstructure’, size and volume fraction of the primary α grains was around 25% higher than for the ‘fine microstructure’ (Fig. 1 (a & b, Table 1)) due to the slow cooling rate allowing some further growth of the primary α. The reduced cooling rate also led to an average lamellae spacing of 1.8 µm, compared to 1.1 µm for the faster cooling rate and also to wider secondary α colonies. The ‘coarse microstructure’ displayed mainly colonies within the transformed β phase regions, whereas the ‘fine microstructure’ exhibited a mixture of well-defined colonies as well as areas with a fine, basketweave type, structure and more crystallographic variants (Fig. 1 (e-h)).

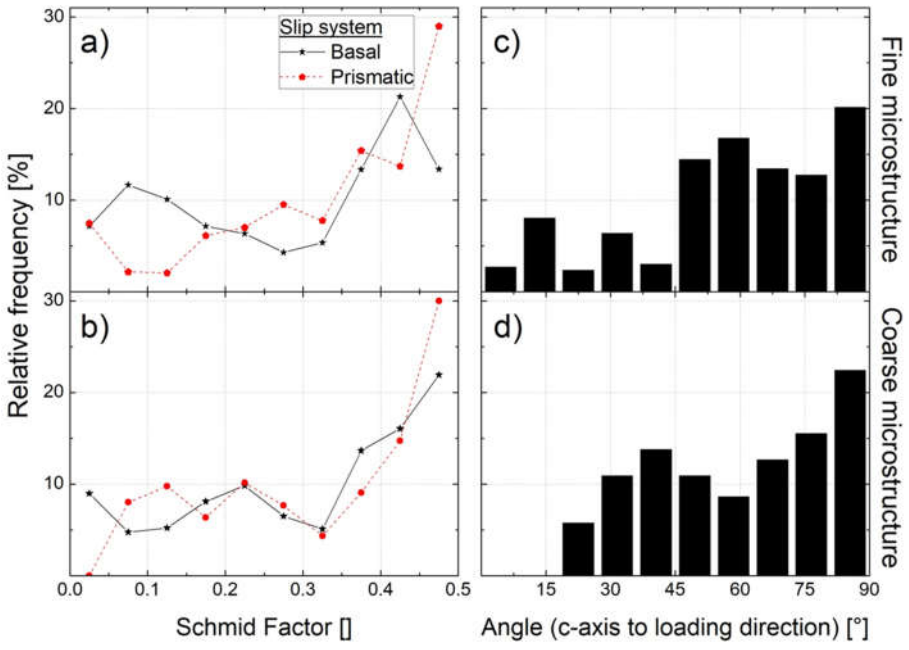

Fig. 2: Relative frequency distribution of (**a** & **b**) Schmid factors for basal (black) and prismatic (red) slip, and (**c** & **d**) angles between c-axis and loading direction for all grains in the HRDIC area.

In the presence of several possible slip modes, the local texture of a material greatly influences slip mode activity. While Schmid factor calculations can only be an approximation in a polycrystalline aggregate, due to the uncertainty in principle stress direction, the Schmid factor distributions shown in Fig. 2 still provide some indications in terms of how comparable the two microstructures are regarding local textures and which <a> type slip might be more likely. For both microstructures, the

frequencies of Schmid factors larger than 0.45 is higher for prismatic than for basal slip (Fig. 2 (a & b)) suggesting preferential activation of prismatic slip in both cases assuming similar CRSS for both slip systems.

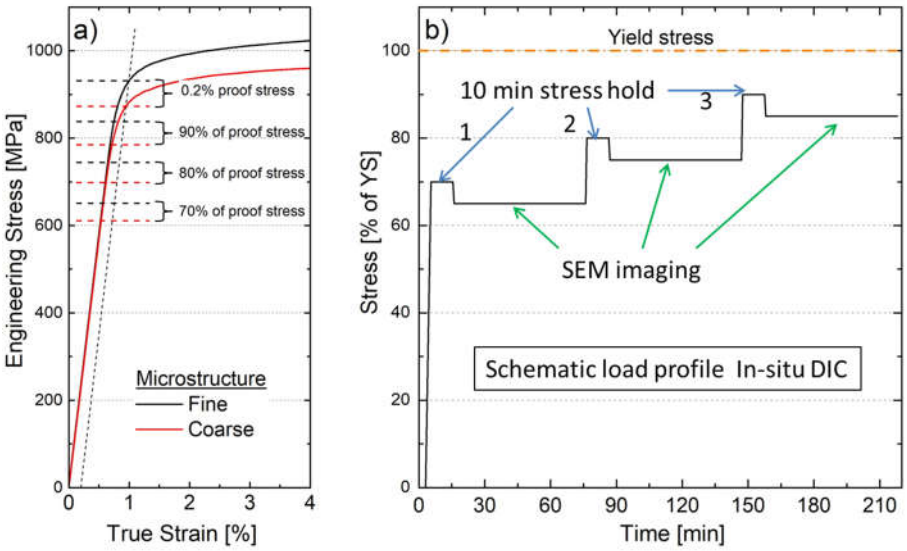

Fig. 3: (**a**) The solid lines show stress-strain curves for material with fine (black) and coarse (red) microstructure. The absolute stresses relating to 70, 80 and 90% of the 0.2% proof stress are indicated by dashed lines. (**b**) The schematic shows the load profile of the DIC-experiment, indicating the stress-holding and imaging steps.

As expected, uniaxial tensile testing revealed a higher 0.2% proof stress ($\sigma_{0.2\%}$) value for the 'fine microstructure' (934 MPa) compared to the 'coarse microstructure' (905 MPa). Based on these values, the relative load steps as a percentage of $\sigma_{0.2\%}$ were calculated for the in-situ loading experiment (Fig. 3, Table 2).

3.2 HRDIC results

3.2.1 Strain localisation

Since the images for the HRDIC analysis were acquired while being under load, the deformation maps show combined values of elastic and plastic strain. The amount of elastic strain has been estimated based on the modulus and the applied stress (Table 2). For the strain maps presented in Fig. 4 (a - e) the difference between the theoretical elastic strain and the average of the recorded HRDIC maps are smaller than the uncertainty of the HRDIC analysis (Table 2). In these cases, the average plastic strains are too low to be quantified. Still, the 99th percentiles can be used for all maps to analyse the heterogeneity of the strain distribution, as this parameter is sensitive to the local strain values in the slip bands. Fig 4 (g, h) highlight any grains that are not well aligned for either prismatic or basal <a> type slip, showing that the region of the 'fine microstructure' does indeed show a few grains that display very low Schmid factors for <a> type slip. This was not observed for the region in the 'coarse microstructure'.

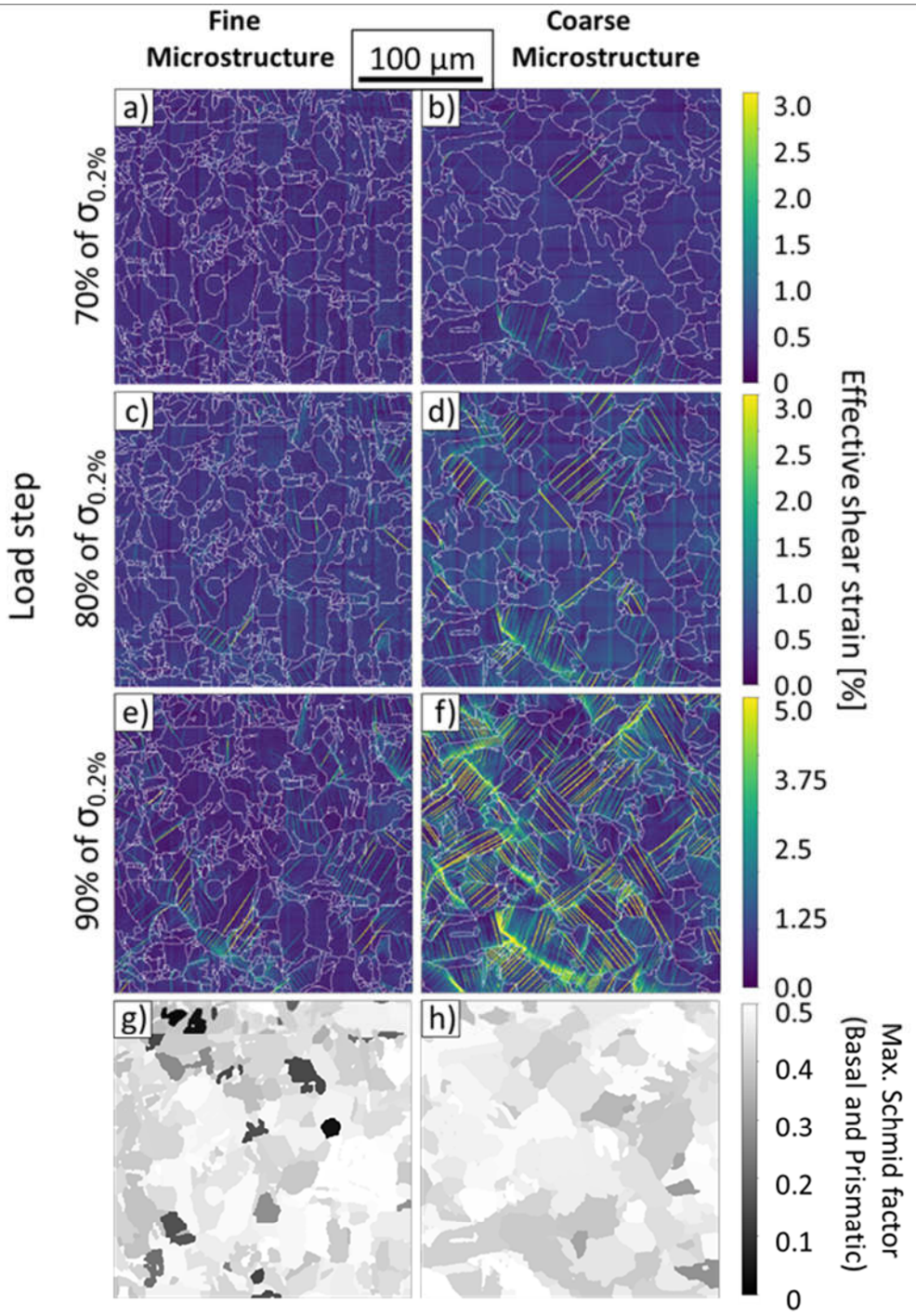

Fig. 4: Maps showing effective shear strain maps at 70% (**a** & **b**), 80% (**c** & **d**) and 90% (**e** & **f**) of the 0.2% proof stress, and (**g** & **h**) maximum Schmid factors (basal and prismatic slip) for both material with fine (**a**, **c**, **e, g**) and coarse (**b**, **d**, **f, h**) microstructure.

Both samples exhibit plastic deformation in the form of discrete slip bands at 70% of $\sigma_{0.2\%}$ (Fig. 4, (a & b)), with all the slip bands being intragranular and their length being equal to or less than the grain size. The slip band length tends to be longer in the 'coarser microstructure' due to larger grains. With increasing applied load, strain values in existing slip bands increase, new slip bands develop, and slip is activated in more grains. For increasing average plastic strains, diffuse areas of slip start to develop, particularly in the transformed β phase, as the spacing between slip bands becomes narrower and gets close to the resolution limit (Fig.6 (e - f), Fig. 13). Slip is still assumed to be accommodated by the formation of slip bands, but due to the small spacing the discrimination of slip bands is no longer possible with the used experimental technique, resulting in areas that

seem to have deformed completely homogeneously, respectively by diffuse slip instead of localised slip bands. At 80% and 90% of $\sigma_{0.2\%}$, sharp slip along/near grain boundaries can be observed in a few areas in the 'coarse microstructure'. Despite the lower absolute applied stress, the 'coarse microstructure' exhibits higher average strain values and strain localisation at all load steps.

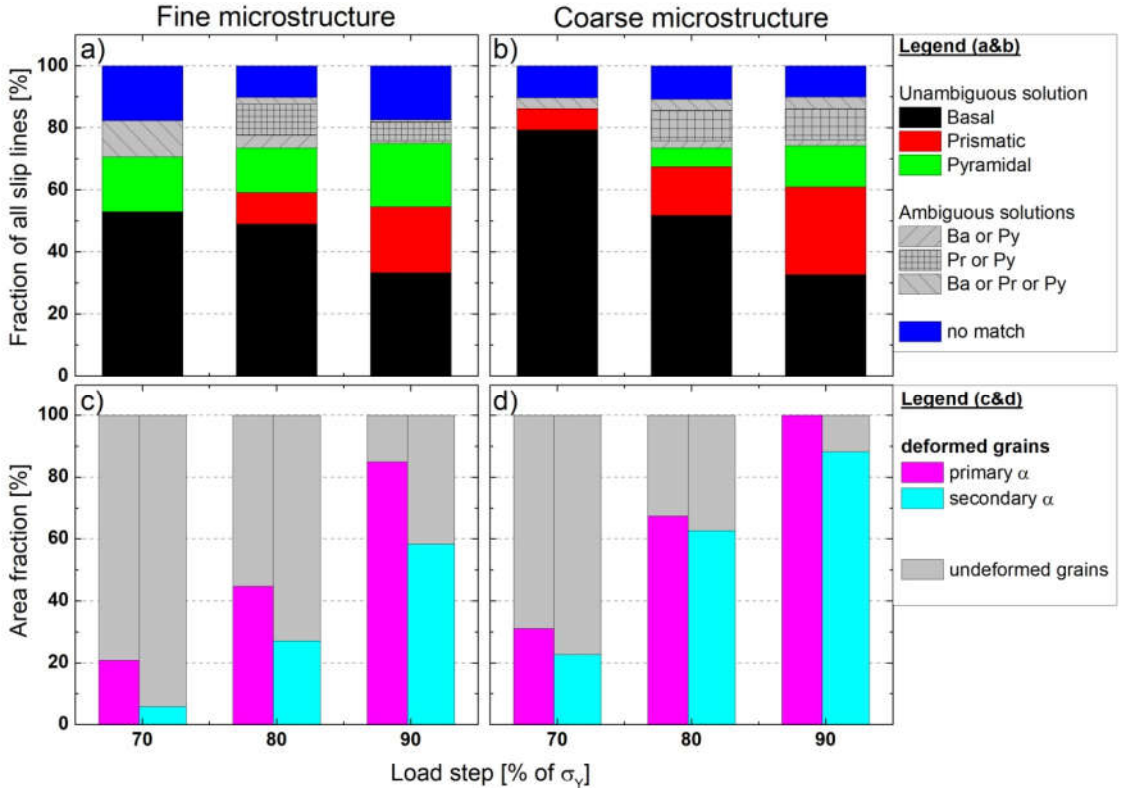

Fig. 5: (**a** & **b**) Relative frequencies of, both, unambiguously and ambiguously identified slip systems as a fraction of all observed slip systems. (**c** & **d**) Relative frequencies of primary α grains (magenta) and secondary α colonies (light blue) that have plastically deformed in the HRDIC experiment at the specific load steps for (**a & c**) fine and (**b & d**) coarse microstructure.

In the 'coarse microstructure' around 0.9% plastic strain accumulated after 10 minutes holding at 90% of $\sigma_{0.2\%}$, indicating susceptibility to cold creep at stress levels below the 0.2% proof stress obtained during standard tensile testing. No average plastic strain accumulation was observed for 'fine microstructure'.

3.2.2 Slip system activity

Slip trace analysis (Fig. 5 (a, b)) shows that for both microstructures basal <a>-type slip is the dominant slip system at the first load step. At this load-step, the 'fine microstructure' also displays some pyramidal but no prismatic slip, while 'coarse microstructure' shows the opposite behaviour. It should be noted that there are ambiguous solutions for both microstructures. Hence, no slip mode can be completely excluded based on this analysis. Interestingly, the fraction of pyramidal slip is always higher in the 'fine microstructure' than in the 'coarse microstructure'. With increasing load, the number of new grains found to deform by basal slip reduces, while the number of grains deforming by the other two slip modes increases; hence the relative fraction of basal slip decreases and the fraction of prismatic slip, in particular, increases. At 90% of $\sigma_{0.2\%}$, the fraction of basal and prismatic slip is of a similar magnitude. It is also worth noting that in both microstructures at 70% and 80% of $\sigma_{0.2\%}$, no prismatic slip was observed in primary α grains, while at 90% of $\sigma_{0.2\%}$ prismatic slip was observed in both constituents.

3.2.3 Primary α grains and secondary α colonies

The fractions of deformed primary α grains and secondary α colonies are given as relative values weighted by area in Fig. 5 (c & d). Grains were considered as 'deformed' when at least one slip line was observed. For all loading steps and both microstructures, the fraction of deformed primary α grains is higher than the fraction of deformed secondary α colonies. This difference is more pronounced for the 'fine microstructure'. Furthermore, the number of activated grains is always greater in the 'coarse microstructure'. While the majority of grains in the 'coarse microstructure' were deformed plastically at 90% of $\sigma_{0.2\%}$, many grains stayed undeformed in the 'fine microstructure' despite having high Schmid factors (> 0.4) for <a>-type slip.

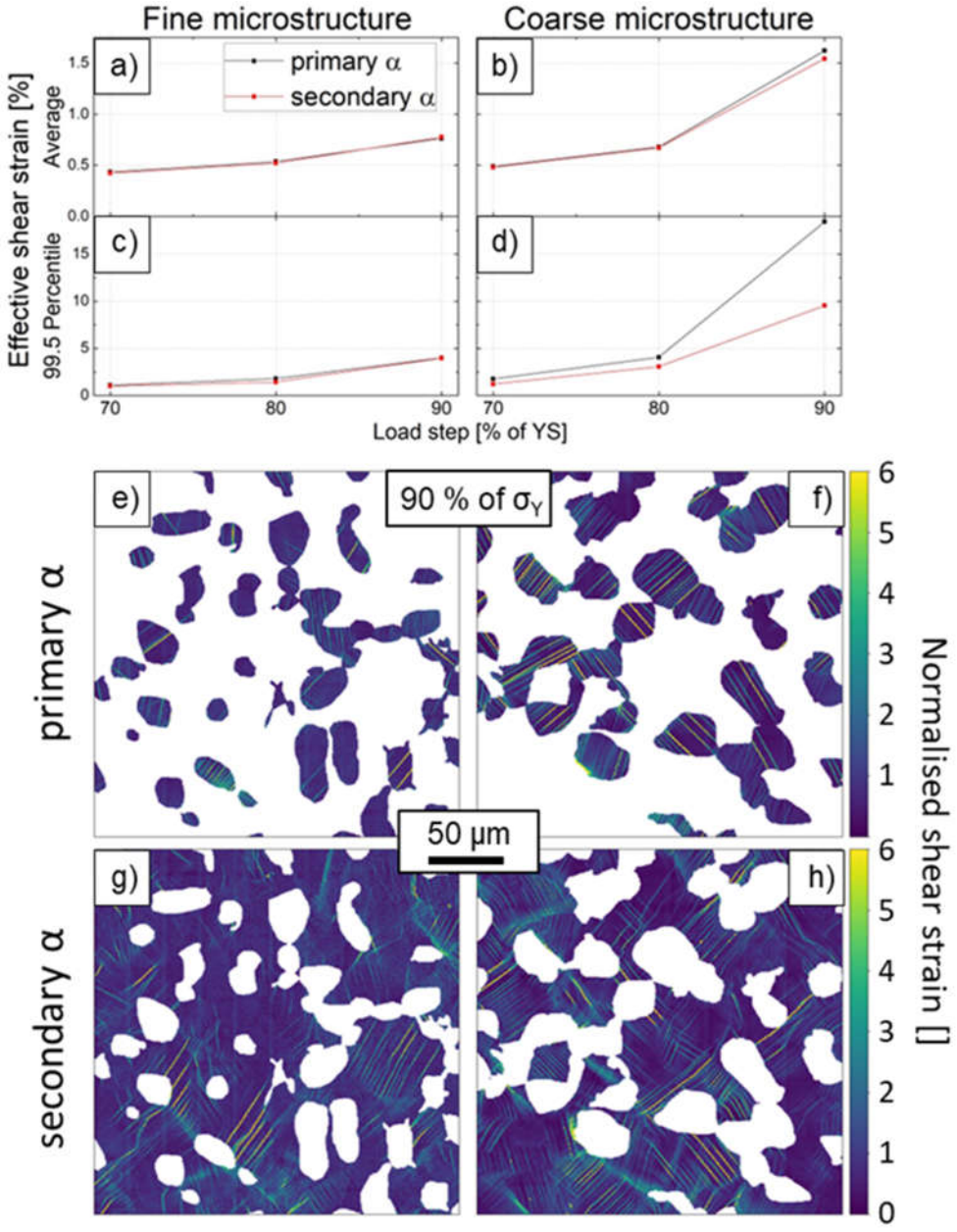

Fig. 6: Plots of average values (**a** & **b**) and the 99.5th percentile (**c** & **d**) of effective shear strain at all load steps, separately for the primary α and secondary α constituents. The strain maps (**e** - **h**) show normalised effective shear strain values, separately for the primary α (**e** & **f**) and secondary α (**g** & **h**) constituents.

To further investigate the slip trace orientation within secondary α lamellae a frequency distribution plot of the angle between slip trace and long direction of secondary α lamellae was generated, which didn't show any clear correlations: angles in the complete range of 0° to 90° between slip traces and lamellae were observed (Fig. A 1).

In the 'fine microstructure', the average effective shear strain values, as well as the 99.5th percentiles, were identical for both constituents at all load steps (Fig. 6, (a & c)). Potential differences in strain distribution may not be quantified for the 'fine microstructure', due to the low overall strain values. The average effective shear strain values were also identical for the 'coarse microstructure' (Fig. 6c). However, the 99.5th percentile (Fig. 6d) values were higher in the primary α grains than in the secondary α colonies, which is particularly apparent at 90% of $\sigma_{0.2\%}$. For both material conditions, the segmented strain maps at the 90% of $\sigma_{0.2\%}$ load step (Fig. 6 (e-h)) show that plastic deformation in the primary α grains is mainly in the form of discrete slip bands, while for secondary α lamellae, a combination of discrete slip bands and diffuse slip can be observed. The 'coarse microstructure' also displays wider slip trace spacing in the primary α grains than in secondary α colonies.

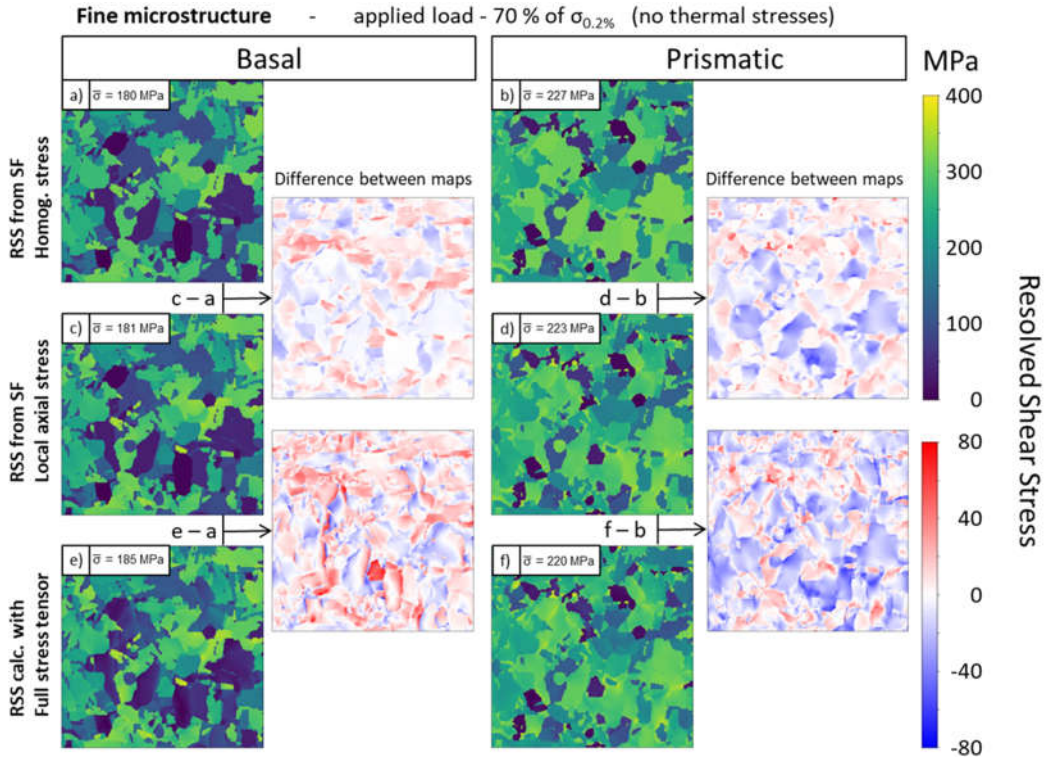

Fig. 7: Maps of resolved shear stress RSS on (**a**,**c** & **e**) basal and (**b**,**d** & **f**) prismatic slip systems for the material with fine microstructure. The simulations are for loading to 70% of 0.2% proof stress of initially stress free material. The RSS values have been calculated according to three different approaches. Additionally, maps showing the difference between the calculation methods are displayed.

3.3 Crystal plasticity modelling – RSS analysis

Fig. 7 presents calculated RSS maps utilising the three different methods described earlier. When considering the first method using Schmid factors and assuming the same stress at each point in the sample (equation 3), constant RSS values are calculated for each grain as there are no variations in local stresses, Fig. 7 (a & b). As RSS values are linearly related to the Schmid factor values, average RSS values are higher for prismatic than basal slip, with the same ratio between

the slip systems as for the average SF values (Fig. 2 (a & b), Table 3). The differences in the frequency distributions of the RSS values (Fig. 8 (a & b)) and the Schmid factor values (Fig.2 (a & b)) only arises from the different bin-sizes.

In comparison, when elastic anisotropy and local stresses are considered (Fig. 7 (c & d)), variations of RSS values within grains are introduced. The average standard deviation of RSS values within single grains is 5 MPa for both slip systems and microstructures. Locally, the relative changes in the RSS maps are identical for all slip systems, as only the local stresses, but not the Schmid factor values, have changed. The frequency distributions of RSS values (Fig. 8 (c & d)) are less scattered for higher than average values compared to the initial approach.

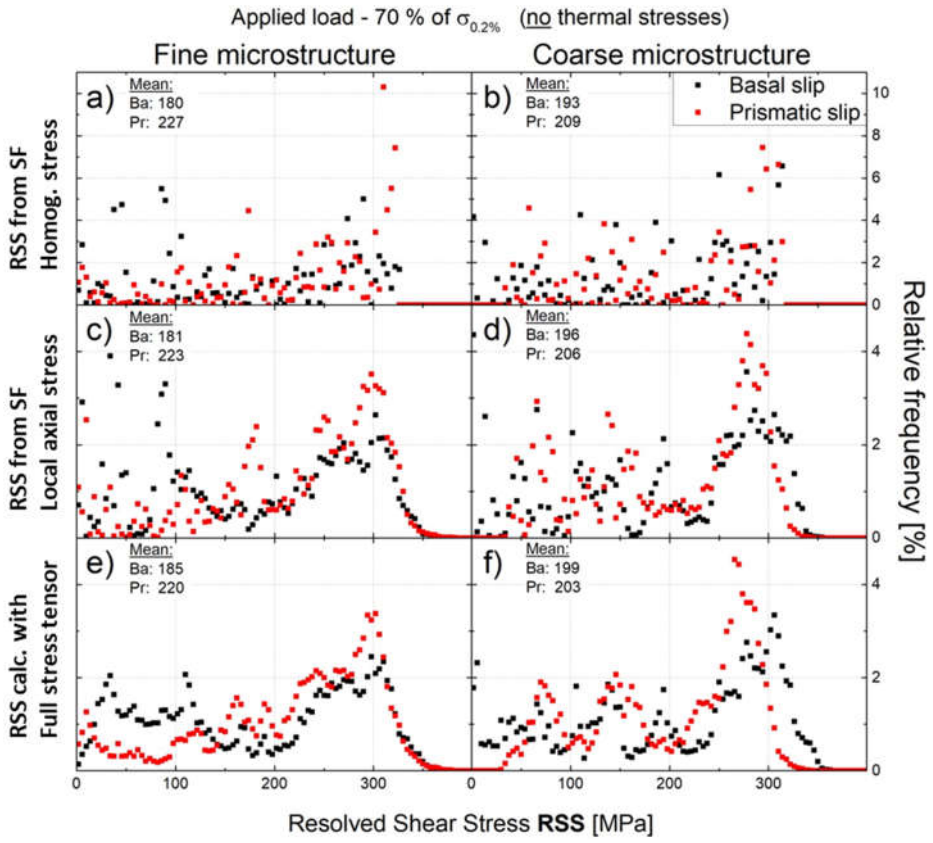

Fig. 8: Histograms of resolved shear stresses RSS from crystal plasticity simulations, both for basal and prismatic slip. RSS values have been calculated (**a** & **b**) from SF – homogeneous stress, (**c** & **d**) from SF – local axial stresses, and (**e** & **f**) with full stress tensor. The simulations are for loading to 70% of 0.2% proof stress of initially stress free material, both for (**a**, **c** & **e**) fine and (**b**, **d** & **f**) coarse microstructure.

For calculations of RSS values based on the full stress tensor (equation 5), the RSS frequency distributions appear less scattered for the complete range (Fig. 8 (e & f)) and the spread of RSS values within grains increases further ('fine microstructure': 9 MPa; 'coarse microstructure': 8 MPa). The local changes are different for basal and prismatic slip. In large parts of the analysed area, RSS values for basal slip increase or at least stay constant, while RSS values for prismatic slip decrease in many areas (Fig. 7 (e & f)) compared to the calculations assuming homogeneous axials stresses. This brings the average RSS values of both slip systems further together. The highest RSS values (95th percentile) are similar for both slip systems in the 'fine microstructure', while for the 'coarse microstructure'; the maximum RSS values for basal slip are 27 MPa higher than for prismatic slip (Table 3).

Overall, using more detailed calculations reduces the difference in average RSS values between basal and prismatic slip, and further increases the spread of RSS values within grains (Table 3). Regarding the 95th percentile, RSS values increase for basal slip and decrease for prismatic slip.

Table 3: RSS values, mean and 95th percentile values of the complete maps , for basal and prismatic slip, using three different calculation methods.

RSS values [Mpa]		SF - homog. Stress		SF - local axial stress		Full Stress Tensor	
Microstructure	Slip system	mean	95th PCTL	mean	95th PCTL	mean	95th PCTL
Fine	Basal	180	315	181	319	185	320
	Prismatic	227	323	223	322	220	319
Coarse	Basal	193	313	196	320	199	323
	Prismatic	209	310	205	304	203	296

PCTL: percentile

3.4 Crystal plasticity – correlation to experimental data

The average RSS values of each grain, based on the simulations using the full stress tensor, are presented in respect of their orientation in IPF-plots, Fig. 9 (a,b and e,f). To highlight the regions of highest Schmid factor for the respective slip modes within the IPF-plot, contour lines have been added. In addition, Fig. 9 (c, d) highlights the grains that do display basal slip traces after loading to 70% of $\sigma_{0.2\%}$.

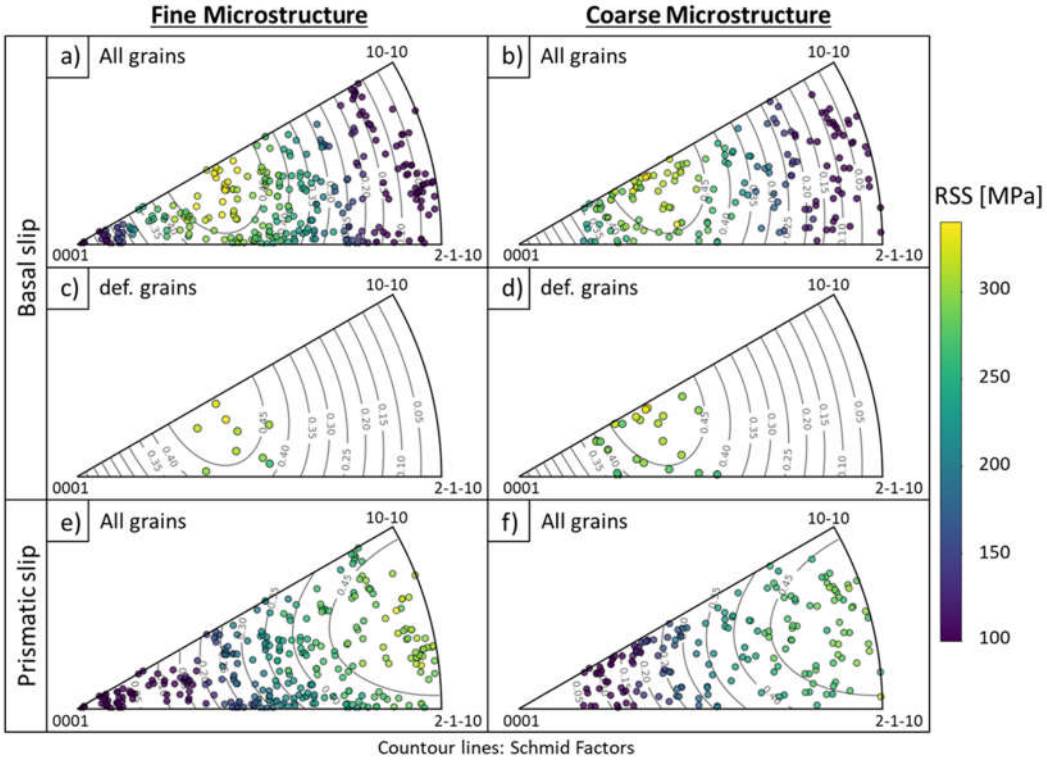

Fig. 9: Resolved Shear Stress (RSS) values for (**a** – **d**) basal and (**e** & **f**) prismatic slip for (**a**, **c** & **e**) fine microstructure and (b, d & f) coarse microstructure. (**c** & **d**) Grains in which basal slip has been identified at 70% of $\sigma_{0.2\%}$ in the HRDIC experiment are plotted separately.

In terms of grain averages, the maximum RSS values are approximately 20 MPa ('fine microstructure') to 30 MPa ('coarse microstructure') higher for basal than for prismatic slip. Generally, RSS values appear to be positively correlated to Schmid factor values, for both material conditions and both slip systems. Fig. 9 (c & d) shows that at 70% of $\sigma_{0.2\%}$ the declination angles of all deformed grains in the 'fine microstructure' are distributed symmetrically around 45°, with

declination angles being higher than 39° and Schmid factors higher than 0.42. For the 'coarse microstructure,' a shift towards the 0001 pole is observed. The deformed grains have declination angles as low as 26°, correlating to a Schmid factor of approximately 0.38.

3.5 Effect of thermal residual stresses

Fig. 10, (a & b) shows the frequency distribution of the calculated thermal residual stresses along the c-axis for both material conditions. On average there is compressive stress of just over 10 MPa along the c-axis for both microstructure conditions. Compressive residual stresses parallel to the c-axis were expected, as the thermal expansion coefficient is lower in this direction [49]. However, there are grains with compressive as well as tensile stresses along the c-axis, while there are also large numbers of grains that have no or low tensile stresses along the c-axis. For the simulated temperature difference (ΔT = 500 K), compressive stresses reach up to 125 MPa, around 50 MPa higher than the maximum tensile stresses.

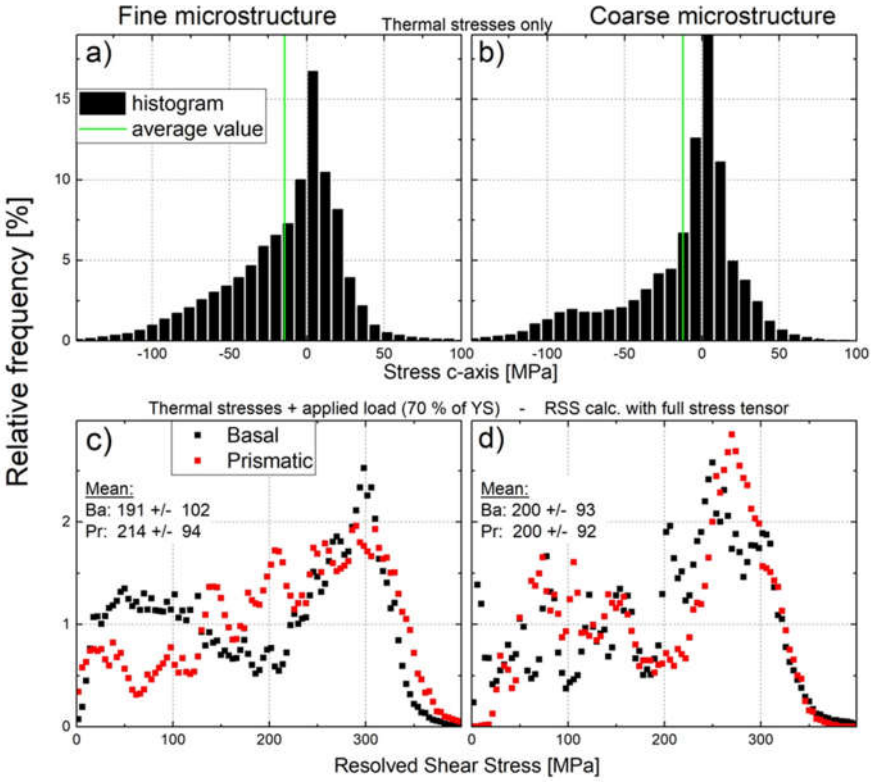

Fig. 10: Results from CP-simulation: (**a** & **b**) Relative frequency distribution of thermal residual stress along the c-axis, for cooling from 800 K to room temperature. (**c** & **d**) Relative frequency distribution of RSS values for material with thermal residual stresses loaded to 70% of 0.2% proof stress.

In Fig. 10 (c & d), the frequency distributions of basal and prismatic RSS values have been plotted for a simulation combining thermal residual stresses (ΔT = 500 K) and uniaxial loading (70% of $\sigma_{0.2\%}$). As the thermal residual stresses along c-axis can be of either nature, there is no uniform change in RSS values and local RSS values might increase or decrease, leading to a broadening of the main peak at around 275 to 300 MPa. As a result, maximum RSS values, particularly for prismatic slip, are higher in Fig. 10 (c & d) compared to the calculations that do not consider thermal residual stresses, Fig.9, (e & f). Overall, the average RSS values for prismatic slip decrease slightly, whilst almost no change is observed for basal slip.

4 Discussion

Effect of microstructure on strain localisation

By separating the transformed β phase from the primary α grains it was possible to identify and quantify the strain localisation in the two constituents. It was observed that the initial slip traces form more readily in primary α grains, implying that the transformed β phase has higher strength, particularly for the materials with a fine transformation product, as dislocations here have a shorter mean free path. Hence, the transformation product leads to a stronger Hall-Petch type strengthening [81], [82] resulting in higher macroscopic strength and the fine secondary α product in the 'fine-microstructure' is also likely to further constrain the deformation of the primary α grains. It is interesting that in the case of the 'coarse microstructure', primary α grains and secondary α colonies are of a similar size. Due to the higher Al concentration and presence of α_2-precipitates, one might expect primary α grains to have a higher strength than secondary α colonies [5], [9], [33], [43]. However, we observe the contrary, suggesting that the α/β ligament structure, despite the low volume fraction of β-phase, provides some additional strengthening by hindering the transfer of dislocations across lath boundaries [83] [46].

In primary α grains, strain was observed to be more localised in discrete slip bands compared to the more diffuse slip bands observed in the secondary α colonies, particularly in the 'coarse microstructure', which could be explained by element partitioning of Aluminium enhancing α_2 precipitation in primary α grains, which are known to promote slip planarity [9], [81], [84]. Lunt et al. reported that reduced levels of α_2 in the transformed β phase results in more diffuse and wavy slip in secondary α, which agrees well with the current observations [9].

Cold creep susceptibility

Titanium is well known to be highly susceptible to cold creep, which can be seen in the context of limited strain hardening of the hexagonal closed packed α phase due to the limitation of different Burger's vectors. Consequently, strain hardening does heavily rely on variations of grain orientations and a secondary α constituent with a fine basketweave, as seen in Fig. 1 (e-h), is expected to reduce the susceptibility of cold creep.

In the present case, the cold creep susceptibility is higher for the sample with the coarser transformation product compared to the fine transformation product when subjected to a 10-minute load-hold at stress levels below the 0.2% proof stress and is in good agreement with [13], [15], [18], [24], where a reduction of grain size lowers the susceptibility to cold creep. As demonstrated in Fig. 5 (c-d), in the case of the 'fine microstructure', slip at low stress levels is localised mainly in primary α grains, which is to be expected as they are considerably larger than any single secondary α colony. Furthermore, the primary α grains are separated from each other by plastically undeformed transformed β phase, preventing the link-up/transfer of slip between grains and limiting the maximum slip length to the size of single primary α grains. This will result in fewer dislocation pile-up at grain boundaries and thus reduces local stress concentrations [19], [85]. On the other hand, in the coarser transformation product, slip is activated readily in both constituents even at the low stress levels. In the 'coarse micro-structure', the larger grain size and higher volume fraction of primary α grains increase the probability of neighbouring primary α grains being connected. If these grains have similar crystallographic orientations, the transfer of slip and formation of interconnected slip bands is more likely. The time-dependent deformation during cold creep is limited by pinned dislocations requiring thermal activation to overcome obstacles, e.g. at precipitates, dislocation

networks, interstitials or boundaries [14], [16], [86]. Therefore, a shorter distance between obstacles results in a slower deformation rate, fitting well with the observation that a finer microstructure, where distances between boundaries are shorter, exhibit lower creep rate.

Active slip modes

For both material conditions, basal slip was the dominant slip mode at low stress levels (70 and 80%) under cold creep loading conditions. Similar observations have been reported in the literature for different near-α and α+β Ti-alloys, in particular Ti-6Al-4V, Ti-6242 and Ti-6246 [28], [41], [87]–[89]. While local texture strongly influences strain localisation at higher strain levels, the initial activation of slip systems is expected to be mainly influenced by the orientation of each grain and not the local grain neighbourhood [31], [40]. With increasing stress levels, but still below the yield stress, prismatic slip starts to be activated in individual grains that are particularly well oriented for this slip mode, Fig, 5 (a & b). At the highest load step (90% of $\sigma_{0.2\%}$), the number of newly activated slip systems is higher for prismatic than for basal slip, indicating the beginning changeover from basal to prismatic slip as the dominant slip mode. This is in good agreement with previous studies where deformation was studied well beyond the proof stress. These studies have consistently reported prismatic slip and not basal slip to be the dominant slip mode [38], [90].

The initial hypothesis to explain the prevalence of basal slip during the onset of plasticity was that the elastic strain heterogeneity plays a crucial role at this stage. It can be seen from Fig. 9 that high Schmid factor values for basal slip are associated with grains having their c-axis more orientated towards the loading direction than for prismatic slip. The Schmid factor contour lines for basal slip show that the highest values are obtained for a range of inclination angles between the loading direction and the c-axis. It is interesting to note that for the ‘coarse microstructure’, Fig. 9 (d), there is a tendency that the grains with early basal slip are more likely to have a small inclination angle between the loading direction and the c-axis, promoting the idea that they might experience higher RSS values related to the elastic anisotropy. However, the same is not observed for the ‘fine microstructure’ in Fig. 9 (c).

The CP-simulations did provide some support for the hypothesis in the case of the ‘coarse microstructure’ but failed to do the same for the ‘fine microstructure’. While the consideration of elastic anisotropy increased average RSS values for basal slip relative to the values for prismatic slip, the average values of the whole region of interest are still higher for prismatic slip. Regarding the highest, local RSS values (using the 95th percentile) the picture changes with values for basal slip being higher in ‘coarse microstructure’, but RSS values of the two slip systems are almost identical in ‘fine microstructure’. Regarding the grain averaged RSS values, the maximum values for basal slip are higher than for prismatic slip in both microstructures. However, the studied regions contain grains well aligned for prismatic slip, both primary α grains as well as secondary α colonies, that did not show any signs of plasticity, despite having RSS values higher than the grains that deformed early by basal slip.

To further explore the effect of the declination angle between the loading direction and c-axis, Fig. 11 is presented. It clearly shows that due to elastic anisotropy, axial stresses in the loading direction increase for lower declination angles and are up to 20% higher than the macroscopically applied stress. Based on the higher axial stresses in grains well aligned for basal slip, the increase of the calculated RSS values for basal slip when considering elastic anisotropy becomes apparent. It also, of course, explains the principle that grains deformed by basal slip in the ‘coarse

microstructure' on average have declination angles smaller than 45° (Fig. 9). On the other hand, this effect cannot be observed for the 'fine microstructure.' Due to the fine morphology and high strength of the transformed β phase, deformation is almost entirely confined to primary α grains. At the same time, only one primary α grain and otherwise secondary α colonies had declination angles in the range that resulted in basal slip activity in the 'coarse microstructure'. Therefore, there is the possibility that the 'fine microstructure' does not support the hypothesis stated above, due to a lack of suitability oriented primary α grains in the analysed region. It should be pointed out that there was one primary α grain that has its c-axis almost parallel to the loading direction, though the basal slip related Schmid factor is low. Hence, there remains some uncertainty if the elastic anisotropy can indeed fully explain the dominance of basal slip during the onset of plasticity while assuming similar CRSS values for basal and prismatic slip.

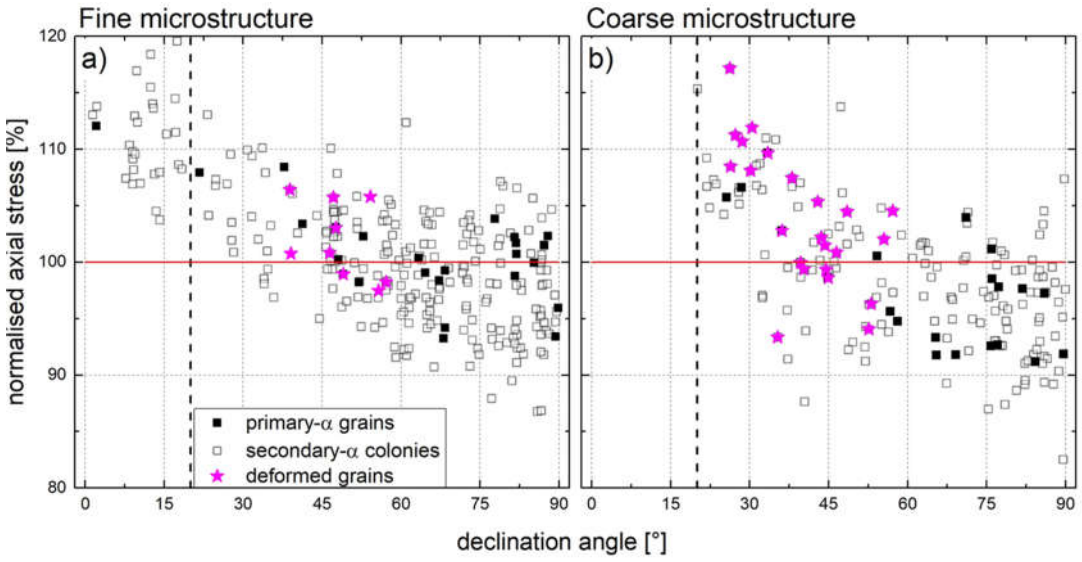

Fig. 11: Grain average axial stresses normalised by the macroscopic axial stress for **a**) fine microstructure and **b**) Coarse microstructure.

An alternative consideration is that CRSS values are lower for basal than for prismatic slip, as reported recently in [28], [39]–[41]. However, a lower CRSS value for basal slip does not explain the changeover from dominant basal to prismatic slip as plasticity proceeds. Here the work by Hutchinson et al. might provide an explanation [47]. Firstly, their theoretical consideration concludes that CRSS values recorded on single crystals do not directly re ect the applied shear stresses that are necessary to activate di erent slip modes in polycrystalline materials. They state that most hardening contributions are not proportional to the CRSS values but are additional to them. Therefore, if basal slip is activated due to a lower CRSS value, the relative difference of the CRSS values of the basal and prismatic slip would decrease in a polycrystalline material with increasing strain levels and the fraction of all slip systems would converge.

Complementary to this argument, it is interesting to note that higher work hardening rates have been reported for basal slip compared to prismatic slip [91]. Such increased hardening rate might be due to cross-slip onto prismatic and pyramidal planes, resulting in complex interactions between dislocations and reducing dislocation mobility [92]. Therefore, after the initial dominance of basal slip, the accumulative CRSS and large hardening contribution may reduce basal slip activity at the expense of prismatic slip activity. Besides, recent work on exploring strain rate sensitivity of individual slip systems in Ti has highlighted that basal slip exhibits a greater strain rate sensitivity

than prismatic slip [46], [91], [93]. As strain rate sensitivity and strain hardening are closely linked, these observations further confirm that basal slip strain hardens more easily than prismatic slip.

Considering that the work is purely based on surface observations, it is also interesting to explore the direction of shear in respect to the surface. We assume that slip at a free surface is easier to initiate than in the bulk material, as there are no constraints of neighbouring grains, making slip easier for Burger's vectors with a larger out-of-plane component. Fig. 12 shows the frequency distribution for the angle between Burger's vectors and sample surface of grains deformed by basal slip (23 grains) in the material with 'coarse microstructure' together with all grains that have RSS values higher than the calculated average value. This translates to an additional 99 grains well aligned for basal slip and 97 grains well aligned for prismatic slip. Firstly, for grains well aligned for basal slip, the associated Burger's vectors have a larger out-of-plane component than for grains well aligned for prismatic slip. Secondly, grains that have deformed by basal slip tend to have a greater out-of-plane Burger's vector direction than grains well aligned for basal slip, which have not deformed. As a maximum Schmid factor for basal slip is achieved for grains with a declination angle of 45° one would expect an equal distribution around this angle for grains deformed by basal slip.

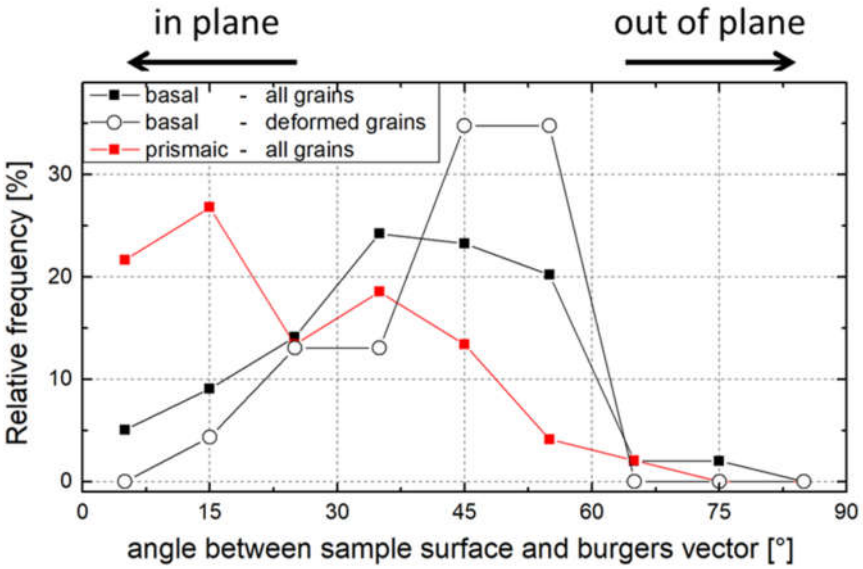

Fig. 12: : Relative frequency distributions of angles between Burger's vectors and the free sample surface for grains with RSS values higher than the mean value of the complete sample, regarding basal and prismatic slip separately, as well as the grains which unambiguously deformed by basal slip in the HRDIC experiment in the 'coarse microstructure'.

It is noticeable that the sample with the finer transformation product exhibits a higher frequency of pyramidal slip at all load steps, with most of it being localised in the transformed β phase. As the fine transformation product displays no activation of slip during the early loading stage, high stresses are achieved in this constituent making activation of pyramidal <c+a> slip, which has a higher CRSS value [85] than basal and prismatic slip, more likely. In addition, the fine transformation product provides a hardening increment that increases the effective CRSS values in polycrystals for all slip systems equally and therefore reduces the relative difference between them [47].

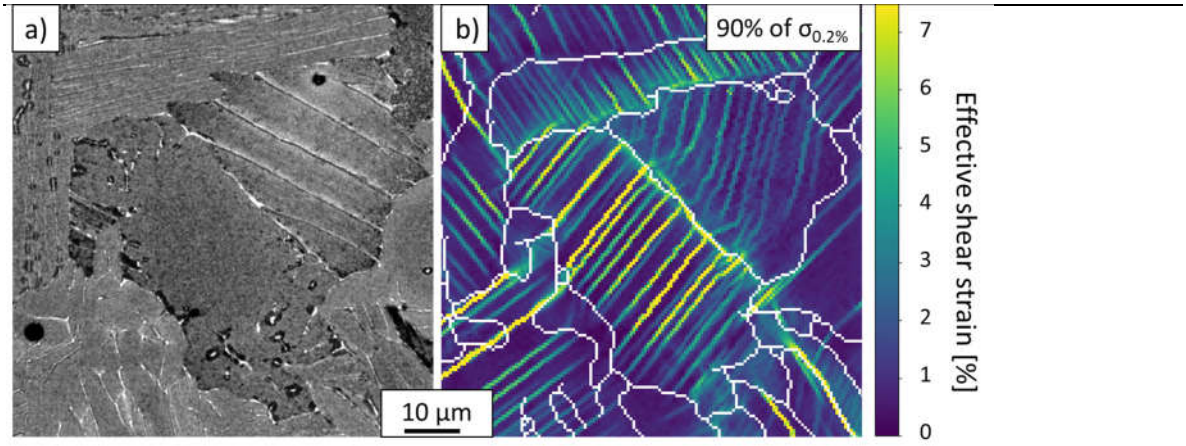

Fig. 13: (**a**) BSE-SEM image of 'coarse microstructure' in undeformed condition and (**b**) effective shear strain map at 90% of $\sigma_{0.2\%}$, which is a sub-set of Fig. 4 (**f**).

Effect of thermal residual stresses

Thermal residual stresses have been simulated assuming a temperature difference of 500 K, not considering the temperature dependence of the thermal expansion coefficients [49] and not allowing for stress relaxations during cooling. While the magnitude of the thermal residual stresses is an overestimation [49], the results clearly show the trend of how the thermal residual stresses increase RSS values for prismatic slip relative to basal slip, which stands in contrast to the observation of basal slip being activated before prismatic slip. Therefore, thermal residual stresses should be considered in future studies that aim to determine CRSS values for all slip systems.

Implications

The work has demonstrated that basal slip is the dominant slip mode in the near-α Ti-alloy studied here for stresses below macroscopic yield and under cold creep loading conditions. It seems likely that this is an observation generally applicable to Ti-alloys since it has been observed previously for other alloys [25]–[30]. It highlights the importance basal slip may have for deformation mechanisms associated with triggering CDF. Furthermore, transformed β phase regions obtained in a bimodal microstructure can effectively reduce the slip length that develops during the onset of plasticity if they are sufficiently strengthened by having a fine lath structure and a basketweave structure.

Recent studies on CDF have reported that the normal of facets formed during CDF loading is tilted approximately 30° from the loading direction [94], while in earlier work the plane normal of facets were reported to be parallel to the loading direction [21], [95]. Interestingly, we have observed early activation of basal slip in grains with a declination angle of the basal plane normal as low as 26° in respect to the loading direction. Generally, facets have been reported close to parallel to the (0002)-plane [21], [95], [96]. Hence, a hypothesis to develop from the work is that the damage associated with the shear along basal planes, that have a normal comparatively parallel to the loading direction, might be enabling decohesion and facet formation [97]. It seems that such process would not require neighbouring hard grains or any 'rogue grain' combinations [19], [86], [98], which are often considered to be a requirement for load shedding and CDF [99]. Finally, these slip bands have formed during initial loading and load hold, in the absence of cyclic loading indicating that the location of facets might be predefined by the initial, local plastic deformation during the first load cycle, while cyclic loading will be required for opening the facets and crack propagation.

5 Conclusion

The present work has investigated the deformation mechanisms during cold creep deformation for applied stresses below the proof stress for the near-α Ti-alloy TIMETAL®834. It has been shown that secondary α colonies, particularly for fine transformation products, are stronger than primary α grains and that slip is more localised in discrete slip bands in primary α grains. This leads to lower susceptibility to cold creep deformation in material with fine transformation product. For cold creep loading conditions, basal slip is the dominant slip mode during initial plastic deformation, independently of the material condition, suggesting the importance of this slip mode to the cold dwell fatigue failure mechanism. Neither the consideration of the elastic anisotropy of α titanium phase nor the consideration of the anisotropy of the thermal expansion coefficient unambiguously explained the dominance of basal slip at low applied stresses. Only in the case of the coarse microstructure it seems possible to relate the early basal slip dominance to the elastic anisotropy of α titanium. While this might be related to some simplifications in the CP-model, it might also require the consideration that CRSS values are lower and strain hardening rates are higher for basal than for prismatic slip, as it has recently been reported in the literature.

6 References

[1] L. Germain, N. Gey, M. Humbert, P. Bocher, and M. Jahazi, Acta Mater., vol. 53, no. 13, pp. 3535–3543, 2005.

[2] S. Hardt, H. J. Maier, and H. J. Christ, Int. J. Fatigue, vol. 21, no. 8, pp. 779–789, 1999.

[3] A. Kumar, N. Singh, and V. Singh, Mater. Charact., vol. 51, no. 4, pp. 225–233, 2003.

[4] A. K. Singh and C. Ramachandra, J. Mater. Sci., vol. 32, no. 1, pp. 229–234, 1997.

[5] K. V. S. a I. Srinadh, N. Singh, and V. Singh, Bull. Mater. Sci., vol. 30, no. 6, pp. 595–600, 2007.

[6] A. Radecka, P. A. J. Bagot, T. L. Martin, J. Coakley, V. A. Vorontsov, M. P. Moody, H. Ishii, D. Rugg, and D. Dye, Acta Mater., vol. 112, pp. 141–149, 2016.

[7] A. Radecka, J. Coakley, V. A. Vorontsov, T. L. Martin, P. A. J. Bagot, M. P. Moody, D. Rugg, and D. Dye, Scr. Mater., vol. 117, pp. 81–85, 2016.

[8] C. Dichtl, Z. Zhang, H. Gardner, P. Bagot, A. Radecka, D. Dye, M. Thomas, R. Sandala, J. Q. da Fonseca, and M. Preuss, Mater. Charact., vol. 164, p. 110327, Jun. 2020.

[9] D. Lunt, T. Busolo, X. Xu, J. Quinta da Fonseca, and M. Preuss, Acta Mater., vol. 129, pp. 72–82, May 2017.

[10] B. S. S. C. Rao, M. Srinivas, and S. V. Kamat, Mater. Sci. Eng. A, vol. 520, no. 1, pp. 29–35, 2009.

[11] Titanium Metal Corporation, 2020. [Online]. Available: https://www.timet.com/assets/local/documents/datasheets/alphaalloys/834.pdf. [Accessed: 27-Oct-2020].

[12] M. Whittaker, P. Jones, C. Pleydell-Pearce, D. Rugg, and S. Williams, Mater. Sci. Eng. A, vol. 527, no. 24, pp. 6683–6689, 2010.

[13] M. A. Imam and C. M. Gilmore, Metall. Trans. A, vol. 10, no. 4, pp. 419–425, 1979.

[14] B. C. Odegard and A. W. Thompson, Metall. Trans., vol. 5, no. 5, pp. 1207–1213, 1974.

[15] T. Neeraj, D.-H. Hou, G. S. Daehn, and M. J. Mills, Acta Mater., vol. 48, no. 6, pp. 1225–1238, Apr. 2000.

[16] A. W. Thompson and B. C. Odegard, Metall. Trans., vol. 4, no. 4, pp. 899–908, 1973.

[17] H. P. Chu, NASA Tech. Memo. 104641, pp. 1–14, 1997.

[18] W. H. Miller, R. T. Chen, and E. A. Starke, Metall. Trans. A, vol. 18, no. 8, pp. 1451–1468, 1987.

[19] F. P. E. Dunne and D. Rugg, Fatigue Fract. Eng. Mater. Struct., vol. 31, no. 11, pp. 949–958, 2008.

[20] M. . Bache, Int. J. Fatigue, vol. 25, no. 9, pp. 1079–1087, 2003.

[21] M. Bache, Int. J. Fatigue, vol. 19, no. 93, pp. 83–88, 1997.

[22] S. Ghosh, M. Mills, S. Rokhlin, V. Sinha, W. Soboyejo, and J. Williams, US Dept. Transp. Aviat. Auth. report, DOT/FAA/AR-06/24, 2007.

[23] J. Qiu, Y. Ma, J. Lei, Y. Liu, A. Huang, D. Rugg, and R. Yang, Metall. Mater. Trans. A Phys. Metall. Mater. Sci., vol. 45, no. 13, pp. 6075–6087, 2014.

[24] A. Ready, P. Haynes, B. Grabowski, D. Rugg, and A. Sutton, Proc.R.Soc.A, vol. 473, no. 2203, 2017.

[25] C. Lavogiez, S. Hémery, and P. Villechaise, Int. J. Fatigue, vol. 131, no. July 2019, p. 105341, 2019.

[26] S. Hémery, A. Naït-Ali, M. Guéguen, J. Wendorf, A. T. Polonsky, M. P. Echlin, J. C. Stinville, T. M. Pollock, and P. Villechaise, Acta Mater., vol. 181, pp. 36–48, 2019.

[27] S. Hémery, P. Nizou, and P. Villechaise, Mater. Sci. Eng. A, vol. 709, pp. 277–284, Jan. 2018.

[28] S. Hémery and P. Villechaise, Mater. Sci. Eng. A, vol. 697, pp. 177–183, Jun. 2017.

[29] S. Hémery, A. Nait-Ali, and P. Villechaise, Mech. Mater., vol. 109, pp. 1–10, Jun. 2017.

[30] F. Bridier, P. Villechaise, and J. Mendez, Acta Mater., vol. 53, no. 3, pp. 555–567, 2005.

[31] S. Hémery, V. T. Dang, L. Signor, and P. Villechaise, Metall. Mater. Trans. A, vol. 49, no. 6, pp. 2048–2056, Jun. 2018.

[32] M. F. Savage, J. Tatalovich, and M. J. Mills, Philos. Mag., vol. 84, no. 11, pp. 1127–1154, 2004.

[33] J. C. Williams, R. G. Baggerly, and N. E. Paton, Metall. Mater. Trans. A Phys. Metall. Mater. Sci., vol. 33, no. 13, pp. 837–850, 2002.

[34] H. Li, D. E. Mason, T. R. Bieler, C. J. Boehlert, and M. A. Crimp, Acta Mater., 2013.
[35] M. F. Savage, J. Tatalovich, M. Zupan, K. J. Hemker, and M. J. Mills, Mater. Sci. Eng. A, vol. 319–321, pp. 398–403, 2001.
[36] T. S. Jun, G. Sernicola, F. P. E. Dunne, and T. B. Britton, Mater. Sci. Eng. A, vol. 649, pp. 39–47, 2016.
[37] J. Gong and A. J. Wilkinson, Acta Mater., vol. 57, no. 19, pp. 5693–5705, 2009.
[38] Y. Xiong, P. Karamched, C.-T. Nguyen, C. M. Magazzeni, E. Tarleton, and A. J. Wilkinson, SSRN Electron. J., 2020.
[39] P. R. Dawson, D. E. Boyce, J. S. Park, E. Wielewski, and M. P. Miller, Acta Mater., vol. 144, pp. 92–106, 2018.
[40] M. Kasemer, M. P. Echlin, J. C. Stinville, T. M. Pollock, and P. Dawson, Acta Mater., vol. 136, pp. 288–302, 2017.
[41] S. Hémery and P. Villechaise, Scr. Mater., vol. 130, pp. 157–160, Mar. 2017.
[42] S. Hémery and P. Villechaise, Acta Mater., vol. 141, pp. 285–293, Dec. 2017.
[43] S. Hémery and P. Villechaise, Metall. Mater. Trans. A Phys. Metall. Mater. Sci., vol. 49, no. 10, pp. 4394–4397, 2018.
[44] S. Suri, G. B. Viswanathan, T. Neeraj, D.-H. Hou, and M. J. Mills, Acta Mater., vol. 47, no. 3, pp. 1019–1034, 1999.
[45] F. Benmessaoud, M. Cheikh, V. Velay, V. Vidal, and H. Matsumoto, Mater. Sci. Eng. A, vol. 774, no. December 2019, p. 138835, 2020.
[46] Z. Zhang, T. S. Jun, T. B. Britton, and F. P. E. Dunne, J. Mech. Phys. Solids, vol. 95, pp. 393–410, 2016.
[47] W. B. Hutchinson and M. R. Barnett, Scr. Mater., vol. 63, no. 7, pp. 737–740, 2010.
[48] G. Lütjering and J. C. Williams, Ed. Springer, vol. second edi, pp. 1–442, 2007.
[49] Z. Zheng, P. Eisenlohr, T. R. Bieler, D. C. Pagan, and F. P. E. Dunne, JOM, Sep. 2019.
[50] R. R. Pawar and V. T. Deshpande, Acta Crystallogr. Sect. A, vol. 24, no. 2, pp. 316–317, 1968.
[51] Z. Chen and S. H. Daly, Exp. Mech., vol. 57, no. 1, pp. 115–127, Jan. 2017.
[52] K. Prasad, R. Sarkar, P. Ghosal, D. V. V. Satyanarayana, S. V. Kamat, and T. K. Nandy, Mater. Sci. Eng. A, vol. 528, no. 22–23, pp. 6733–6741, 2011.
[53] F. Di Gioacchino and J. Quinta da Fonseca, Exp. Mech., vol. 53, no. 5, pp. 743–754, 2013.
[54] Y. Luo, J. Ruff, R. Ray, Y. Gu, H. J. Ploehn, and W. A. Scrivens, Chem. Mater., vol. 17, no. 20, pp. 5014–5023, 2005.
[55] D. Lunt, X. Xu, T. Busolo, J. Quinta da Fonseca, and M. Preuss, Scr. Mater., vol. 145, pp. 45–49, 2018.
[56] J. Schindelin, I. Arganda-Carreras, E. Frise, V. Kaynig, M. Longair, T. Pietzsch, S. Preibisch, C. Rueden, S. Saalfeld, B. Schmid, J.-Y. Tinevez, D. J. White, V. Hartenstein, K. Eliceiri, P. Tomancak, and A. Cardona, Nat. Methods, vol. 9, p. 676, Jun. 2012.
[57] ASTM International - E8/E8M 16a, pp. 1–27, 2009.
[58] M. D. Atkinson, J. M. Donoghue, and J. Q. da Fonseca, Mater. Charact., vol. 168, no. June, p. 110561, 2020.
[59] M. A. Sutton, N. Li, D. Garcia, N. Cornille, J. J. Orteu, S. R. McNeill, H. W. Schreier, X. Li, and A. P. Reynolds, Exp. Mech., vol. 47, no. 6, pp. 789–804, 2007.
[60] J. T. L. Thong, K. W. Lee, and W. K. Wong, Scanning, vol. 23, no. 6, pp. 395–402, 2001.
[61] P. Tomancak, S. Preibisch, and S. Saalfeld, Bioinformatics, vol. 25, no. 11, pp. 1463–1465, 2009.
[62] La Vision - Germany, [Online]. Available: https://www.lavision.de/en/company.php. [Accessed: 27-Oct-2020].
[63] D. Lunt, R. Thomas, M. Roy, J. Duff, M. Atkinson, P. Frankel, M. Preuss, and J. Quinta da Fonseca, Mater. Charact., vol. 163, no. November 2019, p. 110271, 2020.
[64] M. D. Atkinson, R. Thomas, A. Harte, P. Crowther, and J. Quinta da Fonseca, 2020.
[65] C. R. Harris et al., Nature, vol. 585, no. 7825, pp. 357–362, 2020.
[66] T. Goswami, Int. J. Fatigue, vol. 21, no. 1, pp. 55–76, 1999.
[67] C. M. Cepeda-Jiménez, J. M. Molina-Aldareguia, and M. T. Pérez-Prado, Jom, vol. 68, no. 1, pp. 116–126, 2016.
[68] X. Xu, D. Lunt, R. Thomas, R. P. Babu, A. Harte, M. Atkinson, J. Q. da Fonseca, and M. Preuss, Acta Mater., vol. 175, pp. 376–393, 2019.

[69] X. Cheng, G. Wu, and J. Zhao, pp. 828–832, 2013.
[70] F. Roters, P. Eisenlohr, C. Kords, D. D. Tjahjanto, M. Diehl, and D. Raabe, Procedia IUTAM, vol. 3, pp. 3–10, 2012.
[71] F. Roters, P. Eisenlohr, T. Bieler, and D. Raabe, Crystal Plasticity Finite Element Methods. 2010.
[72] F. Roters, P. Eisenlohr, L. Hantcherli, D. D. Tjahjanto, T. R. Bieler, and D. Raabe, Acta Mater., vol. 58, no. 4, pp. 1152–1211, 2010.
[73] A. Ambard, L. Guétaz, F. Louchet, and D. Guichard, Mater. Sci. Eng. A, vol. 319–321, pp. 404–408, 2001.
[74] E. Héripré, M. Dexet, J. Crépin, L. Gélébart, A. Roos, M. Bornert, and D. Caldemaison, Int. J. Plast., vol. 23, no. 9, pp. 1512–1539, 2007.
[75] T. Maiti and P. Eisenlohr, Scr. Mater., vol. 145, pp. 37–40, 2018.
[76] R. A. Lebensohn, A. D. Rollett, and P. Suquet, Jom, vol. 63, no. 3, pp. 13–18, 2011.
[77] R. A. Lebensohn, A. K. Kanjarla, and P. Eisenlohr, Int. J. Plast., vol. 32–33, pp. 59–69, 2012.
[78] R. Berry and G. Raynor, Research, vol. 6, pp. 21s-23s, 1953.
[79] J. Spreadborough and J. W. Christian, Proc. Phys. Soc., vol. 74, no. 5, pp. 609–615, 1959.
[80] C. J. McHargue and J. P. Hammond, Acta Metall., vol. 1, no. 6, 1953.
[81] D. Banerjee and J. C. Williams, Def. Sci. J., vol. 36, no. 2, pp. 191–206, 1986.
[82] E. O. Hall, Proc. Phys. Soc. Sect. B, vol. 64, no. 9, pp. 742–747, 1951.
[83] S. Waheed, Z. Zheng, D. S. Balint, and F. P. E. Dunne, Acta Mater., vol. 162, pp. 136–148, 2019.
[84] G. Welsch and W. Bunk, Metallurgical and materials transactions., vol. 13, no. 5. Published jointly by the Minerals Metals & Materials Society and ASM International, Warrendale, PA ;, pp. 889–899, 1982.
[85] Z. Zhang, M. A. Cuddihy, and F. P. . Dunne, Proc.R.Soc.A, 2015.
[86] F. P. E. Dunne, D. Rugg, and A. Walker, Int. J. Plast., vol. 23, no. 6, pp. 1061–1083, 2007.
[87] C. Lavogiez, S. Hémery, and P. Villechaise, Scr. Mater., vol. 183, no. 0001, pp. 117–121, 2020.
[88] F. Bridier, P. Villechaise, and J. Mendez, Acta Mater., vol. 56, no. 15, pp. 3951–3962, 2008.
[89] M. P. Echlin, J. C. Stinville, V. M. Miller, W. C. Lenthe, and T. M. Pollock, Acta Mater., vol. 114, pp. 164–175, Aug. 2016.
[90] Z. Zhang, D. Lunt, H. Abdolvand, A. J. Wilkinson, M. Preuss, and F. P. E. Dunne, Int. J. Plast., vol. 108, no. April, pp. 88–106, 2018.
[91] T. S. Jun, Z. Zhang, G. Sernicola, F. P. E. Dunne, and T. B. Britton, Acta Mater., vol. 107, pp. 298–309, 2016.
[92] D. Caillard, M. Gaumé, and F. Onimus, Acta Mater., vol. 155, pp. 23–34, 2018.
[93] Z. Zhang, T. S. Jun, T. B. Britton, and F. P. E. Dunne, Acta Mater., vol. 118, pp. 317–330, 2016.
[94] P. O. Tympel, T. C. Lindley, E. A. Saunders, M. Dixon, and D. Dye, Acta Mater., vol. 103, pp. 77–88, 2016.
[95] M. R. Bache, W. J. Evans, B. Suddell, and F. R. M. Herrouin, Int. J. Fatigue, vol. 23, pp. 153–159, 2001.
[96] V. Sinha, M. J. Mills, and J. C. Williams, Metall. Mater. Trans. A Phys. Metall. Mater. Sci., vol. 37, no. 6, pp. 2015–2026, 2006.
[97] W. J. Evans and M. R. Bache, Int. J. Fatigue, vol. 16, no. 7, pp. 443–452, 1994.
[98] D. Rugg, M. Dixon, and F. P. E. Dunne, J. Strain Anal. Eng. Des., vol. 42, no. 4, pp. 269–279, 2007.
[99] V. Hasija, S. Ghosh, M. J. Mills, and D. S. Joseph, Acta Mater., vol. 51, no. 15, pp. 4533–4549, 2003.

7 Appendix

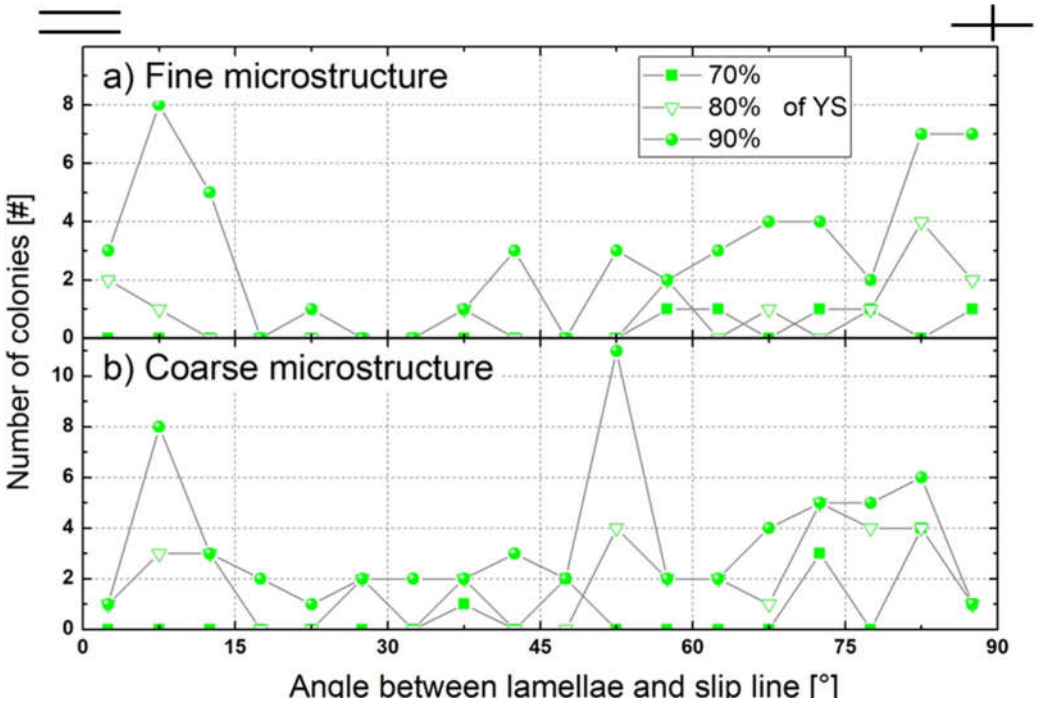

Fig. A 1: Absolute frequency distribution of angles between slip line and lamellae in deformed secondary α colonies in (**a**) fine and (**b**) coarse microstructure.

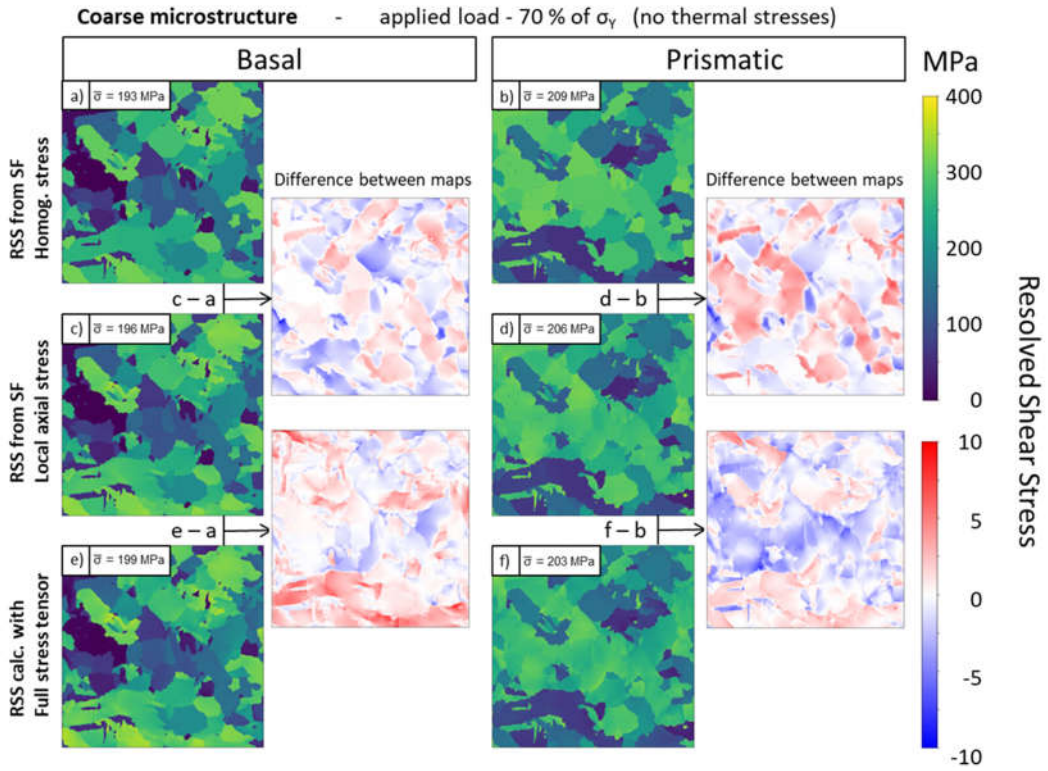

Fig. A 2: Maps of resolved shear stress RSS on basal and prismatic slip systems for the material with coarse microstructure. The simulations are for loading to 70% of 0.2% proof stress of initially stress-free material. The RSS values have been calculated according to three different approaches. Additionally, maps showing the difference between the calculation methods are displayed.

5 Summary and Conclusion

The role of microstructure on strain localisation was studied in the near α titanium alloy TIMETAL®834, during initial loading after 10 minutes load/hold periods at stresses below macroscopic yield. Comparisons were made between samples with large and small prior β grain sizes, and coarse and fine transformations products.

In-depth material characterisation showed that creating a coarser transformation product by applying slower cooling rates after the solution heat treatment, simultaneously results in larger primary α grains due to grain growth. Element segregation leads to the formation of a core-shell structure in these grains, with the shell being depleted in β stabilising elements, resulting in fewer α_2 precipitates, or even a complete absence of these particles in these regions. This shows that it is not possible to vary one microstructural parameter by adapting the TMP route without changing other microstructural features. Material characterisation also showed that the sizes of prior-β grains in the analysed samples were not uniform and that the outlines of the grains can be diffuse. This may be due to partial break up or recrystallization of the β grains during TMP.

In-situ HRDIC, in combination with EBSD mapping, was used to study the deformation mechanisms at applied stresses below the macroscopic yield point. For all microstructures, plastic deformation in the form of discrete slip bands was observed at stresses as low as 70% of $\sigma_{0.2\%}$. The deformation in the near-α Ti alloys TIMETAL®834 with bi-modal microstructure after dwell at stresses below yield proceeds as follows. Initial slip is localised in primary α grains and the activated slip is of basal type. Generally, secondary α colonies appear to have a higher strength than primary α grains, particularly when the cooling rate after the solution heat treatment was high and fine secondary α colonies, or a combination of fine α secondary α colonies and a basketweave structure, were formed. In the material with fine transformation product, slip activation in colonies is particularly difficult, and therefore slip during the first load-step was almost exclusively restricted to primary α grains and slip bands were separated from each other by undeformed secondary α colonies. On the other hand, slip was readily activated in colonies for the material condition with coarse transformation product even for the lowest applied stress, leading to the formation of slip traces across several grains. Longer slip bands can lead to the pile-up of more dislocations at grain boundaries, leading to higher stress-concentrations and later on time dependant stress redistributions, which could be a reason why, according to reports in the literature, samples with coarser microstructures generally exhibit a higher susceptibility to cold creep and CDF.

For initial plastic deformation, basal slip was identified to be the dominant slip mode, but for increasing applied stresses a changeover to prismatic slip was observed. The effect of elastic anisotropy on local stress states and residual stresses caused by the anisotropy of the thermal expansion coefficient were investigated using full-field elastically anisotropic modelling. The elastic stresses determined by modelling showed that elastic anisotropy could not explain the early activation of basal slip, leading to the conclusion that CRSS values are lower for basal than for prismatic slip. The changeover from basal to prismatic slip as dominant slip mode for increasing stresses was explained by strain hardening effects that decrease the relative difference between all slip systems and the higher strain rate sensitivity for basal slip compared to prismatic slip, which leads to a higher absolute increase of slip resistance for basal slip.

The elastic anisotropy leads to increased stresses in grains with small declination angles between the loading direction and the c-axis of the grain and therefore the activation of basal slip has been observed in grains with declination angles as low as 26°. These grains are potential sites for the formation of facets under CDF loading conditions. According to proposed mechanisms for CDF, the formation of facets requires a ‘rogue’ grain combination, where slip is initially activated in a soft grain and load shedding induces slip in an adjacent hard grain. This is in contradiction with the results of this study, where basal slip was not only activated in well-aligned grain but also directly in hard grains with low declination angles. The presence of ‘rogue’ grain combinations could have enhanced the activation of slip in grains with low declination angles even further, but it appears that this grain combination is not obligatory for it. This gives a larger number of sites for the activation of facets than when restricting the criteria to the ‘rogue’ grain combination. This observation and the fact that basal slip is the dominant slip mode under cold creep loading conditions should be considered in the development of models for predicting CDF behaviour/deformation.

6 Future Work

An ex-situ HRDIC experiment, applying loading conditions comparable to the in-situ experiment in this study, should be conducted to investigate the effect of a core-shell structure in primary α grains on slip patterns. It has been demonstrated that segregation effects during cooling after the solution heat treatment lead to the formation of a core-shell structure in primary α grains in alloys with bi-modal microstructures. Lower strength and different slip behaviour may be expected in the shell-regions, due to the lower Al-concentration and the absence of α_2-precipitates. A different slip pattern in the shell regions may influence the interaction of dislocations with grain boundaries, e.g. pile-ups or slip transmission. In this study, as an in-situ approach was applied, the spatial resolution of the HRDIC analysis was too low to investigate such effects, while high enough spatial resolutions can be achieved in ex-situ experiments.

Additional experiments should be conducted on the same material, utilising techniques that allow slip trace analysis or observation on a larger length scale. As grains of the high-temperature β-phase can be large (several mm across) compared to the area that has been covered by in-situ HRDIC, in this study 250x250 µm², it was difficult to investigate the effect of the prior β-grain morphology on slip behaviour. This could be SEM-based ex-situ DIC, which enables longer imaging-times and therefore the coverage of larger areas. Also applying a larger speckle pattern would enable the imaging of larger areas, as images can be recorded at a lower spatial resolution. Further, optical DIC could be used, which enables to imaging of areas several times larger than in SEM-based DIC. Also, as has been demonstrated, slip trace observation using optical dark-field microscopy can be used to observe local slip events, while covering areas in the cm-range.

The in-situ HRDIC experiments and CP-modelling performed in this study should be repeated on TIMETAL®834 samples with sharp microtextured regions to investigate how those influences local stress states/concentrations, early slip activation, time dependant development of slip patterns and macroscopic creep behaviour. The material investigated in the current study was free of preferential crystallographic orientations as well as micro-textured regions, not allowing any conclusions about how such microstructural features would influence the strain evolution under cold creep loading conditions.

The slip behaviour has been investigated for different load steps at room temperature, for a dwell time of 10 minutes. The same experiment should be repeated at elevated temperature (> 230°C [1]) to investigate the effect of temperature on slip behaviour. This would be of interest, as it has been observed, that the susceptibility to CDF is diminishing for increasing temperatures and therefore also a change in slip behaviour and deformation mechanisms could be expected. Furthermore, HRDIC could be used to investigate the slip behaviour at a constant stress level, but at different time steps, to investigate the evolutions of the slip pattern with time during cold creep deformation. To be able to test enough time steps, new in-situ set-ups, with automated imaging and mechanical loading, could be used.

The creep tests performed in creep rigs should be repeated using cylindrical samples, instead of flat dog-bone specimens, with a larger cross-section. Creep tests carried out in this study showed that the creep-rate is sensitive to small changes in the applied load, particularly for stresses close to the 0.2 % proof stress, making it difficult to investigate and quantify the differences in cold creep

susceptibility of the different material conditions. The dog-bone specimens used for this test had cross-sections of only 3 mm², making it difficult to apply accurate stresses in the used set-up. Furthermore, flat specimens may be susceptible to bending and torsion, which could lead to strain artefacts. These effects could be reduced by using cylindrical specimens with a larger cross-section.

3D-EBSD analysis should be applied to investigate the microstructure beneath the area on the surface analysed by HRDIC. This data could be used to create more representative representations of the microstructure for CP simulations. In the current study, quasi 3D or 2.5D microstructures which were created by extruding 2D EBSD maps, where used for the CP simulations. With this approach, it was not possible to investigate the effect of the underlying microstructure on slip activity at the sample surface.

7 Appendix

7.1 Microstructural characterisation

7.1.1 Optical microscopy

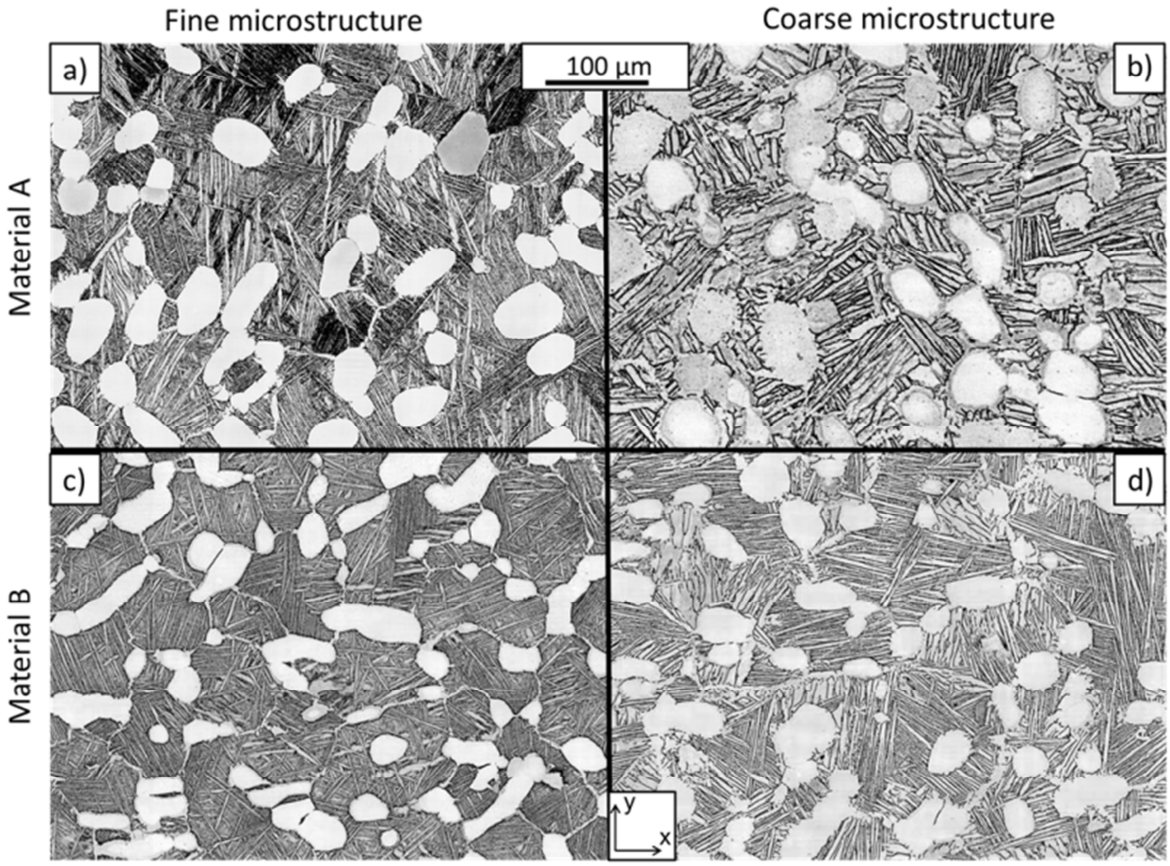

Fig. 7-1: Optical micrographs of the microstructure of a) & b) Material A and c) & d) Material B with a) & c) fine and b) & d) coarse microstructure.

Table 7-1: Summary of the material characterisation based on the micrographs in Fig. 7-1.

	Material A		Material B	
Microstructure	Fine	Coarse	Fine	Coarse
Lamella spacing	1.2 ± 0.1 µm	2.5 ± 0.8 µm	1.1 ± 0.3 µm	1.8 ± 0.4 µm
Primary α Volume fraction	19.7 ± 0.7 %	24.6 ± 0.8 %	18.2 ± 1.0 %	23.1 ± 0.3 %
Average α(P) grain size (area)	506 ± 9 µm²	551 ± 48 µm²	379 ± 18 µm²	469 ± 11 µm²
Colonie length	41 ± 15 µm	58 ± 16 µm	37 ± 12 µm	39 ± 16 µm
Colonie width	29 ± 7 µm	32 ± 14 µm	25 ± 11 µm	23 ± 8 µm

7.1.2 Grain morphology of α- and high temperature β-phase

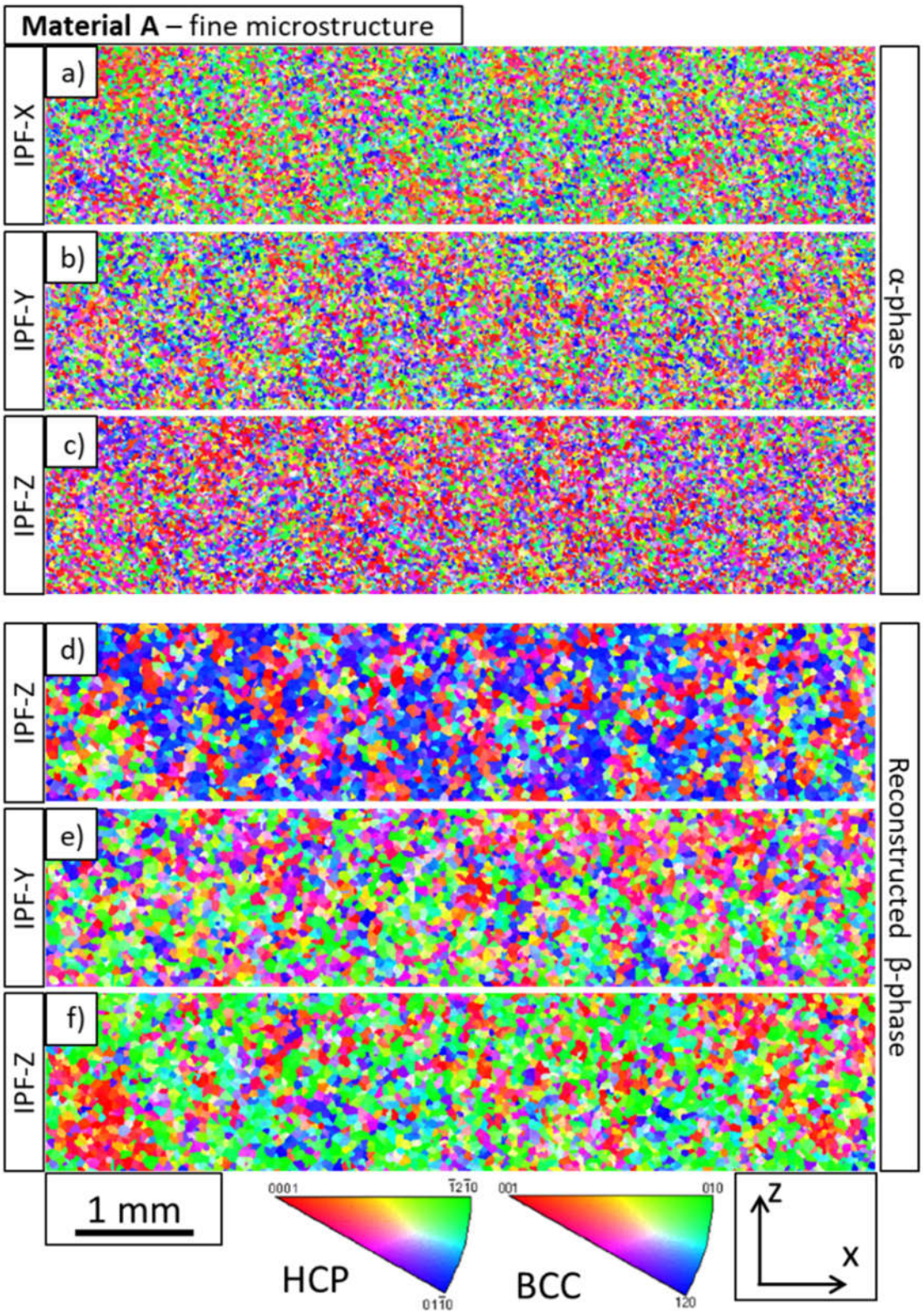

Fig. 7-2: Crystallographic orientation maps for 'Material A – fine microstructure'. The orientation and location of the analysed area is identical to the ROI in the HRDIC experiments. The maps for the α-phase (**a - c**) have been recorded by EBSD mapping, the maps of the high temperature β-phase (**d - f**) having been created using β-reconstruction software.

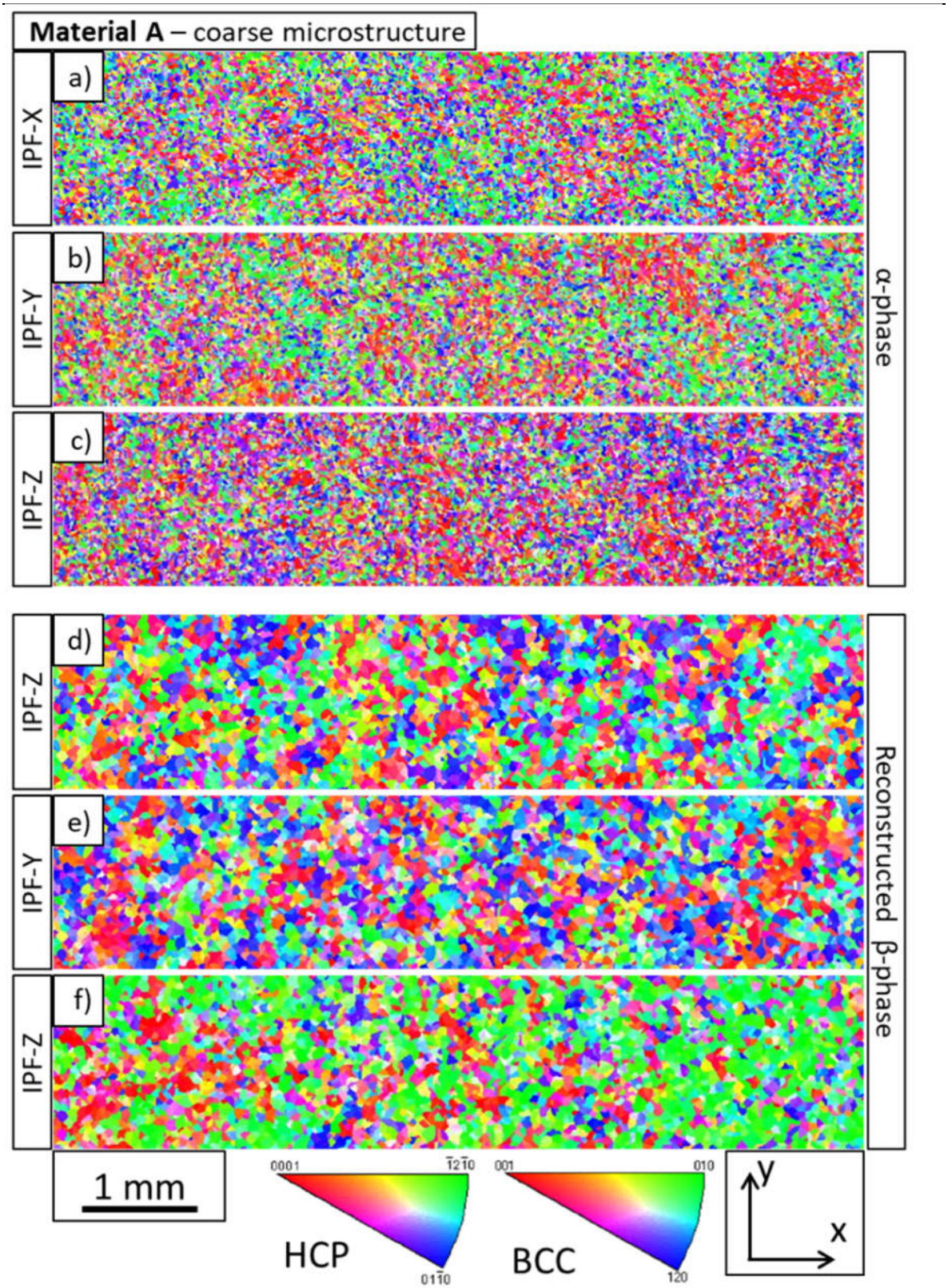

Fig. 7-3: Crystallographic orientation maps for 'Material A – coarse microstructure'. The orientation and location of the analysed area is identical to the ROI in the HRDIC experiments. The maps for the α-phase (**a - c**) have been recorded by EBSD mapping, the maps of the high temperature β-phase (**d - f**) having been created using β-reconstruction software.

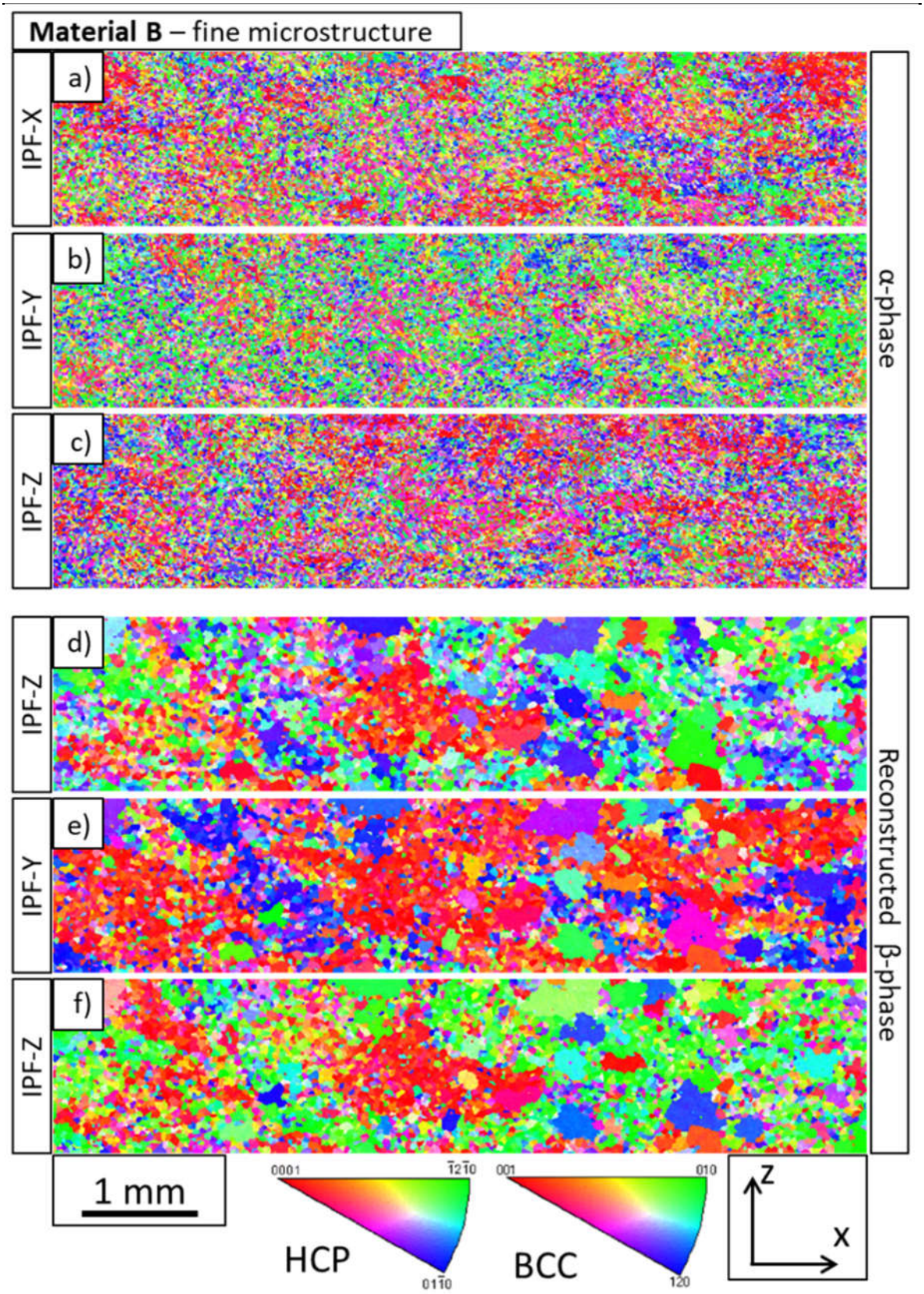

Fig. 7-4: Crystallographic orientation maps for 'Material B – fine microstructure'. The orientation and location of the analysed area is identical to the ROI in the HRDIC experiments. The maps for the α-phase (**a - c**) have been recorded by EBSD mapping, the maps of the high temperature β-phase (**d - f**) having been created using β-reconstruction software.

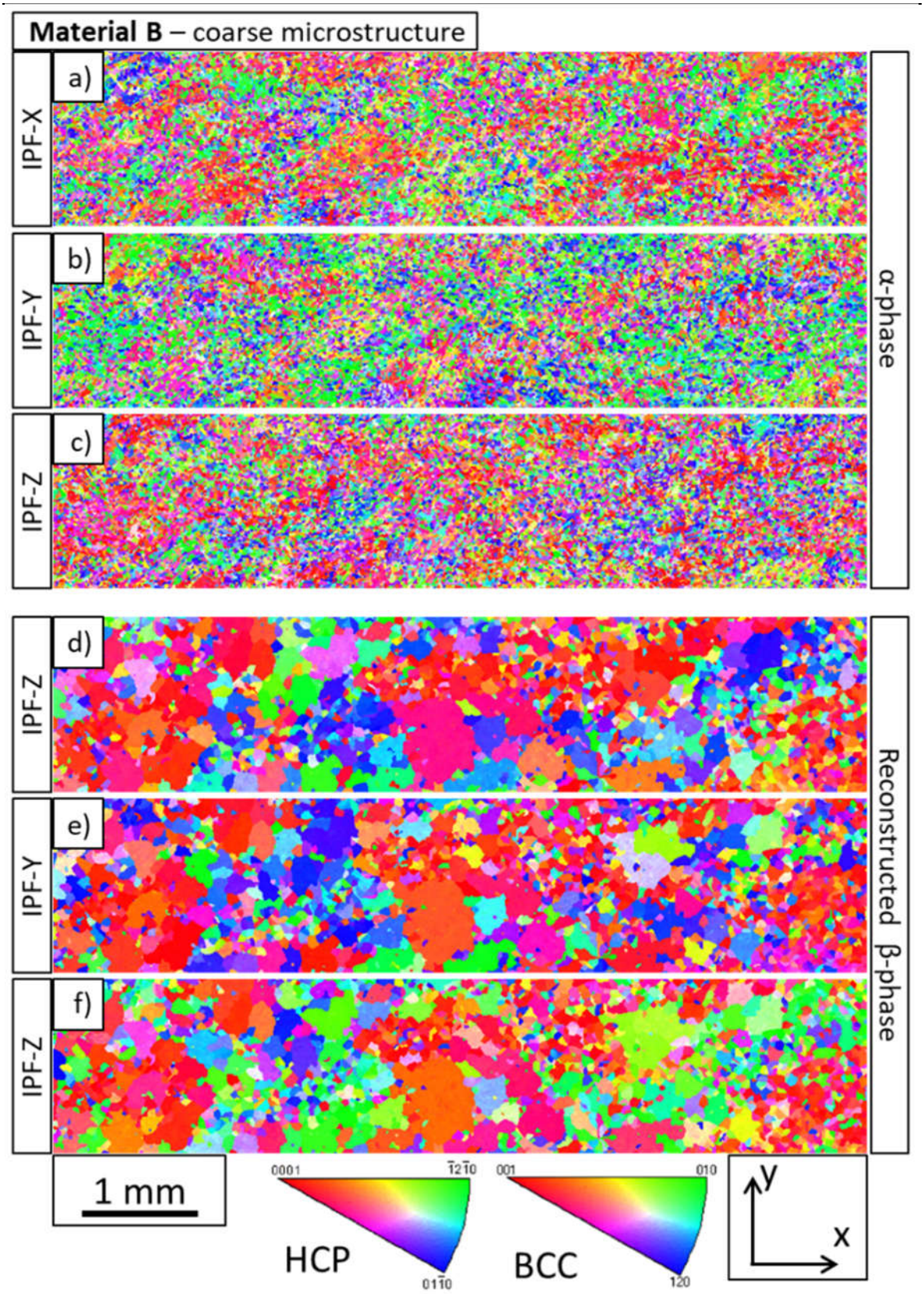

Fig. 7-5: Crystallographic orientation maps for 'Material B – coarse microstructure'. The orientation and location of the analysed area is identical to the ROI in the HRDIC experiments. The maps for the α-phase (**a - c**) have been recorded by EBSD mapping, the maps of the high temperature β-phase (**d - f**) having been created using β-reconstruction software.

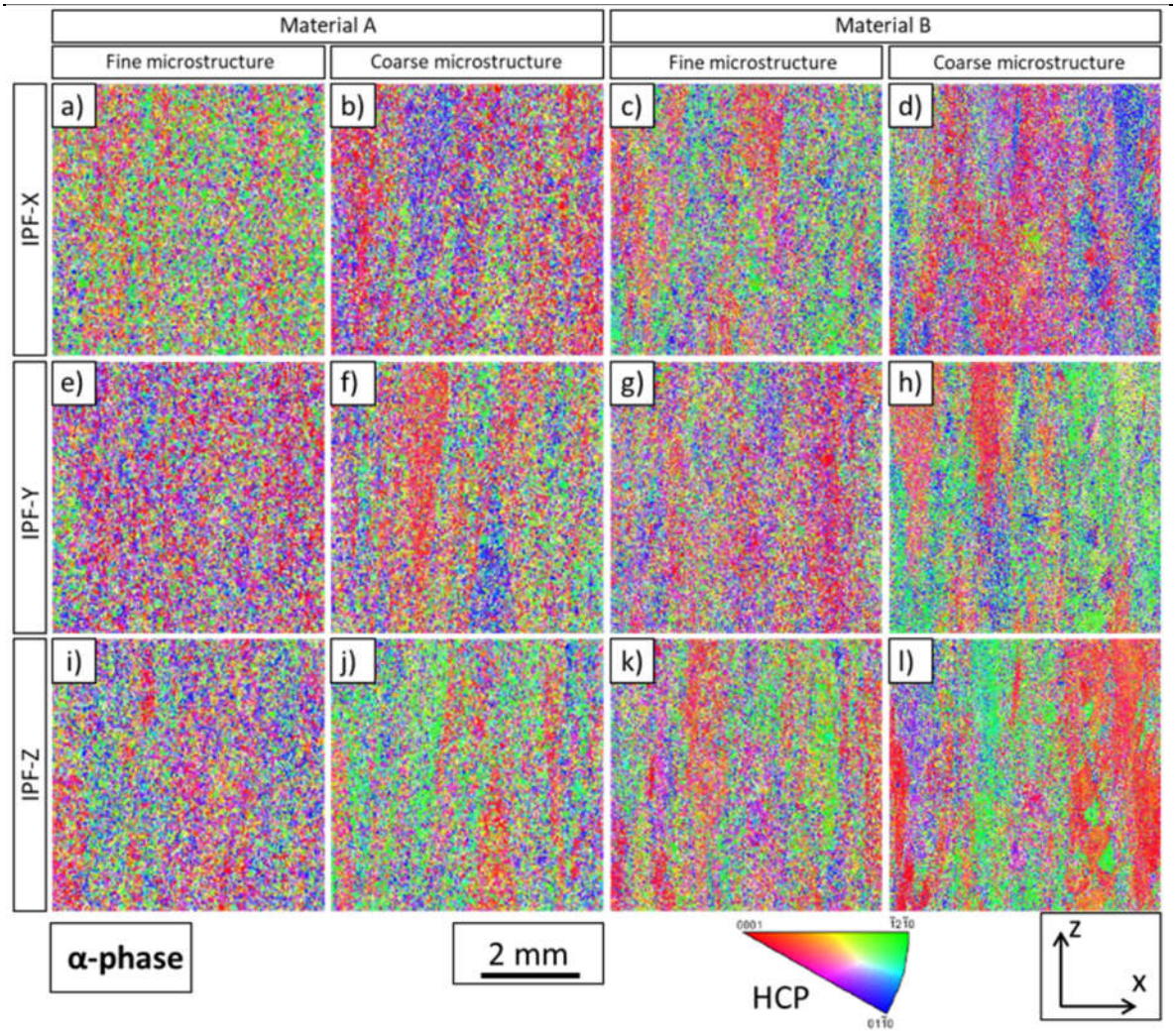

Fig. 7-6: Crystallographic orientation maps of the α-phase for all material conditions, showing the microstructure through the sample thickness.

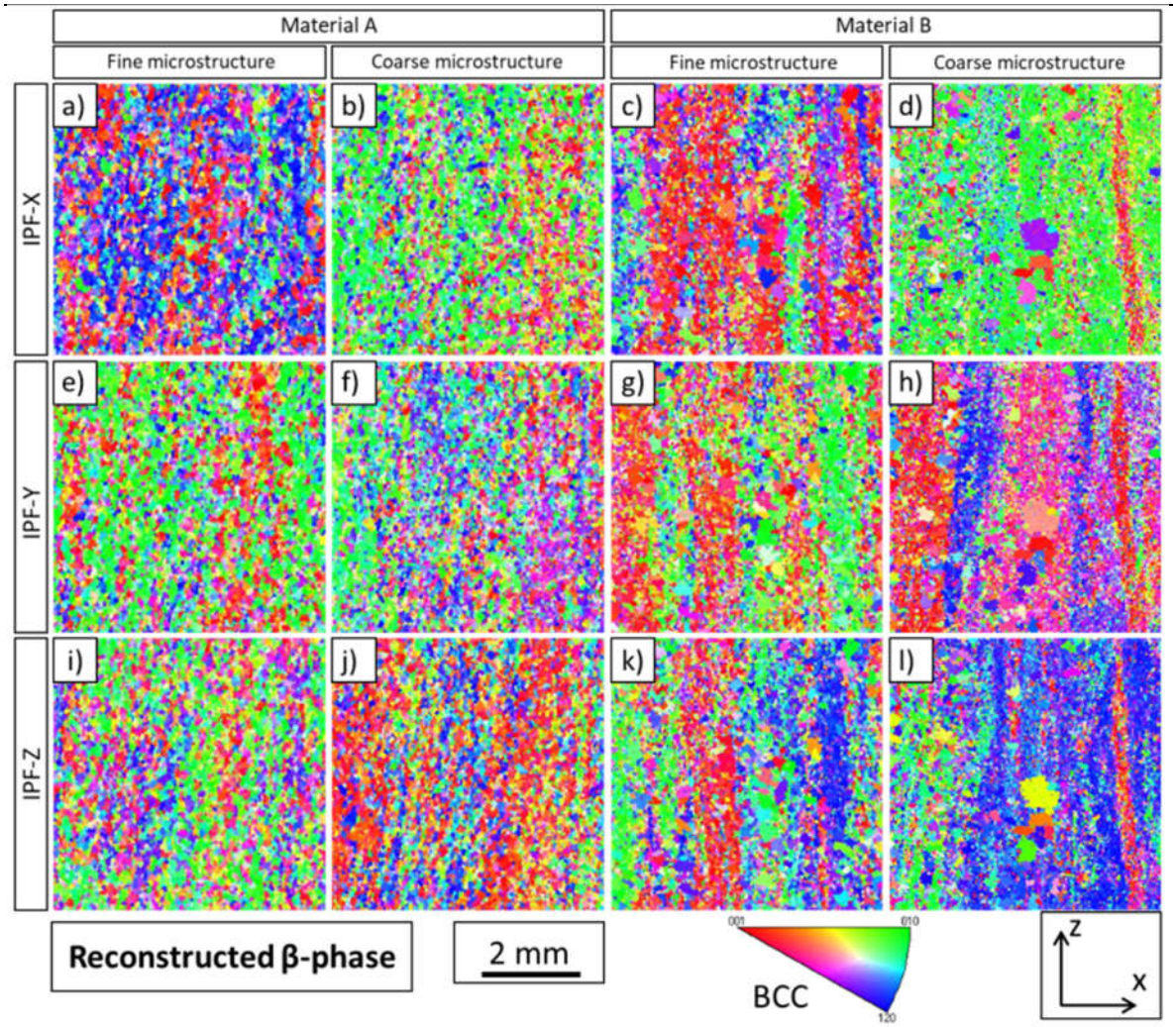

Fig. 7-7: Crystallographic orientation maps of the reconstructed high-temperature ß-phase for all material conditions, showing the microstructure through the sample thickness.

7.1.3 Morphology of β-phase

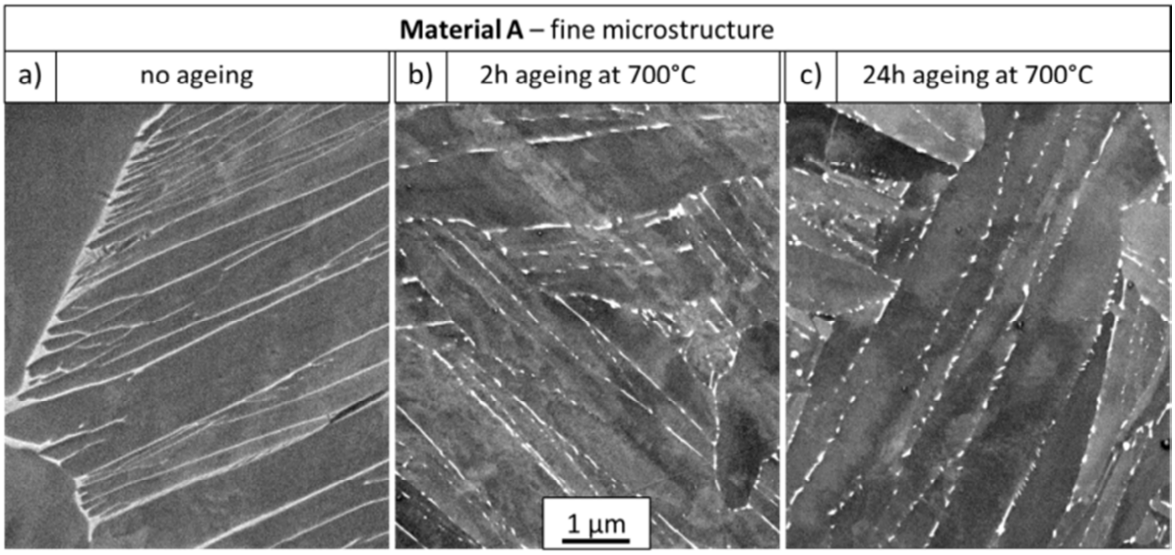

Fig. 7-8: BSE-SEM image of 'Material A – fine microstructure', revealing the morphology of the β-phase for **a)** no ageing, **b)** 2h ageing at 700°C and **c)** 24h ageing at 700°C after the solution heat treatment.

7.1.4 Characterisation of silicide precipitates

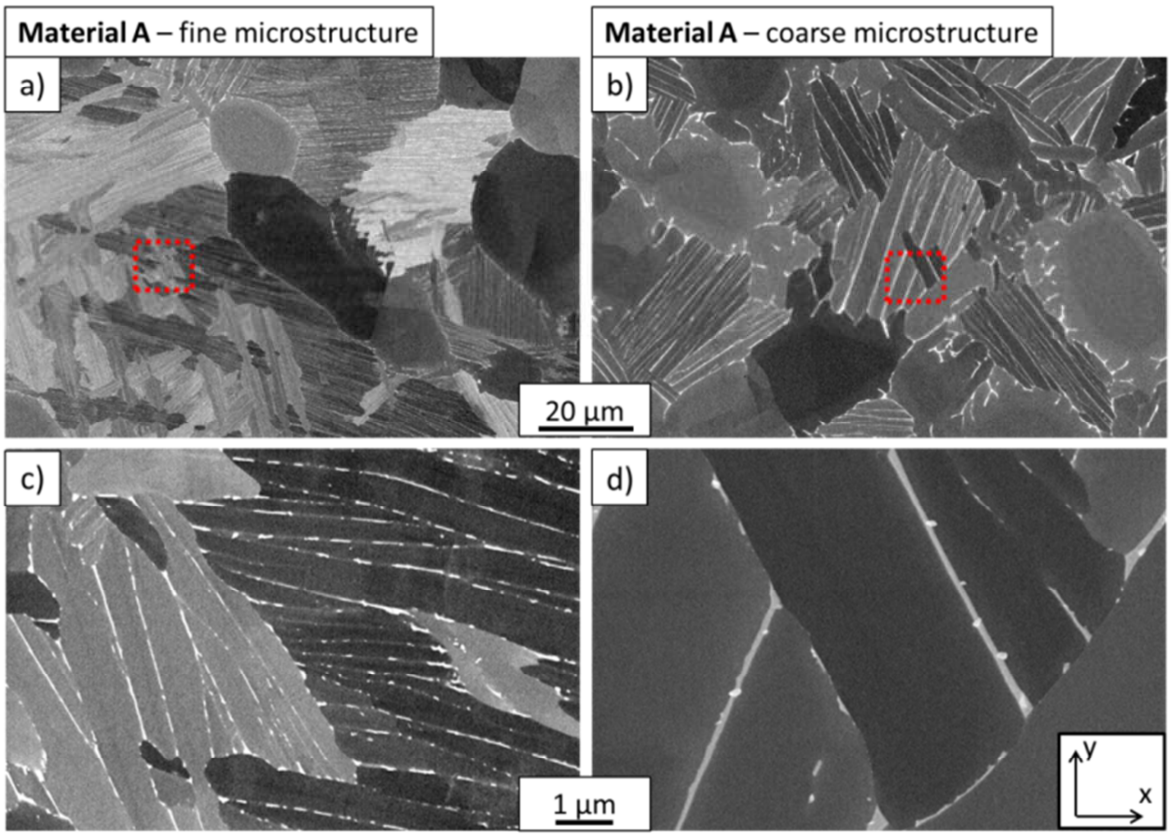

Fig. 7-9: BSE-SEM images at (**a & b**) low and (**c & d**) high magnification of α/β-lamellae in (**a & c**) 'Material A – fine microstructure' and (**b & d**) 'Material A – coarse microstructure'

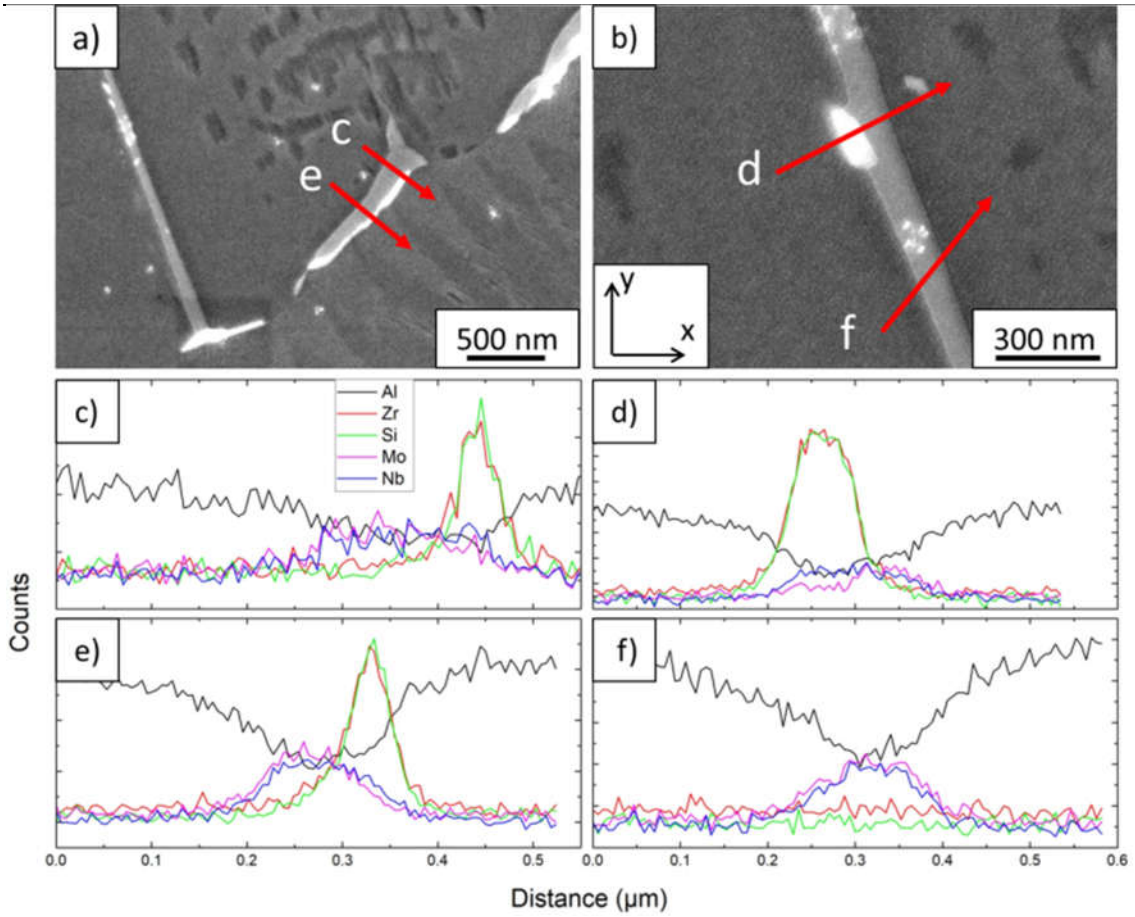

Fig. 7-10: (**a & b**) SE-SEM images and (**c - f**) SEM-EDS line scans of silicides at boundaries between β-phase and (**a, c & e**) primary-α phase and (**b, d & f**) secondary-α phase.

7.2 Mechanical testing

7.2.1 Baseline characterisation

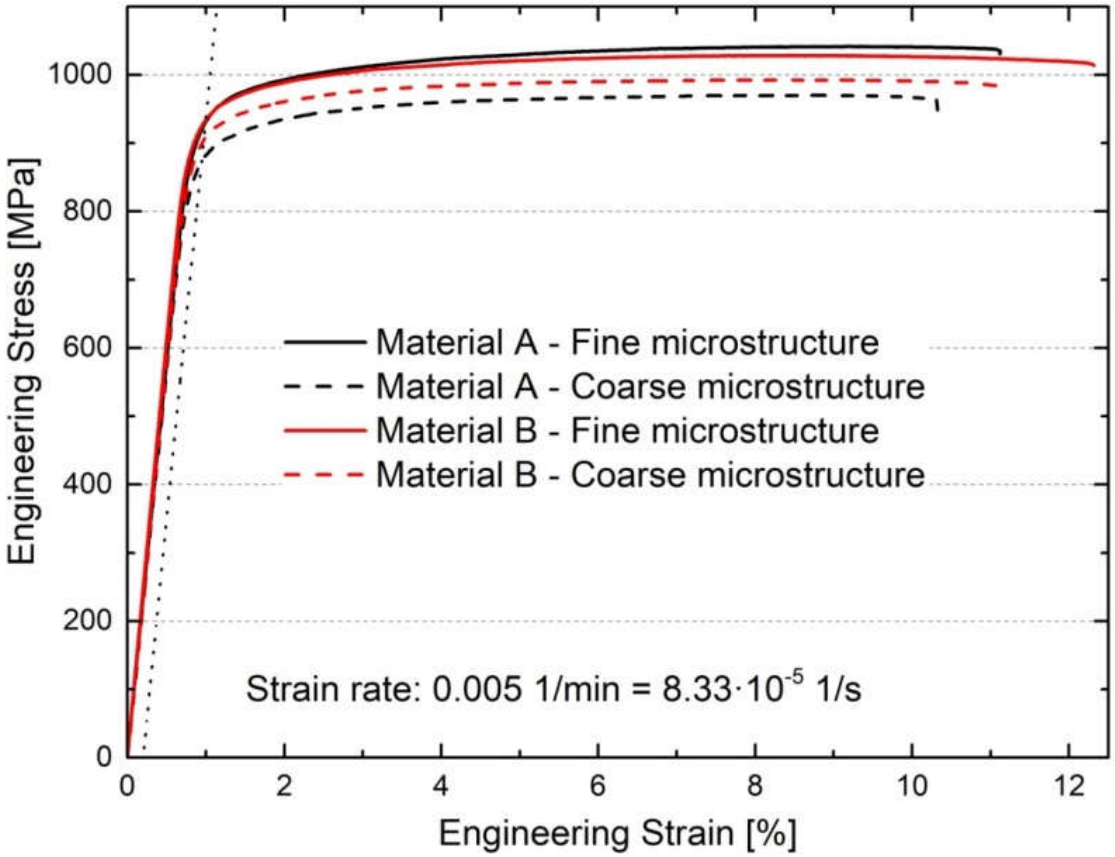

Fig. 7-11: Stress-strain curves for all material conditions recorded at a strain rate of $8.33 \cdot 10^{-5}$ 1/s. The dotted line indicates a plastic strain of 0.2% for a stiffness of 117 GPa.

Table 7-2: Results of the mechanical baseline characterisation in **Fig. 7-11**.

Material	Microstructure	Young's modulus		0.2 % Proof stress		UTS [MPa]
		μ [GPa]	σ [GPa]	Strain [%]	Stress [MPa]	
A	Coarse	117	1	0.9	873	970
	Fine	114	1	1.0	931	1042
B	Coarse	116	1	1.0	905	992
	Fine	122	1	1.0	934	1029

μ mean value
σ standard deviation

7.2.2 Ex-situ creep testing

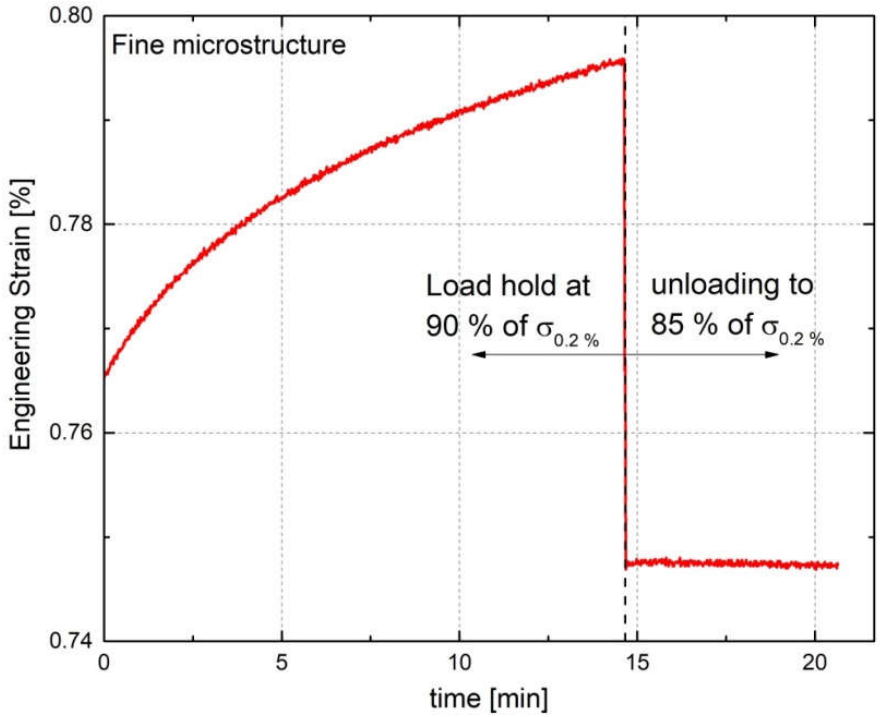

Fig. 7-12: Engineering strain plotted as a function of time, for a load-hold at initially 90% of $\sigma_{0.2\%}$, followed by a reduction of load to 85% of $\sigma_{0.2\%}$.

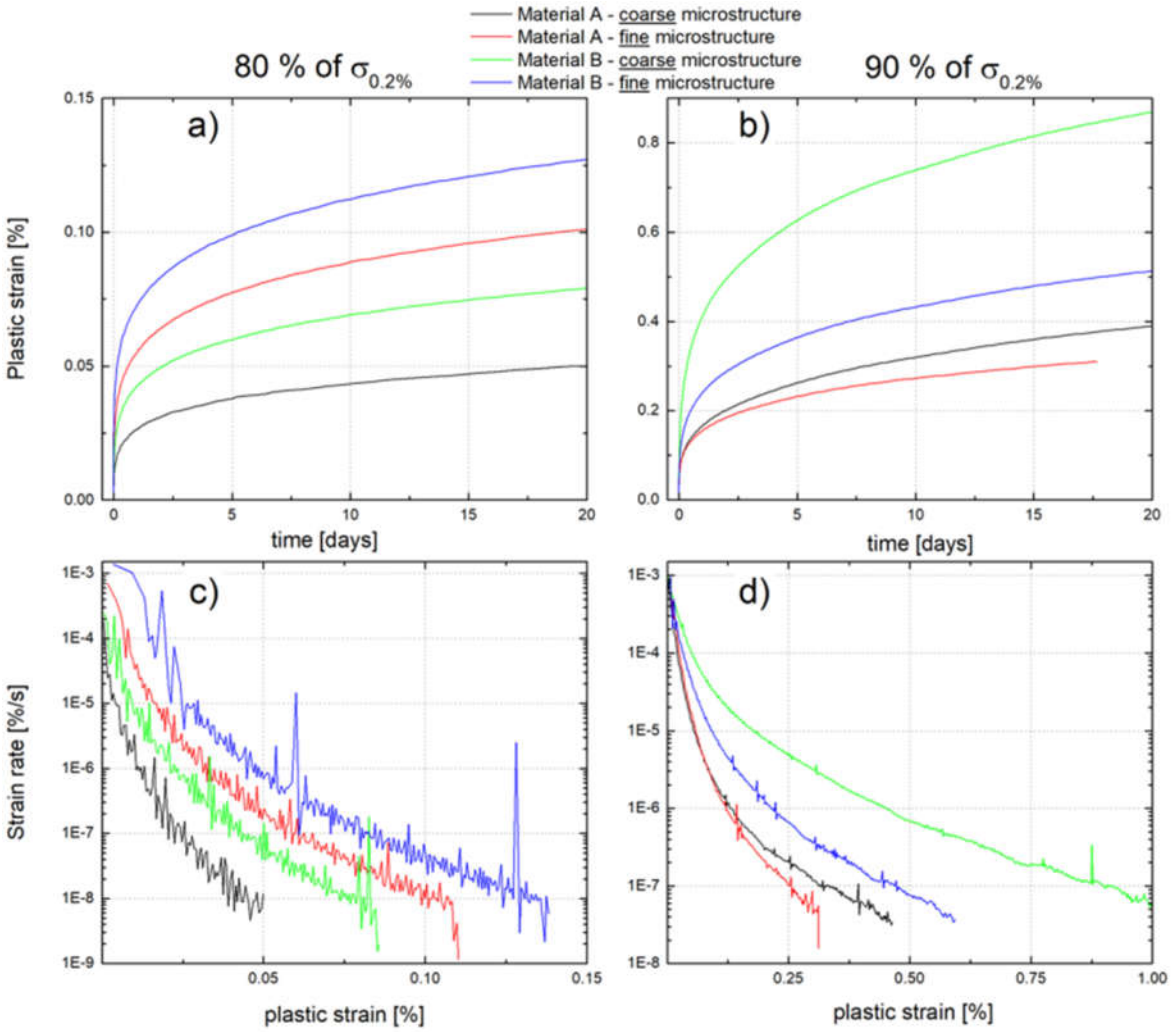

Fig. 7-13: (**a & b**) Plastic strain as a function of time and (**c & d**) strain rate as a function of plastic strain for room temperature creep test at (**a & c**) 80% of $\sigma_{0.2\%}$ and (**b & d**) 90% of $\sigma_{0.2\%}$.

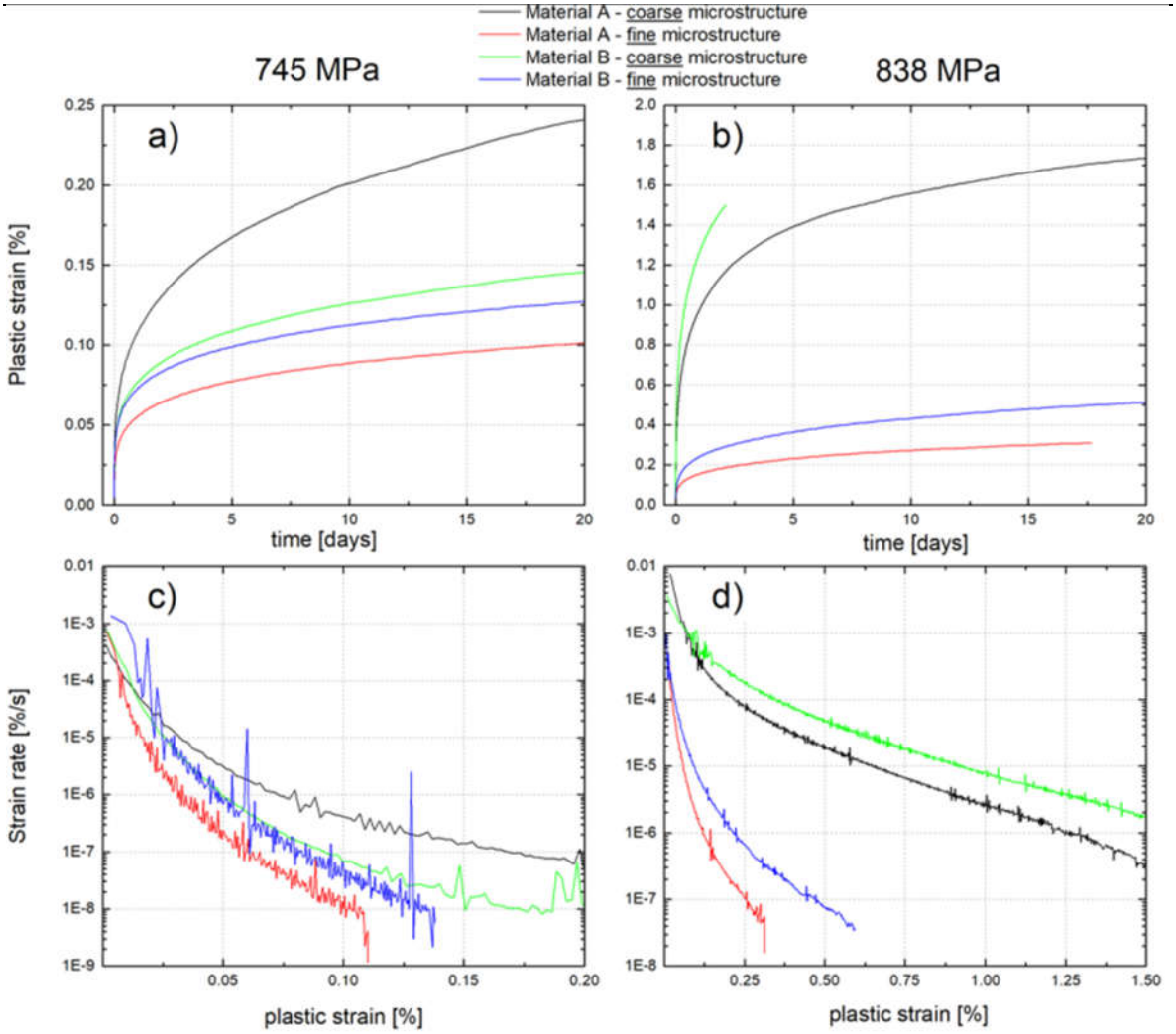

Fig. 7-14: (**a & b**) Plastic strain as a function of time and (**c & d**) strain rate as a function of plastic strain for room temperature creep test. All samples have been test at the same absolute load of (**a & c**) 745 MPa and (**b & d**) 838 MPa.

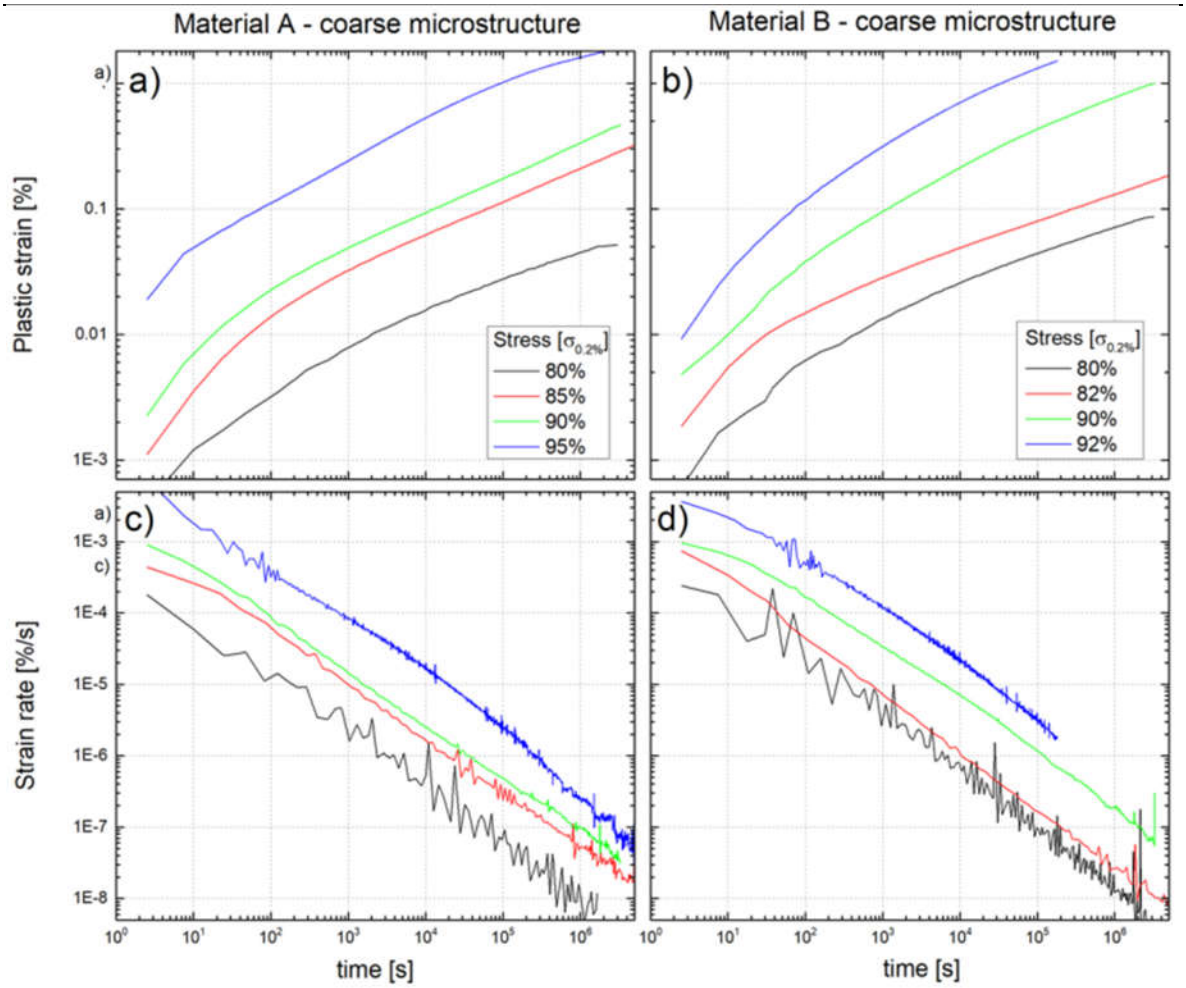

Fig. 7-15: (**a & b**) Plastic strain and (**c & d**) strain rate as a function of time for room temperature creep testing of two material conditions (**a & c**) 'Material A- coarse microstructure' and (**c & d**) 'Material B- coarse microstructure' at four different stress levels.

7.2.3 Slip trace analysis – optical microscopy

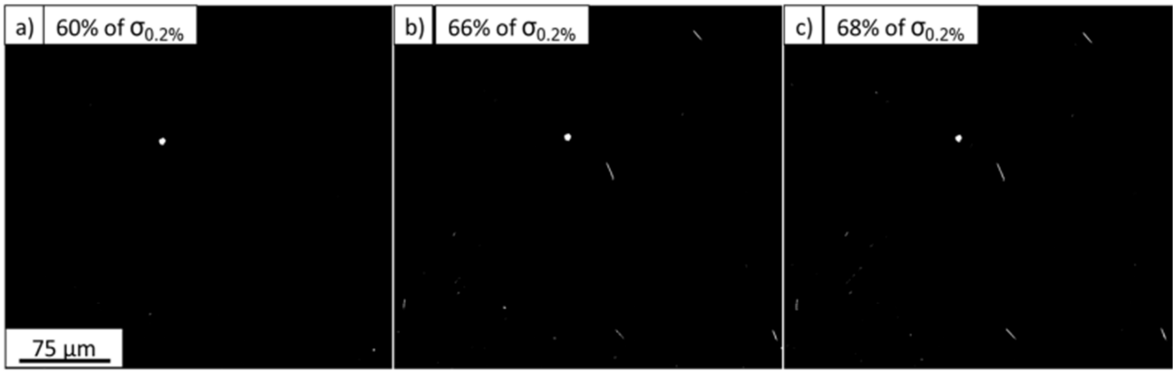

Fig. 7-16: Observation of the formation of the first slip traces at a) 60%, b) 66% and c) 68% of $\sigma_{0.2\%}$ in material with coarse microstructure using optical dark-field microscopy.

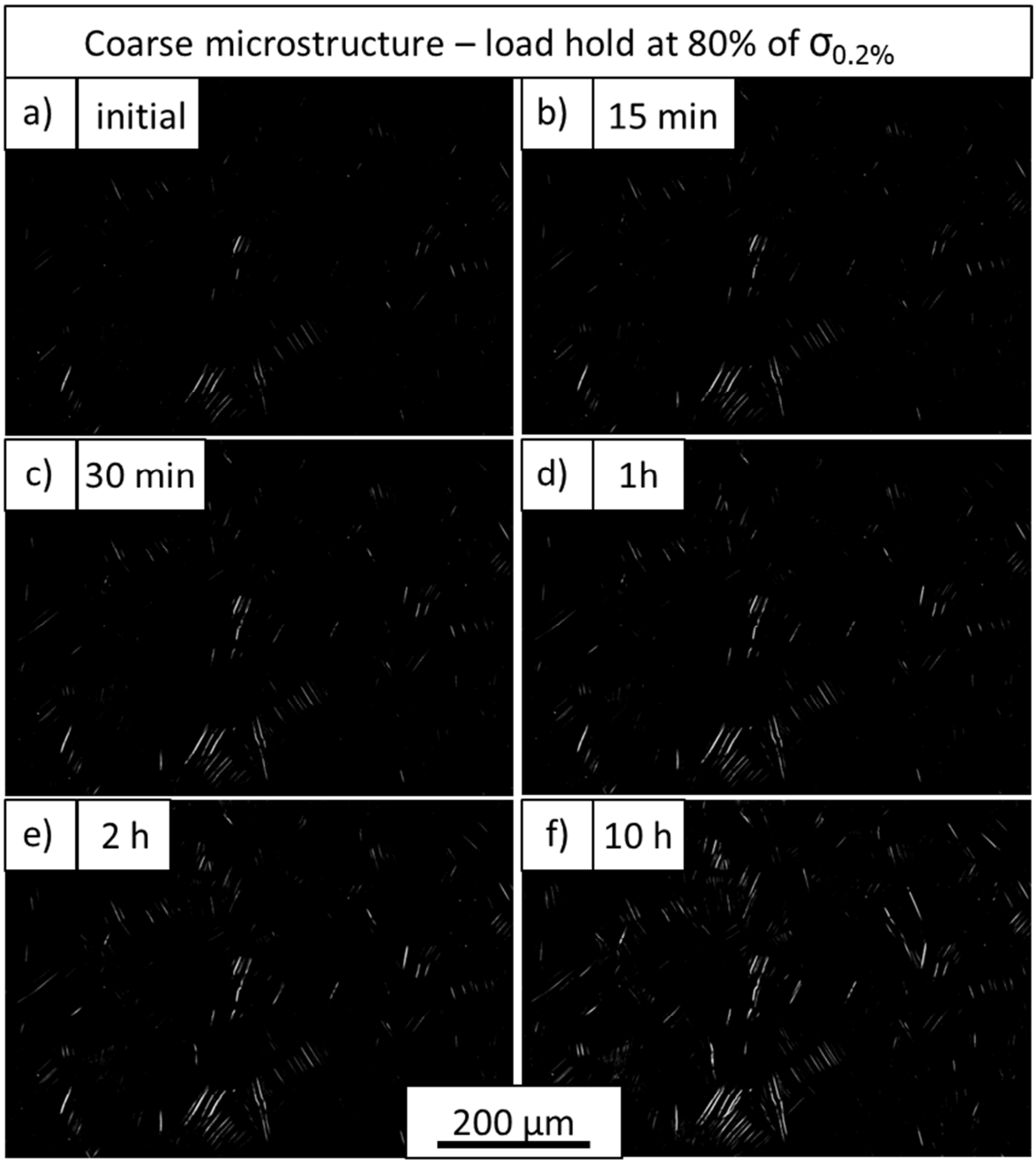

Fig. 7-17: Development of the slip pattern during cold-creep deformation at 80% of $\sigma_{0.2\%}$ in material with coarse microstructure at different time steps. Image a) ('initial') was recorded directly after applying the mechanical load.

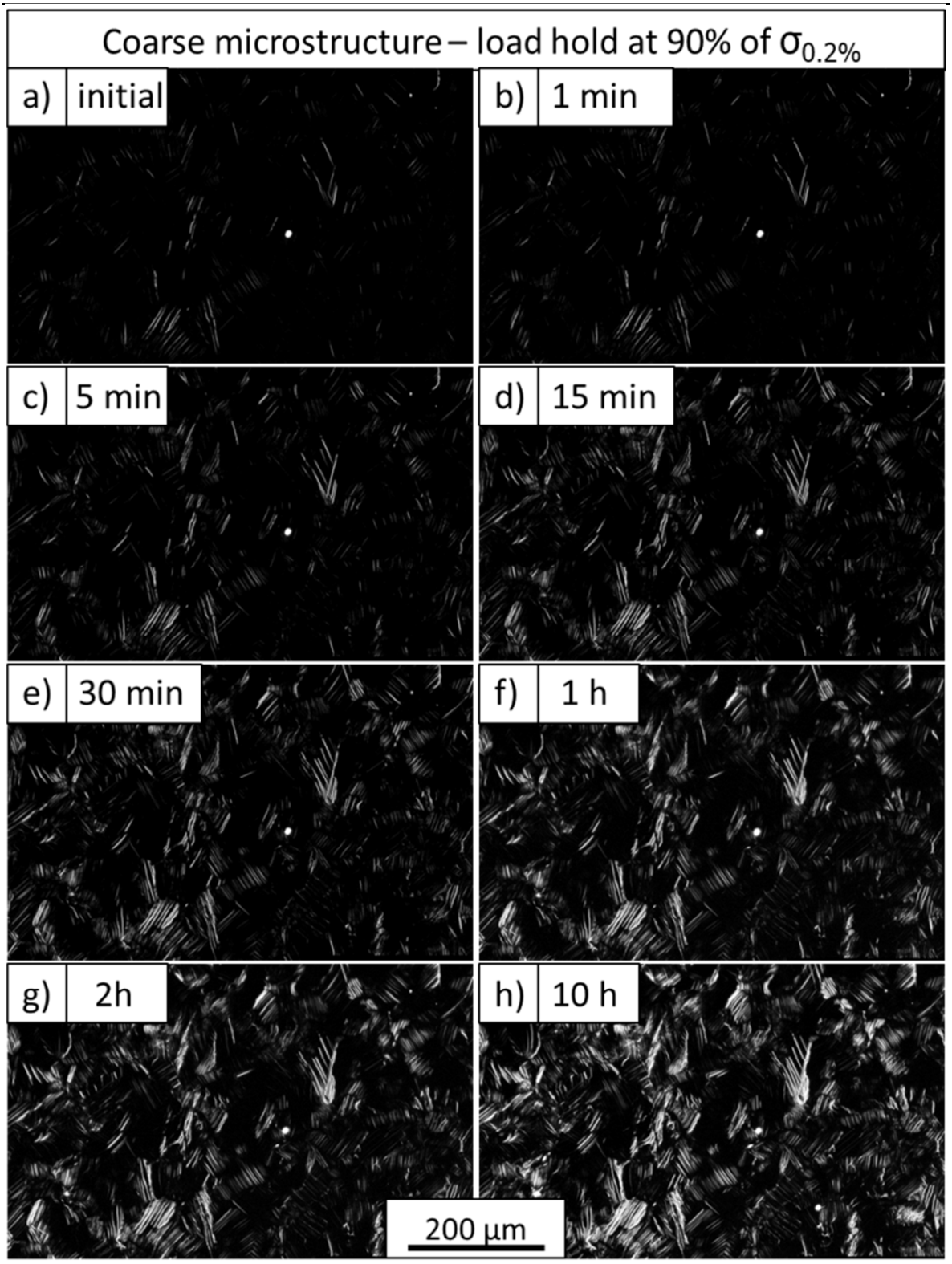

Fig. 7-18: Development of the slip pattern during cold-creep deformation at 90% of $\sigma_{0.2\%}$ in material with coarse microstructure at different time steps. Image a) ('initial') was recorded directly after applying the mechanical load.

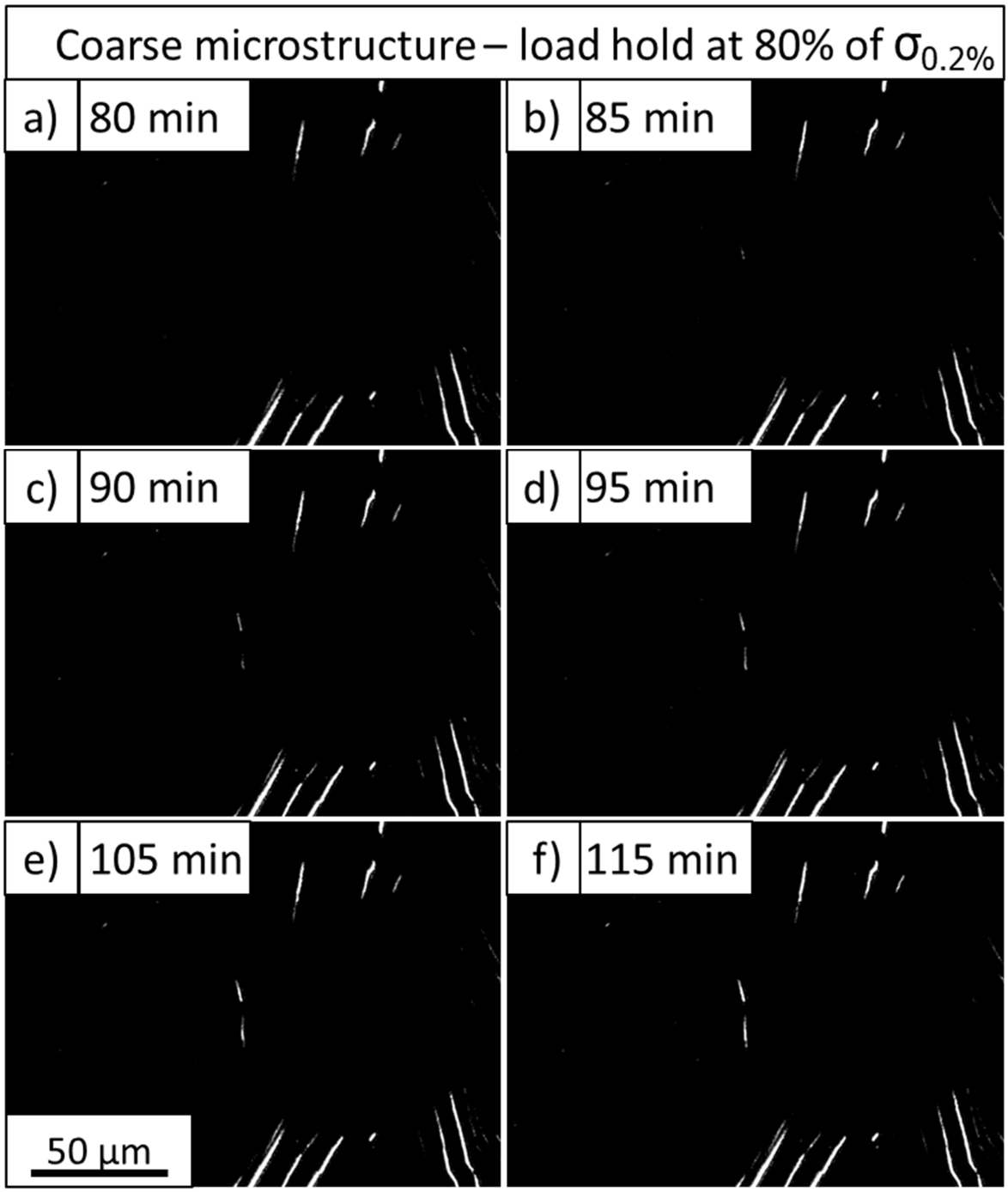

Fig. 7-19: Optical dark-field micrographs showing the appearance of a new slip trace in material with coarse microstructure during room temperature creep testing at 80% of $\sigma_{0.2\%}$ 80 minutes after applying the load.

8 Bibliography

[1] K. V. S. Srinadh and V. Singh, *Bull. Mater. Sci.*, vol. 27, no. 4, pp. 347–354, 2004.

[2] A. Kumar, N. Singh, and V. Singh, *Mater. Charact.*, vol. 51, no. 4, pp. 225–233, 2003.

[3] X. Wang, M. Jahazi, and S. Yue, *Mater. Sci. Eng. A*, vol. 434, no. 1–2, pp. 188–193, 2006.

[4] S. Hardt, H. J. Maier, and H. J. Christ, *Int. J. Fatigue*, vol. 21, no. 8, pp. 779–789, 1999.

[5] G. Lütjering and J. C. Williams, *Ed. Springer*, vol. second edi, pp. 1–442, 2007.

[6] V. S. Moxson, O. N. Senkov, and F. H. Froes, *Jom*, vol. 52, no. 5, pp. 24–26, 2000.

[7] L. Bolzoni, E. M. Ruiz-Navas, and E. Gordo, *Mater. Sci. Eng. A*, vol. 687, no. January, pp. 47–53, 2017.

[8] F. H. Froes, *Jom*, vol. 50, no. 9, pp. 41–43, 1998.

[9] B. Gunawarman, M. Niinomi, T. Akahori, T. Souma, M. Ikeda, and H. Toda, *Mater. Sci. Eng. C*, vol. 25, no. 3, pp. 304–311, 2005.

[10] A. D. Hartman, S. J. Gerdemann, J. S. Hansen, and P. C. Turner, *Jom*, vol. 50, no. 9, pp. 16–19, 1998.

[11] G. Crowley, *Adv. Mater. Process.*, no. November, p. 25, 2003.

[12] A. K. Sachdev, K. Kulkarni, Z. Z. Fang, R. Yang, and V. Girshov, *Jom*, vol. 64, no. 5, pp. 553–565, 2012.

[13] C. Cui, B. M. Hu, L. Zhao, and S. Liu, *Mater. Des.*, vol. 32, no. 3, pp. 1684–1691, 2011.

[14] M. Niinomi, *Encycl. Biomed. Eng.*, vol. 1–3, pp. 213–224, 2018.

[15] M. Peters, J. Hemptenmacher, J. Kumpfert, and C. Leyens, *Structure and Properties of Titanium and Titanium Alloys*. 2005.

[16] A. K. Gogia, *Def. Sci. J.*, vol. 55, no. 2, pp. 149–173, 2005.

[17] D. Eylon, S. Fujishiro, P. J. Postans, and F. H. Froes, *JOM J. Miner. Met. Mater. Soc.*, vol. 36, no. 11, pp. 55–62, 1984.

[18] G. Marsh, *Reinf. Plast.*, vol. 54, no. 6, pp. 20–24, 2010.

[19] M. Mandel and L. Krüger, *Materwiss. Werksttech.*, vol. 43, no. 4, pp. 302–309, 2012.

[20] B. Kolesnikov, L. Herbeck, and A. Fink, *Compos. Struct.*, vol. 83, no. 4, pp. 368–380, 2008.

[21] M. Hashish, *WJTA Am. Waterjet Conf.*, 2013.

[22] J. Horsley, *29th Jt. Propuls. Conf. Exhib.*, vol. AIAA 93-26, 1993.

[23] C. Ramachandra, A. K. Singh, and G. M. K. Sarma, *Metall. Trans. A*, vol. 24, no. 6, pp. 1273–1280, 1993.

[24] F. Yin and A. Gangoli Rao, *Aeronaut. J.*, vol. 121, no. 1245, pp. 1605–1626, 2017.

[25] I. Weiss and S. L. Semiatin, *Mater. Sci. Eng. A*, vol. 263, pp. 243–256, 1999.

[26] B. S. S. C. Rao, M. Srinivas, and S. V. Kamat, *Mater. Sci. Eng. A*, vol. 520, no. 1, pp. 29–35, 2009.

[27] N. Singh and V. Singh, *Mater. Sci. Eng. A*, vol. 325, no. 1–2, pp. 324–332, 2002.

[28] N. Singh, Gouthama, and V. Singh, *Int. J. Fatigue*, vol. 29, no. 5, pp. 843–851, 2007.

[29] Titanium Metal Corporation, 2020. [Online]. Available: https://www.timet.com/assets/local/documents/datasheets/alphaalloys/834.pdf. [Accessed: 27-Oct-2020].

[30] A. Radecka, J. Coakley, V. A. Vorontsov, T. L. Martin, P. A. J. Bagot, M. P. Moody, D. Rugg, and D. Dye, *Scr. Mater.*, vol. 117, pp. 81–85, 2016.

[31] P. S. Davies, The University of Sheffield, 2009.

[32] K. U. Yazar, S. Mishra, A. Karmakar, A. Bhattacharjee, and S. Suwas, *Metall. Mater. Trans. A Phys. Metall. Mater. Sci.*, 2020.

[33] M. J. Thomas, B. P. Wynne, and M. W. Rainforth, *Mater. Sci. Forum*, vol. 495–497, no. 0001, pp. 693–698, 2005.

[34] N. S. Reddy, C. S. Lee, J. H. Kim, and S. L. Semiatin, *Mater. Sci. Eng. A*, vol. 434, no. 1–2, pp. 218–226, 2006.

[35] M. . Bache, *Int. J. Fatigue*, vol. 25, no. 9, pp. 1079–1087, 2003.

[36] Y. W. Kim, *Jom*, vol. 41, no. 7, pp. 24–30, 1989.

[37] D. M. Dimiduk, *Mater. Sci. Eng. A*, vol. 263, no. 2, pp. 281–288, 1999.

[38] C. A. A. Stubbington and S. Pearson, *Eng. Fract. Mech.*, vol. 10, no. 4, pp. 723–756, Jan. 1978.

[39] BEA, 2020.

[40] H. M. Flower, *Mater. Sci. Technol.*, vol. 6, no. 11, pp. 1082–1092, 1990.

[41] D. Rugg, M. Dixon, and F. P. E. Dunne, *J. Strain Anal. Eng. Des.*, vol. 42, no. 4, pp. 269–279, 2007.

[42] Australian Transport Safety Bureau, *ATSB Transp. Saf. Rep.*, no. June, pp. 1–305, 2013.

[43] D. Rugg, T. B. Britton, J. Gong, A. J. Wilkinson, and P. A. J. Bagot, *Mater. Sci. Eng. A*, vol. 599, pp. 166–173, 2014.

[44] D. Rugg, D. Furrer, and N. Brewitt, *Mater. Process. Texture*, pp. 521–532, 2008.

[45] J. L. Murray, *Bull. Alloy Phase Diagrams*, vol. 2, no. 1, pp. 48–55, 1981.

[46] T. Bacci, G. Pradelli, B. Tesi, C. Badini, and C. Gianoglio, *Mater. Chem. Phys.*, vol. 25, no. 3, pp. 237–250, 1990.

[47] D. Banerjee and J. C. Williams, *Acta Mater.*, vol. 61, no. 3, pp. 844–879, 2013.

[48] A. Zarkades and F. R. Larson, *Elasticity of Titanium Sheet Alloys*. Pergamon Press Ltd, 1970.

[49] R. Boyer, G. Welsch, and E. W. Collings, ASM International.

[50] M. Kasemer, M. P. Echlin, J. C. Stinville, T. M. Pollock, and P. Dawson, *Acta Mater.*, vol. 136, pp. 288–302, 2017.

[51] J. W. Martin, *Mater. Eng.*, pp. 71–132, 2006.

[52] S. K. Kar, The Ohio State University, 2005.

[53] N. Gey, P. Bocher, E. Uta, L. Germain, and M. Humbert, *Acta Mater.*, vol. 60, no. 6–7, pp. 2647–2655, 2012.

[54] L. Germain, N. Gey, M. Humbert, P. Bocher, and M. Jahazi, *Acta Mater.*, vol. 53, no. 13, pp. 3535–3543, 2005.

[55] A. Moreau, L. Toubal, P. Bocher, M. Humbert, E. Uta, and N. Gey, 2013.

[56] D. G. Leo Prakash, P. Honniball, D. Rugg, P. J. Withers, J. Quinta da Fonseca, and M. Preuss, *Acta Mater.*, vol. 61, no. 9, pp. 3200–3213, 2013.

[57] E. Uta, N. Gey, P. Bocher, M. Humbert, and J. Gilgert, *J. Microsc.*, vol. 233, no. 3, pp. 451–459, 2009.

[58] M. Humbert, L. Germain, N. Gey, P. Bocher, and M. Jahazi, *Mater. Sci. Eng. A*, vol. 430, no. 1, pp. 157–164, 2006.

[59] M. J. Thomas, B. P. Wynne, and W. M. Rainforth, *Mater. Charact.*, vol. 55, no. 4–5, pp. 388–394, 2005.

[60] P. Bocher, M. Jahazi, L. Germain, P. Wanjara, N. Gey, and M. Humbert, *Solid State Phenom.*, vol. 105, pp. 127–132, 2005.

[61] L. Germain, N. Gey, M. Humbert, P. Vo, M. Jahazi, and P. Bocher, *Acta Mater.*, vol. 56, no. 16, pp. 4298–4308, 2008.

[62] D. Qiu, R. Shi, D. Zhang, W. Lu, and Y. Wang, *Acta Mater.*, vol. 88, pp. 218–231, 2015.

[63] M. G. Glavicic, P. A. Kobryn, T. R. Bieler, and S. L. Semiatin, vol. 346, pp. 50–59, 2003.

[64] M. Whittaker, P. Jones, C. Pleydell-Pearce, D. Rugg, and S. Williams, *Mater. Sci. Eng. A*, vol. 527, no. 24, pp. 6683–6689, 2010.

[65] N. Singh and V. Singh, *Mater. Sci. Eng. A*, vol. 485, no. 1, pp. 130–139, 2008.

[66] M. L. Thomsen and D. W. Hoeppner, *Int. J. Fatigue*, vol. 20, no. 4, pp. 309–317, 1998.

[67] A. K. Singh and C. Ramachandra, *J. Mater. Sci.*, vol. 32, no. 1, pp. 229–234, 1997.

[68] A. Radecka, P. A. J. Bagot, T. L. Martin, J. Coakley, V. A. Vorontsov, M. P. Moody, H. Ishii, D. Rugg, and D. Dye, *Acta Mater.*, vol. 112, pp. 141–149, 2016.

[69] G. Lütjering and S. Weissmann, *Acta Metall.*, vol. 18, no. 7, pp. 785–795, Jul. 1970.

[70] L. R. Zeng, H. L. Chen, X. Li, L. M. Lei, and G. P. Zhang, *J. Mater. Sci. Technol.*, vol. 34, no. 5, pp. 782–787, 2018.

[71] A. Singh, I. Balasundar, J. P. Gautam, and T. Raghu, *Procedia Struct. Integr.*, vol. 14, pp. 78–88, 2019.

[72] M. Legros, A. Couret, and D. Caillard, *J. Mater. Sci.*, vol. 41, no. 9, pp. 2647–2657, 2006.

[73] S. Hémery and P. Villechaise, *Scr. Mater.*, vol. 130, pp. 157–160, Mar. 2017.

[74] K. Tanaka, K. Okamoto, H. Inul, Y. Mlnonishl, M. Yamaguch, and M. Koiwa, *Philos. Mag. A Phys. Condens. Matter, Struct. Defects Mech. Prop.*, vol. 73, no. 5, pp. 1475–1488, 1996.

[75] A. Gysler and S. Weissmann, *Mater. Sci. Eng.*, vol. 27, no. 2, pp. 181–193, 1977.

[76] K. V. S. a I. Srinadh, N. Singh, and V. Singh, *Bull. Mater. Sci.*, vol. 30, no. 6, pp. 595–600, 2007.

[77] B. Borchert and M. Daeubler, in *Sixth World Conference on Titanium. I*, 1988, pp. 467–472.

[78] D. Lunt, T. Busolo, X. Xu, J. Quinta da Fonseca, and M. Preuss, *Acta Mater.*, vol. 129, pp. 72–82, May 2017.

[79] S. L. Semiatin, V. Seetharaman, and I. Weiss, *Jom*, vol. 49, no. 6, pp. 33–39, 1997.

[80] G. Lütjering, *Mater. Sci. Eng. A*, vol. 243, no. 1, pp. 32–45, 1998.

[81] A. Mitchell, *Jom*, vol. 49, no. 6, pp. 40–42, 1997.

[82] G. C. Obasi, S. Birosca, D. G. Leo Prakash, J. Quinta da Fonseca, and M. Preuss, *Acta Mater.*, vol. 60, no. 17, pp. 6013–6024, 2012.

[83] G. C. Obasi, R. J. Moat, D. G. Leo Prakash, W. Kockelmann, J. Quinta da Fonseca, and M. Preuss, *Acta Mater.*, vol. 60, no. 20, pp. 7169–7182, 2012.

[84] I. Balasundar, T. Raghu, and B. P. Kashyap, *Int. J. Mater. Form.*, vol. 8, no. 1, pp. 85–97, 2015.

[85] V. Chandravanshi, K. Prasad, V. Singh, A. Bhattacharjee, and V. Kumar, *Int. J. Fatigue*, vol. 91, pp. 100–109, 2016.

[86] K. Muszka, M. Lopez-Pedrosa, K. Raszka, M. Thomas, W. M. Rainforth, and B. P. Wynne, *Metall. Mater. Trans. A Phys. Metall. Mater. Sci.*, vol. 45, no. 13, pp. 5997–6007, 2014.

[87] O. N. Senkov, J. J. Valencia, S. V Senkova, M. Cavusoglu, and F. H. Froes, *Mater. Sci. Technol.*, vol. 18, no. 12, pp. 1471–1478, 2002.

[88] A. A. Salem, J. B. Shaffer, D. P. Satko, S. L. Semiatin, and S. R. Kalidindi, *Integr. Mater. Manuf. Innov.*, vol. 3, no. 1, pp. 322–343, 2014.

[89] I. Bantounas, D. Dye, and T. C. Lindley, *Acta Mater.*, vol. 58, no. 11, pp. 3908–3918, 2010.

[90] H. Wu, Z. Sun, J. Cao, and Z. Yin, *J. Mater. Eng. Perform.*, vol. 28, no. 2, pp. 788–799, 2019.

[91] D.-G. Lee, S. Lee, C. S. Lee, and S. Hur, *J. Kor. Inst. Met. Mater.*, vol. 39, no. 12, pp. 1406–1413, 2001.

[92] E. Schmid and W. Boas, *Hughes Co., London*, 1950.

[93] F. Bridier, P. Villechaise, and J. Mendez, *Acta Mater.*, vol. 53, no. 3, pp. 555–567, 2005.

[94] Z. Zhang, T. S. Jun, T. B. Britton, and F. P. E. Dunne, *J. Mech. Phys. Solids*, vol. 95, pp. 393–410, 2016.

[95] Z. Zheng, S. Waheed, D. S. Balint, and F. P. E. Dunne, *Int. J. Plast.*, vol. 104, pp. 23–38, May 2018.

[96] F. D. Rosi, F. C. Perkins, and L. L. Seigle, *Jom*, vol. 8, no. 2, pp. 115–122, 1956.

[97] R. V. Mises, *ZAMM - Zeitschrift für Angew. Math. und Mech.*, vol. 8, no. 3, pp. 161–185,

1928.

[98] T. B. Britton, F. P. E. Dunne, and A. J. Wilkinson, *Proc. R. Soc. A Math. Phys. Eng. Sci.*, vol. 471, no. 2178, pp. 20140881–20140881, 2015.

[99] P. G. Partridge, *Metall. Rev.*, vol. 12, no. 1, pp. 169–194, Jan. 1967.

[100] J. C. Williams, R. G. Baggerly, and N. E. Paton, *Metall. Mater. Trans. A Phys. Metall. Mater. Sci.*, vol. 33, no. 13, pp. 837–850, 2002.

[101] R. Ding, J. Gong, A. J. Wilkinson, and I. P. Jones, *Acta Mater.*, vol. 76, pp. 127–134, 2014.

[102] S. Suri, G. B. Viswanathan, T. Neeraj, D.-H. Hou, and M. J. Mills, *Acta Mater.*, vol. 47, no. 3, pp. 1019–1034, 1999.

[103] S. Naka and A. Lasalmonie, *J. Mater. Sci.*, vol. 18, no. 9, pp. 2613–2617, 1983.

[104] D. B. Williams and C. B. Carter, in *Transmission electron microscopy*, Springer, 1996, pp. 3–17.

[105] A. Akhtar and E. Teghtsoonian, *Metall. Mater. Trans. A*, vol. 6, no. 12, pp. 2201–2208, 1975.

[106] A. Akhtar, *Metall. Trans. A*, vol. 6, no. 5, pp. 1105–1113, 1975.

[107] S. Naka, A. Lasalmonie, P. Costa, L. P. Kubin, and L. P. Kubin, *Philos. Mag. A Phys. Condens. Matter, Struct. Defects Mech. Prop.*, vol. 57, no. 5, pp. 717–740, 1988.

[108] X. Xu, D. Lunt, R. Thomas, R. P. Babu, A. Harte, M. Atkinson, J. Q. da Fonseca, and M. Preuss, *Acta Mater.*, vol. 175, pp. 376–393, 2019.

[109] H. Conrad, *Prog. Mater. Sci.*, vol. 26, no. 2–4, pp. 123–403, 1981.

[110] I. P. Jones and W. B. Hutchinson, *Acta Metall.*, vol. 29, no. 6, pp. 951–968, 1981.

[111] A. A. Pochettino, N. Gannio, C. V. Edwards, and R. Penelle, *Scr. Metall. Mater. States)*, vol. 27, no. 12, pp. 463–466, 1992.

[112] A. Fitzner, D. G. L. Prakash, J. Q. Da Fonseca, M. Thomas, S. Y. Zhang, J. Kelleher, P. Manuel, and M. Preuss, *Acta Mater.*, vol. 103, pp. 341–351, 2016.

[113] C. Lavogiez, S. Hémery, and P. Villechaise, *Int. J. Fatigue*, vol. 131, no. July 2019, p. 105341, 2019.

[114] S. Hémery, A. Naït-Ali, M. Guéguen, J. Wendorf, A. T. Polonsky, M. P. Echlin, J. C. Stinville, T. M. Pollock, and P. Villechaise, *Acta Mater.*, vol. 181, pp. 36–48, 2019.

[115] S. Hémery, P. Nizou, and P. Villechaise, *Mater. Sci. Eng. A*, vol. 709, pp. 277–284, Jan. 2018.

[116] S. Hémery and P. Villechaise, *Mater. Sci. Eng. A*, vol. 697, pp. 177–183, Jun. 2017.

[117] S. Hémery, A. Nait-Ali, and P. Villechaise, *Mech. Mater.*, vol. 109, pp. 1–10, Jun. 2017.

[118] S. Hémery, V. T. Dang, L. Signor, and P. Villechaise, *Metall. Mater. Trans. A*, vol. 49, no. 6, pp. 2048–2056, Jun. 2018.

[119] M. F. Savage, J. Tatalovich, and M. J. Mills, *Philos. Mag.*, vol. 84, no. 11, pp. 1127–1154, 2004.

[120] H. Li, D. E. Mason, T. R. Bieler, C. J. Boehlert, and M. A. Crimp, *Acta Mater.*, 2013.

[121] M. F. Savage, J. Tatalovich, M. Zupan, K. J. Hemker, and M. J. Mills, *Mater. Sci. Eng. A*, vol. 319–321, pp. 398–403, 2001.

[122] T. S. Jun, G. Sernicola, F. P. E. Dunne, and T. B. Britton, *Mater. Sci. Eng. A*, vol. 649, pp. 39–47, 2016.

[123] J. Gong and A. J. Wilkinson, *Acta Mater.*, vol. 57, no. 19, pp. 5693–5705, 2009.

[124] Y. Xiong, P. Karamched, C.-T. Nguyen, C. M. Magazzeni, E. Tarleton, and A. J. Wilkinson, *SSRN Electron. J.*, 2020.

[125] P. R. Dawson, D. E. Boyce, J. S. Park, E. Wielewski, and M. P. Miller, *Acta Mater.*, vol. 144, pp. 92–106, 2018.

[126] S. Hémery and P. Villechaise, *Acta Mater.*, vol. 141, pp. 285–293, Dec. 2017.

[127] S. Hémery and P. Villechaise, *Metall. Mater. Trans. A Phys. Metall. Mater. Sci.*, vol. 49, no.

10, pp. 4394–4397, 2018.

[128] F. Benmessaoud, M. Cheikh, V. Velay, V. Vidal, and H. Matsumoto, *Mater. Sci. Eng. A*, vol. 774, no. December 2019, p. 138835, 2020.

[129] W. B. Hutchinson and M. R. Barnett, *Scr. Mater.*, vol. 63, no. 7, pp. 737–740, 2010.

[130] M. P. Echlin, J. C. Stinville, V. M. Miller, W. C. Lenthe, and T. M. Pollock, *Acta Mater.*, vol. 114, pp. 164–175, Aug. 2016.

[131] D. Lunt, J. Q. Fonseca, D. Rugg, and M. Preuss, *Mater. Sci. Eng. A*, no. April, pp. 1–34, 2016.

[132] T. S. Jun, Z. Zhang, G. Sernicola, F. P. E. Dunne, and T. B. Britton, *Acta Mater.*, vol. 107, pp. 298–309, 2016.

[133] Z. Zhang, T. S. Jun, T. B. Britton, and F. P. E. Dunne, *Acta Mater.*, vol. 118, pp. 317–330, 2016.

[134] S. Hémery and P. Villechaise, *Acta Mater.*, vol. 171, pp. 261–274, 2019.

[135] M. Bache, *Int. J. Fatigue*, vol. 19, no. 93, pp. 83–88, 1997.

[136] A. Ready, P. Haynes, B. Grabowski, D. Rugg, and A. Sutton, *Proc.R.Soc.A*, vol. 473, no. 2203, 2017.

[137] Z. Zhang, M. A. Cuddihy, and F. P. . Dunne, *Proc.R.Soc.A*, 2015.

[138] W. J. Evans and M. R. Bache, *Int. J. Fatigue*, vol. 16, no. 7, pp. 443–452, 1994.

[139] F. P. E. Dunne and D. Rugg, *Fatigue Fract. Eng. Mater. Struct.*, vol. 31, no. 11, pp. 949–958, 2008.

[140] Z. Song and D. W. Hoeppner, *Int. J. Fatigue*, vol. 10, no. 4, pp. 211–218, 1988.

[141] M. A. Cuddihy, A. Stapleton, S. Williams, and F. P. E. Dunne, *Int. J. Fatigue*, vol. 97, pp. 177–189, 2017.

[142] T. Goswami, *Int. J. Fatigue*, vol. 21, no. 1, pp. 55–76, 1999.

[143] E. E. Sackett, L. Germain, and M. R. Bache, *Int. J. Fatigue*, vol. 29, no. 9–11, pp. 2015–2021, 2007.

[144] P. O. Tympel, T. C. Lindley, E. A. Saunders, M. Dixon, and D. Dye, *Acta Mater.*, vol. 103, pp. 77–88, 2016.

[145] J. Qiu, Y. Ma, J. Lei, Y. Liu, A. Huang, D. Rugg, and R. Yang, *Metall. Mater. Trans. A Phys. Metall. Mater. Sci.*, vol. 45, no. 13, pp. 6075–6087, 2014.

[146] Z. Zheng, D. S. Balint, and F. P. E. Dunne, *J. Mech. Phys. Solids*, vol. 107, pp. 185–203, 2017.

[147] H. H. Stroh, *R. Soc. R. Sci. Phys.*, 1954.

[148] F. P. E. Dunne, D. Rugg, and A. Walker, *Int. J. Plast.*, vol. 23, no. 6, pp. 1061–1083, 2007.

[149] M. R. Bache, W. J. Evans, B. Suddell, and F. R. M. Herrouin, *Int. J. Fatigue*, vol. 23, pp. 153–159, 2001.

[150] V. Sinha, M. J. Mills, and J. C. Williams, *Metall. Mater. Trans. A Phys. Metall. Mater. Sci.*, vol. 37, no. 6, pp. 2015–2026, 2006.

[151] S. K. Jha, C. J. Szczepanski, P. J. Golden, W. J. Porter, and R. John, *Int. J. Fatigue*, vol. 42, pp. 248–257, 2012.

[152] G. Venkatramani, S. Ghosh, and M. Mills, *Acta Mater.*, vol. 55, no. 11, pp. 3971–3986, Jun. 2007.

[153] S. Waheed, Z. Zheng, D. S. Balint, and F. P. E. Dunne, *Acta Mater.*, vol. 162, pp. 136–148, 2019.

[154] I. Bantounas, D. Dye, and T. C. Lindley, *Acta Mater.*, vol. 57, no. 12, pp. 3584–3595, 2009.

[155] Y. Guo, T. B. Britton, and A. J. Wilkinson, *Acta Mater.*, vol. 76, pp. 1–12, 2014.

[156] F. Bridier, P. Villechaise, and J. Mendez, *Acta Mater.*, vol. 56, no. 15, pp. 3951–3962, 2008.

[157] D. Lunt, X. Xu, T. Busolo, J. Quinta da Fonseca, and M. Preuss, *Scr. Mater.*, vol. 145, pp. 45–49, 2018.

[158] T. Neeraj, D.-H. Hou, G. S. Daehn, and M. J. Mills, *Acta Mater.*, vol. 48, no. 6, pp. 1225–1238, Apr. 2000.

[159] B. C. Odegard and A. W. Thompson, *Metall. Trans.*, vol. 5, no. 5, pp. 1207–1213, 1974.

[160] M. A. Imam and C. M. Gilmore, *Metall. Trans. A*, vol. 10, no. 4, pp. 419–425, 1979.

[161] A. W. Thompson and B. C. Odegard, *Metall. Trans.*, vol. 4, no. 4, pp. 899–908, 1973.

[162] W. J. Harrison, M. T. Whittaker, and R. J. Lancaster, *Mater. Sci. Eng. A*, vol. 574, pp. 130–136, Jul. 2013.

[163] H. P. Chu, *NASA Tech. Memo. 104641*, pp. 1–14, 1997.

[164] W. H. Miller, R. T. Chen, and E. A. Starke, *Metall. Trans. A*, vol. 18, no. 8, pp. 1451–1468, 1987.

[165] T. Neeraj and M. . Mills, *Mater. Sci. Eng. A*, vol. 319–321, pp. 415–419, Dec. 2001.

[166] K. Prasad, R. Sarkar, P. Ghosal, D. V. V. Satyanarayana, S. V. Kamat, and T. K. Nandy, *Mater. Sci. Eng. A*, vol. 528, no. 22–23, pp. 6733–6741, 2011.

[167] C. Dichtl, Z. Zhang, H. Gardner, P. Bagot, A. Radecka, D. Dye, M. Thomas, R. Sandala, J. Q. da Fonseca, and M. Preuss, *Mater. Charact.*, vol. 164, p. 110327, Jun. 2020.

[168] H. Modin and S. Modin, *Metall. Microsc.*, no. 1, pp. 24–112, 1973.

[169] H. Modin and S. Modin, *Metall. Microsc.*, pp. 1–23, 1973.

[170] J. Schindelin, I. Arganda-Carreras, E. Frise, V. Kaynig, M. Longair, T. Pietzsch, S. Preibisch, C. Rueden, S. Saalfeld, B. Schmid, J.-Y. Tinevez, D. J. White, V. Hartenstein, K. Eliceiri, P. Tomancak, and A. Cardona, *Nat. Methods*, vol. 9, p. 676, Jun. 2012.

[171] A. Bogner, P. H. Jouneau, G. Thollet, D. Basset, and C. Gauthier, *Micron*, vol. 38, no. 4, pp. 390–401, 2007.

[172] F. Krumeich, *Lab. Inorg. Chem. disponível e*, pp. 3–8, 2011.

[173] L. H. Veneklasen and B. M. Siegel, *J. Appl. Phys.*, vol. 43, no. 12, pp. 4989–4996, 1972.

[174] G. E. Lloyd, *Mineral. Mag.*, vol. 51, no. 359, pp. 3–19, 1987.

[175] D. C. Joy, *J. Microsc.*, vol. 136, no. 2, pp. 241–258, 1984.

[176] D. J. Dingley and D. P. Field, *Mater. Sci. Technol.*, vol. 13, no. 1, pp. 69–78, 1997.

[177] W. Reuter, vol. 25, pp. 80–119, 1971.

[178] J. T. Sagar, S. R. Burgess, C. McCarthy, and X. Li, *Microelectron. Reliab.*, vol. 64, pp. 367–369, 2016.

[179] S. Burgess, J. Sagar, J. Holland, X. Li, and F. Bauer, *Micros. Today*, vol. 25, no. 2, pp. 20–29, 2017.

[180] M. Klerk, *Philips Tech. Rev.*, vol. 34, no. 11–12, pp. 370–374, 1974.

[181] H. E. Çubukçu, O. Ersoy, E. Aydar, and U. Çakir, *Micron*, vol. 39, no. 2, pp. 88–94, 2008.

[182] D. Drouin, A. R. Couture, D. Joly, X. Tastet, V. Aimez, and R. Gauvin, *Scanning J. Scanning Microsc.*, vol. 29, no. 3, pp. 92–101, 2007.

[183] D. Drouin, A. R. Couture, and R. Gauvin, Universite de Sherbrooke, Quebec, Canada, 2011.

[184] F. Di Gioacchino and J. Quinta da Fonseca, *Exp. Mech.*, vol. 53, no. 5, pp. 743–754, 2013.

[185] N. Mori, T. Oikawa, T. Katoh, J. Miyahara, and Y. Harada, *Ultramicroscopy*, vol. 25, no. 3, pp. 195–201, 1988.

[186] B. H. Armstrong, *J. Quant. Spectrosc. Radiat. Transf.*, vol. 7, no. 1, pp. 61–88, Jan. 1967.

[187] M. K. Miller, *Atom probe tomography: analysis at the atomic level*. Springer Science & Business Media, 2012.

[188] T. F. Kelly and M. K. Miller, *Rev. Sci. Instrum.*, vol. 78, no. 3, 2007.

[189] B. Gault, M. P. Moody, J. M. Cairney, and S. P. Ringer, *Atom probe microscopy*, vol. 160. Springer Science & Business Media, 2012.

[190] K. Thompson, D. Lawrence, D. J. Larson, J. D. Olson, T. F. Kelly, and B. Gorman,

Ultramicroscopy, vol. 107, no. 2–3, pp. 131–139, 2007.

[191] O. C. Hellman, J. A. Vandenbroucke, J. Rüsing, D. Isheim, and D. N. Seidman, *Microsc. Microanal.*, vol. 6, no. 05, pp. 437–444, 2000.

[192] D. J. Larson, T. Prosa, R. M. Ulfig, B. P. Geiser, and T. F. Kelly, *New York, US Springer Sci.*, 2013.

[193] T. Homma, A. Arafah, D. Haley, M. Nakai, M. Niinomi, and M. P. Moody, *Mater. Sci. Eng. A*, vol. 709, pp. 312–321, Jan. 2018.

[194] C. A. Williams, D. Haley, E. A. Marquis, G. D. W. Smith, and M. P. Moody, *Ultramicroscopy*, vol. 132, pp. 271–278, 2013.

[195] ASTM International - B348-13, pp. 1–8, 2014.

[196] ASTM International - E8/E8M 16a, pp. 1–27, 2009.

[197] P. Thévenaz, U. E. Ruttimann, and M. Unser, *IEEE Trans. Image Process.*, vol. 7, no. 1, pp. 27–41, 1998.

[198] Y. Luo, J. Ruff, R. Ray, Y. Gu, H. J. Ploehn, and W. A. Scrivens, *Chem. Mater.*, vol. 17, no. 20, pp. 5014–5023, 2005.

[199] M. A. Sutton, N. Li, D. Garcia, N. Cornille, J. J. Orteu, S. R. McNeill, H. W. Schreier, X. Li, and A. P. Reynolds, *Exp. Mech.*, vol. 47, no. 6, pp. 789–804, 2007.

[200] J. T. L. Thong, K. W. Lee, and W. K. Wong, *Scanning*, vol. 23, no. 6, pp. 395–402, 2001.

[201] P. Tomancak, S. Preibisch, and S. Saalfeld, *Bioinformatics*, vol. 25, no. 11, pp. 1463–1465, 2009.

[202] La Vision - Germany, [Online]. Available: https://www.lavision.de/en/company.php. [Accessed: 27-Oct-2020].

[203] *MechMicroMan/DefDAP, Mechanics of microstructures at Manchester*, 2020. [Online]. Available: https://github.com/MechMicroMan/DefDAP. [Accessed: 27-Oct-2020].

[204] C. R. Harris *et al.*, *Nature*, vol. 585, no. 7825, pp. 357–362, 2020.

[205] C. M. Cepeda-Jiménez, J. M. Molina-Aldareguia, and M. T. Pérez-Prado, *Jom*, vol. 68, no. 1, pp. 116–126, 2016.

[206] D. Lunt, R. Thomas, M. Roy, J. Duff, M. Atkinson, P. Frankel, M. Preuss, and J. Quinta da Fonseca, *Mater. Charact.*, vol. 163, no. November 2019, p. 110271, 2020.

[207] Z. Chen and S. H. Daly, *Exp. Mech.*, vol. 57, no. 1, pp. 115–127, Jan. 2017.

[208] X. Cheng, G. Wu, and J. Zhao, pp. 828–832, 2013.

[209] F. Roters, P. Eisenlohr, C. Kords, D. D. Tjahjanto, M. Diehl, and D. Raabe, *Procedia IUTAM*, vol. 3, pp. 3–10, 2012.

[210] F. Roters, P. Eisenlohr, T. Bieler, and D. Raabe, *Crystal Plasticity Finite Element Methods*. 2010.

[211] F. Roters, P. Eisenlohr, L. Hantcherli, D. D. Tjahjanto, T. R. Bieler, and D. Raabe, *Acta Mater.*, vol. 58, no. 4, pp. 1152–1211, 2010.

[212] R. A. Lebensohn, A. D. Rollett, and P. Suquet, *Jom*, vol. 63, no. 3, pp. 13–18, 2011.

[213] R. A. Lebensohn, A. K. Kanjarla, and P. Eisenlohr, *Int. J. Plast.*, vol. 32–33, pp. 59–69, 2012.

[214] A. Ambard, L. Guétaz, F. Louchet, and D. Guichard, *Mater. Sci. Eng. A*, vol. 319–321, pp. 404–408, 2001.

[215] E. Héripré, M. Dexet, J. Crépin, L. Gélébart, A. Roos, M. Bornert, and D. Caldemaison, *Int. J. Plast.*, vol. 23, no. 9, pp. 1512–1539, 2007.

[216] T. Maiti and P. Eisenlohr, *Scr. Mater.*, vol. 145, pp. 37–40, 2018.

[217] R. R. Pawar and V. T. Deshpande, *Acta Crystallogr. Sect. A*, vol. 24, no. 2, pp. 316–317, 1968.

[218] X. Gao, W. Zeng, S. Zhang, and Q. Wang, *Acta Mater.*, vol. 122, pp. 298–309, 2017.